Coastal Flooding & Storm Protection
Program Field Verification Program

MATHEMATICAL MODELING
OF THREE-DIMENSIONAL COASTAL
CURRENTS AND SEDIMENT DISPERSION:
MODEL DEVELOPMENT AND APPLICATION

BY

Y.P. SHENG

WOODS HOLE OCEANOGRAPHIC INSTITUTION

Woods Hole, Massachusetts

CERC-83-2

MATHEMATICAL MODELING
OF THREE-DIMENSIONAL COASTAL
CURRENTS AND SEDIMENT DISPERSION:
MODEL DEVELOPMENT AND APPLICATION

by

Y. P. Sheng

Aeronautical Research Associates of Princeton, Inc.
50 Washington Road, P. O. Box 2229
Princeton, N. J. 08540

WHOI
DOCUMENT
COLLECTION

Dr. William D. Grant

**US Army Corps
of Engineers**

MBL/WHOI

0 0301 0072117 1

REPORT DOCUMENTATION PAGE		READ INSTRUCTIONS BEFORE COMPLETING FORM
1. REPORT NUMBER Technical Report CERC-83-2	2. GOVT ACCESSION NO.	3. RECIPIENT'S CATALOG NUMBER
4. TITLE (and Subtitle) MATHEMATICAL MODELING OF THREE-DIMENSIONAL COASTAL CURRENTS AND SEDIMENT DISPERSION: MODEL DEVELOPMENT AND APPLICATION		5. TYPE OF REPORT & PERIOD COVERED Final report
		6. PERFORMING ORG. REPORT NUMBER
7. AUTHOR(s) Y. P. Sheng		8. CONTRACT OR GRANT NUMBER(s) Contract No. DACW39-80-C-0087
9. PERFORMING ORGANIZATION NAME AND ADDRESS Aeronautical Research Associates of Princeton, Inc. 50 Washington Road, P. O. Box 2229 Princeton, N. J. 08540		10. PROGRAM ELEMENT, PROJECT, TASK AREA & WORK UNIT NUMBERS Coastal Flooding and Storm Protection Program; Field Verification Program
11. CONTROLLING OFFICE NAME AND ADDRESS Office, Chief of Engineers, U. S. Army Washington, D. C. 20314		12. REPORT DATE September 1983
		13. NUMBER OF PAGES 297
14. MONITORING AGENCY NAME & ADDRESS(if different from Controlling Office) U. S. Army Engineer Waterways Experiment Station Hydraulics Laboratory P. O. Box 631, Vicksburg, Miss. 39180		15. SECURITY CLASS. (of this report) Unclassified
		15a. DECLASSIFICATION/DOWNGRADING SCHEDULE

16. DISTRIBUTION STATEMENT (of this Report)

Approved for public release; distribution unlimited.

17. DISTRIBUTION STATEMENT (of the abstract entered in Block 20, if different from Report)

18. SUPPLEMENTARY NOTES
Available from National Technical Information Service, 5285 Port Royal Road, Springfield, Va. 22161.

19. KEY WORDS (Continue on reverse side if necessary and identify by block number)

Circulation	Sediment transport	Turbulence
Coastal currents	Simulation	Variable grid
Hydrodynamics	Three-dimensional model	Waves
Mississippi Sound	Tides	

20. ABSTRACT (Continue on reverse side if necessary and identify by block number)

    A comprehensive model of coastal currents and sediment dispersion has been formulated and applied to the Mississippi Sound and adjacent continental shelf waters. The study combines mathematical modeling of various hydrodynamic and sedimentary processes with laboratory and field experiments. Of primary importance is the development of an efficient and comprehensive three-dimensional, finite-difference model of Coastal, Estuarine, and Lake Currents (CELC3D). The model resolves currents driven by tide, wind, and density
(Continued)

DD FORM 1473 EDITION OF 1 NOV 65 IS OBSOLETE
1 JAN 73

20. ABSTRACT (Concluded)

gradient. It has been spplied to the Mississippi Sound, and results agree
well with measured surface displacements and currents during two episodes.

Rates of entrainment and deposition of the Mississippi Sound sedi-
ments have been studied in a laboratory flume. Effects of (1) bottom
shear stress, (2) bed properties, (3) salinity of water, and (4) sediment
type on the erodability of sediments have been examined. Results of the
laboratory study have been incorporated into the bottom boundary conditions
for a three-dimensional sediment dispersion model. Gravitational settling
and particle size distribution of the Mississippi Sound sediments were
also studied in laboratories.

Bottom boundary layer dynamics and wave effect on sediment dispersion
have been studied by means of a turbulent transport model and a wave model.
Model simulations of sediment dispersion in the Mississippi Sound agree
well with available data from ship surveys.

PREFACE

i

The FVP Project Manager was Dr. R. Peddicord, Environmental Laboratory (EL), WES, under the general supervision of Dr. R. Engler, Chief, Contaminant Mobility and Regulatory Criteria Group; Mr. D. Robey, Chief, Ecosystem Research and Simulation Division; and Dr. J. Harrison, Chief, EL. The FVP is managed in EL through the Office of Environmental Effects of Dredging Programs, Mr. C. C. Calhoun, Jr., Manager. Technical Monitors of the FVP were Dr. J. Hall, Operations Division, OCE, and Dr. W. Klesch, Planning Division, OCE.

Commanders and Directors of WES during contract performance and the publication of this report were COL John L. Cannon, CE, COL Nelson P. Conover, CE, and COL Tilford C. Creel, CE. Technical Director was Mr. F. R. Brown.

ii

MATHEMATICAL MODELING OF THREE-DIMENSIONAL COASTAL CURRENTS
AND SEDIMENT DISPERSION

TABLE OF CONTENTS

LIST OF FIGURES

vii

.

LIST OF TABLES

LIST OF SYMBOLS

A	matrix defined in Eq. (3.2); also mean tidal amplitude in (5.1)
A_H	lateral eddy viscosity
A_v	vertical eddy viscosity
A_{vo}	vertical eddy viscosity in neutrally stratified water
A_x	expression defined in Eq. (2.8)
A_y	expression defined in Eq. (2.9)
a	tidal amplitude
a_o	acceleration of a dissipation eddy
a_{ij}	coefficients for the equation of state
a_x, a_y	coefficients in Eq. (2.22) for horizontal grid stretching
a_λ	acceleration of an eddy with length scale λ
B	matrix defined in Eq. (3.2)
B_x, B_y	expressions defined in Eq. (2.25) and (2.26), respectively
b_x, b_y	coefficients in Eq. (2.22) for horizontal grid stretching
C	concentration of suspended sediments
C_c	Chezy coefficient
C_d	bottom drag coefficient
C_{da}	wind stress drag coefficient
C_{eq}	equilibrium concentration
c_f	skin friction coefficient
c_x, c_y	coefficients in Eq. (2.22) for horizontal grid stretching
D	reference length scale in the vertical direction; also vector in Eq. (3.2)
D_B	Brownian diffusion coefficient
D_H	lateral eddy diffusivity
D_v	vertical eddy diffusivity of sediments

xiii

D_{vo}	vertical eddy diffusivity in neutrally stratified water
D_x, D_y	expressions defined in Eq. (2.37) and (2.38), respectively
d	depth of frictional influence
E	rate of entrainment of sediment
E_H	horizontal Ekman number
E_v	vertical Ekman number
e	collision efficiency
F	nodal factor
F_c	friction coefficient
Fr	Froude number
Fr_i	internal Froude number
f	Coriolis parameter
G	Greenwich phase or epoch
G_o	shearing rate of dissipation eddy
G_λ	shearing rate of an eddy with length scale λ
g	gravitational acceleration
H	water depth plus surface displacement
h	mean water depth
I	grid index in the x-direction; also unity matrix
J	grid index in the y-direction
K	grid index in the z-direction
K_H	lateral thermal diffusivity
K_v	vertical thermal diffusivity

K_{vo}	vertical thermal diffusivity in neutrally stratified water
k	von-Karman constant
L	reference length in the horizontal direction; also Monin-Obukhov similarity length
m	integer
m_1, m_2, m_3	coefficients used in defining ϕ_1, ϕ_2, and ϕ_3
N	Brünt-Vaisala period; also collision rate
n	Mannings' n
n_1, n_2	number density of sediment particles
p	pressure in water
p_a	atmospheric pressure
Pr	Prandtl number
Pr_v	vertical Prandtl number
q	square root of twice the turbulent kinetic energy
r	radius of particles
r_c	critical radius of particles
r_{12}	radius of collision cylinder
R_h	hydrodynamic resistance to deposition
R_s	sublayer resistance
Ri	Richardson number
Ro	Rossby number
S	salinity; also source term
Sc	Schmidt number

Sc_H	lateral Schmidt number
Sc_v	vertical Schmidt number
T	temperature or tidal period
T_1, T_2, T_3, T_4	characteristic time scales associated with time-dependent, wind-driven motion in a shallow sea
T_f, T_c, T_i, T_{dh}, T_{dv}, T_e, T_g, T_{gi}	time scales defined in Table 2.3
t	time
U	vertically-integrated velocity in the x-direction
u	velocity in the x-direction
u_1	x-velocity at z_1 above the bottom
u_{100}	x-velocity at 100 cm above the bottom
u_w	wind velocity in the x-direction
u_{wa}	wave orbital velocity
u_*	friction velocity
u'	$\equiv u - U/H$
V	vertically-integrated velocity in the y-direction
v	velocity in the y-direction
v_1	y-velocity at z_1 above the bottom
v_d	deposition velocity
v_w	wind velocity in the y-direction
v'	$\equiv v - V/H$
W	vector defined in Eq. (3.2)

W^*	intermediate solution of the external mode algorithm
w	vertical velocity in the z-direction
w_s	settling velocity of sediments
x	horizontal coordinate
y	horizontal coordinate
z	vertical coordinate
z_o	roughness length
z_1	reference height above the bottom
α	horizontally stretched coordinate corresponding to x
α_v	coefficient of volumetric expansion
β	$\equiv gD/L^2 f^2$
γ	horizontally stretched coordinate corresponding to y
ϵ	dissipation rate of turbulence
ϵ_{ijK}	alternating tensor
ρ	density
σ	vertically stretched coordinate
σ_1, σ_2, σ_3	coefficients used in defining ϕ_1, ϕ_2 and ϕ_3
σ_t	density anomaly
Λ	macroscale of turbulent eddies
λ	length scale of turbulent eddy; also longitude
λ_o	length scale of dissipation eddy
λ_x, λ_y	expressions defined in Eq. (3.1)

ϕ	latitude; also weighting factor
ϕ_s	stability function for constant flux layer
ϕ_1, ϕ_2 ϕ_3	stability functions for eddy coefficients
ν	kinematic viscosity
$\nu, \nu_1,$ ν_2, ν_3	collision kernels
τ	shear stress
τ_{bx}, τ_{by}	bottom shear stress in x and y directions, respectively
τ_r	particle relaxation time
τ_{sx}, τ_{sy}	surface shear stress in x and y directions, respectively
ζ	surface displacement
Ω	earth's rotation rate
ω	vertical velocity in the σ-direction; also tidal frequency
μ	viscosity
χ	astronomical argument
δ_x, δ_y	central-difference spatial operator

Superscripts

—	denotes ensemble averages or dimensional quantities
'	denotes fluctuation about the mean
*	denotes dimensionless quantities

Subscripts

r	denotes reference quantities

CONVERSION FACTORS, U. S. CUSTOMARY TO METRIC (SI)
UNITS OF MEASUREMENT

U. S. customary units of measurement used in this report can be converted to metric (SI) units as follows:

Multiply	By	To Obtain
inches	2.54	centimeters
feet	0.3048	meters
yards	0.9144	meters
fathoms	1.8288	meters
miles (U. S. statute)	1.609344	kilometers
miles (U. S. nautical)	1.852	kilometers
square feet	0.09290304	square meters
square miles (U. S. statute)	2.589988	square kilometers
cubic feet	0.02831685	cubic meters
cubic yards	0.7645549	cubic meters
miles (U. S. statute) per hour	0.44704	meters per second
knots (international)	0.5144444	meters per second
foot-pounds (force)	1.355818	newton-meters
degrees (angular)	0.01745329	radians
gram/liter	1	kilogram/cubic meter
pound/cubic foot	16.02	kilogram/cubic meter

1. INTRODUCTION

1.1 Coastal Currents and Sediment Transport

The Corps of Engineers are responsible for a variety of coastal projects such as the deepening of navigation channels, the disposal of dredged materials, and the construction of shore protection structures. These coastal projects are influenced by, and in return can influence, the existing hydrodynamic and sedimentary regimes of the coastal environment. Before a coastal project can be carried out, impact analyses should be performed to ensure that both economic efficiency and environmental quality will be optimally maintained. As a first step, existing hydrodynamic and sedimentary regimes in the coastal environment should be quantitatively studied. Next, impact due to a number of alternative plans for the coastal project should be quantitatively assessed. To meet both these requirements, an accurate predictive tool for coastal currents and sediment transport is urgently needed. Physical models and field and laboratory studies may be used to aid the ultimate construction of a comprehensive mathematical model.

In a broad sense, coastal water starts from the shoreline and extends seaward much farther beyond the wave breaking zone to the continental shelf where water depth may be several hundred meters. As such, coastal currents are influenced by fresh water river inflow, wind, tide, and large-scale ocean circulation. At the ocean surface, short-period wind waves are generally present whose effects can reach the bottom of shallow coastal waters. In the water column, the water is generally turbulent with strong mixing. Relatively slow internal waves may also be present. With the additional influences of earth rotation and complex coastal geometry and topography, the hydrodynamic regime within a coastal environment is extremely complicated.

Sediment transport in a coastal environment is strongly influenced by the hydrodynamic regime. Sediments enter into the coastal environment via fresh water inflow during high runoff periods, erosion of the shoreline, and disposal of dredged materials. Generally, relatively fine clay and silt particles comprise a major portion of these sediments. These sediments can be transported by the coastal currents over some distance before depositing on the ocean bottom. Strong coastal currents and/or high waves can cause

1

significant bottom shear stress and hence entrain the bottom sediments. Usually, complicated transport-deposition-entrainment cycles lead to large spatial and temporal variations in sediment distribution within any given coastal environment. Hence, a comprehensive impact analysis must address not only the short-term effect, but also the long-term influence of a coastal project.

Sediments containing a large fraction of clay minerals are generally cohesive in nature and can form flocs of various sizes. The particle size distribution is greatly influenced by the turbulence and the salinity and as such, can vary appreciably with time and location. Deposition and entrainment of the cohesive sediments at the bottom of coastal waters are quite different from those for the non-cohesive sand particles. Consequently, a comprehensive sediment transport model should contain quantitative information on these processes.

1.2 Coastal Ecosystem

Coastal currents and sediment transport can significantly affect the other components within a coastal ecosystem. Some examples are given here. Of primary importance is the direct influence of coastal currents on the transport of a variety of water quality parameters and biota. The fine cohesive sediments, entering from rivers or dredged from the navigation channels, may contain nutrients or other undesirable materials adsorbed onto the particles. Depletion of oxygen within the lower water column may occur due to the formation of a sharp density gradient such as the thermocline. Properties of the bottom sediments may be greatly influenced by the bottom-feeding organisms, organic matter, and bacteria. Feeding action of the benthos may also influence the diffusion of chemical species within the bottom water and the surfacial sediments.

A diagram illustrating the complex interactions occurring among the various components of a coastal ecosystem is shown in Figure 1.1. Rectangles indicate the hydrodynamic components while circles indicate the other components. Interactions among the various non-hydrodynamic components may occur both within the water column and below the sediment-water interface. It is apparent from this diagram that a comprehensive understanding of the

2
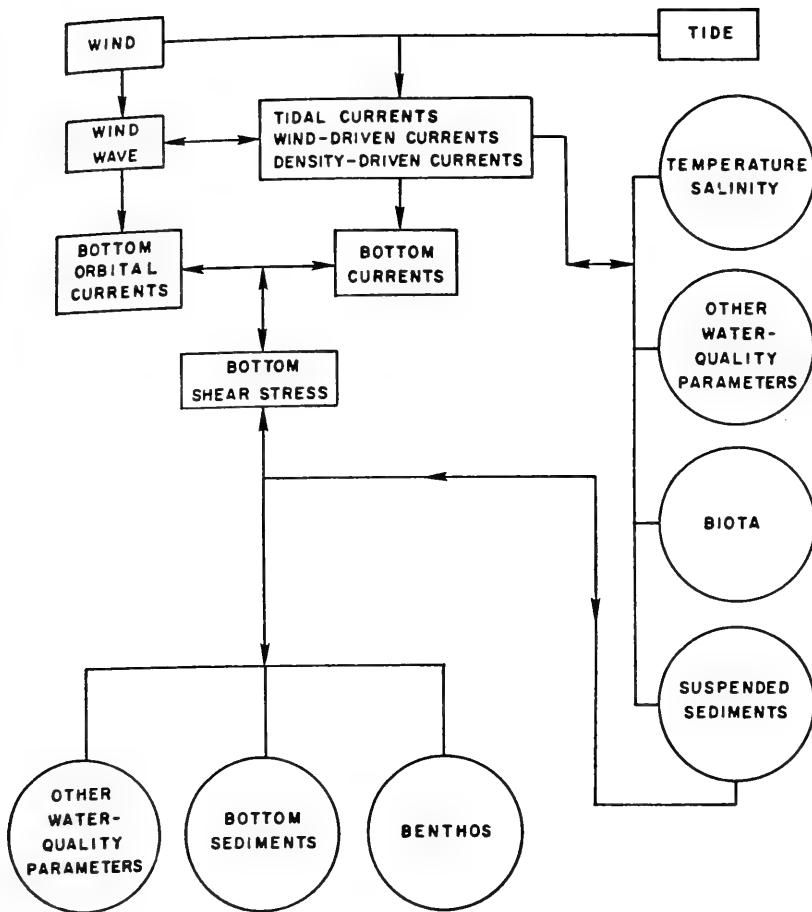
Figure 1.1. Schematics of dynamic interactions among various components of the coastal ecosystem.

hydrodynamic and sedimentary regimes forms the foundation for understanding the complex ecosystem dynamics. Mathematical modeling is the only viable means to incorporate all the detailed dynamics into a quantitative predictive tool.

1.3 Past Modeling Studies

Comprehensive modeling studies of coastal currents and sediment transport, incorporating all the major components shown in Figure 1.1, are relatively scarce. This is partly due to the lack of detailed understanding on the complex hydrodynamic and sedimentary processes, and partly due to the lack of efficient mathematical models suitable for long-term simulations. Sheng and Lick (1979) and Sheng (1980) studied the waves, currents, and transport of cohesive sediments over a large coastal area of Lake Erie, a large lake comparable in size to the Long Island Sound. A three-dimensional hydrodynamic model was used to compute the wind-driven currents while a parametric wave model was used to compute the bottom orbital currents. Results from these models were then used as input to a three-dimensional sediment transport model. Deposition and entrainment of cohesive sediments were studied in the laboratory and results properly incorporated into the model. Simulation was performed over a three-day period and model results compared well with data. Swain and Houston (1982) studied the currents and transport of non-cohesive sediments around a beach using a two-dimensional numerical model. Ariathurai et al. (1977) used a two-dimensional, finite-element model to study the transport of cohesive sediments in the Savannah River over one tidal cycle. Koh and Chang (1973) developed a model for predicting the short-term fate of dredged material after disposal. Simplified ambient flow conditions were assumed and the entrainment process was not included.

Models of varying degrees of complexity for computing coastal currents are available and are reviewed in Chapter 2. Relevant sediment transport models are discussed in Chapters 6 and 7.

4

1.4 The Mississippi Sound

The Mississippi Sound and adjacent areas (Figure 1.2) is a region receiving greater attention due to increasing utilization of its resources, including the dredging of shipping channels and the disposal of dredged materials. A study of the area was initiated by the U.S. Army Corps of Engineers in 1977 to determine "whether the present and proposed dredged material disposal methods for maintenance and construction should be modified in any way at this time in the interest of economic efficiency and environmental quality" (USAEMB, 1979).

Extensive effort was made to summarize the various resources and economy of the study area in an attempt to define the "without condition" to allow impact assessment of alternatives. However, past studies on the most vital resource - the hydrologic resource - of the study area appeared to be rather limited, generally qualitative, and oftentimes resulted from scattered and unrelated efforts. It was hence recognized that "much research is required before a thorough picture of the local water mass dynamics is available" (USAEMB, 1979).

A recent study (Outlaw, 1981) of tidal data indicates that O1 (period=25.82 hours) and K1 (period=23.94 hours) are the predominant tidal constituents in the study area with mean amplitude of both constituents near 15 cm. The tides in the entire Gulf of Mexico have been studied numerically by Reid and Whitaker (1981). Using a 0.25^o grid spacing, their model covers the study area with only 9 grid points along the east-west direction and 5 points along the north-south direction. Schmalz (1982) studied the tidal currents within the study area by means of a two-dimensional numerical model. Despite a few studies in the past (Eleuterius, 1973; 1976; Gaul, 1967; Christmas, 1973), little is known about the wind-driven currents and density-driven currents in the study area. Knowledge about the bottom currents is particularly lacking. Field studies indicated that an appreciable horizontal salinity gradient may sometimes exist in the study area.

There have been a few previous modeling efforts for the overall circulation of the Gulf of Mexico. Baer, et al. (1968) first attempted to compute the Gulf circulation patterns while excluding all topographical

5
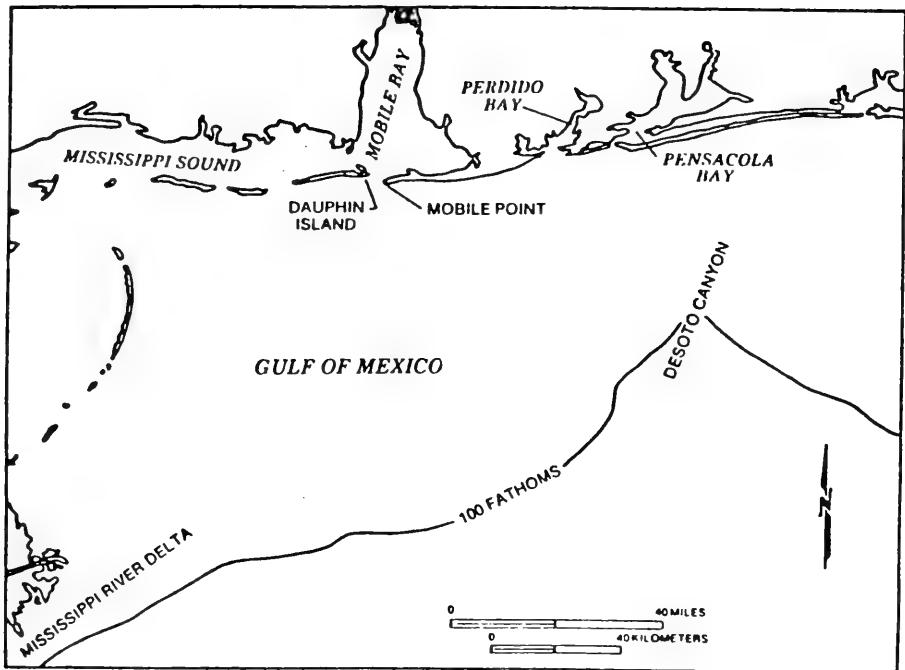
Figure 1.2. Mississippi Sound and adjacent coastal areas of the Gulf of Mexico.

effects and any surface or bottom influences. West and Reid (1972), using a two-layer quasi-geostrophic model, were able to qualitatively simulate the annual cycle of Loop Current intrusion. Hurlbert and Thompson (1980) used a similar model, a barotropic and a reduced gravity model to simulate the dynamics of the Loop Currents and its eddy shedding.

Past studies on sediment dynamics in the Mississippi Sound and offshore areas are even more scarce. The primary source of sediment in the study area is sediments derived in the large river basins. The Mississippi River has contributed and still contributes large amounts of sediments to the western reach of the study area. To a smaller degree, the Pearl, Pascagoula, and Mobile Rivers also introduce considerable quantities of sediments into the Mississippi Sound and the Mobile Bay (Boone, 1973). Based on limited studies, Upshaw, et al. (1966) indicated the overall surface sediment distribution pattern of the study area as shown in Figure 1.3. In general, the surface sediments in the offshore area become increasingly coarse eastward, from the silty sediments off the Mississippi Delta to the sandy sediments off the Florida Coast.

1.5 Purpose and Scope of the Present Study

The major purpose of this study is to construct the framework of a predictive mathematical model for coastal currents and sediment transport. The basic framework that we intend to follow is shown in Figure 1.4. A comprehensive model constructed from this framework, we believe, should ultimately meet the need for impact analyses of a wide variety of coastal projects within the Corps of Engineers.

Our approach combines the efforts of mathematical modeling, laboratory experiments, and field studies. Of primary importance in this study is the development of a comprehensive and efficient three-dimensional hydrodynamic model of coastal currents. At the early stage of the present study, extensive hydrodynamic data were being collected within the Mississippi Sound. These data are used to compare with predicted results of the three-dimensional hydrodynamic model. In addition, laboratory experiments are carried out to quantify the settling, deposition, and entrainment of cohesive sediments from the Mississippi Sound. Other aspects studied include the effect of turbulence

7
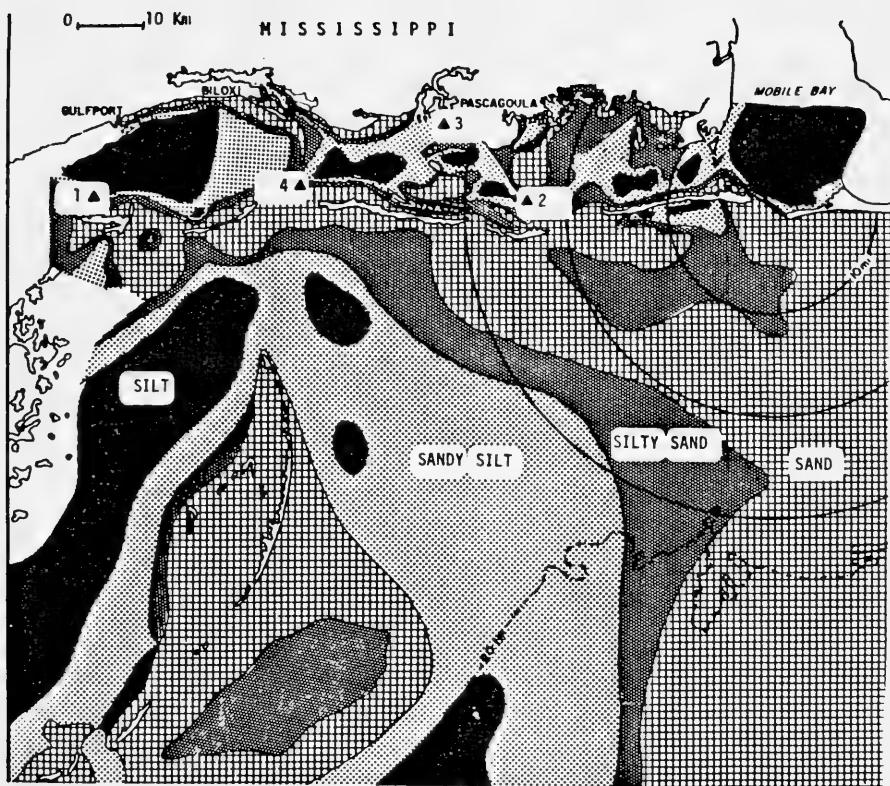
Figure 1.3. Sedimentary map of the Mississippi Sound and adjacent coastal waters.

8
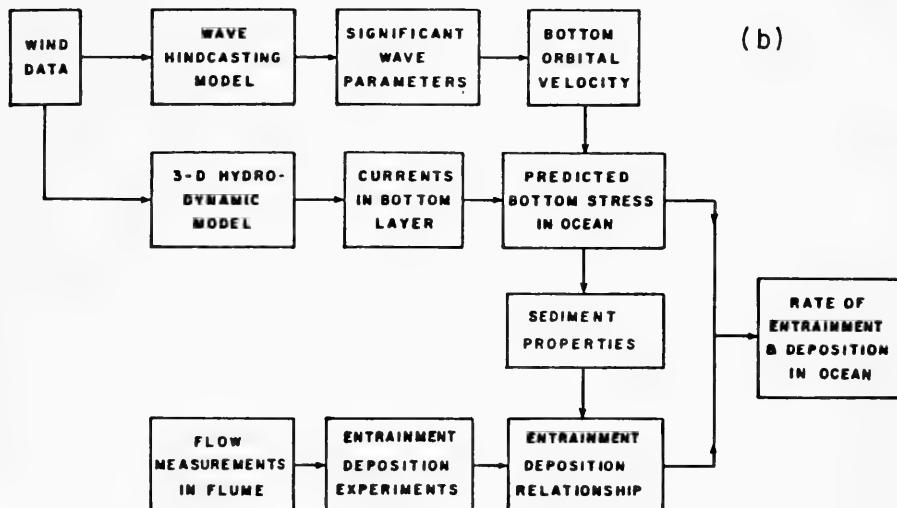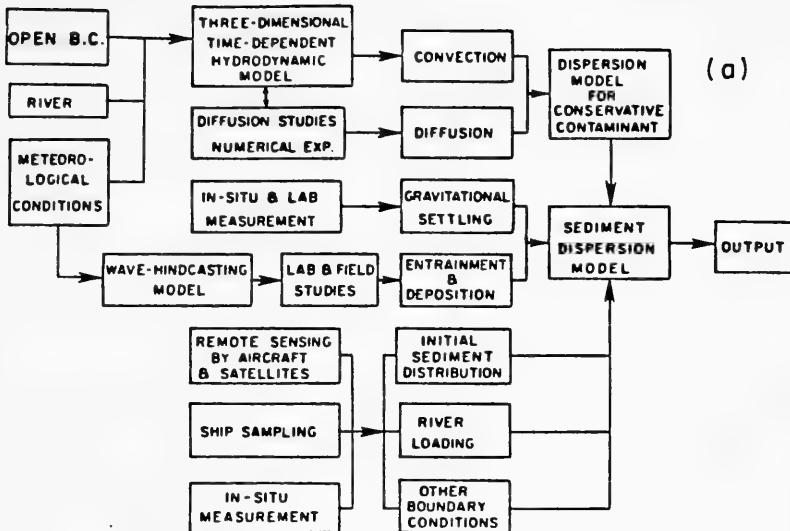
Figure 1.4. (a) Schematics of a comprehensive sediment transport model.

(b) Detailed schematics for defining deposition and entrainment of sediments.

on sediment particle dynamics, the bottom boundary layer dynamics, and the wave climate within a coastal environment. Results from these studies are systematically incorporated into a quantitative analysis of the sedimentary regime within the Mississippi Sound.

A detailed description of the hydrodynamic model will be given in Chapter 2. Numerical algorithms of the hydrodynamic model are described in Chapter 3, followed by model evaluation tests in Chapter 4. Dynamic simulations of coastal currents within the Mississippi Sound and adjacent continental shelf are presented in Chapter 5. The transport, entrainment, and deposition of cohesive sediments are described in Chapter 6. A sediment transport model for the Mississippi Sound is described in Chapter 7. The last chapter, Chapter 8, gives conclusions and recommendations.

2. HYDRODYNAMIC MODEL

2.1 A Review

There exist various time and length scales in the hydrodynamic processes of large bodies of water, ranging from the small scale of the surface waves (1 sec < T < 20 sec, 1 cm < L < 500 m), the mesoscale corresponds to the internal and inertial waves (N^{-1} < T < f^{-1}, 100 m < L < 100 Km), to the large scale associated with the long waves (tides, storm surges, and seiches). In addition, turbulent processes that affect the mean circulation and the dispersion of contaminants have to be addressed. Due to the lack of detailed understanding and the limitation of computer resources, existing numerical models of large scale processes do not resolve the small scale and the mesoscale range, but resort to parameterizing the processes in these ranges.

In addition to the difference in the resolved spatial and time scales, models can differ substantially in numerical features and hence have quite different numerical efficiencies and accuracies. Anticipating long-term simulations for a variety of flow situations, an ideal numerical model should be comprehensive (containing the proper physics) and generalized (requiring minimal tuning, and adaptable to various applications) in terms of its dynamic features, while accurate (containing little numerical damping) and economic (computationally efficient) in terms of its numerical features. To allow relative ease in distinguishing one model from another, it is convenient to classify models in terms of their dynamic features as listed in Table 2.1: spatial dimension, time variation, air-sea interface, scale of interest, turbulence parameterization, and forcing. Table 2.2 lists numerical method, equations solved, time-differencing scheme, spatial-differencing scheme, grid structure, and host computer as the primary numerical features that distinguish models from one another.

11

Table 2.1

Classification of Models According to Important Dynamic Features

	Spatial Dimension	Time Variation	Air-Sea Interface	Scale of Interest	Turbulence Parameterization	Forcing
Types of Models	0-D (Box)	Steady-State	Free-Surface	Global	Eddy-Viscosity	Wind-Driven Circulation
	1-D	Time-Dependent	Rigid-Lid	Limited-Area:	Two-Equation	Density-Driven Circulation
	2-D:			Open-Coast	Reynolds-Stress	
	Vertically-Integrated			Near-Shore		
	Laterally-Averaged			Large-Scale		Pressure-Driven Circulation
	X-Z			Boundary Layer:		
	3-D:			Bottom Boundary-Layer		Tidal Circulation
	Discrete					
	Layered			Mixed-Layer		
				Lateral Boundary-Layer		
				etc.		

Table 2.2

Classification of Models According to Important Numerical Features

Numerical Method	Equations Solved	Time-Differencing Scheme	Spatial-Differencing Scheme	Grid Structure	Host Computer
Finite-Difference	Primitive	Explicit	Advection Terms:	Rectangular	Mini
	Surface Displacement	Implicit	Upwind	Cylindrical	Main Frame
Finite-Element		Semi-Implicit	Second-Order	Spherical	
	Velocities		Higher-Order		
Spectral	Temperature	Leapfrog	Flux-corrected Transport	Uniform	Non-Virtual
	Density	Forward-Time		Non-Uniform	Virtual
			Poisson Solver:		
	Poisson		Iterative	Boundary-Fitted	
	Stream Function		Direct Solver		Vector-ized
	Vorticity			Stretched	Non-Vector-ized
	Pressure			Non-Stretched	
	Surface Displace-ment				

13

Numerical Method

Due to their relative simplicity and ease of resolving complex physical phenomena, finite difference models have been widely used in the study of coastal currents. The finite-element method (based on the Galerkin technique), despite its ability to resolve complex geometry in the computational domain, has several disadvantages: (1) It is relatively more complicated and expensive to program, particularly for additional nonlinear terms; (2) It requires relatively more computational effort per time step; and (3) It is not well suited for problems exhibiting highly-localized effects such as sharp density gradients across a coastal front or a thermocline. The spectral method, while considered to possess superior accuracy, has the same basic disadvantages as the finite-element method. Recent advancement in the numerical generation of boundary-fitted coordinates has added further flexibility to the finite difference method, thus making it the optimum method for simulation of coastal currents.

Spatial Dimension

Due to the limitation in computer resources, earlier numerical models generally resolved only one or two spatial dimensions. One-dimensional models are widely used for simple parametric studies and are often amenable to analytic solutions. They have been used to study tidal currents and water-quality parameters in estuaries (e.g., Harleman, 1975). The so-called link-node model (e.g., Pagenkopf, et al., 1977) is actually based on the superposition of one-dimensional models.

Two-dimensional models are relatively easy to use and may provide reasonable answers when flow in the third dimension is relatively homogeneous. Among the various types of two-dimensional models listed in Table 2.1, the most widely used is probably the vertically-integrated model, which is obtained by integrating the three-dimensional equations of motion in the vertical direction. It has been used extensively for simulating tides, storm surges, and pollutant transport in coastal environments (e.g., Leendertse, 1970; Butler, 1980). Due to the lack of vertical resolution, however, the vertically-integrated models are not adequate for studying such problems as wind-driven currents and sediment transport in coastal waters. More recently,

14

with the improvement in numerical techniques and computer resources, three-dimensional models have become more advanced. The following discussion centers on the three-dimensional models.

Time Variation

If the time scale of the dominant forcing (e.g., wind) is larger than the other characteristic time scales of the water body, a quasi-steady state exists and one may use a steady-state model which essentially removes the effect of time variation from the problem. One may also utilize the steady-state model to study a series of wind-driven events while using different eddy viscosities to simulate the varying randomness effects. The steady-state model has been used extensively for studying currents in enclosed bodies of water such as lakes and reservoirs (e.g., Sheng and Lick, 1972; Sheng, 1975). For instance, if the winter winds over Lake Erie remain relatively steady for more than 1 day, the currents can be predicted with reasonable accuracy by means of a three-dimensional, steady-state, wind-driven circulation model. For coastal studies, however, the steady-state analysis may not always be valid.

Air-Sea Interface

Free-surface models allow the vertical movement of air-sea interface and hence the propagation of surface gravity waves. Earlier free-surface models usually solved for the primitive equations with an explicit time-marching scheme (e.g., Leendertse and Liu, 1975; Forristal, et al., 1977; Sheng, 1975). Although the numerical algorithm was rather straightforward, the numerical time step was severely restricted by the time for the surface gravity wave to propagate the distance of one spatial grid (on the order of a few seconds). Recently, more efficient free-surface models which do not contain this limit ($\Delta t \sim 30$ min) have been developed (e.g., Sheng, et al., 1978). If the time period of interest is much greater than the dominant seiche periods in the water body, however, one can use a rigid-lid model which treats the air-sea interface as a rigid lid with no vertical motion and hence eliminates the gravity wave propagation altogether. A larger numerical time step is allowed this way. The trade-off is that one now has to solve a Poisson equation for the surface pressure which may offset the gain in the

maximum allowable time step. The rigid-lid model has been used quite extensively to study circulations in the atmosphere (Mason and Sykes, 1978; Lewellen and Sheng, 1981), oceans (Bryan, 1969) and lakes (Sheng, 1975; Bennett, 1977).

Scale of Interest

Global circulation in an enclosed basin can generally be resolved with a numerical model and a grid encompassing the entire basin. In coastal waters, however, limited-area models with a fine grid resolution in the nearshore region are often desired. In such a case, proper coupling between the nearshore region and the offshore region not resolved by the model is required. Open boundary conditions need to be properly specified to ensure correct forcing and to eliminate computational modes and numerical instability. These aspects shall be addressed later.

Even if one's interest is only in the large-scale motion in a water body, the ability of a numerical model to simulate realistic events may still depend upon how well the model parameterizes the important small-scale (boundary-layer) processes. Consider relatively deep water under the action of wind and earth rotation. There are generally seven layers in the vertical direction when proper averaging in time and space is performed on the flow variables:

(1) a very thin laminar sublayer below the free surface, within which the velocity varies linearly with depth,

(2) a constant flux layer within which the velocity varies logarithmically with depth,

(3) a surface turbulent Ekman layer within which turbulent mixing is important.

(4) a generally non-turbulent geostrophic core within which the velocity varies relatively little with depth,

(5) a bottom turbulent Ekman layer,

(6) a constant flux layer near the bottom, and

(7) a very thin laminar sublayer adjacent to the bottom.

16

The above description of the various vertical layers is a convenient idealization and is not expected to be valid at all times in waters of all depths. For instance, the classical turbulent Ekman layer has a thickness on the order of u_*/f and is based on a steady-state force balance between the wind stress and the Coriolis force in a neutrally stratified water column. In reality, however, wind mixing seldom reaches the neutral Ekman layer depth due to the presence of buoyancy and/or other dynamic processes (e.g., wind forcing) containing time scales much smaller than the rotational time scale. Strong convective mixing may also destroy the distinct Ekman spiral. Across the air-sea interface, mutual interactions of atmosphere and ocean take place within the ocean mixed layer and the atmospheric marine boundary layer. On windy days, the air-sea interface is quite rough due to strong wave actions and the ocean mixed layer is strongly influenced by the wave-turbulence interactions. Turbulence generated by wave breaking plays a dominant role in the mixed layer dynamics (as well as in the surf zone dynamics), but our understanding on this subject is still rather primitive. Another factor having strong influence on the mixed layer dynamics is the density stratification. A stable stratification decreases the turbulent mixing while an unstable stratification increases turbulent mixing. Strong convective events in calm weather may lead to organized features similar to the rolls of vortices in the atmosphere (Lewellen, Teske, and Sheng, 1980). In deep waters below the surface mixed layer, patches of turbulence can be generated due to the presence of internal waves. (Garrett and Munk, 1972 and 1975).

In shallow coastal waters, the surface and bottom Ekman layers may merge and are comparable to the water depth. Dynamics of the relatively thin sublayers (~1 cm) and constant flux layers (~1 m) play rather important roles in affecting the transport of such materials as heat, sediment, nutrient, oxygen, and oil slick, which are introduced into the water bodies at the surface or bottom boundaries. Oscillatory flow or roughness features may introduce additional thin logarithmic layers adjacent to the boundary. Along the bottom of shallow waters such as tidal marshes, vegetation canopy may also exist.

Due to the abundance of bottom feeding organisms, the relatively thin bottom boundary layer in the ocean is often called the benthic boundary layer. Dynamics within the benthic boundary layer affect the animal community, the sediment movement, and the diffusion of chemical species and as such have received great attention from all disciplines of oceanography. Over the shallow coastal waters, wave-induced oscillatory flow interacts with the slowly varying current within a thin layer above the bottom to cause movement of sediment and other materials. Models capable of predicting the benthic boundary layer dynamics in shallow water are needed to accurately predict bottom flow and resulting sediment movement.

In the interior of a relatively large lake or ocean, the lateral turbulent diffusion is generally smaller than the vertical turbulent diffusion. Adjacent to the coastlines, thin lateral boundary layers exist within which lateral turbulent mixing is also important. Tee (1976) studied the tidally-induced residual currents in the Bay of Fundy and suggested the importance of the lateral boundary layer in generating the large residual eddies. However, most large-scale circulation models use numerical grid spacings which are larger than the lateral boundary layer thickness and hence do not adequately resolve the detailed boundary layer dynamics.

Turbulence Parameterization

One of the most important features in numerical hydrodynamic models for coastal currents is the parameterization of turbulence. Most existing models utilize the concept of an eddy viscosity. Eddy-viscosity models are relatively easy to use and can give reasonable results if sufficient data are available to establish the validity of the model parameters. Once the model has been sufficiently calibrated for a given site, it is then suitable for performing parametric studies or long-term simulations at that site. However, the proper eddy viscosity formulation depends on both the process and the environment of interest. Great discrepancy exists among the various empirical formulations of eddy coefficients. There is a great need to reduce the empirical "tuning" of the eddy coefficients which is often required to achieve good agreement between model output and data.

Despite the wide application of eddy viscosity models in simulating the large-scale circulation in water bodies, many dynamic processes cannot be accurately simulated by the eddy viscosity models. This is particularly true in highly stratified and/or highly oscillatory flow conditions, such as the mixed layer dynamics and the benthic boundary layer dynamics. Under these circumstances, the turbulence is generally not in equilibrium with the mean flow gradients and one has to use models that resolve the time rate of change, convection, diffusion, production, and dissipation of turbulence. These Reynolds stress models, also called second-order closure models, solve the dynamic equations for the mean flow variables as well as the second-order turbulent correlations. The dynamic nature of this type of model permits one to use a universal set of model constants for a wide variety of flow simulations without having to do site-specific parameter tuning normally required for eddy viscosity models. Although fully three-dimensional application of such a model is still limited by the prohibitive computational cost, one can use simplified versions of this model to derive a physically more meaningful eddy coefficient formulation. A brief discussion on the formulation and applications of a Reynolds stress model is given in Appendix D.

Forcing

Models can also be classified according to the type of forcing (in parenthesis) as either a wind-driven circulation model (wind), a density-driven circulation model (density gradient), a storm surge model (storm), or a tidal circulation model (tide). In the most general case, all the forcings should be resolved by the numerical model.

Model for the Present Study

For the present study, an efficient three-dimensional, time-dependent, free-surface model has been developed. Forcings including tides, winds, and density gradients are properly resolved. To better resolve the complex geometry and bottom topography in coastal waters, vertical as well as horizontal stretchings are applied to the generally non-uniform coordinates. A special effort has been made to significantly improve the computational efficiency of the model such that long-term simulation can be performed. In

19

the following, the basic equations and boundary conditions will be first described. The various model features are then discussed in detail.

2.2 Basic Equations and Boundary Conditions

The mean equations of motion for an incompressible fluid in the presence of both a gravitational and a Coriolis body force, with the mean variables denoted by lower-cases and the turbulent fluctuations by primed lower-cases, may be written in general tensor notation as follows:

$$\frac{\partial u_i}{\partial x_i} = 0 \tag{2.1}$$

$$\frac{\partial u_i}{\partial t} + u_j \frac{\partial u_i}{\partial x_j} = - \frac{\partial \overline{u_i' u_j'}}{\partial x_j} - \frac{1}{\rho} \frac{\partial p}{\partial x_i} + g_i - 2 \, \varepsilon_{ijk} \Omega_j u_k \tag{2.2}$$

$$\frac{\partial T}{\partial t} + u_j \frac{\partial T}{\partial x_j} = - \frac{\partial \overline{u_j' T'}}{\partial x_j} \tag{2.3}$$

$$\frac{\partial S}{\partial t} + u_j \frac{\partial S}{\partial x_j} = - \frac{\partial \overline{u_j' S'}}{\partial x_j} \tag{2.4}$$

$$\rho = \rho(T,S) \tag{2.5}$$

where u_i are the velocity components, x_i are the rectangular coordinates, t is the time, $\overline{u_i' u_j'}$ are the Reynolds stresses, ρ is the density, p is the pressure, g_i is the gravitational acceleration vector, T is the temperature, T_0 is the reference temperature, ε_{ijk} is the unit alternating tensor, Ω is the angular velocity of earth, $\overline{u_j' T'}$ are the heat fluxes, S is the salinity, and $\overline{u_j' S'}$ are the salt fluxes. In writing the above equations, the Boussinesq approximation has been made such that the only effect of the density variation is in the gravitational body force term in the momentum equation (2.2). Molecular

20

diffusion terms have been discarded anticipating high Reynolds number applications.

This system of equations (2.1)-(2.5) is not complete owing to the presence of the Reynolds stress and the flux terms. A hierarchy of turbulence models has been developed to resolve this problem (see, for example, Appendix D). Conventional eddy-viscosity models employ a stress-strain law for time-averaged turbulent flows in a similar form as that for a Newtonian fluid in laminar motion. The Reynolds stress terms are replaced by the products of a mean flow gradient and an eddy viscosity, which is prescribed as a constant or some algebraic function of local flow properties.

Time-Averaged Equations for the Mean Variables

Assuming hydrostatic pressure distribution (valid when vertical acceleration is negligible compared to the vertical pressure gradient) and employing the eddy-viscosity concept, the basic equations (2.1)-(2.4) can be written for a right-handed coordinate system $(x_1, x_2, x_3) = (x, y, z)$, where x and y are the horizontal coordinates and z points vertically upward, as:

$$\frac{\partial u}{\partial x} + \frac{\partial v}{\partial y} + \frac{\partial w}{\partial z} = 0 \tag{2.6}$$

$$\frac{\partial u}{\partial t} + \frac{\partial u^2}{\partial x} + \frac{\partial uv}{\partial y} + \frac{\partial uw}{\partial z} = fv - \frac{1}{\rho_0}\frac{\partial p}{\partial x} + \frac{\partial}{\partial x}\left(A_H \frac{\partial u}{\partial x}\right)$$

$$+ \frac{\partial}{\partial y}\left(A_H \frac{\partial u}{\partial y}\right) + \frac{\partial}{\partial z}\left(A_V \frac{\partial u}{\partial z}\right) \tag{2.7}$$

$$\frac{\partial v}{\partial t} + \frac{\partial uv}{\partial x} + \frac{\partial v^2}{\partial y} + \frac{\partial vw}{\partial z} = - fu - \frac{1}{\rho_0}\frac{\partial p}{\partial y} + \frac{\partial}{\partial x}\left(A_H \frac{\partial v}{\partial x}\right)$$

$$+ \frac{\partial}{\partial y}\left(A_H \frac{\partial v}{\partial y}\right) + \frac{\partial}{\partial z}\left(A_V \frac{\partial v}{\partial z}\right) \tag{2.8}$$

$$\frac{\partial p}{\partial z} = - \rho g \qquad (2.9)$$

$$\frac{\partial T}{\partial t} + \frac{\partial uT}{\partial x} + \frac{\partial vT}{\partial y} + \frac{\partial wT}{\partial z} = \frac{\partial}{\partial x} \left(K_H \frac{\partial T}{\partial x} \right) + \frac{\partial}{\partial y} \left(K_H \frac{\partial T}{\partial y} \right) + \frac{\partial}{\partial z} \left(K_v \frac{\partial T}{\partial z} \right)$$
$$(2.10)$$

$$\frac{\partial S}{\partial t} + \frac{\partial uS}{\partial x} + \frac{\partial vS}{\partial y} + \frac{\partial wS}{\partial z} = \frac{\partial}{\partial x} \left(D_H \frac{\partial S}{\partial x} \right) + \frac{\partial}{\partial y} \left(D_H \frac{\partial S}{\partial y} \right) + \frac{\partial}{\partial z} \left(D_v \frac{\partial S}{\partial z} \right)$$
$$(2.11)$$

where u, v, and w are the velocities in x, y, and z directions, f is the Coriolis parameter defined as $2\Omega\sin\phi$ where ϕ is the latitude, ρ_0 is the reference density, A_H, K_H, and D_H are the horizontal eddy coefficients, and A_v, K_v, and D_v are the vertical eddy coefficients. The nonlinear inertia terms and the advection terms have been written in conservative forms. Variable eddy coefficients are allowed in the above equations. Source/sink terms may be included in (2.10) and/or (2.11) to account for such effects as radiation, precipitation and evaporation, etc.

Due to the different scales and intensities associated with the horizontal and vertical turbulent eddies in large lakes and oceans, the lateral eddy coefficients ($A_H \sim 10^2$ to 10^6 cm^2/sec) are typically several orders of magnitude larger than the vertical eddy coefficients ($A_v \sim 1$ to 10^2 cm^2/sec). The determination of realistic values and forms of the eddy coefficients is a major and difficult task in the modeling of lake and ocean currents.

Boundary Conditions for Mean Variables

Boundary conditions at the free-surface are: (a) the wind stress is specified,

$$
\rho_0 \, A_v \left(\frac{\partial u}{\partial z}, \frac{\partial v}{\partial z} \right) = (\tau_{sx}, \tau_{sy}) = \rho_a C_{da} (u_w^2 + v_w^2)^{1/2} \, (u_w, v_w) \qquad (2.12)
$$

where τ_{sx} and τ_{sy} are the wind stresses in the x and y directions respectively, ρ_a is the air density, C_{da} is the drag coefficient, u_w and v_w are wind velocities at a certain height (6 m or 10 m) above the surface; (b) the kinematic condition is satisfied,

$$
w = \frac{\partial \zeta}{\partial t} + u \, \frac{\partial \zeta}{\partial x} + v \, \frac{\partial \zeta}{\partial y} \qquad (2.13)
$$

where ζ is the displacement of the free surface; (c) the dynamic condition is satisfied,

$$
p = p_a \qquad (2.14)
$$

where p_a is the atmospheric pressure, and (d) the heat flux is specified,

$$
\rho_0 K_v \frac{\partial T}{\partial z} = q_s = H_s \, (T - T_e) \qquad (2.15)
$$

where H_s is the surface heat exchange coefficient, and T_e is an equilibrium air temperature at which the surface and heat flux q_s is zero.

Utilizing the dynamic boundary condition (2.13), the vertical momentum equation can be integrated vertically to yield:

$$
p = - \int_{\zeta}^{z} \rho g \, dz + p_a \qquad (2.16)
$$

The pressure gradient terms in Eqs. (2.7) and (2.8) can thus be replaced by,

$$\frac{\partial p}{\partial x} = -g \int_{\zeta}^{z} \frac{\partial \rho}{\partial x} \, dz + \rho_s g \frac{\partial \zeta}{\partial x} + \frac{\partial p_a}{\partial x} \qquad (2.17)$$

$$\frac{\partial p}{\partial y} = -g \int_{\zeta}^{z} \frac{\partial \rho}{\partial y} \, dz + \rho_s g \frac{\partial \zeta}{\partial y} + \frac{\partial p_a}{\partial y} \qquad (2.18)$$

where ρ_s is the density at the free surface.

The transfer of momentum and heat at the air-sea interface is extremely complicated. A proper treatment requires understanding of the planetary boundary layer, the mixed layer of oceans, and their interactions. Most models of lake or ocean currents resort to empirical formulae as shown above. Based on the wind speed at 6 m above the surface, Wilson (1960) used a value of 0.00237 for C_{da} during strong winds and 0.00166 for light winds. Hicks (1972) considered wind speed at 10 m above the surface and arrived at C_{da} of 0.001 for low wind and 0.0015 for high wind. Additional complications surrounding the specification of surface shear stress include the determination of the time-dependent wind field, the relationship between the over-land wind and the over-water wind, and the effect of atmospheric stability on the simple quadratic stress law (2.12). H_s and T_e in (2.15) depend on the wind speed, air temperature, humidity, and solar and terrestial radiation. Empirical methods to evaluate H_s and T_c can be found in Edinger and Geyer (1967). An alternative approach by TVA (1972) treats the sensible heat transfer and the evaporative heat loss separately.

At the bottom, the boundary conditions are: (a) a quadratic stress law is used.

$$\rho \, A_v \left(\frac{\partial u}{\partial z}, \frac{\partial v}{\partial z} \right) = (\tau_{bx}, \tau_{by}) = \rho \, C_d \, (u_1^2 + v_1^2)^{1/2} \, (u_1, v_1) \qquad (2.19)$$

where C_d is the drag coefficient, and u_1 and v_1 are horizontal velocities at a point z_1 above the bottom; (b) the heat flux or temperature is specified.

Based on limited studies (Sternberg, 1972), constant value of C_d on the order of 0.004 have been used in the past. Recent studies of tidal currents in a shallow estuary found C_d to be on the order of 0.035 (Brown and Trask, 1980). A more rigorous way of determining C_d is to utilize the Monin-Obukhov similarity relationships valid within the constant flux layer. If z_1 is within the constant flux layer above the bottom, C_d can be shown to be (Sheng, 1980):

$$C_d = k^2 \left[\ln(z_1/z_0) + \phi_s(z_1/L) \right]^{-2} \qquad (2.20)$$

where k is the von Karman constant, z_0 is the roughness height, and ϕ_s is a stability function characterizing the stability of the bottom boundary layer (Businger et al. 1971; Lewellen, 1977), and $L \equiv u_*^3/kg\alpha_v \overline{w'T'}$ is the Monin-Obukhov similarity length, where α_v is the coefficient of volumetric expansion and $\overline{w'T'}$ is the vertical heat flux.

It can be shown that the stability may increase (unstable case) or decrease (stable case) the drag coefficient by as much as 40%. Indeed, this definition of C_d should also be used within the constant flux layers below the free surface as well as above the air-sea interface. Huang and Sloss (1981) used a Richardson-number-dependent C_{da} suggested by Deardorff (1968) in a study of the monthly mean circulation in Lake Ontario.

Others (Forristal et al., 1977; Blumberg and Mellor, 1981) used linear bottom stress laws instead of the quadratic stress law (2.18). It should be pointed out that the bottom stress is relatively unimportant in deep waters. In relatively shallow coastal waters, however, the bottom stress can be of the same order of magnitude as the wind stress. In such cases, numerically modeled currents are quite sensitive to the bottom stress formula used in the model. The no-slip condition, $(u,v,w) = 0$, has been used by many modelers, but is valid only if the laminar sublayer is adequately resolved by an extremely fine vertical (≤ 1 cm) grid in the numerical model. This will be discussed further.

2.3 Time Scales and Dimensionless Parameters

It is convenient to rewrite the above system of equations and boundary conditions in dimensionless form such that the relative orders of magnitude of the various terms become more apparent. However, it is instructive to first examine the time scales associated with the large scale motions in a lake. Assuming H and L as the reference lengths in lateral and vertical directions, U_r as the reference velocity, and $\Delta\rho$ as the reference density difference in stratified flow, $(A_H)_r$, $(A_V)_r$, $(K_H)_r$, and $(K_V)_r$ as the reference eddy coefficients, several time scales can be defined as in Table 2.3.

The list in Table 2.3 is not meant to be exhaustive. For example, two time scales for the turbulent thermal diffusion, T_{th} and T_{tv}, can be defined similar to T_{dh} and T_{dv} by replacing the eddy viscosities with the eddy diffusivities. The inverse of the Brunt-Vaisala frequency, $N^{-1} = (1/\rho_r \; \partial\rho/\partial z)^{-0.5}$, the time scale of the lowest mode of free oscillation in a stably stratified fluid, can be used instead of T_{gi}. Other time scales will be mentioned at appropriate places later. A number of dimensionless parameters can be defined from the ratio of these time scales and are listed in Table 2.4.

The time scales and dimensionless numbers so defined in Tables 2.3 and 2.4 are very useful in comparing the relative importance of various terms in the equations of motion. If the Coriolis terms in the momentum equation is of order 1, then orders of the unsteady, nonlinear, lateral diffusion, and vertical diffusion terms are Un, Ro, E_H, and E_V, respectively.

2.4 Vertical Grid Resolution

Two types of vertical grid are generally used in the finite-difference models of coastal currents. In the first type, the vertical domain of the water body is separated by layers of constant depth as was done by Leendertse and Liu (1975). Although the overall features of the flow field may be well represented, this type of grid has two potential problems: (1) unless a large number of layers is used, there is generally insufficient resolution in the shallow nearshore region and hence the nearshore dynamics is poorly represented, (2) continuous variation in the bottom topography cannot be

26

Table 2.3

Representative Time Scales of Large Scale Motion in Coastal Waters

Time Scale	Forcing	Convection	Inertial Oscillation	Lateral Diffusion	Vertical Diffusion	Ekman Layer Diffusion	Seiche	Internal Seiche
Symbol	T_f	T_c	T_i	T_{dh}	T_{dv}	T_e	T_g	T_{gi}
Order of Magnitude	$\dfrac{1}{\omega}$	$\dfrac{1}{U_r}$	$\dfrac{1}{f}$	$\dfrac{L^2}{(A_H)_r}$	$\dfrac{D^2}{(A_v)_r}$	$\dfrac{D}{2f}$	$\dfrac{L}{(gD)^{\frac{1}{2}}}$	$\dfrac{L}{(\Delta\rho/\rho_0 gD)^{\frac{1}{2}}}$

Table 2.4

Representative Dimensionless Numbers

Number	Unsteady	Rossby	Lateral Ekman	Vertical Ekman	Froude	Internal Froude	Lateral Peclet	Vertical Peclet
Symbol	Un	Ro	E_H	E_v	Fr	Fr_i	Pe_H	Pe_v
Definition	$\dfrac{\omega}{f}$	$\dfrac{U_r}{fL}$	$\dfrac{(A_H)_r}{fL^2}$	$\dfrac{(A_v)_r}{fD^2}$	$\dfrac{U_r}{(gD)^{\frac{1}{2}}}$	$\dfrac{U_r}{(\Delta\rho gD/\rho)^{\frac{1}{2}}}$	$\dfrac{U_r L}{(K_H)_r}$	$\dfrac{U_r D}{(K_v)_r}$
Physical Meaning	$\dfrac{T_i}{T_f}$	$\dfrac{T_i}{T_c}$	$\dfrac{T_i}{T_h}$	$\dfrac{T_i}{T_{dv}}$	$\dfrac{T_g}{T_c}$	$\dfrac{T_{gi}}{T_c}$	$\dfrac{T_{th}}{T_c}$	$\dfrac{LT_{kv}}{DT_c}$

.

easily resolved with a regular rectangular grid. Because of the second problem, estimate on bottom flow and stress may be distorted. Although an irregular grid spacing may be used at the bottom to better resolve the topography, it makes the finite difference treatment of the bottom cells more cumbersome.

The second type of grid is a vertically-stretched grid, the so-called σ-stretching, which leads to a smooth representation of the topography and, additionally, the same order of vertical resolution for the shallow and deeper parts of the water body. Basically, the vertical coordinate z is transformed into a new coordinate σ:

$$\sigma = \frac{z-\zeta(x,y,t)}{h(x,y)+\zeta(x,y,t)} \tag{2.21}$$

Using this relationship, the water column at any location between $z=\zeta$ and $z=-h$ is transformed into a layer between $\sigma=0$ and $\sigma=-1$. (Figure 2.1). This transformation introduces additional terms to the equation of motion (Appendix A). However, most of the additional terms introduced by the stretching are contained in the horizontal diffusion terms. Since horizontal diffusion is generally small compared to the vertical diffusion and horizontal advection, only the leading terms need to be retained in general. Significant simplification of the equations may result if one assumes that $\zeta \ll h$ and hence $\sigma=z/h$. However, this assumption may lead to some error if one intends to apply the model to shallow waters where flooding and drying of land may occur during storm surges.

2.5 Lateral Grid Resolution

Earlier models of global ocean or lake circulations generally used a relatively coarse uniform rectangular grid in the horizontal direction of the computational domain. However, complex shoreline and bottom topography and islands often exist in a lake or coastal environment. To better resolve the shoreline geometry and internal features, and additionally allow proper coupling between the various regions of a coastal environment, a smoothly varying non-uniform grid can be used. As shown in Figure 2.2, a non-uniform horizontal grid in the real space (x,y) is mapped into a uniform horizontal grid in the computational space (α,γ) by the following piecewise reversible transformations:

$$x = a_x + b_x \alpha^{c_x} \quad , \quad y = a_y + b_y \gamma^{c_y} \tag{2.22}$$

where a_x, b_x, c_x, a_y, b_y and c_y are user-specified stretching coefficients (Appendix B). By applying a smoothly varying grid transformation, whose functional as well as first derivatives are continuous, many stability problems commonly associated with variable grid schemes are eliminated provided that all derivatives are centered in the stretched system (α,γ,σ).

This lateral stretching does not add any extra terms to the equations of motion, although the stretching coefficients as defined by $\mu_x = d\alpha/dx$ and $\mu_y = d\gamma/dy$ now appear in all of the spatial derivative terms.

.

$$\sigma = \frac{z - \zeta}{\zeta + h} \approx \frac{z}{h}$$
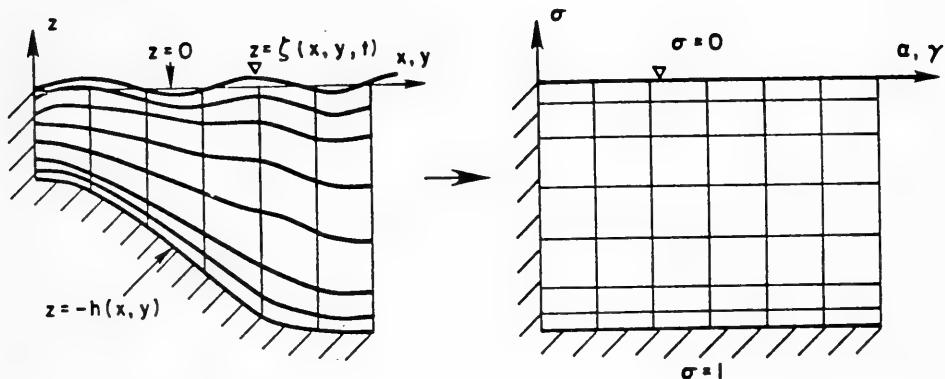
Figure 2.1. Vertical stretching of the coordinates.

$$x = a_x + b_x \, \alpha^{c_x}; \; y = a_y + b_y \, \gamma^{c_y}$$
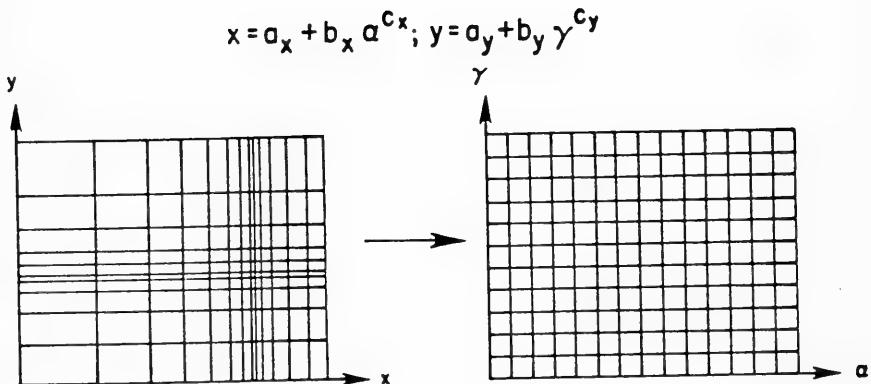
Figure 2.2. Lateral stretching of the coordinates.

2.6 Grid Alignment

In the present model, a staggered grid is used in both the horizontal and vertical directions of the computational domain (Figure 2.3). Along the shoreline, the normal velocities are zero or specified by river inflow or outflow. In the vertical direction, the free surface and the bottom both fall on the full grid points where the vertical velocities and turbulent fluxes are computed or specified. The horizontal velocities are computed at the half grid points in the vertical direction. Many models, however, use a vertical grid which computes the horizontal velocities at the full grid points including the free surface and bottom. Special finite-difference treatment was thus required for the boundary points.

2.7 Dimensionless Equations and Boundary Conditions in the Transformed Coordinates

Dimensionless Variables

It is convenient to write the above system of equations and boundary conditions in non-dimensional form and in the transformed coordinates (α, γ, σ) by defining the following non-dimensional quantities:

$$(u^\star, v^\star, w^\star) = (u, v, wL/D)/U_r$$

$$(x^\star, y^\star, z^\star) = (x, y, zL/D)/L$$

$$(\tau_x^\star, \tau_y^\star) = (\tau_x^W, \tau_y^W)/\rho_r(A_v)_r U_r$$

$$t^\star = tf \ , \qquad q_s^\star = q/\rho_r(K_v)_r T_r \tag{2.23}$$

$$\rho^\star = (\rho - \rho_r)/\rho_r \ , \quad T^\star = (T - T_r)/T_r \ , \qquad \zeta^\star = g\zeta/fU_r L$$

$$A_H^\star = A_H/(A_H)_r \ , \qquad K_H^\star = K_H/(K_H)_r \ , \qquad D_H^\star = D_H/(D_H)_r$$

$$A_v^\star = A_v/(A_v)_r \ , \quad K_v^\star = K_v/(K_v)_r \ , \qquad D_v^\star = D_v/(D_v)_r$$

31
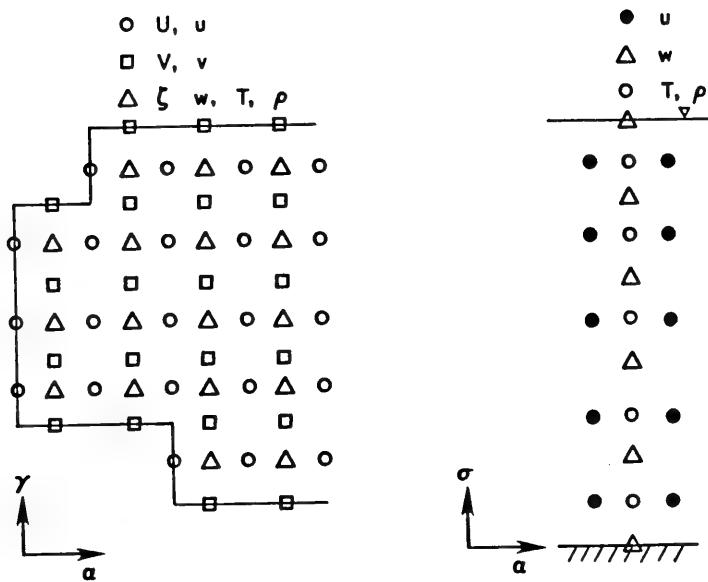
Figure 2.3.   Staggered numerical grid.

where quantities with subscript r are reference quantities, and D and L are reference length scales in vertical and horizontal directions. Notice that (α, γ) have been written into (x, y) for clarity.

Dimensionless Equations

Suppressing the asterisk (*) for clarity, the non-dimensional governing equations in the transformed coordinates become:

Continuity:

$$\frac{\partial \zeta}{\partial t} + \frac{\beta}{\mu_x} \frac{\partial Hu}{\partial x} + \frac{\beta}{\mu_y} \frac{\partial Hv}{\partial y} + H \frac{\partial \omega}{\partial \sigma} = 0 \tag{2.24}$$

x-Momentum:

$$\frac{1}{H} \frac{\partial Hu}{\partial t} = - \frac{\partial \zeta}{\mu_x \partial x} + v - \frac{Ro}{H} \left(\frac{\partial Huu}{\mu_x \partial x} + \frac{\partial Huv}{\mu_y \partial y} + \frac{\partial Hu\omega}{\partial \sigma} \right) + \frac{E_v}{H^2} \frac{\partial}{\partial \sigma} \left(A_v \frac{\partial u}{\partial \sigma} \right)$$

$$- \frac{Ro}{Fr^2 \mu_x} \left[H \int_\sigma^0 \frac{\partial \rho}{\partial x} d\sigma + \frac{\partial H}{\partial x} \left(\int_\sigma^0 \rho d\sigma + \sigma \rho \right) + \frac{\partial p_a}{\partial x} \right] \tag{2.25}$$

$$+ E_H \left[\frac{\partial}{\mu_x \partial x} \left(A_H \frac{\partial u}{\mu_x \partial x} \right) + \frac{\partial}{\mu_y \partial y} \left(A_H \frac{\partial u}{\mu_y \partial y} \right) + H.O.T. \right]$$

$$\equiv - \frac{\partial \zeta}{\mu_x \partial x} + \frac{E_v}{H^2} \frac{\partial}{\partial \sigma} \left(A_v \frac{\partial u}{\partial \sigma} \right) + B_x$$

y-Momentum:

$$\frac{1}{H} \frac{\partial Hv}{\partial t} = - \frac{\partial \zeta}{\mu_y \partial y} - u - \frac{Ro}{H} \left(\frac{\partial Huv}{\mu_x \partial x} + \frac{\partial Hvv}{\mu_y \partial y} + \frac{\partial Hv\omega}{\partial \sigma} \right) + \frac{E_v}{H^2} \frac{\partial}{\partial \sigma} \left(A_v \frac{\partial v}{\partial \sigma} \right)$$

33

$$- \frac{Ro}{Fr^2 \mu_y} \left[H \int_\sigma^0 \frac{\partial \rho}{\partial y} \, d\sigma + \frac{\partial H}{\partial y} \left(\int_\sigma^0 \rho \, d\sigma + \sigma \rho \right) + \frac{\partial p_a}{\partial y} \right] \qquad (2.26)$$

$$+ \frac{E_H}{H} \left[\frac{\partial}{\mu_x \partial x} \left(A_H \frac{\partial Hv}{\mu_x \partial x} \right) + \frac{\partial}{\mu_y \partial y} \left(A_H \frac{\partial Hv}{\mu_y \partial y} \right) + \text{H.O.T.} \right]$$

$$\equiv - \frac{\partial \zeta}{\mu_y \partial y} + \frac{E_v}{H^2} \frac{\partial}{\partial \sigma} \left(A_v \frac{\partial v}{\partial \sigma} \right) + B_y$$

Heat:

$$\frac{1}{H} \frac{\partial HT}{\partial t} = - \frac{Ro}{H} \left(\frac{\partial HuT}{\mu_x \partial x} + \frac{\partial HvT}{\mu_y \partial y} + H \frac{\partial \omega T}{\partial \sigma} \right)$$

$$+ \frac{Ro}{Pe_v D/L} \frac{\partial}{H^2 \partial \sigma} \left(K_v \frac{\partial T}{\partial \sigma} \right) \qquad (2.27)$$

$$+ \frac{Ro}{Pe_H H} \left[\frac{\partial}{\mu_x \partial x} \left(K_H \frac{\partial HT}{\mu_x \partial x} \right) + \frac{\partial}{\mu_y \partial y} \left(K_H \frac{\partial HT}{\mu_y \partial y} \right) + \text{H.O.T.} \right]$$

Salinity:

$$\frac{1}{H} \frac{\partial HS}{\partial t} = - \frac{Ro}{H} \left(\frac{\partial HuS}{\mu_x \partial x} + \frac{\partial HvS}{\mu_y \partial y} + H \frac{\partial \omega S}{\partial \sigma} \right)$$

$$+ \frac{Ro}{Sc_v D/L} \frac{\partial}{H^2 \partial \sigma} \left(D_v \frac{\partial S}{\partial \sigma} \right) \qquad (2.28)$$

$$+ \frac{Ro}{Sc_H H} \left[\frac{\partial}{\mu_x \partial x} \left(D_H \frac{\partial HS}{\mu_x \partial x} \right) + \frac{\partial}{\mu_y \partial y} \left(D_H \frac{\partial HS}{\mu_y \partial y} \right) + \text{H.O.T.} \right]$$

34

Equation of State:

$$\rho = \rho(T,S) \tag{2.29}$$

where $\beta \equiv gD/L^2 f^2$, H is the sum of local depth and surface displacement, and the higher order terms (H.O.T.) containing horizontal gradients of the water depth can be generally neglected in the computation. The exact form of the equation of state is discussed in Appendix C. The vertical velocity in the stretched coordinates, ω, is computed from:

$$\omega = -\frac{\beta}{H}\int_{-1}^{\sigma}\left(\frac{\partial Hu}{\mu_x \partial x} + \frac{\partial Hv}{\mu_y \partial y}\right) d\sigma + \frac{\beta(1+\sigma)}{H}\int_{-1}^{0}\left(\frac{\partial Hu}{\mu_x \partial x} + \frac{\partial Hv}{\mu_y \partial y}\right) d\sigma \tag{2.30}$$

Dimensionless Boundary Conditions

The boundary conditions, in the transformed coordinates and in non-dimensional form, at the surface ($\sigma=0$) are:

$$A_v \left(\frac{\partial u}{\partial \sigma}, \frac{\partial v}{\partial \sigma}\right) = HD \ (\tau_{sx}, \ \tau_{sy});$$

$$\omega = 0; \quad \frac{\partial T}{\partial \sigma} = \frac{HD}{K_v} q_s; \quad \frac{\partial S}{\partial \sigma} = 0 \tag{2.31}$$

while at the bottom ($\sigma=-1$) are:

$$A_v \left(\frac{\partial u}{\partial \sigma}, \frac{\partial v}{\partial \sigma}\right) = \frac{H}{E_v} (\tau_{bs}, \ \tau_{by}) = \frac{U_r}{(A_v)_r} DH \ C_d \ (u_1^2 + v_1^2)^{1/2} \ (u_1, \ v_1);$$

$$\omega = 0; \quad \frac{\partial T}{\partial \sigma} = 0; \quad \frac{\partial S}{\partial \sigma} = 0 \tag{2.32}$$

Along the shoreline where river inflow or outflow may occur, the conditions are:

$$u = u \ (x, \ y, \ \sigma); \quad v = v \ (x, \ y, \ \sigma); \quad \omega \neq 0;$$

$$T = T \ (x, \ y, \ \sigma); \quad S = S \ (x, \ y, \ \sigma) \tag{2.33}$$

Along the open boundaries, either the surface elevation y is specified as a function of time and time, or the normal gradient of ζ is set to zero:

$$\zeta = \zeta \ (x, \ y, \ t) \quad \text{or} \quad \frac{\partial \zeta}{\partial n} = 0 \quad ; \tag{2.34}$$

$$\left(\frac{\partial u}{\partial n}, \ \frac{\partial v}{\partial n} \right) = 0 \quad \text{or} \quad u = u \ (x, \ y, \ \sigma, \ t); \quad v = v \ (x, \ y, \ \sigma, \ t) \tag{2.35}$$

The exact form of the open boundary condition depends on the relative importance of the various forcings including tides, winds, and baroclinic effects. Open boundary conditions will be discussed further in the realistic simulations of the coastal currents.

2.8 External Mode

In the present study, numerical computation of the internal mode, which is governed by the slower baroclinic vertical flow structure dynamics, is separated from the computation of the vertically-integrated variables (external mode), which are governed by the fast barotropic dynamics. This so-called "mode splitting" technique resulted in significant improvement of the numerical efficiency of a three-dimensional hydrodynamic model for Lake Erie (Sheng et al., 1978) and was detailed in Sheng and Lick (1980). Basically, it allows for computation of the three-dimensional flow structures with minimal additional cost over computation of the two-dimensional flow with a vertically-integrated model.

Vertically-Integrated Equations

The external mode, as described by the water level (ζ) and the vertically-integrated mass fluxes (U and V), is governed by the following equations:

$$\frac{\partial \zeta}{\partial t} + \beta \left(\frac{\partial U}{\mu_x \partial x} + \frac{\partial V}{\mu_y \partial y} \right) = 0 \qquad (2.36)$$

$$\frac{\partial U}{\partial t} = - \frac{H}{\mu_x} \frac{\partial \zeta}{\partial x} + V - \frac{Ro}{H} \left[\frac{\partial}{\mu_x \partial x} \left(\frac{U^2}{H} \right) + \frac{\partial}{\mu_y \partial y} \left(\frac{UV}{H} \right) \right]$$

$$- \frac{Ro}{Fr^2} \int_{-1}^{0} \left[H \int_{\sigma}^{0} \frac{\partial \rho}{\mu_x \partial x} \, d\sigma + \frac{\partial H}{\mu_x \partial x} \left(\int_{\sigma}^{0} \rho d\sigma + \sigma \rho \right) + \frac{H}{\mu_x} \frac{\partial p_a}{\partial x} \right] H d\sigma$$

$$+ \tau_{sx} - \tau_{bx} + \int_{-1}^{0} H \, (H.D.)_x \, d\sigma \equiv - \frac{H}{\mu_x} \frac{\partial \zeta}{\partial x} + D_x \qquad (2.37)$$

37

$$\frac{\partial V}{\partial t} = -\frac{H}{\mu_y}\frac{\partial \zeta}{\partial y} - U - \frac{Ro}{H}\left[\frac{\partial}{\mu_x \partial x}\left(\frac{UV}{H}\right) + \frac{\partial}{\mu_y \partial y}\ \frac{V^2}{H}\right]$$

$$-\frac{Ro}{Fr^2}\int_{-1}^{0}\left[H\int_{\sigma}^{0}\ \frac{\partial\rho}{\mu_y \partial y}\ d\sigma + \frac{\partial H}{\mu_y \partial y}\left(\int_{\sigma}^{0}\rho d\sigma + \sigma\rho\right) + \frac{H}{\mu_y}\ \frac{\partial P_a}{\partial y}\right]Hd\sigma$$

$$+ \tau_{sy} - \tau_{by} + \int_{-1}^{0} H\ (H.D.)_y\ d\sigma \equiv -\frac{H}{\mu_y}\frac{\partial \zeta}{\partial y} + D_y \qquad (2.38)$$

where the vertically-integrated velocities are defined as

$$(U,\ V) \equiv \int_{-1}^{0} H\ (u,v)\ d\sigma \qquad (2.39)$$

and $(H.D.)_x$ and $(H.D.)_y$ represent the horizontal diffusion terms shown in Equations (2.25) and (2.26), respectively. Notice that simplifying approximations have been made in deriving the nonlinear terms shown in (2.37) and (2.38). A more general representation of these terms should include a unity-order multiplication factor which depends on the vertical shapes of horizontal velocities (Sheng et al., 1978). Due to difficulty in estimating the shape parameter which is usually a function of time and space, most vertically integrated models use the approximate nonlinear terms and hence underestimate the nonlinear effects. Chen (1981) attempted to account for this effect of a non-uniform velocity profile in a vertically-integrated model by introducing an internal stress term. In the present three-dimensional model, the nonlinear inertia terms can be accurately computed from the three-dimensional velocity field and hence no approximations are required of the vertical shapes of horizontal velocities.

Bottom Boundary Condition

The bottom stress terms τ_{bx} and τ_{by} appearing in the above external mode equations are computed from the vertical velocity profiles, available from the internal mode computations, and the quadratic stress law (2.32). Conventional vertically-integrated models, however, compute the bottom stresses based on the vertically-integrated velocities through the following dimensional formula:

$$(\tau_{bx}, \tau_{by}) = \frac{\rho g}{C_c^2 H} (U^2 + V^2)^{1/2} (U,V) \tag{2.40}$$

where C_c is the Chezy coefficient derived from analysis on one-dimensional pipe flows:

$$C_c = 8.21 \ H^{1/6}/n \quad [cm/sec] \tag{2.41}$$

where n is the Manning's n in units of $(cm)^{1/6}$. Values of Manning's n have been suggested for a variety of surface materials (e.g., Pao, 1967) in open channel flows. When such a formula is used to compute coastal currents, a great deal of effort has to be spent in tuning the Manning's n in order to achieve good fit between computed and measured results on surface displacements or volume transports.

39

2.9 Internal Mode

Internal Mode Equations

The internal mode of the flow is described by the vertical flow structures and the temperature and salinity distributions. Defining perturbation (not necessarily infinitesimal) velocities as $u' \equiv u - U/H$ and $v' \equiv v - V/H$, the equations for the internal mode are obtained by subtracting the vertically-averaged momentum equations from the three-dimensional equations:

$$\frac{1}{H} \frac{\partial Hu'}{\partial t} = B_x - \frac{D_x}{H} + \frac{1}{H^2} \frac{\partial}{\partial \sigma} \left[A_v \frac{\partial}{\partial \sigma} \left(\frac{Hu'+U}{H} \right) \right] \qquad (2.42)$$

$$\frac{1}{H} \frac{\partial Hv'}{\partial t} = B_y - \frac{D_y}{H} + \frac{1}{H^2} \frac{\partial}{\partial \sigma} \left[A_v \frac{\partial}{\partial \sigma} \left(\frac{Hv'+V}{H} \right) \right] \qquad (2.43)$$

where B_x and B_y, defined in (2.25) and (2.26), represent <u>all terms</u> in the transformed three-dimensional momentum equations except the surface slopes and the vertical diffusion terms, and D_x and D_y are defined in the vertically-integrated equations (2.37) and (2.38). Notice that the above equations retain the three-dimensionality and hence are different from the model of Nihoul and Ronday (1982), which is actually a superposition of a lateral two-dimensional model and a vertical one-dimensional model.

The above equations do not contain the surface slope terms and hence a large time step (much larger than the limit imposed by the gravity wave propagation) may be used in the numerical computation. The internal mode also includes equations for temperature, salinity, and vertical velocity as defined by Eqs. (2.27), (2.28), and (2.30).

Turbulence Parameterization

At this point, it is appropriate to discuss the parameterization of turbulence in the present model. A semi-empirical theory of vertical mixing is used in this study. The effect of stratification, as measured by the Richardson number, Ri, on the intensity of vertical turbulent mixing is parameterized by a number of empirical stability functions:

$$A_V = A_{VO} \; \phi_1(Ri); \quad K_V = K_{VO} \; \phi_2(Ri); \quad D_V = D_{VO} \; \phi_3(Ri); \quad (2.44)$$

where

$$Ri = \frac{-gHh}{U_r^2(1+\rho)} \; \frac{\partial \rho}{\partial \sigma} \left[\left(\frac{\partial u}{\partial \sigma} \right)^2 + \left(\frac{\partial v}{\partial \sigma} \right)^2 \right]^{-1} \quad (2.45)$$

where A_{VO}, K_{VO}, and D_{VO} are the eddy coefficients in the absence of any density stratification and ϕ_1, ϕ_2, and ϕ_3 are stability functions. Typically they are written as:

$$\phi_1 = (1+\sigma_1 Ri)^{m_1} \; ; \quad \phi_2 = (1+\sigma_2 Ri)^{m_2} \; ; \quad \phi_3 = (1+\sigma_3 Ri)^{m_3} \quad (2.46)$$

where the constants σ_1, σ_2, σ_3, m_1, m_2, and m_3 are generally determined empirically by comparing model output with measured data. As shown in Figure 2.4(a), great discrepancy exists among the various empirical forms of the stability functions. Much of the discrepancy resulted from (1) the difference in numerical schemes used; (2) the different turbulent regime of the water bodies studied; and (3) the difference in resolution of the model and the measured data. In addition, the critical Richardson numbers, at which turbulence is completely damped by buoyancy, given by these formulas are much too high compared to the measured value of 0.25 (Erikson, 1978). To unify this discrepancy, stability functions may be determined from a second-order closure model of turbulence (Appendix D). Assuming a balance between turbulence production and dissipation, i.e., the so-called "super-equilibrium" condition (Donaldson, 1973), we can obtain a simpler set of algebraic relationships between the turbulent correlations and mean flow gradients. As shown in Figure 2.4(b), such a stability function leads to a critical

41
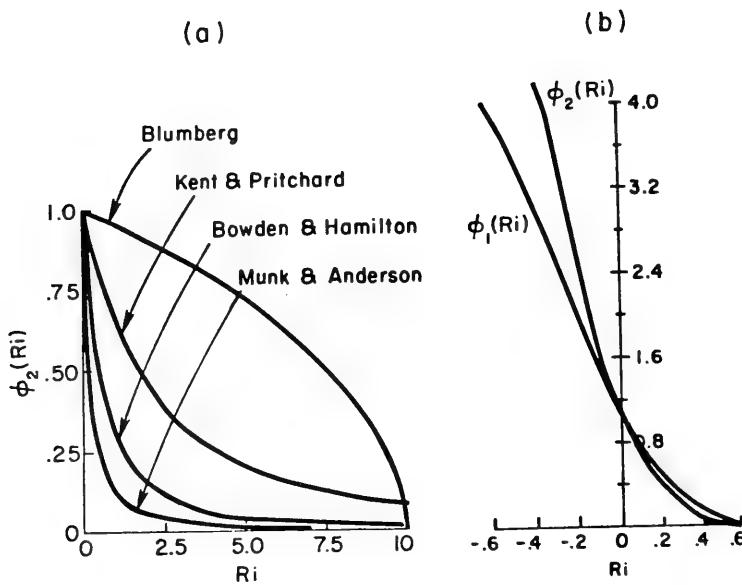
Figure 2.4. (a) Empirical stability functions of vertical turbulent
                 eddy coefficients.

             (b) Stability functions determined from a second-order closure
                 model of turbulent transport.

Richardson number on the order of 0.5, much closer to the correct value of 0.25. For simplicity, the stability function ϕ_3 for salinity is assumed to be the same as ϕ_2 for temperature.

The eddy coefficients in the absence of any stratification are assumed to be of the following form for A_{v_0}:

$$A_{v_0} = \frac{U_r \Lambda^2}{H} \left[\left(\frac{\partial u}{\partial \sigma} \right)^2 + \left(\frac{\partial v}{\partial \sigma} \right)^2 \right]^{0.5} \tag{2.47}$$

where Λ is a length scale. In general, Λ is assumed to be a parabolic function of σ with its peak value at mid-depth not exceeding a certain fraction of the local depth.

Although lateral eddy coefficients $(A_H \sim 10^2$ to $10^6 \text{ cm}^2/\text{sec})$ are typically several orders of magnitude higher than the vertical eddy coefficients $(A_v \sim 1$ to $10^2 \text{ cm}^2/\text{sec})$, the net effect of lateral turbulent diffusion is generally small compared to the lateral advection and vertical turbulent diffusion, except within the thin lateral boundary layers. Murthy (1976) found that the lateral mixing in the open waters of Lake Ontario increases with the size of the tracer cloud. With a cloud size of 1 km, his formula gives a lateral diffusion coefficient on the order of $10^5 \text{ cm}^2/\text{sec}$ in the epilimnion, while a value two orders of magnitude smaller in the hypolimnion. Csanady (1963), on the other hand, measured a much smaller value of $400 \text{ cm}^2/\text{sec}$ in the epilimnion under similar conditions. Numerical experiments in Lake Erie (Sheng, 1975) indicate that the lateral diffusion coefficient has little effect on the large scale circulation.

For the first grid point above the bottom, the vertical diffusion terms in Eqs. (2.42) and (2.43) contain the bottom shear stresses. A quadratic stress law with a physically meaningful drag coefficient, as shown in Eqs. (2.19) and (2.20), derived from boundary layer dynamics, is used. The physical roughness of the coastal environment is correctly reflected in such a formulation.

43

3. NUMERICAL ALGORITHMS

3.1 External Mode Algorithm

Treating implicitly all the terms in the continuity equation (2.36) while only the time derivatives and the surface slopes in the momentum equations (2.37) and (2.38), one can obtain the following finite-difference equations:

$$(I + \phi\lambda_x + \phi\lambda_y)W^{n+1} = [I + (1-\phi)\lambda_x + (1-\phi)\lambda_y]W^n + \Delta t D^n \qquad (3.1)$$

where

$$\lambda_x = \frac{A\Delta t}{\mu_x \Delta x} \delta_x; \qquad \lambda_y = \frac{B\Delta t}{\mu_y \Delta y} \delta_y;$$

$$A = \begin{pmatrix} 0 & \beta & 0 \\ H & 0 & 0 \\ 0 & 0 & 0 \end{pmatrix}; \quad B = \begin{pmatrix} 0 & 0 & \beta \\ 0 & 0 & 0 \\ H & 0 & 0 \end{pmatrix}; \quad D = \begin{pmatrix} 0 \\ D_x \\ D_y \end{pmatrix}; \quad W = \begin{pmatrix} \zeta \\ U \\ V \end{pmatrix} \qquad (3.2)$$

where I is the identity matrix, $(\Delta x, \Delta y)$ are the horizontal grid spacings, Δt is the time step, D_x and D_y are terms in Eqs. (2.37) and (2.38) excluding the time derivatives and the surface slopes, superscripts n+1 and n indicate present and previous time step of integration, δ_x and δ_y are central difference spatial operators, and ϕ is a weighting factor, $0 < \phi < 1$. If $\phi = 0$, Eq. (3.1) reduces to a two-step explicit scheme. If $\phi > 0$ the resulting schemes are implicit, with $\phi = 1/2$ corresponding to the Crank-Nicholson scheme and $\phi = 1$ corresponding to the fully implicit scheme. Factorizing equation (3.1) and neglecting terms of $O(\Delta t^2)$ yields the following equations:

x-sweep: $\qquad (I + \phi\lambda_x) W^* = [I + (1-\phi)\lambda_x + (1-2\phi)\lambda_y] W^n + \Delta t D^n \qquad (3.3)$

y-sweep: $\qquad (I + \phi\lambda_y) W^{n+1} = W^* + \phi\lambda_y W^n \qquad (3.4)$

The two equations can be solved consecutively in an efficient manner by inversion of tridiagonal matrices in the x direction (x-sweep) and y direction (y-sweep). Furthermore, only two variables need to be solved during each sweep thus resulting in significant saving than solving the original equation (3.1). The main advantage of this implicit method is that much larger time step can be used. Courant number based on the maximum propagation speed of the surface gravity wave, $(g\bar{H}_{max})^{0.5} \Delta t/\Delta x$, may now be as large as 100, compared to the limit of 1 for explicit method. The maximum time step is now governed by the advection speed in the system:

$$\underset{x,y}{Min} \left[\frac{\Delta x, \Delta y}{(g\bar{H})^{0.5}} \right] \ll \Delta t < \underset{x,y}{Min} \left(\frac{U}{H \Delta x} + \frac{V}{H \Delta y} \right)^{-1} \tag{3.5}$$

The traditional ADI method when applied to (3.1) uses a different factorization than the present method (3.3) and (3.4). It was found that the present method is more stable than the traditional ADI method (Butler and Sheng, 1982). At very high Courant number, however, the present method may have a stability problem when waves are propagating along the diagonals of the grid. A rule of thumb is to stay within a Courant number of 10. Alternatively, one can derive a Poisson equation for ζ from Eqs. (2.36) to (2.38) and solve it with iterative or direct methods.

3.2 Internal Mode Algorithm

Treating the internal mode equations (2.42) and (2.43) with a two-level scheme and a vertically implicit scheme, one obtains the following finite difference equations:

$$\frac{H^{n+1}}{H^n} u'^{n+1} = u'^n + \Delta t \left(B_x - \frac{D_x}{H} \right) + \frac{\Delta t}{H^2} \frac{\partial}{\partial \sigma} \left[A_v \frac{\partial}{\partial \sigma} \left(H^{n+1} u'^{n+1}/H^n + U^{n+1}/H^n \right) \right] \tag{3.6}$$

$$\frac{H^{n+1}}{H^n} v'^{n+1} = v'^n + \Delta t \left(B_y - \frac{D_y}{H} \right) + \frac{\Delta t}{H^2} \frac{\partial}{\partial \sigma} \left[A_v \frac{\partial}{\partial \sigma} \left(H^{n+1} v'^{n+1}/H^n + V^{n+1}/H^n \right) \right] \tag{3.7}$$

The bottom friction terms in both equations are also treated implicitly to ensure unconditional numerical stability in shallow waters. The vertical implicit scheme is essential since applying an explicit scheme in shallow water environment may require an exceedingly small time step on the order of a few seconds. In addition, care must be taken to ensure that the vertically-integrated perturbation velocities at each horizontal location (i,j) always equal to zero:

$$\sum_{K=1}^{K_{max}} u'_{i,j,K} = 0 \qquad \sum_{K=1}^{K_{max}} v'_{i,j,K} = 0 \qquad (3.8)$$

The computations of the u' and v' equations are governed by a stability criterion similar to equation (3.5), except with the vertically-integrated velocities replaced by the local three-dimensional velocities. After u'^{n+1} and v'^{n+1} are obtained, u and v can be computed from:

$$u^{n+1} = u'^{n+1} + U^{n+1}/H^{n+1} \qquad (3.9)$$

$$v^{n+1} = v'^{n+1} + V^{n+1}/H^{n+1} \qquad (3.10)$$

Following these, the vertical velocities ω^{n+1} and w^{n+1} can be computed from:

$$\omega^{n+1} = -\frac{\beta}{H^{n+1}} \sum_{K=1}^{K} \left(\frac{\Delta Hu}{\mu_x \Delta x} + \frac{\Delta Hv}{\mu_y \Delta y} \right)^{n+1} \Delta\sigma$$

$$+ \frac{\beta(1+\sigma)}{H^{n+1}} \sum_{K=1}^{KM} \left(\frac{\Delta Hu}{\mu_x \Delta x} + \frac{\Delta Hv}{\mu_y \Delta y} \right)^{n+1} \Delta\sigma \qquad (3.11)$$

$$w^{n+1} = H^{n+1} \omega^{n+1} + \frac{1+\sigma}{\beta} \frac{\zeta^{n+1} - \zeta^n}{\Delta t} \qquad (3.12)$$

46

.

After the velocities are computed, the code computes the temperature, salinity and sediment concentration if so desired. These equations are solved with the same two-time-level scheme and implicit vertical diffusion treatment.

3.3 Flow Chart

A flow chart of the solution algorithm is shown in Figure 3.1. The model can be run exclusively in the external mode with fairly large time step and various choices of bottom friction formulation. The internal mode may be updated as often as desired so long as the CFL condition is not violated.

3.4 General Numerical Consideration

Time-Differencing

Although the finite-difference equations derived above assumed a two-time-level scheme in general, three-time-level (leapfrog) scheme involving variables at n+1, n, and n-1 th levels have also been tested for some idealized problems. The three-level scheme essentially introduces second order time derivatives and hence increases the order of the original differential equations. Two disjoint solutions will develop in time and this is the so-called "time-splitting" problem (Roache, 1972). Ad-hoc fixes developed to control this problem include time smoothing (Asselin, 1972; Simons, 1974) and an occasional switch to the two-level scheme. However, extreme care must be exercised to objectively monitor the time-splitting problem and to ensure the phases of gravity waves are not affected. If the time-splitting problem could be properly monitored and controlled, the three-level scheme does exhibit somewhat less numerical damping due to the time-centering of the advective terms. In the three-level scheme, however, the lateral diffusion terms in the momentum equations have to be lagged in time (n-1 th level) to ensure numerical stability (Roache, 1972).

47
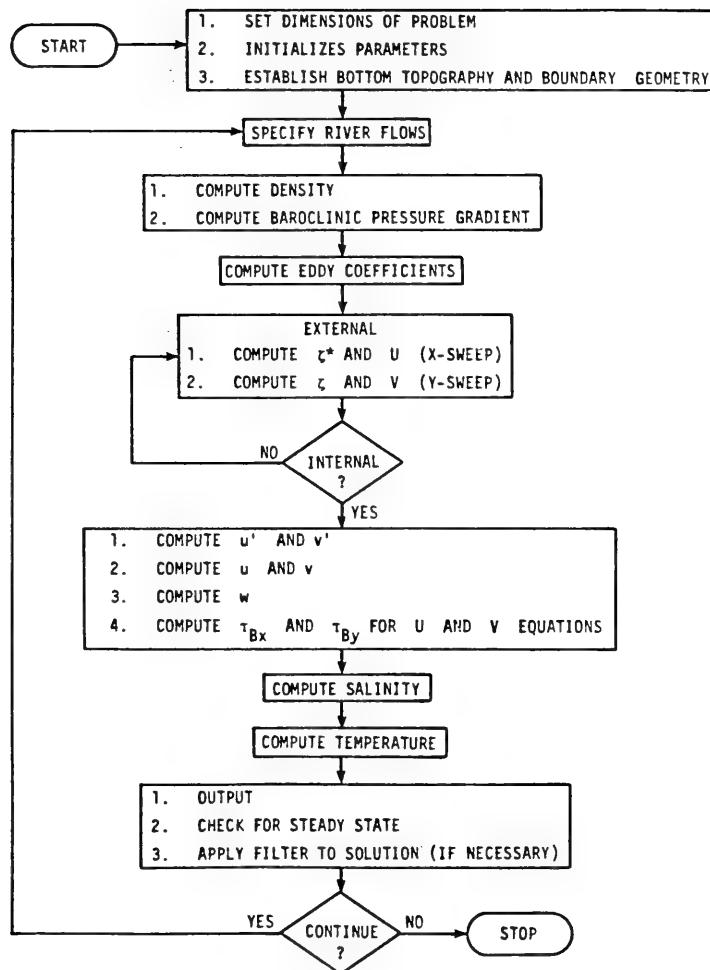
Figure 3.1. Flow chart of the three-dimensional hydrodynamic model.

Advective Schemes

Numerical treatment of advective terms is a subject of long and continuing interest in the field of numerical analysis. Various second-order schemes and the more complex higher-order schemes have been considered for the present modeling effort. Arakawa, in a series of papers, (Arakawa, 1966, 1970; Jespersen, 1974), compared various second-order advective schemes which are classified according to their Jacobians. For example, the J-1 scheme refers to the non-conservative form, the J-3 scheme refers to the conservative form, while the J-6 operator is a combination of J-1 and J-3 schemes. The J-6 operator outperforms the others due to its ability to conserve both the mean square vorticity and the kinetic energy in long simulations. Other alternatives also exist, including the fourth-order scheme, the spline method, and the fully implicit advective scheme.

It was of particular interest to see if the formally more accurate but much more complex fourth-order scheme would allow a reduction in the number of grid points and computational cost to achieve the same order of accuracy as a second-order scheme. For a one-dimensional, two-point boundary value problem and a two-dimensional simulation of the evolution of a Lamb vortex where analytical solutions exist in both cases, our second-order method (the implicit version) was compared with several higher-order methods: (1) the compact implicit block tridiagonal scheme by Kreiss (1975), (2) a similar fifth-order scheme by Thiele (1978), and (3) the operator compact implicit scheme by Hirsh (1975). The tests were performed with a very small time step such that the numerical errors were primarily due to the spatial differencing (Hirsh and Williamson, 1979). The overall efficiency of an advective scheme could be defined as the ratio of the inverse relative error to the amount of computational work (CPU time). It was found that the relative error decreases with the number of grid points, with the fourth-order scheme showing a faster rate of decrease. On the other hand, the computational work increases with the number of grid points, with the fourth order scheme showing a faster rate of increase. The net result is that at a relative error of 5% or more, all the schemes require a comparable number of grid points and have comparable overall efficiencies. The higher-order schemes only gave significantly better overall efficiency at a 1% error level or less. Since it is virtually

49

impossible to achieve such a low error level in simulating complex coastal currents due to uncertainties in model parameters and numerical errors from other terms, implementation of a complex fourth-order scheme to numerical hydrodynamic models does not appear to be justified.

A flux-corrected transport (FCT) method, suitable for simulating flow situations involving discontinuities and sharp gradients (e.g., shockwave, thermocline, front), has been developed by the NRL group (Boris and Book, 1976; Zalesak, 1979). This is a two-step method based on the combination of a lower-order advective scheme (with relatively high numerical diffusion but little numerical dispersion) and a higher-order scheme (with little damping but higher numerical dispersion). In the first step, a lower order calculation is performed. A higher-order scheme is then applied to compute the advective fluxes and the "anti-diffusive fluxes", i.e., the differences between the higher-order and the lower-order fluxes. The second step, a corrective step, adds a limited amount of anti-diffusive fluxes to the lower-order solution such that the new solution is free of overshoots or undershoots. The FCT algorithm was able to accurately resolve shocks and sharp gradients with no apparent penalty in regions where they are absent. Using the second upwind scheme as the lower-order scheme and a second-order scheme as the higher-order scheme, this FCT scheme has been applied to simulate the transport of a concentrated patch of passive contaminant by wind-driven currents in an idealized basin (Sheng, 1981) and was found to yield much better results than the one-step results of a lower-order scheme or a higher-order scheme. This study is included in Appendix E.

4. MODEL EVALUATION TESTS

4.1 Computer Simulation of Vicksburg Tidal Flume

Ippen and Harleman (1961) conducted experiments at the Waterways Experiment Station in Vicksburg, Mississippi to study the influence of various parameters on tidal motion. The experiments were performed in a uniform rectangular flume with one end closed while another end was connected to a large reservoir where sinusoidal tides were generated. The flume was 100 m long, 22.86 cm wide, and 15.24 cm deep. For their Test No. 29, the tidal forcing was:

$$\zeta(0,t) = \zeta_0 \cos\left(\frac{2\pi t}{T}\right) \qquad (4.1)$$

where $\zeta_0 = 1.52$ cm and $T = 600$ sec. For both high water and low water conditions, the water level at selected points along the flume are plotted in Figure 4.1.

To test our three-dimensional numerical model, we ran a simulation of the Vicksburg flume. The parameters used are: $A_v = 1$ cm^2/sec, $C_d = 0.004$, $\Delta x = 5$ m, $\Delta y = 4.56$ cm, $\Delta z = 0.3$ cm. As shown in Figure 4.1, the results obtained with $\Delta t = 5$ sec agree very closely with the measurements. Even at $\Delta t = 30$ sec, the results are only slightly off.

4.2 Comparison with Analytical Results

In this section, the vertically-averaged version of our model was used to simulate the tidal flow in a rectangular bight and the results were compared with the analytical solution.

Consider a square basin of constant depth h and length L. The basin has vertical walls along the West ($x=0$) and the South ($y=0$), while open boundaries along the East ($x=L$) and the North ($y=L$). Neglecting the non-linear terms and horizontal diffusion terms, and also linearizing the bottom friction terms, one obtains the following governing equations in dimensional form:

51
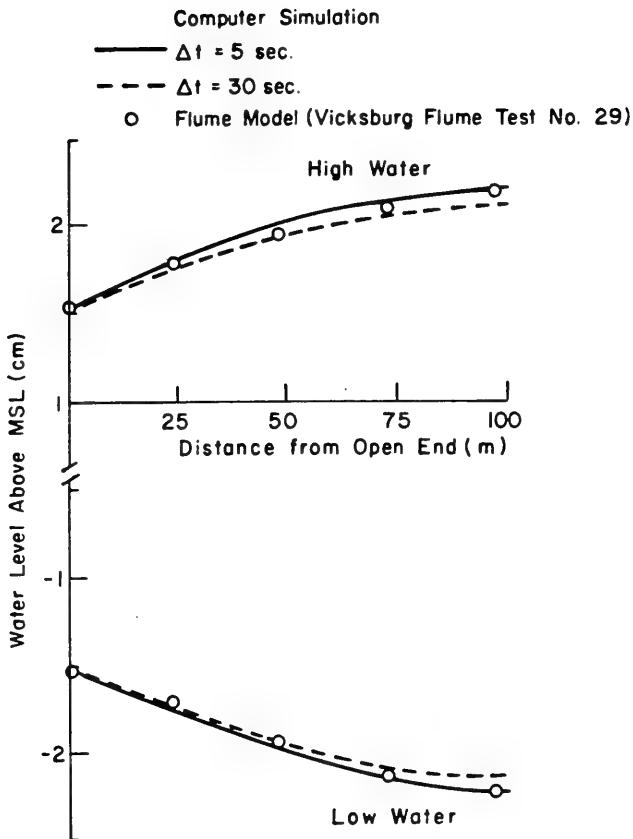
Figure 4.1. Computer simulation of the Vicksburg Tidal Flume.

$$\frac{\partial \zeta}{\partial t} + \frac{\partial U}{\partial x} + \frac{\partial V}{\partial y} = 0 \qquad (4.2)$$

$$\frac{\partial U}{\partial t} = - gh \frac{\partial \zeta}{\partial x} - F_c \frac{U}{H} \qquad (4.3)$$

$$\frac{\partial V}{\partial t} = - gh \frac{\partial \zeta}{\partial y} - F_c \frac{V}{h} \qquad (4.4)$$

where h is the depth and F_c is a friction coefficient carrying the dimension of velocity.

The water level at the open boundaries are selected such that the resulting solution consists of the sum of two progressive waves propagating in the positive and negative x-direction, and two progressive waves propagating in the positive and negative y-direction. Thus (van de Kreeke and Chiu, 1980):

$$(\zeta)_{x=L} = a \cos \sigma t + [2a/(\cosh 2\mu L + \cos 2kL)]$$

$$x [(\cosh \mu y \cos ky \cosh \mu L \cos kL$$

$$+ \sinh \mu y \sin ky \sinh \mu L \sin kL) \cos \sigma t$$

$$- (\sinh \mu y \sin ky \cosh \mu L \cos kL$$

$$+ \cosh \mu y \cos ky \sinh \mu L \sin kL) \sin \sigma t] \qquad (4.5)$$

and ζ at y=L can be represented by an expression similar to Eq. (4.5) with y replaced by x. In Eq. (4.5), 2a is the amplitude of the tide at (x=L, y=L), σ is the angular frequency of the tide, $k_0 = \sigma/(gh)^{1/2}$, $k^2 - \mu^2 = k_0^2$.

The solution of this problem is:

$$\zeta = 2a/(\cosh 2\mu L + \cos 2kL)$$

$$x \{[\cosh \mu L \cos kL (\cosh \mu x \cos kx + \cosh \mu y \cos ky)$$

$$+ \sinh \mu L \sin kL (\sinh \mu x \sin kx + \sinh \mu y \sin ky)] \cos \sigma t$$

$$- [\cosh \mu L \cos kL (\sinh \mu x \sin kx + \sinh \mu y \sin ky)]$$

$$- \sin \mu L \sin kL (\cosh \mu x \cos kx + \cosh \mu y \cos ky)] \sin \sigma t\}$$

$$(4.6)$$

$$U = (2a \sqrt{gh} \, k_0 / \sqrt{\mu^2 + k^2}) / (\cosh 2\mu L + \cos 2 kL)$$

$$x [-(\sinh \mu x \cos kx \cosh \mu L \cos kL + \cosh \mu x \sin kx \sinh \mu L \sin kL)$$

$$x \cos (\sigma t + \theta)$$

$$+ (\cosh \mu x \sin kx \cosh \mu L \cos kL - \sinh \mu x \cos kx \sinh \mu L \sin kL)$$

$$x \sin (\sigma t + \theta)]$$

$$(4.7)$$

where $\theta = \tan^{-1}(\mu/k)$. The expression for V is the same as Eq. (4.7) with x replaced by y. The above solution was first applied to a bight with L=150 km and h=10 m driven by a tide with 2a=30 cm and T=24 hrs. The bottom friction coefficient was assumed to be 0.1 cm/sec. The water level at an instant of time when $\zeta(x=L, y=L) = 0$ and $\zeta(x=0, y=0) = $ maximum is shown in Figure 4.2. Figure 4.3 shows the corresponding velocity field.

Eqs. (4.2) through (4.4), along with the boundary condition shown by Eq. (4.5), were then solved by the vertically-averaged version of our numerical model discussed in the previous chapter. The numerical solutions were computed with $\Delta t=2$ hrs and $\Delta x=15$ km. The computed water level and velocity field agree quite well with the analytical results at corresponding times. As shown in Figure 4.2, the water levels computed by our model compare very well with the analytical results over much of the bight. The numerical model underestimates the water level near the lower left corner by about 10%. The computed velocity field in Figure 4.3 indicates a somewhat smaller

54
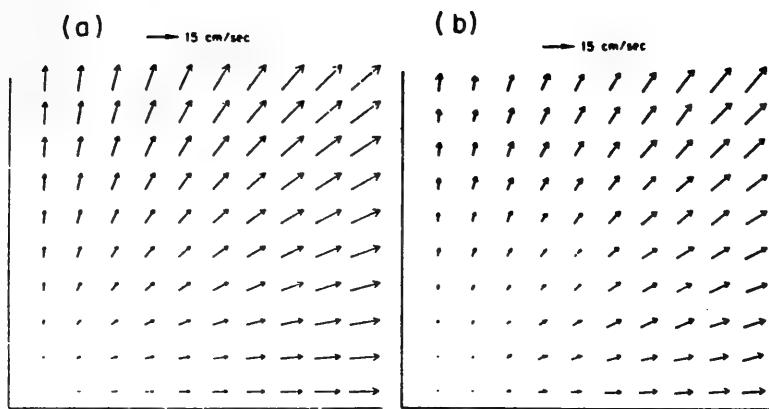
Figure 4.2. Vertically-integrated velocities at an instant when ζ (L,L)=0 and ζ (0,0)=max in an open bight driven by tidal waves along the open boundaries: (a) analytical results, (b) model results
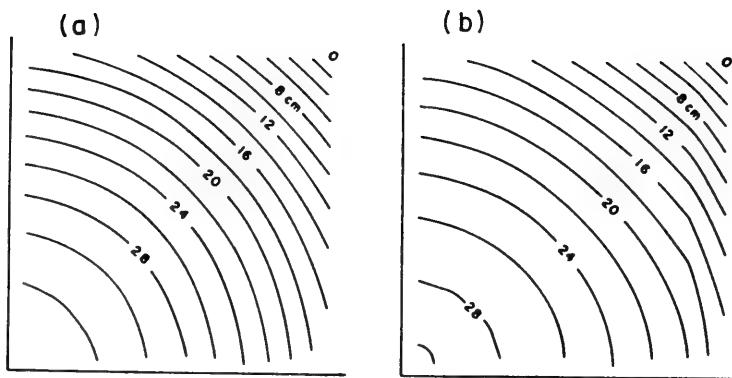
Figure 4.3. Surface displacements corresponding to conditions in Figure 4.2.

magnitude than the analytical results. Notice that the numerical computation was made with a time step of 7200 sec which is much greater than that allowed by an explicit numerical scheme (~ 1000 sec). This is apparently responsible for the damping in the numerical solutions.

4.3 Dominant Time Scales for Wind-Driven Currents in a Shallow Sea

The general three-dimensional, time-dependent motion in a large shallow sea, with complex geometry and topography, as described the basic equations and boundary conditions in the previous section, is too complicated for analytical solution and can only be computed numerically.

Under limiting conditions, however, the system of equations can become linearized and sufficiently simplified such that analytical solutions are available. Although idealized, these analytical solutions can provide much insight into the dynamics of the basin. In addition, they can be used as reference solutions for checking the results from complicated multi-dimensional numerical models.

Steady-State Analysis

Welander (1957) analyzed the steady-state currents in a homogeneous shallow sea, where non-linear inertia and lateral diffusion are negligible compared to Coriolis acceleration and vertical turbulent diffusion, and obtained the following analytical expression (in dimensional form) for horizontal velocities as a function of depth with wind stress and surface slope as parameters:

$$u + iv = \frac{\sinh\lambda(h+z)}{\cosh\lambda h} \frac{(\tau_{sx}+i\tau_{sy})}{\lambda A_v^{3/2}} - \frac{ig}{f} \left(\frac{\cosh\lambda z}{\cosh\lambda h} -1\right) \left(\frac{\partial\zeta}{\partial x} + i\frac{\partial\zeta}{\partial y}\right) \quad (4.8)$$

where $i=(-1)^{0.5}$, $\lambda=(if/Av)^{0.5}$, $z=-h(x,y)$ is the bottom, and $z=\zeta(x,y)$ is the free surface. This solution represents the sum of the drift current, which is proportional to the wind stress, and the slope current, which is proportional to the surface slope. Despite its limitations, this solution has been the basis of many numerical models.

Time-Dependent Analysis

The time-dependent, wind-driven currents in an infinitely long shallow basin with a free surface has been studied in detail by Haq, Lick, and Sheng (1974). Adding time-dependence into Welander's steady-state analysis, they analytically computed the unit drift current and the unit slope current and analyzed the various time scales of large scale motion by examining the asymptotic behavior and singularities of the integro-differential equation for the free surface displacement ζ. The results depend strongly on the following parameter:

$$\beta = \frac{gD}{L^2 f^2} = \left(T_i/T_g\right)^2 \tag{4.9}$$

where D and L are the representative length scales in the vertical and lateral directions. The square root of the parameter can be looked upon as the ratio between the time scales associated with inertial oscillation and the surface gravity wave. Another parameter of importance is D/d, where d is the depth of frictional influence defined as $\pi/(2A_v/f)^{0.5}$.

In the limit of $\beta \to \infty$ (rigid-lid approximation), ζ is a linear combination of two solutions, one of which decays with a time scale T_1, a viscous diffusion time $4\pi^2 D^2/5fd^2$ when D/d<<1 or a spin-up time $2\pi D/fd$ when D/d>>1, while another solution decays with a time scale of T_1 but oscillates with a period of $T_2 = 2L/m(gD)^{0.5}$ (m=1,2,3,...), the period of seiches in a lake. In the limit of $\beta \to 0$, however, it exhibits a decaying oscillatory solution with a period $T_3 = 2\pi/f$ corresponding to inertial oscillation. In addition, there is a decaying solution with a decay time of $T_4 = T_1 L^2 f^2/m^2 \pi^2 gD$ (m=1,2,3...) corresponding to the movement of fluid from one side of the basin to another under the action of a wind stress. For intermediate values of β corresponding to real basins, the general solution consists of: (1) a decaying part that has a decay time varying from T_1 to T_4 as β goes from ∞ to 0, and (2) an imposed decaying oscillatory part with a decaying time of the order of T_1 and a period of oscillation varying from T_2 to T_3 as β goes from ∞ to 0. The rigid-lid model approaches the steady state much quicker than the free-surface model and is only valid in the limit of

$\beta \rightarrow \infty$.

In contrast with the case of an infinitely long basin where there is a single oscillation with a period between T_2 and T_3, the flow in a finite enclosed basin consists of the superposition of two different sets of waves as the result of interaction between the inertial oscillations and the surface gravity waves. Lamb (1932) analyzed the normal modes in a circular basin and found that the period of one of these waves is on the order of T_3, while the period of the other wave goes from T_2 to about $2T_2$ where β goes from ∞ to 0. Analytic solution in such a square basin, driven by a uniform wind stress, was obtained by Haq, Lick, and Sheng (1974) and was found to be quite similar to the solution in a circular basin. These important time scales are very useful for checking the accuracy of numerical results.

Comparison With Numerical Results

A free-surface model has been applied to examine the response of a square basin, with a constant depth of 10 m, to an impulsive wind stress of 1 dyne/cm^2. Constant vertical eddy viscosity of 25 cm^2/sec was assumed such that $E_v = 0.025$. Simulations were carried out in a number of basins with varying horizontal lengths, ranging from 40 km to 100 km, such that β varied from about 4 to about 0.01. In all the cases, due to the relatively small viscous effect, the transient results exhibited two distinct time scales indicating the interaction of two waves in the basin. For large values of 5b, as shown in Figure 4.4, one of the waves has a period (T_1) that corresponds exactly to the period of gravity waves (T_g) while another wave has a period (T_2) slightly larger than the inertial period $(2\pi T_i)$. As β is decreased, t_1 becomes larger than T_g and asymptotes to approximately $2T_g$, while T_2 is increased only slightly. This agrees with the approximate analytical results discussed above.
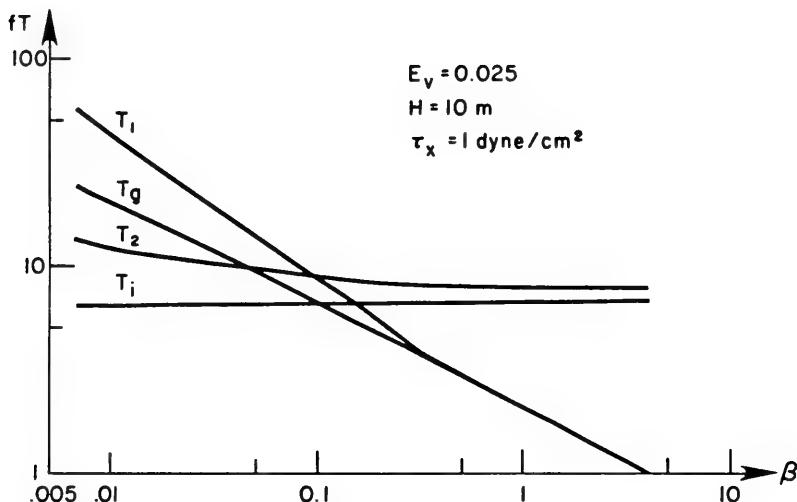
Figure 4.4. Comparison between numerically- and analytically-computed dominant time scales of wind-driven currents in a square enclosed basin with varying β.

.

4.4 Effects of Bottom Boundary Condition on Wind-Driven Currents in a Shallow Sea

Next we shall illustrate the effect of bottom boundary condition on the response of a lake under an impulsive wind stress. Consider a 50 Km square lake with the bottom varying linearly from 2.5 m at y=0 to 7.5 m at y=50 Km. At t=0, a wind stress of 1 dyne/cm^2 is applied in the x direction. Assuming a constant vertical eddy viscosity of 25 cm^2/sec, the vertical Ekman number ranges between 0.44 and 4.0. Based on the analytical results discussed above, for the present case T_1=2.5 hrs, T_2=3 to 5.6 hrs, T_3=17.5 hrs, and T_4 is irrelevant since H/d $\ll$ 1 and β is between 1 and 3. Numerical computations were performed with two types of bottom boundary conditions: (1) quadratic stress law with C_{da}=0.004, and (2) no-slip condition, i.e., (τ_{bx}, τ_{by}) = ρA_v (u_1, v_1)/Δz where u_1 and v_1 are the horizontal velocities at Δz above the bottom. The transient results (Figure 4.5) obtained with the no-slip condition clearly exhibit a decay time on the order of T_1 but T_2 is not apparent in the results. With the quadratic stress law, T_2 is apparent in the results and the decay time is more than doubled than the no-slip case, due primarily to the smaller bottom dissipation. At the steady-state, the vertical profiles of horizontal velocities due to the two different boundary conditions are quite different. As shown in Figure 4.6, the quadratic stress law yields a flatter velocity profile above the bottom much like a turbulent boundary layer over a flat bottom. The no-slip condition, on the other hand, yields a parabolic profile above the bottom resembling a laminar boundary layer. The large difference in the near-bottom currents computed by the two boundary conditions is of particular significance when considering the transport of sediments or other materials near the bottom.

60
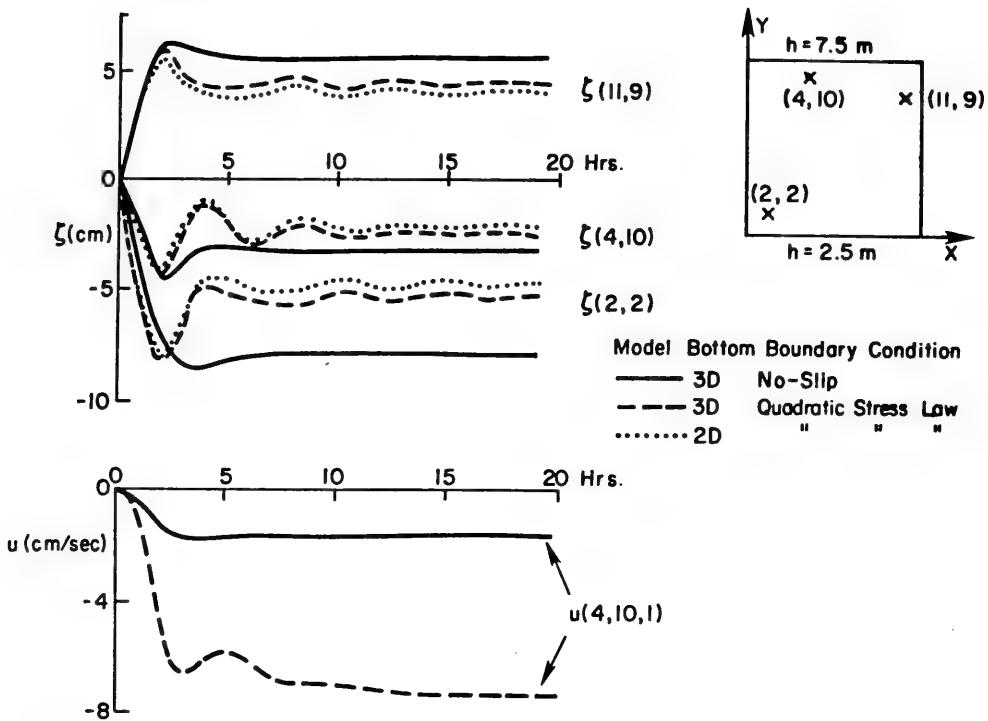
Figure 4.5.   Surface elevation and near-bottom velocity at selected points
in a constant slope enclosed basin driven by uniform wind stress.
Comparison among three numerical models.
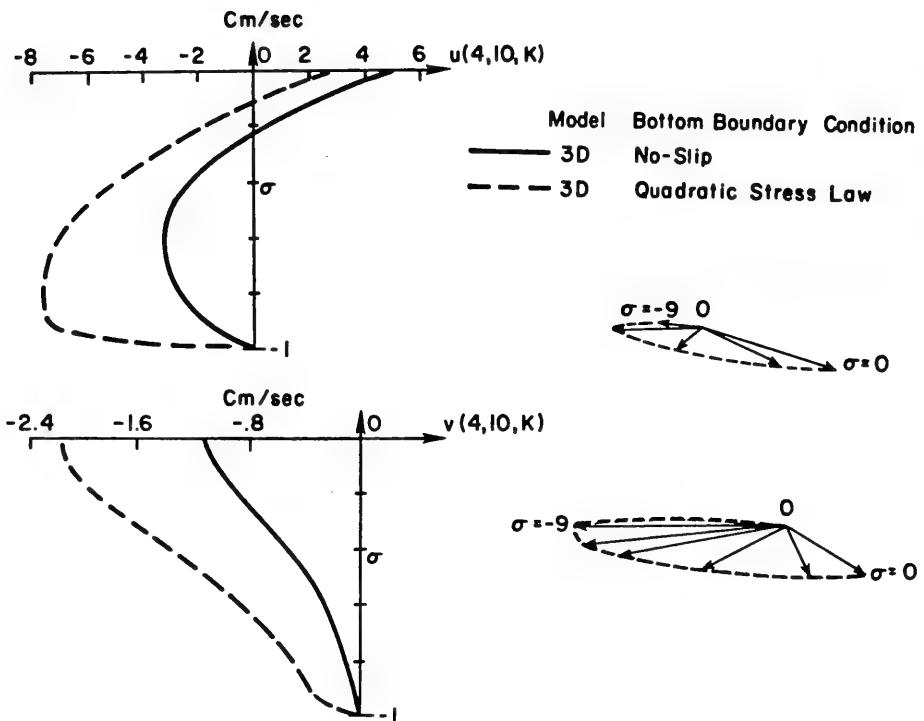
Figure 4.6. Vertical profile of horizontal velocities at a point. Steady-state results computed by the three-dimensional model with two different boundary conditions.

/

4.5 Comparison of Vertically-Integrated Model versus Three-Dimensional Model

As a comparison between the two-dimensional, vertically-integrated and the three-dimensional models, surface elevations computed by the two-dimensional model at selected locations are also shown in Figure 4.5. The quadratic stress law, as shown by Eq. (2.40), with a Manning's n of 0.035 $cm^{1/6}$, was used in the computation. The computed surface elevations of the two-dimensional model agreed well with those of the three-dimensional model. Of course, the two-dimensional model cannot compute the vertical structure of horizontal velocities, as shown in Figure 4.6.

The computed currents over the entire basin are also shown in Figures 4.7. While the vertically-integrated mass fluxes in all three cases exhibit a counter-clockwise gyre, the detailed vertical structure of velocities show appreciable differences. The three-dimensional model with quadratic stress law gives the strongest bottom currents over much of the basin. The near-surface currents in this case are quite weak along the deep end and at some points are opposite to the wind direction. The three-dimensional model with no-slip condition gives weaker currents and somewhat different current structures. The two-dimensional model gives identical current structures at all levels. The corresponding results of surface elevation and bottom shear stress are shown in Figure 4.8. Hence it appears that in the unstratified case, by choosing a proper bottom friction coefficient, the vertically-integrated model can provide a reasonable estimate on the surface elevation and volume transport. Due to the lack of vertical resolution, however, the vertically-integrated model is not suitable for predicting transport of contaminants which are strongly influenced by the three-dimensional flow structures.

4.6 Tidal Response in the Mississippi Sound - Idealized Basin

The three-dimensional model has been applied to simulate the purely tidal currents in the Mississippi Coastal Waters. A 51 x 51 (3 km grid spacing) grid is applied over the idealized coastal area as shown in Figure 4.9. Idealized bottom topography is represented by the contour lines with an interval of 3 meters. Depth within the entire Mississippi Sound is less than

63
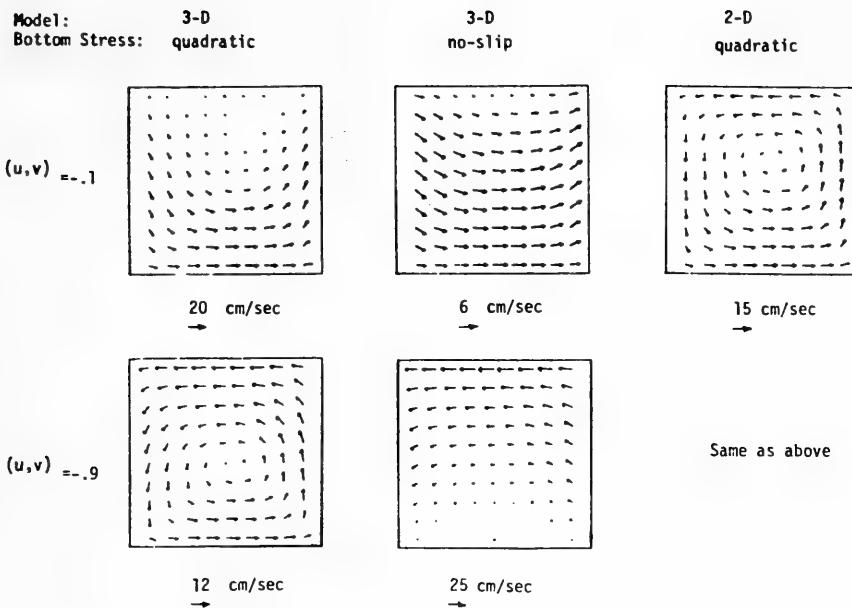
Figure 4.7.   Steady-state velocity field in the enclosed basin.
Results from three models.
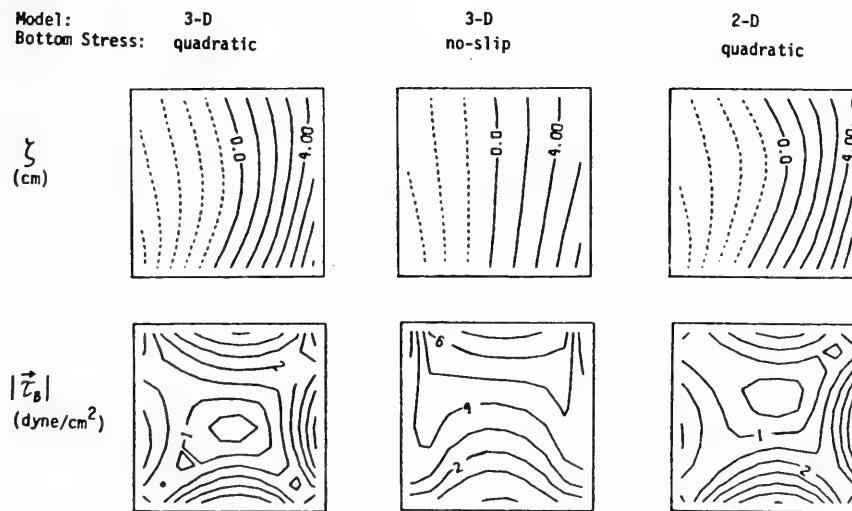
Figure 4.8.   Surface elevation and bottom shear stress in the
enclosed basin. Results from three models.
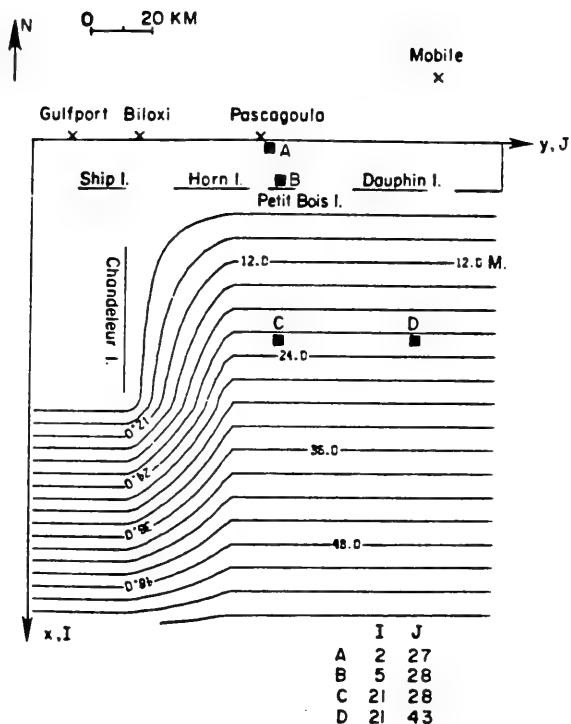
Figure 4.9. Simplified geometry and topography for the Mississippi Sound and adjacent coastal waters.

4 m. In the numerical computation, 5 vertical levels are generally used. Although somewhat idealized, the model basin does include the major barrier islands (Dauphin Island, Petit Bois Island, Horn Island, Ship Island, and Chandeleur Island) and part of the Mobile Bay. An open boundary extends along the South (x=L) and the East (y=L).

Initially, the entire basin is assumed to be quiescent with $\zeta=0$ everywhere. Flow is forced by the following boundary conditions along the open boundaries:

$$\zeta = \zeta_0 \sin \frac{2\pi[t - \phi(x)]}{T} \quad ; \quad \phi(x) = \frac{L-x}{\sqrt{gH_{avg}}} \tag{4.10}$$

where H_{avg} is the average depth between x and x=L along the open boundary. In the following computation, ζ_0 is assumed to be 30 cm and T is taken as 24 hr.

The three-dimensional model with the boundary conditions given by Eqs. (2.31) and (2.32) was run for 4 days until the results reached a quasi-steady state. Constant vertical eddy viscosity of 200 cm^2/sec and C_d of 0.04 were used in the computation. We will present detailed velocity distribution at the flood tide.

The tidal currents within the Mississippi Sound and adjacent waters at the end of 4 days are shown in Figures 4.10. Due to the shallow depths, the mass fluxes in the Mississippi Sound and the Chandeleur Sound are much weaker than those in the deeper offshore waters. However, as shown in Figures 4.10(b) and 4.10(c), the horizontal velocities in the shallow Sound and the deeper offshore waters are actually quite comparable in magnitude. Currents on the order of 15 cm/sec exist within the major passes. Since we are concerned with the transport of sediments in the area, it is interesting to examine the distribution of bottom shear stress. Figure 4.10(d) indicates that relatively high shear stresses exist within the major passes and around the Chandeleur Sound. It is expected that during spring tides, shear stresses in these areas may be sufficient to cause entrainment of the sediments, thus leaving behind the coarser sediments. This is consistent with the sediment distribution map (Figure 1.3) which shows coarser sediments around these areas.
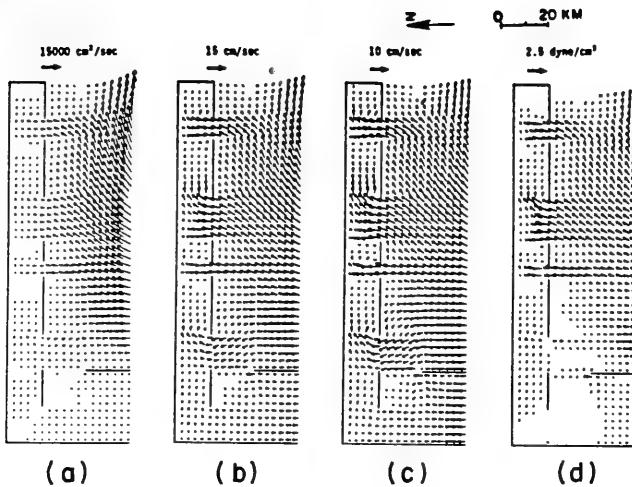
Figure 4.10. Tidal currents and bottom shear stress within the Mississippi Sound and nearby waters after a four day simulation:

(a) vertically-integrated velocities,

(b) velocities at σ=-0.1,

(c) velocities at σ=-0.9,

(d) bottom shear stress.

Based on these results, a preliminary estimate indicates the average flow through the passes is approximately 1.8×10^6 CFS, which is very close to the estimate by Escoffier (1978) as referenced in USAEMD (1979). It is also interesting to note that the maximum shear stresses occur within the major passes. Such high shear stresses, even in the absence of favorable wind waves, may be capable of resuspending fine sediments in the area.

The results at six hours later, although not shown here, indicate flow through the tidal channels has increased and near-surface currents are on the order of 30 cm/sec. The bottom shear stress has also become stronger. The near-bottom horizontal velocities as a function of time are shown in Figure 4.11 for three locations (see Figure 4.9) in the area. The phase relationship between u and v at the deeper location (I=21, J=28) is quite different from that within the Sound.

4.7 Wind-Driven Response in the Mississippi Sound-Idealized Basin

Strong winds frequently exist in the study area. The winds in the Gulf of Mexico are predominantly from the North in winter and South to Southeast in the summer; however, winds are stronger in the winter from the West and the Northwest and in the summer are not as strong but of equal strength in all directions. The land winds are stronger in the winter but no direction is dominant, and in the summer the strongest land winds are from the South to the Southeast. Occasionally, hurricanes of destructive force hit the area. Currents and water level induced by the strong winds can be much greater than those induced by the tide and hence are of primary interest to us.

Assume at t=0, a uniform wind stress of 3 dyne/cm^2 (corresponds to a wind speed of about 10 m/sec) is applied over the entire surface area impulsively. We have computed the response of the region for four different cases: (1) τ_x=+3 dyne/cm^2,   (2) τ_y=+3 dyne/cm^2,   (3) τ_x=-3 dyne/cm^2,   and (4) τ_y=-3 dyne/cm^2. Constant A_v of 200 cm^2/sec and C_D of 0.04 were used in the computations.

Adiabatic boundary conditions are used along the open boundaries. Although this does not allow us to include the effect of shelf waves into the computation, the model can still simulate the local response of the study area
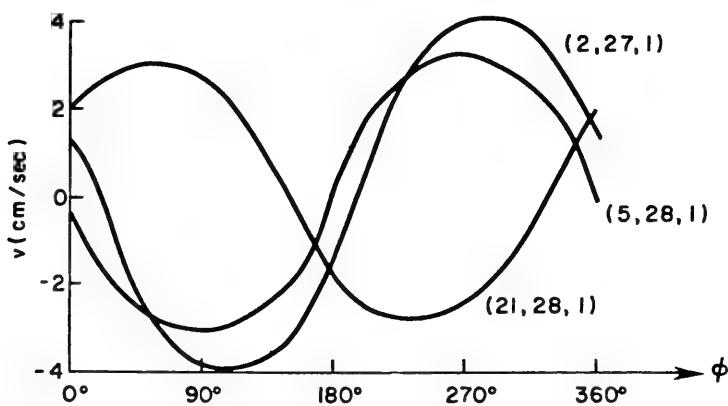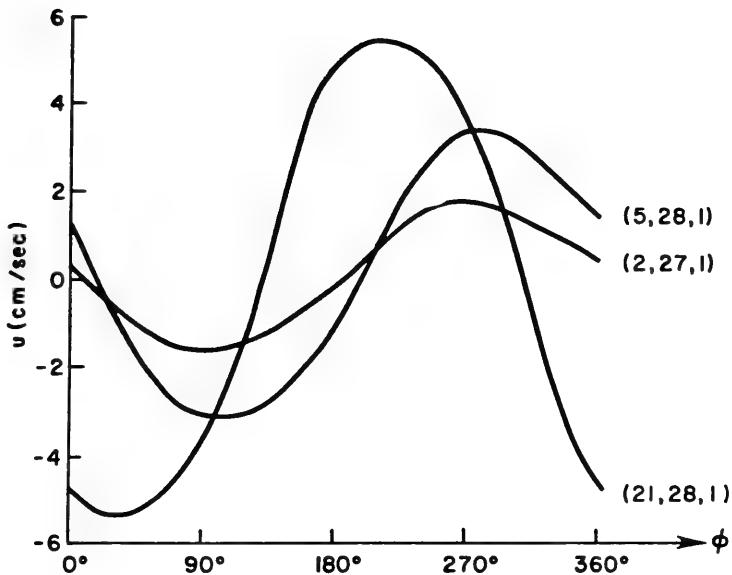
Figure 4.11. Horizontal velocities near the bottom ($\sigma=-0.9$) as a function of time for three locations.

to changing wind conditions. As will be shown later, the response of the shallow Mississippi Sound to an impulsive wind is relatively fast, such that the flow within the Sound essentially reaches steady state before the end of one day. Thus, we can examine the maximum possible current and bottom shear stress within the Sound resulting from a given wind condition. To include the effect of open Gulf circulation (e.g., Loop Current) on the study area, an entire Gulf model may be required to provide the necessary boundary conditions. An alternative would be to measure the variation of major variables along the open boundaries throughout the simulation period.

The response of bottom water to an impulsive wind stress of 3 dyne/cm^2 from the South is shown for three locations (B, C, and D, in Figure 4.9) in Figure 4.12. Within the Sound (B), the bottom current has reached steady state within an inertial period and hence the transient does not clearly show the inertial period. The response at the offshore location (C) is somewhat slower. At Location D, near the open boundary, the response is even slower, as manifested by the distinctive inertial period in its oscillatory bottom current.

The mass fluxes, near-surface currents, near-bottom currents, and bottom shear stresses caused by the same wind over the area are shown in Figure 4.13, for a narrow coastal strip including the Sound. Notice that there is an appreciable difference between the surface currents and the bottom currents. While the surface currents generally have an onshore component, the bottom currents generally show an offshore component. High bottom shear stresses prevail in the area between Horn Island, Ship Island, and the Chandeleur Islands. The shear stresses due to the transient wind-driven currents may be much greater than those due to the tidal currents, and hence are more effective in causing resuspension of sediments. Results for other wind directions can be found in Sheng (1981).

70
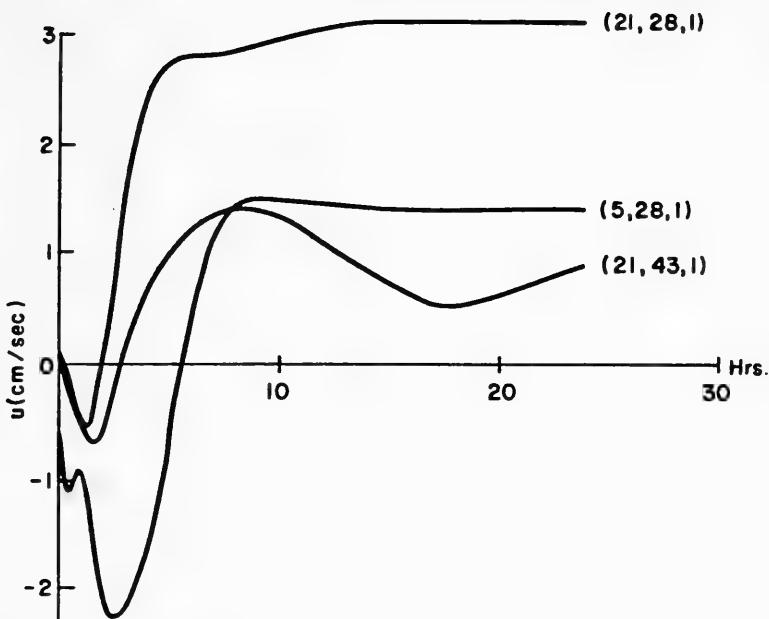
Figure 4.12. Horizontal velocities near the bottom ($\sigma=-0.9$) as a function of time for three locations. Wind-driven currents due to southerly wind.
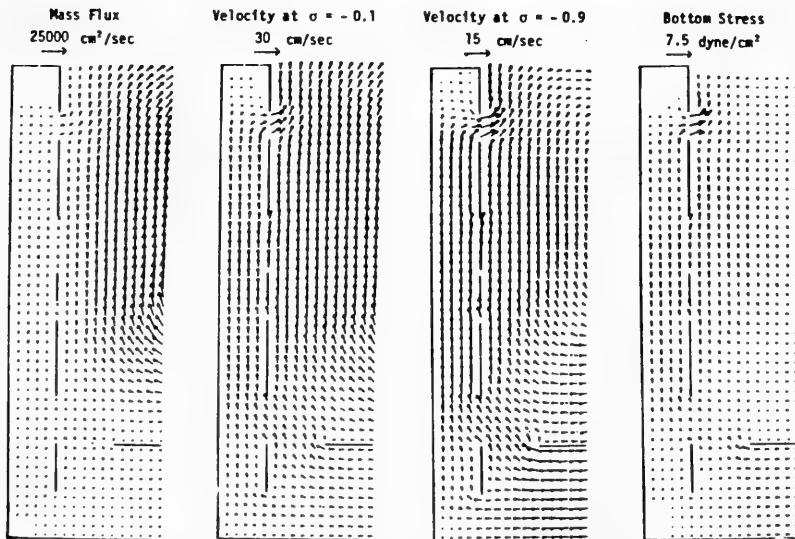
Figure 4.13. Wind-driven currents and bottom shear stress due to a westerly wind.

.

5. DYNAMIC SIMULATION OF COASTAL CURRENTS WITHIN THE MISSISSIPPI SOUND AND ADJACENT CONTINENTAL SHELF

The three-dimensional numerical model of coastal currents as described in previous chapters has been applied to simulate the tide- and wind-driven currents in the Mississippi Sound and adjacent continental shelf waters of the Gulf of Mexico. As shown in Figure 5.1, the horizontal grid is composed of 116 grid points in the y-direction and 60 grid points in the x-direction. The smallest grid spacing in the computational domain is on the order of 1 Km. Figure 5.2 shows the bathymetry of the domain in meters. The domain consists of two open boundaries, one along the East and one along the South. Boundary conditions along these open boundaries must be properly prescribed. For the computation of tidal currents in our study, these boundary conditions are provided by a numerical tide model for the entire Gulf of Mexico (Reid and Whitaker, 1981). The numerical grid used in their study is shown in Figure 5.3.

5.1 Tidal Currents

Tides in the Gulf of Mexico

Gulf tides differ from tides in most other places in the world due to the dominance of the diurnal components K1, O1 and P1 collectively over the semi-diurnal components M2 and S2, except along the western Florida coast. Platzman (1972) and Hensen (1974) found that the period of the lowest mode of long gravity waves in the Gulf might be quite close to the diurnal tide period, hence suggesting a quasi-resonant condition. Garrett (1975) accounted for the possible influence of the tidal impedance of the adjoining seas, which can influence the possible reasonant modes. Reid and Whitaker (1981) developed a numerical tide model for the Gulf based on the vertically-integrated, linearized, Laplace tidal equations in spherical coordinates to portray the barotropic response of the Gulf to tidal forcing. Forcing at ports (Florida strait and Yucatan Channel) was also included with an impedance type condition. Detailed data from 20 tidal gages located in open coastal waters of the Gulf were used for the fine tuning of their model. Their study on the Gulf tides, while confirming that diurnal tide is primarily a co-oscillating tide driven by the adjoining Atlantic Ocean and Caribbean Sea, is by far the most complete and provides a useful option to supply
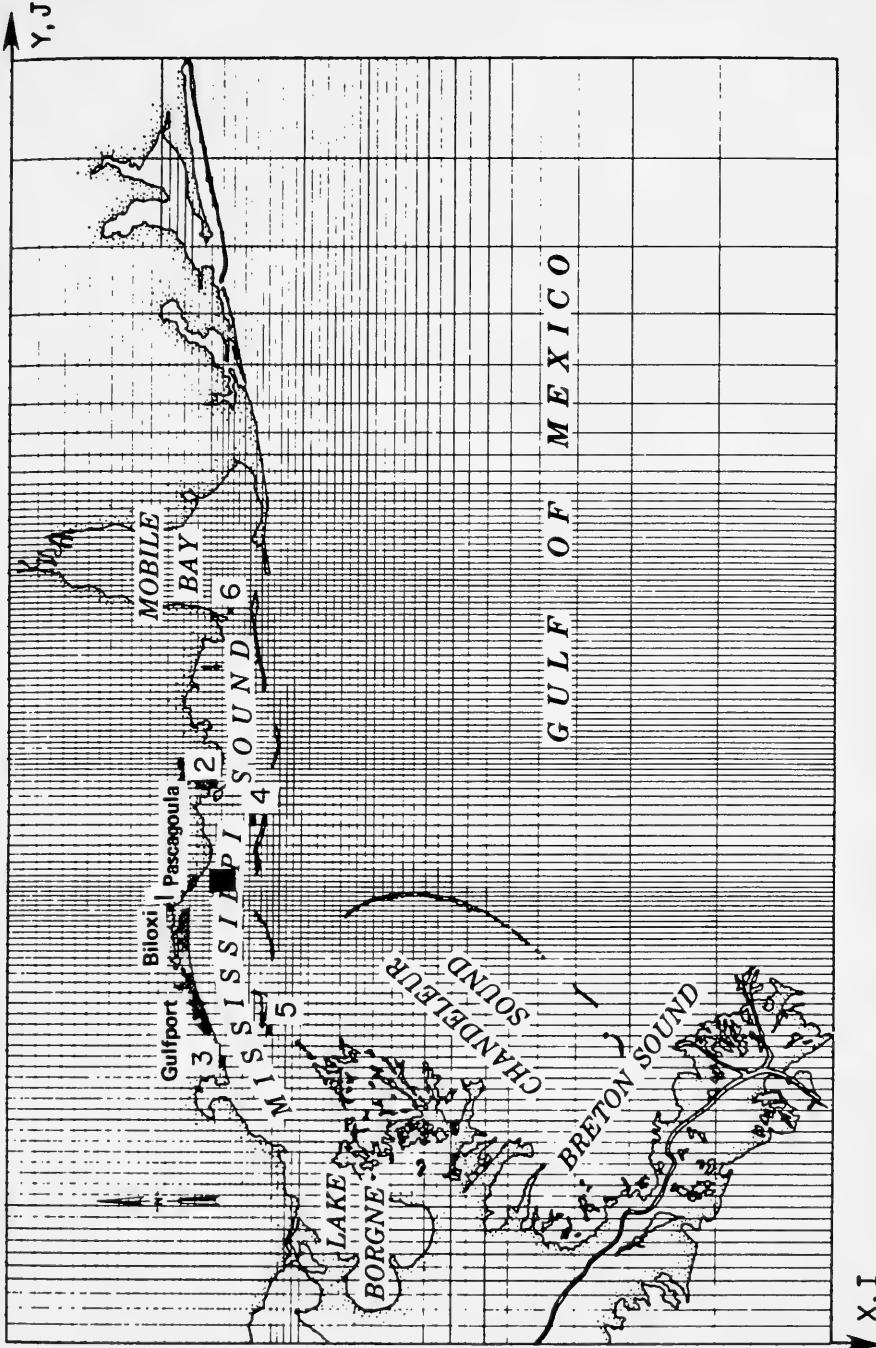
Figure 5.1. Lateral numerical grid used for dynamic simulation of coastal currents within the Mississippi coastal waters.
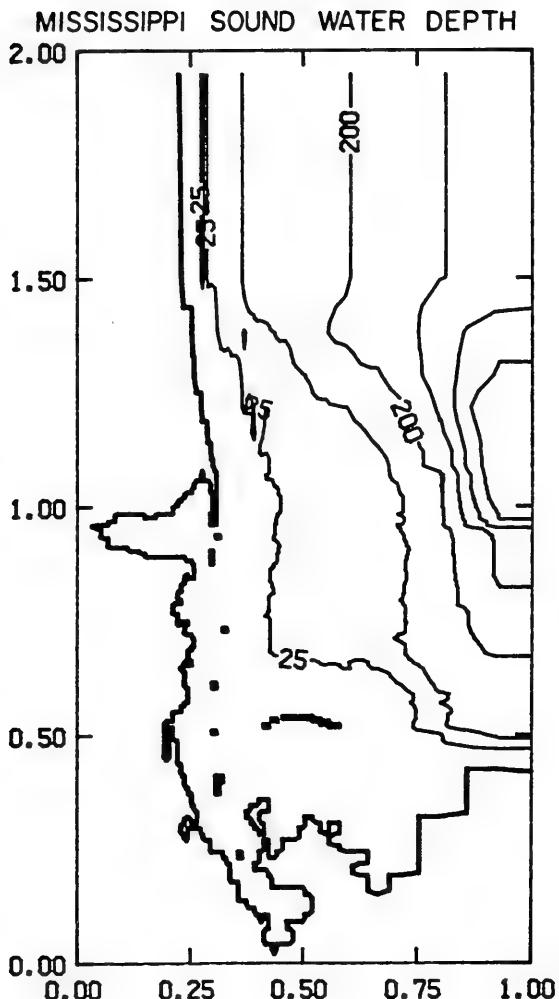
73

Figure 5.2.   Bottom topography of the Mississippi coastal waters.
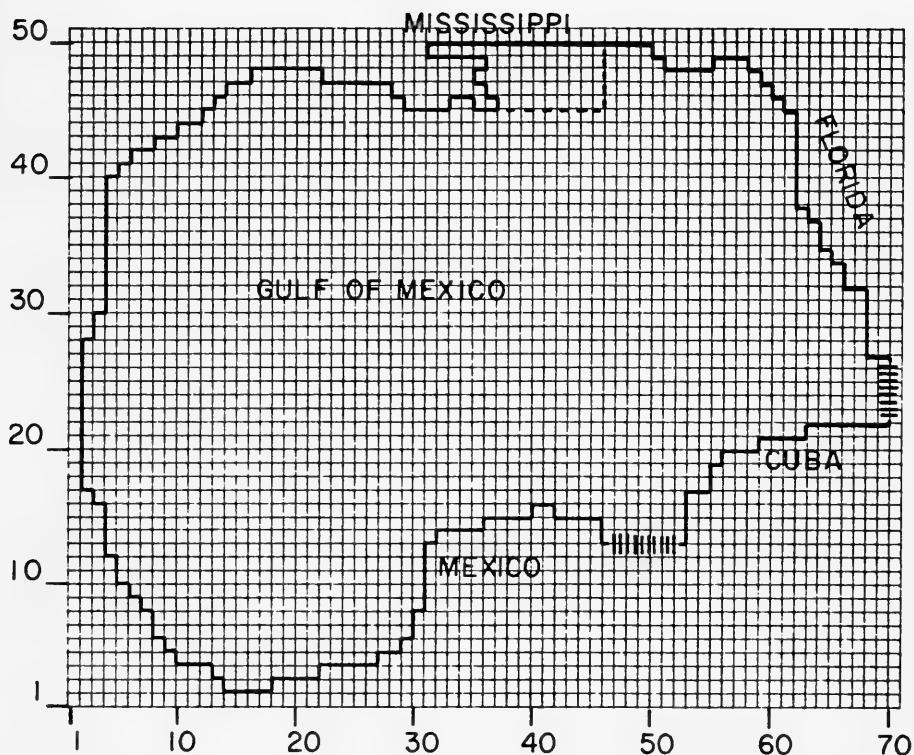
Figure 5.3. Lateral numerical grid used in the tidal simulation of entire Gulf of Mexico.

seaward boundary conditions for high-resolution, limited-area models such as ours.

The water level response for a given tidal constituent is usually expressed in the following form (Shureman, 1941) in terms of the surface displacement ζ:

$$\zeta = F(t) \, A(\lambda,\phi) \, \cos \left[\, \omega t + \chi - G \, (\lambda,\phi) \right] \tag{5.1}$$

where λ is the longitude, ϕ is the latitude, A is the mean amplitude over 18.6 years and G the Greenwich phase or epoch at given position (λ,ϕ), ω is tidal frequency, χ is the astronomical argument, while F is the nodal factor, a slowly varying function of time. Tides at particular stations are characterized by A and G for individual constituents. In our study, A's and G's for 5 constituents (O1, K1, P1, S2 and M2) along the open boundaries of our grid are supplied from Reid and Whitaker's model. Surface displacements at the open boundary stations are determined from a linear combination of those due to the five tidal constituents.

<u>Surface Displacement during a 5-day Simulation (9/20/80 to 9/25/80)</u>

As a first example, tides during 20 Sept. to 25 Sept. 1980 (GMT) are computed with our three-dimensional model. The surface displacements at four stations (see Figure 5.1 for locations) within the Mississippi Sound are compared with measured data in Figure 5.4. Notice that the measured data have been filtered such that variations due to short-period oscillations on the order of a few hours or less are not included. In the beginning, diurnal tides dominate over the semi-diurnal tides. Towards the end of the five-day period, the diurnal tides become somewhat less predominant while the semi-diurnal tides became gradually more apparent. Good agreement is found at all stations.

Surface displacement over the coastal area at the end of the third day of simulation is shown in Figure 5.5. The results exhibit variation in surface displacement from nearly zero along the open boundary to -7 cm within the Mississippi Sound, indicating the phase difference in tide.

76
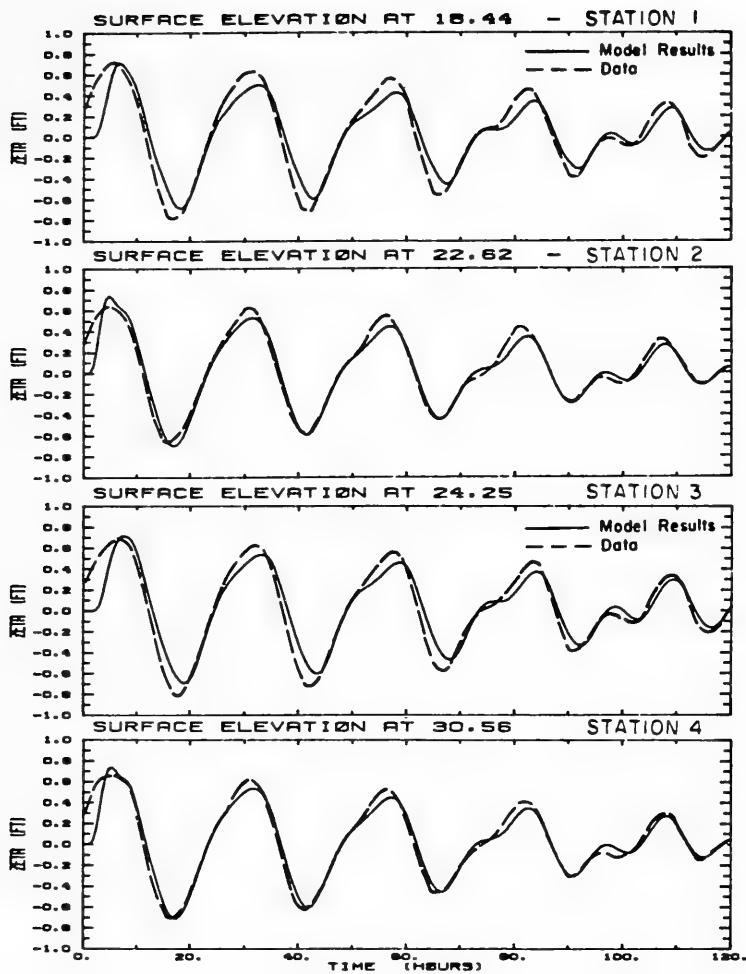
Figure 5.4.   Transient variation of surface displacements* at four stations
               within the Mississippi Sound from 9/20/80 to 9/25/80.

---

* A table for converting the U. S. Customary units of measure found in this
   report to metric (SI) units can be found on page xix.
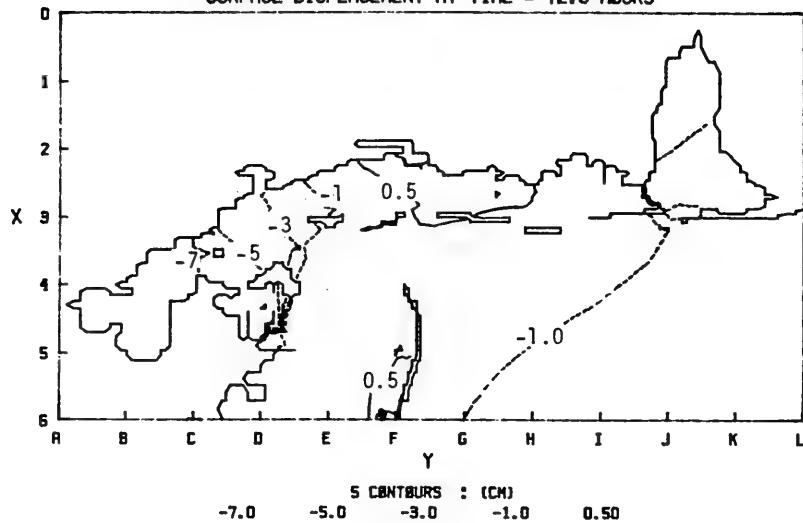
Figure 5.5. Surface displacement contours within the Mississippi coastal waters at 0 hr, 9/23/80.

In this simulation, a relatively large time step of 12 minutes was used for both the external and the internal modes. Seven grid points were used in the vertical direction. A relatively smooth bottom with a roughness length, z_0, of 0.1 cm was assumed. A parabolic length scale, Λ, no more than 25% of the local depth, was assumed in the vertical direction. River inflows from six rivers were considered: Pearl, Jourdon Wolf, Biloxi, W. Pascagoula, Pascagoula, and Mobile.

Currents during the 5-day Simulation (9/20/80 to 9/25/80)

The tide-driven horizontal currents at mid-depth are shown in Figure 5.6 for two stations in the Mississippi Sound. Currents on the order of 1 ft/sec (30 cm/sec) exist at both stations. Again, reasonable agreement is found between data and model results.

The horizontal velocity field at 1 m depth, after 3 days of simulation, is shown in Figure 5.7(a). Relatively large currents exist at the various tidal inlets and in the area between the Ship Island and the Chandeleur Island. Except in these areas, at this instant of time, bottom shear stress generated by the tidal currents are generally less than 0.8 dyne/cm^2. Hence, little sediment resuspension is expected. The horizontal currents at a constant depth of 10 m are shown in Figure 5.7(b). Within the Mississippi Sound and the Chandeleur Sound, the depths are shallower than 10 m and hence no currents are shown.

The velocity field across a transect along the x-z plane, which crosses into the Mobile Bay, is shown in Figure 5.8. Large currents over the left portion of the domain represent flow through the narrow entrance into the Mobile Bay. Once through the entrance, the flow gradually decreases towards the head of the Mobile Bay. The distribution of eddy viscosity within a transect across the Horn Island Pass is shown in Figure 5.9. The values of eddy viscosity at this instant of time are generally less than 20 cm^2/sec. Of course, these values are functions of time.
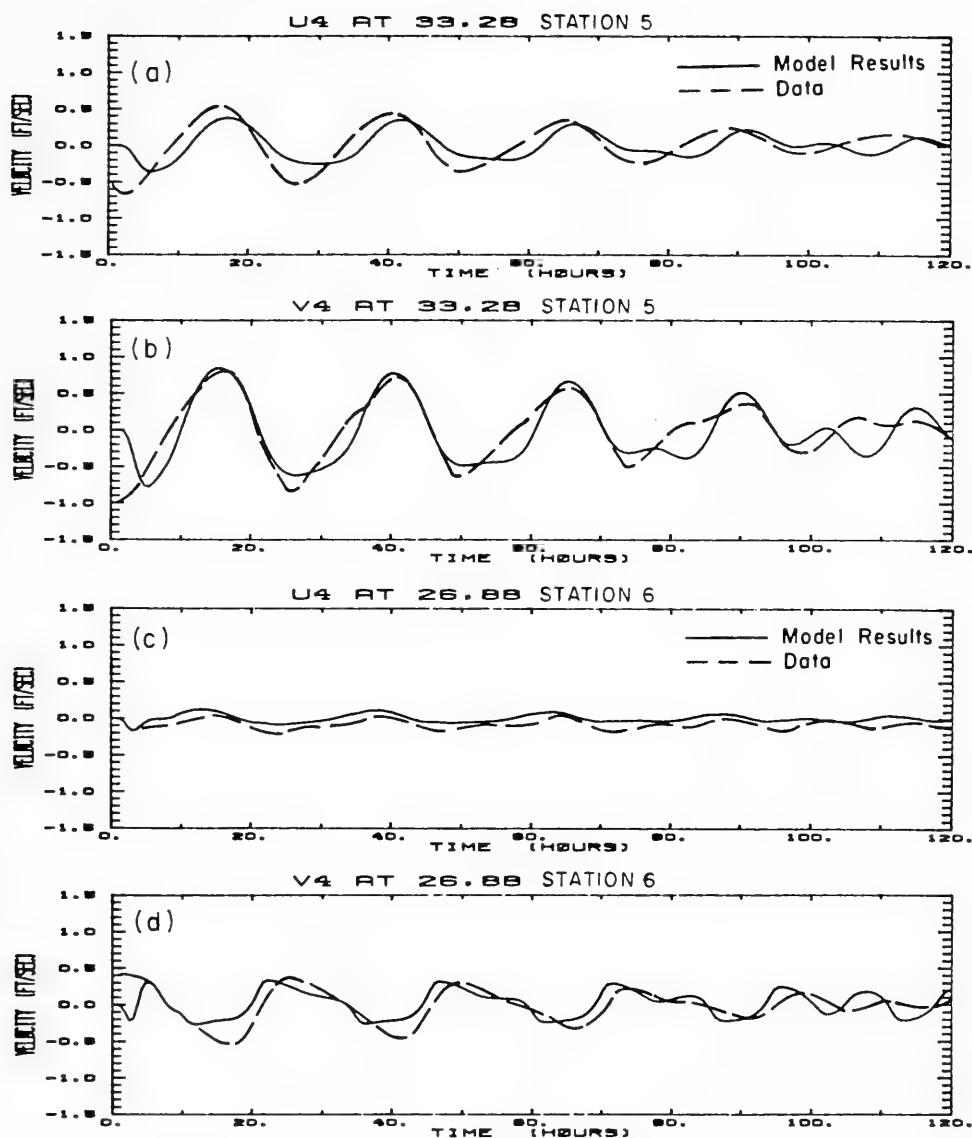
Figure 5.6.   Transient variation of mid-depth velocities at two stations
within the Mississippi Sound from 9/20/80 to 9/25/80.
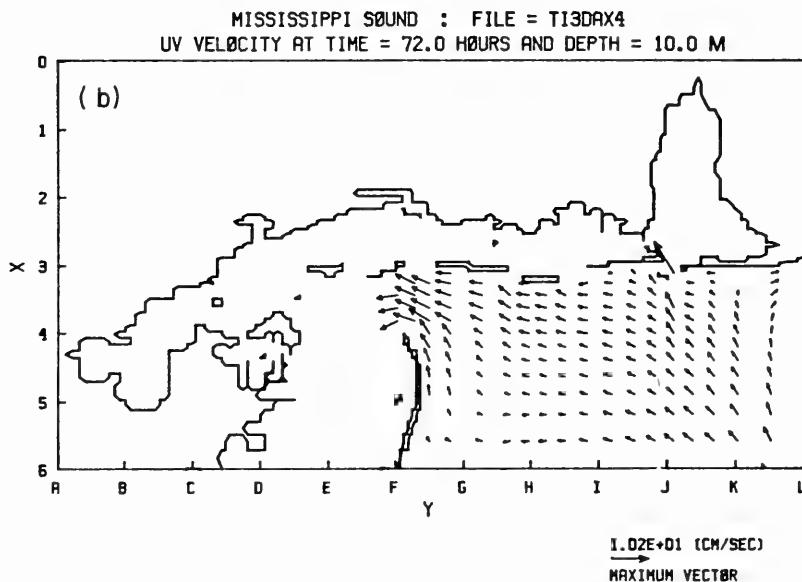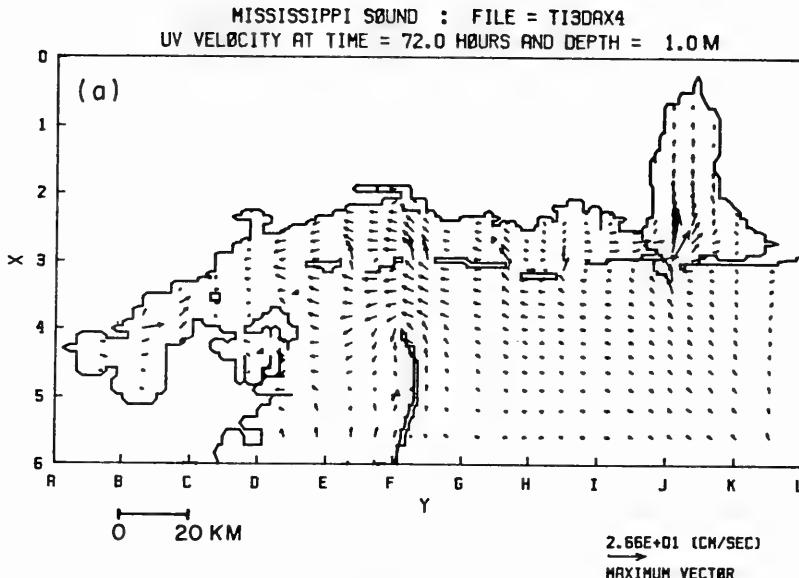
Figure 5.7. Horizontal velocity field at 0 hr, 9/23/80:

    (a) 1 m depth;

    (b) 10 m depth.

MISSISSIPPI SØUND : FILE = TI3DAX4
UW VELØCITY AT TIME = 72.0 HØURS : Y = J.08
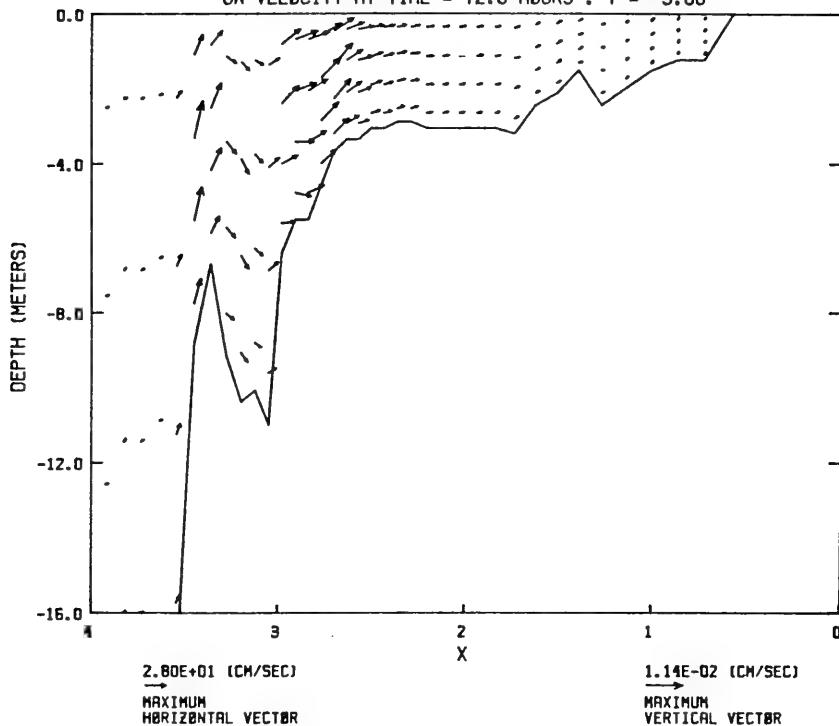
Figure 5.8. Velocity field within a transect across the Mobile Bay
Entrance at 0 hr, 9/23/80.
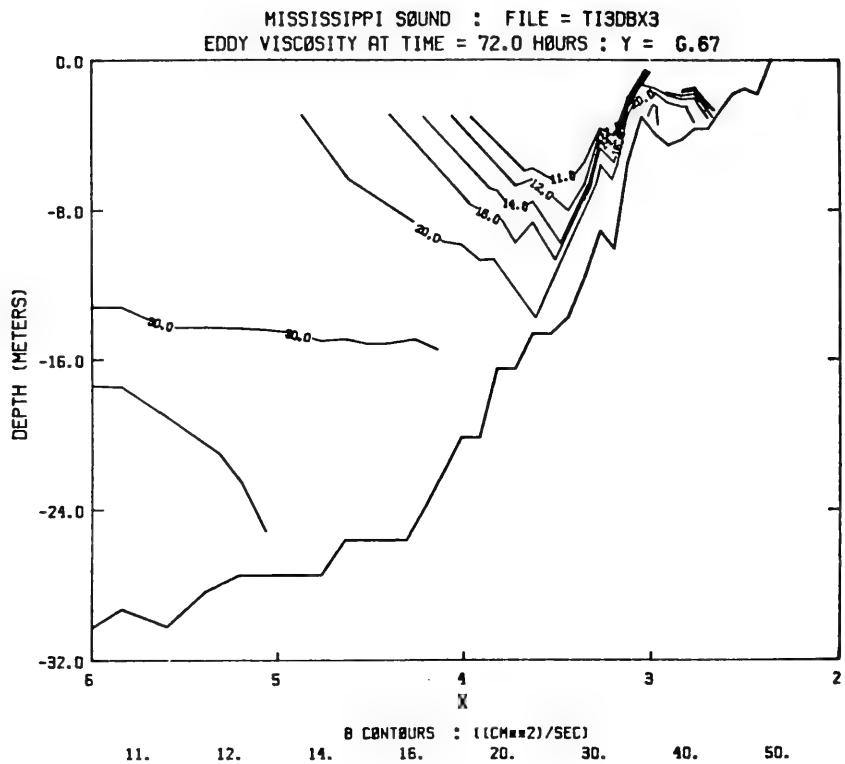
Figure 5.9.   Vertical turbulent eddy viscosity field within a transect across the Horn Island Pass at 0 hr, 9/23/80.

Results of a 3-day Simulation (6/12/80 to 6/15/80)

The same basic model and parameters are used to simulate the tidal currents during a 3-day period during 12 June to 15 June 1980. This period corresponds to a spring tide and hence the surface displacements, as shown in Figure 5.10, are much higher than those during the previous simulation period. Again, good agreement exists at all the stations. Surface contours (Figure 5.11) indicate variation from -9 cm to -24 cm.

The horizontal currents at selected stations throughout the 3-day period are quite strong and compare well with data (Figure 5.12). The velocity field at a constant depth of 1 m, at the end of the simulation period, is shown in Figure 5.13. The relatively stronger currents lead to a stronger bottom stress field as shown in Figure 5.14. Over much of the shallow waters, the bottom shear stress exceeds the critical shear stress for entrainment of sediment (0.8 dyne/cm^2). Velocity field along a transect across the Mobile Bay is shown in Figure 5.15.

Vertical eddy viscosity along a transect across the Horn Island Pass, shown in Figure 5.16, indicates an almost twofold increase from that in Figure 5.9.

Results During a Five-Day Simulation (9/1/80 to 9/6/80)

The ability of the hydrodynamic model to simulate the tidal circulation in the Mississippi Sound has been demonstrated in the two previous simulations. We will now present another 5-day simulation during 1 Sept. to 6 Sept. 1980. The model computed surface displacements at four stations are shown in Figure 5.17. Diurnal tides are dominant during this time period with variation in surface displacement on the order of 1 ft. In the following, we will present the detailed results at 6-hour intervals over one complete tidal cycle, from the 72nd hour to the 96th hour. Residual currents over this tidal cycle are also presented. This will enhance our understanding on the detailed tidal dynamics in the Mississippi Sound. In addition, it will provide a basis to better interpret the sediment transport simulations during this time period, which will be presented in a subsequent chapter.
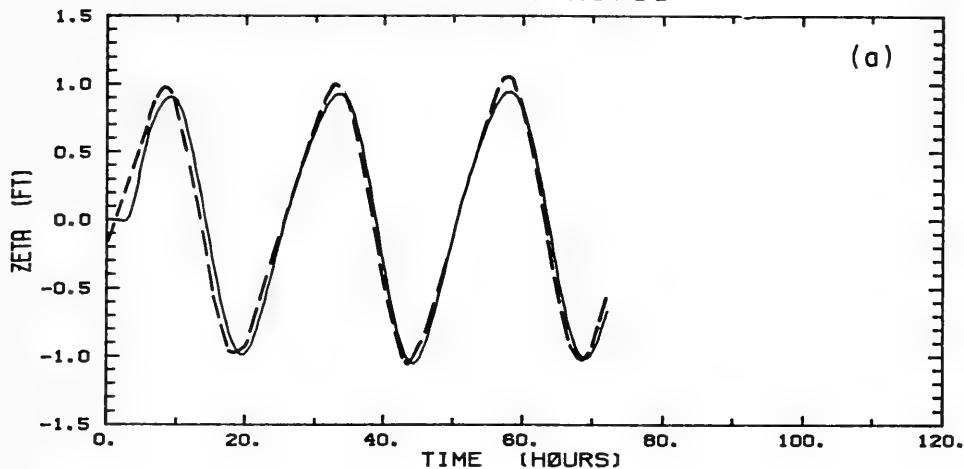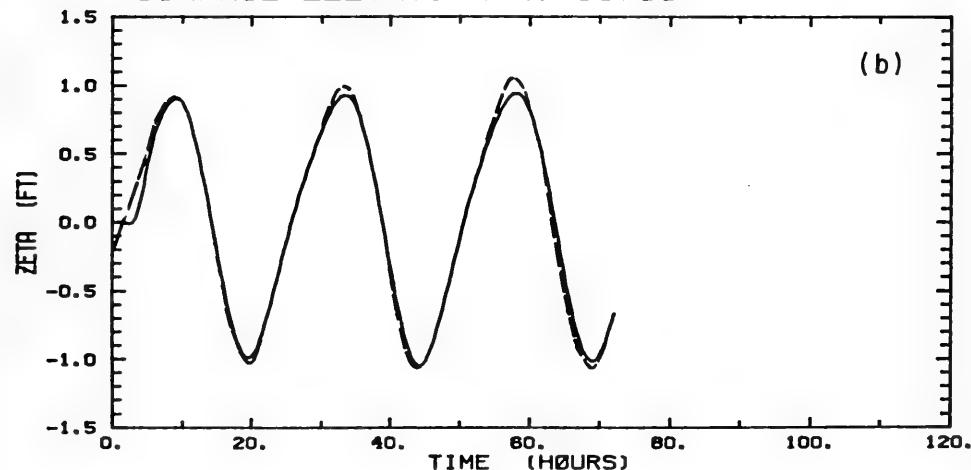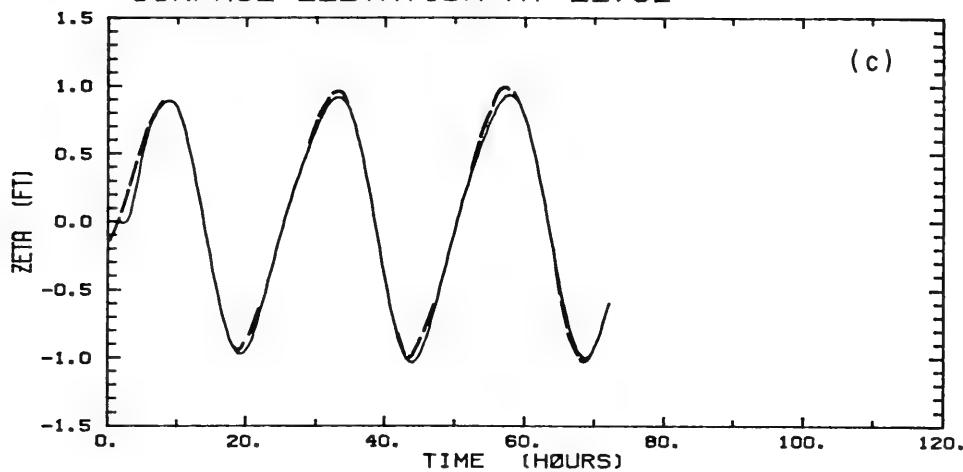
84

Figure 5.10. Transient variation of surface displacements at four stations from 6/12/80 to 6/16/80.

Figure 5.10. Transient variation of surface displacements at four stations from 6/12/80 to 6/16/80.

.
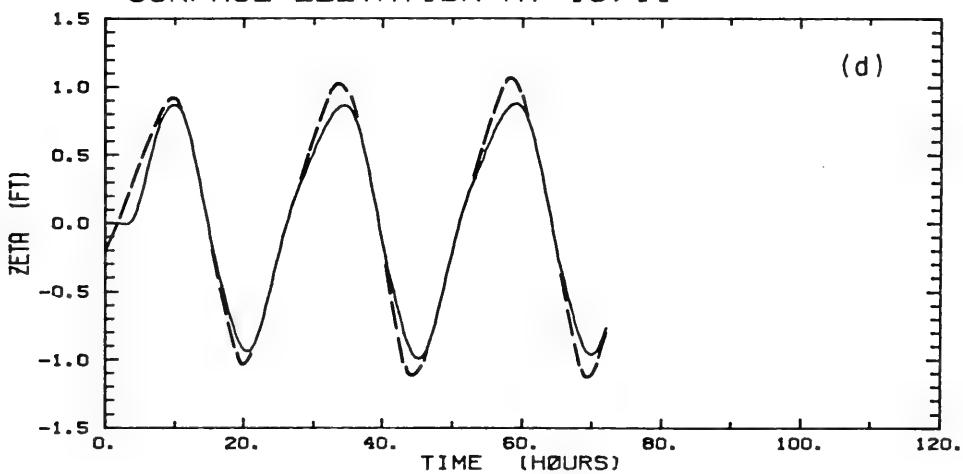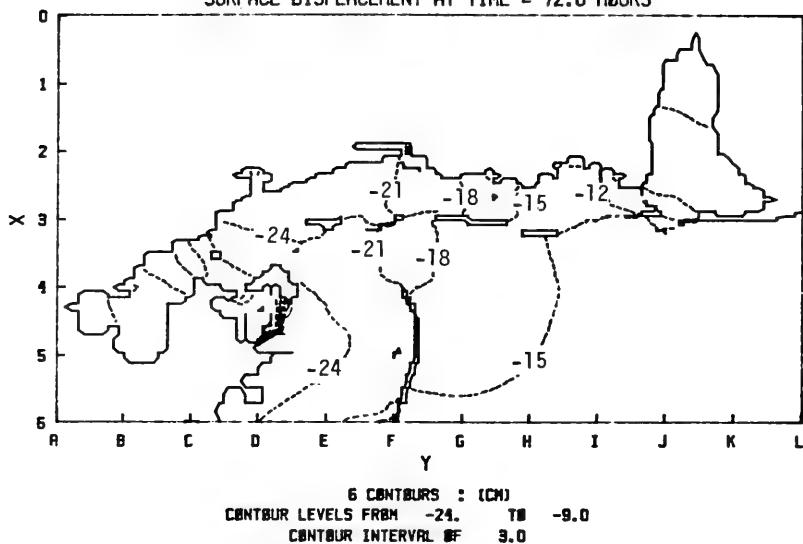
Figure 5.11. Surface displacement contours within the Mississippi coastal waters at 0 hr, 6/16/80.
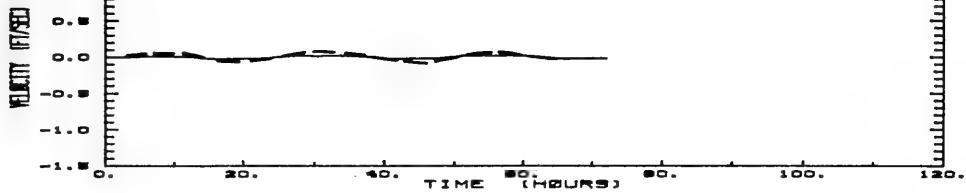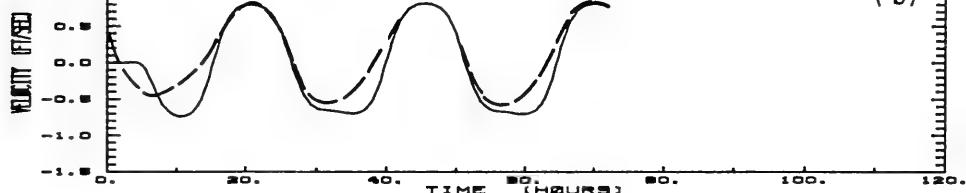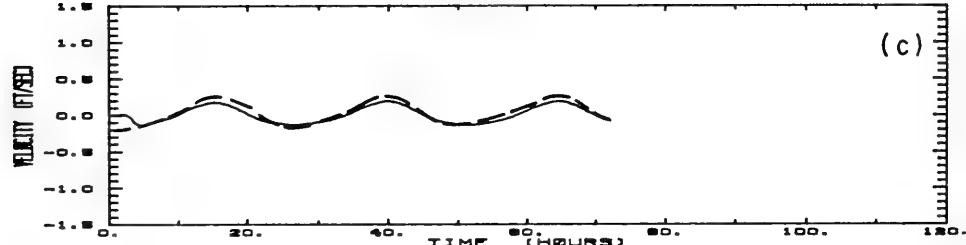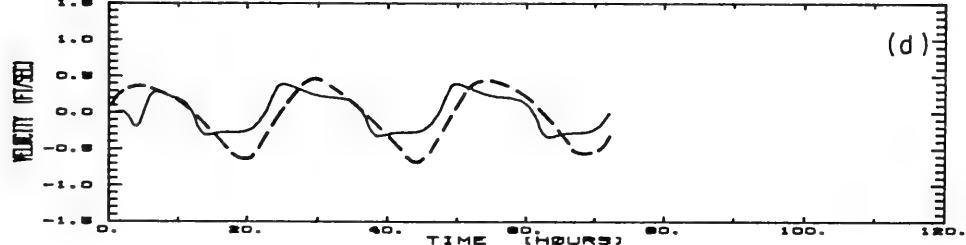
Figure 5.12.   Transient variation of mid-depth velocity at two stations
from 6/12/80 to 6/16/80.
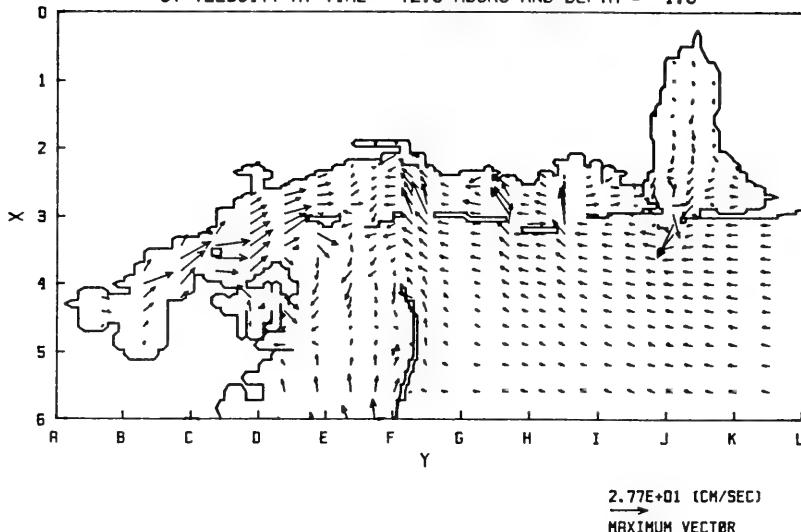
Figure 5.13. Horizontal velocity field at 1 m depth at 0 hr, 6/16/80.
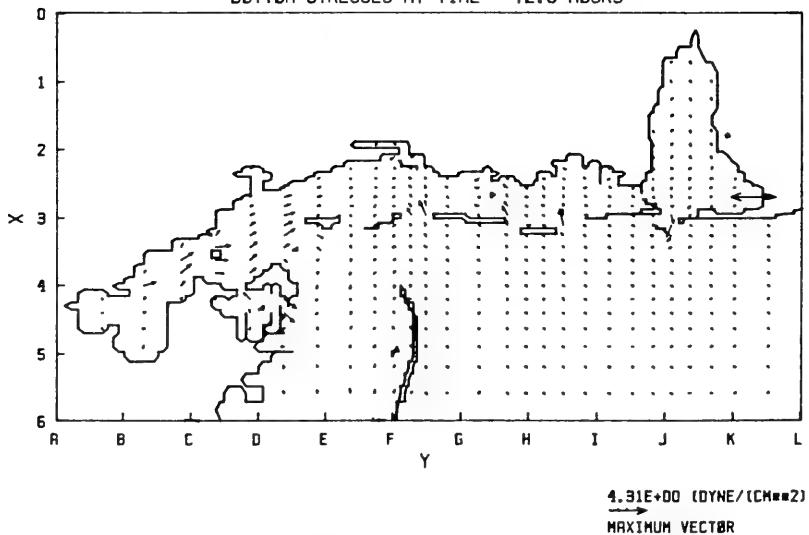
Figure 5.14. Bottom stress field at 0 hr, 6/16/80.

.

MISSISSIPPI SØUND : FILE = TI3DBX3
UW VELØCITY AT TIME = 72.0 HØURS : Y = J.08

Figure 5.15.   Velocity field within a transect across the Mobile Bay
Entrance at 0 hr, 6/16/80.

MISSISSIPPI SOUND : FILE = TI3DAX4
EDDY VISCOSITY AT TIME = 72.0 HOURS :. Y = G.67
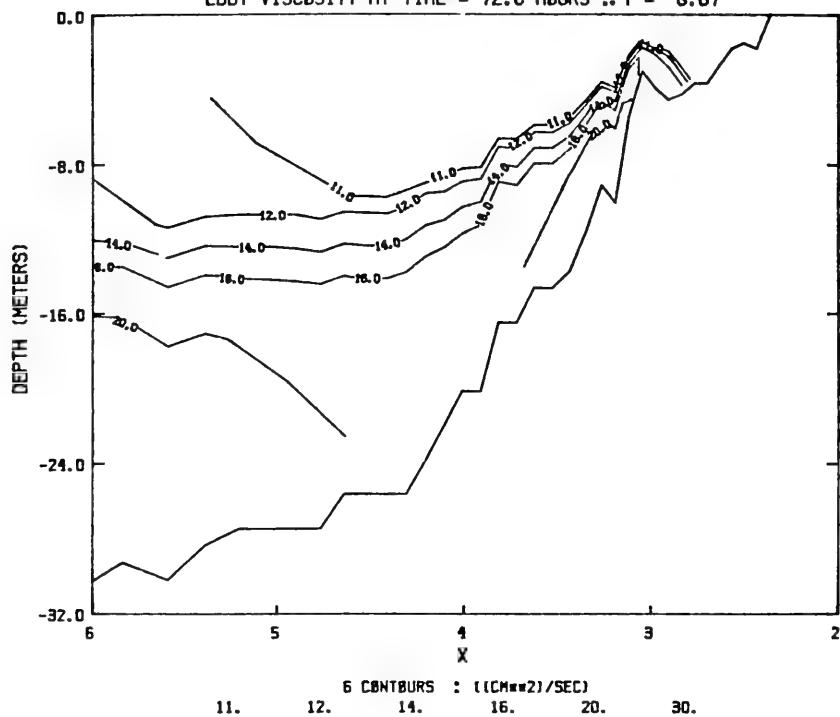
Figure 5.16. Vertical turbulent eddy viscosity within a transect across
the Horn Island Pass at 0 hr, 6/16/80.
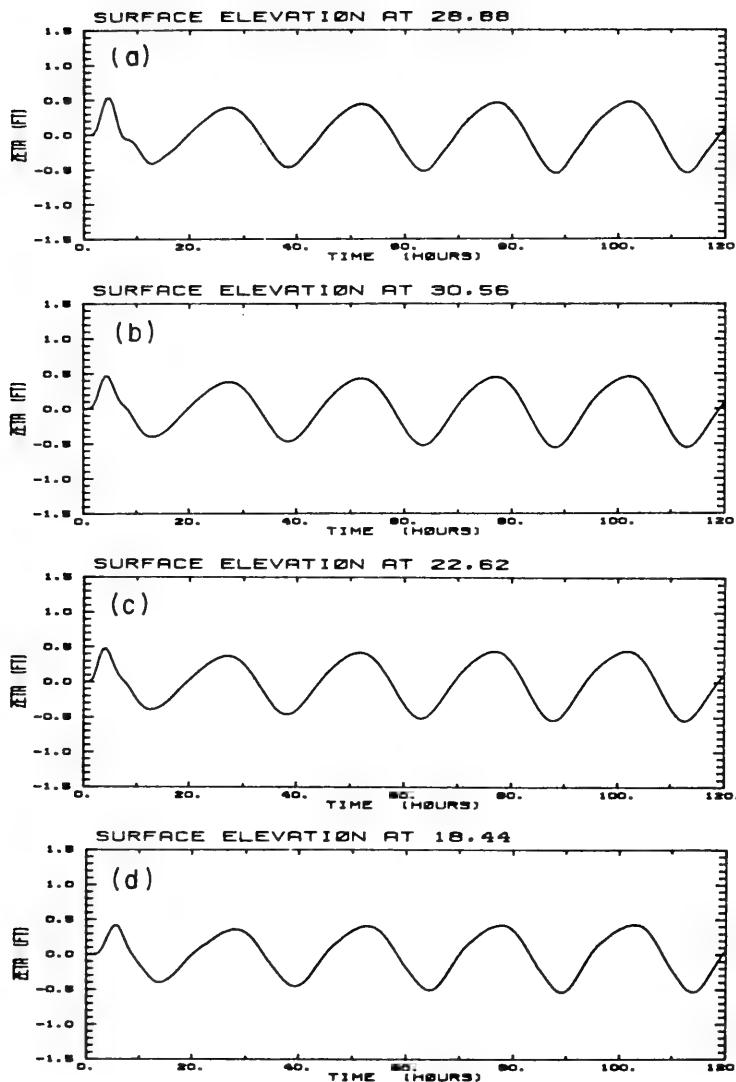
Figure 5.17. Transient variation of surface displacement at four stations
from 9/01/80 to 9/06/80.

Variation of Results During One Tidal Cycle

The surface displacement contours at 6-hour intervals throughout the tidal cycle are shown in Figure 5.18. At the beginning of the tidal cycle, i.e., 72 hours after the initiation of the simulation on 1 Sept. 1980, surface displacements in the area vary from -9 cm within the western end of the Mississippi Sound to about 12 cm along the southern open boundary. Variation in surface displacement along the southern boundary is approximately 4 cm, with an along shore pressure gradient directed to the west. Six hours later, at 78 hours, surface displacements within the Mississippi Sound have reached a peak value on the order of 20 cm. Along the southern open boundary, however, surface displacements have dropped to about 4 cm. Another six hours later, at 84 hours, the situation is almost reversed from that at 72 hours. Surface displacements along the open boundary are on the order of -12 cm. Within the western end of the Mississippi Sound and Lake Borgne, surface displacements are on the order of 12 cm. It is also interesting to note that the along-shore pressure gradient is now directed towards the East. At 90 hours, the entire study area has negative surface displacements, ranging from -4 to -24 cm. At the end of the tidal cycle, 96 hours, the situation is rather similar to that at 72 hours.

The horizontal velocities near the surface and near the bottom, at six-hour intervals, are shown in Figures 5.19 through 5.23. At 72 hours, near-surface currents on the order of 63 cm/sec exist within the tidal inlets. The near-bottom currents, however, are smaller by more than 20%. Currents through the tidal inlets are all directed into the Mississippi Sound. Six hours later, at 78 hours, the currents have decreased by approximately 50%. Currents within the western end of the Mississippi Sound, at this instant of time, have become relatively stronger compared to currents in other areas. Although most tidal inlets show flow into the Sound, outflows are found in Petit Bois Pass and Dog Key Pass. At 84 hours, strong currents on the order of 70 cm/sec are directed out of the Sound. Near-bottom currents are smaller than the near-surface currents by approximately 30%. Little flow exists within the western end of the Sound. At 90 hours, currents are again decreased in magnitude. It is interesting to note that flow is directed into the Sound through the eastern and central tidal inlets, while directed out of

Figure 5.18.   Surface displacement contours within the Mississippi coastal
waters throughout a complete tidal cycle.

(a)   72 hours after 6/12/80;
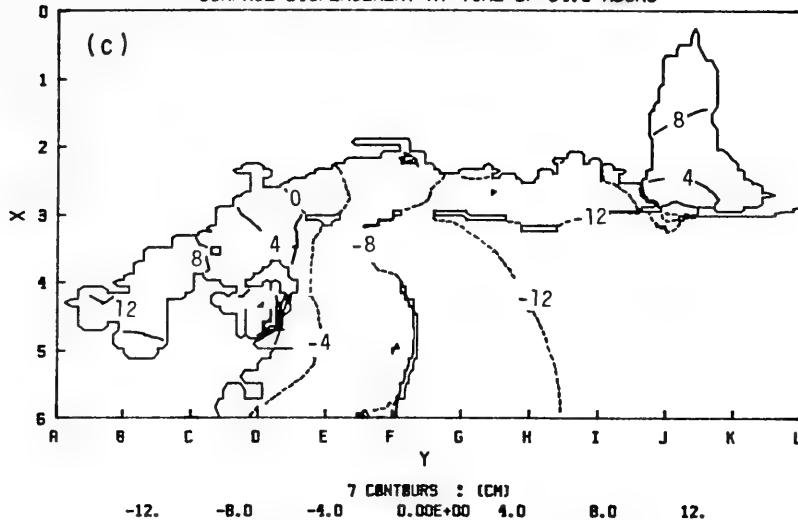
(b)   78 hours;
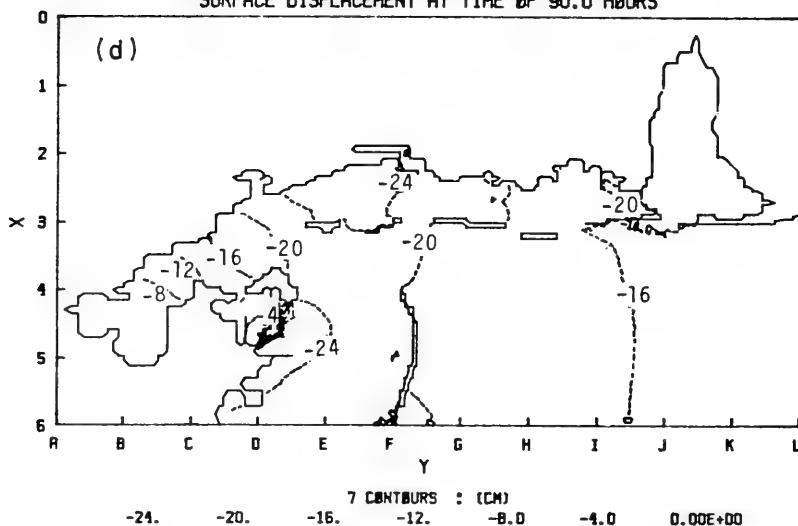
Figure 5.18. Surface displacement contours within the Mississippi coastal waters throughout a complete tidal cycle.

(c) 84 hours;

(d) 90 hours;

MISSISSIPPI SØUND : FILE = TI3DAX7W
SURFACE DISPLACEMENT AT TIME ØF 96.0 HØURS
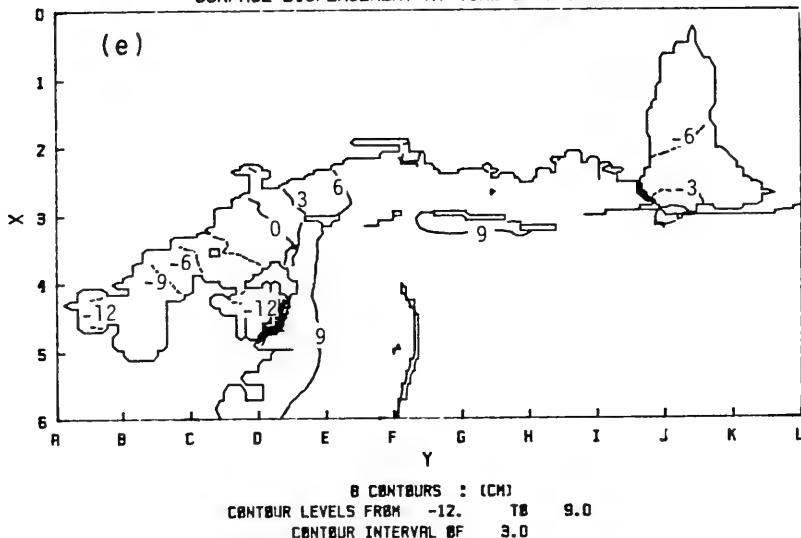
8 CØNTØURS : (CM)
CØNTØUR LEVELS FRØM -12.   TØ   9.0
CØNTØUR INTERVAL ØF   3.0

Figure 5.18. Surface displacement contours within the Mississippi coastal
waters throughout a complete tidal cycle.

(e) 96 hours.
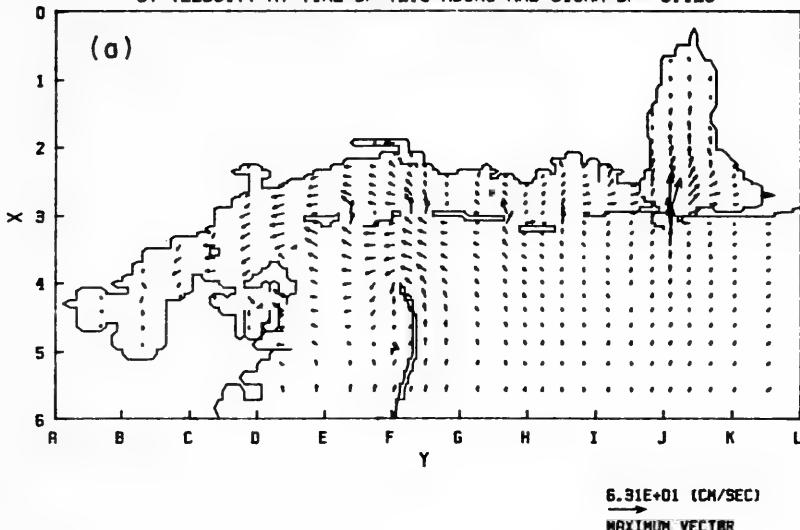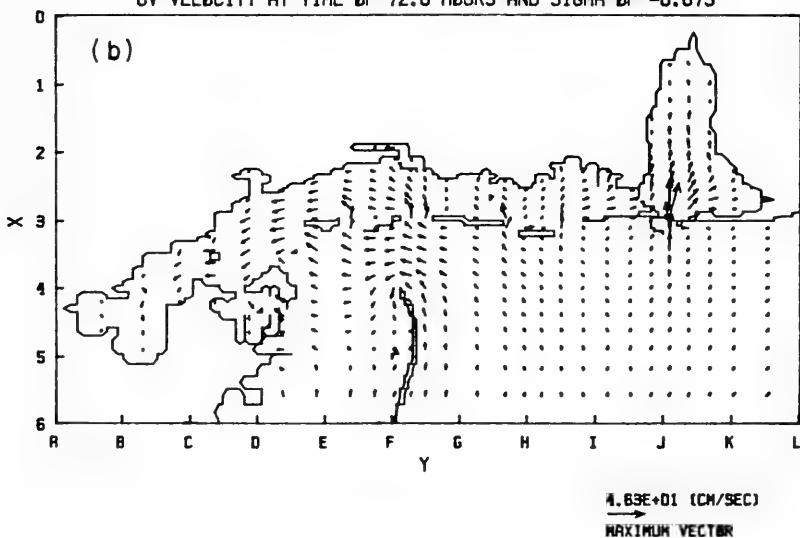
Figure 5.19.   Near-surface and near-bottom horizontal velocity field
at 72 hours after 6/12/80.

MISSISSIPPI SØUND : FILE = TI3DAX7W
UV VELØCITY AT TIME ØF 78.0 HØURS AND SIGMA ØF -0.125

(a)

9.22E+01 (CM/SEC)
MAXIMUM VECTØR

MISSISSIPPI SØUND : FILE = TI3DAX7W
UV VELØCITY AT TIME ØF 78.0 HØURS AND SIGMA ØF -0.875

(b)

2.93E+01 (CM/SEC)
MAXIMUM VECTØR

Figure 5.20.   Same as Figure 5.19 except at 78 hours.

98
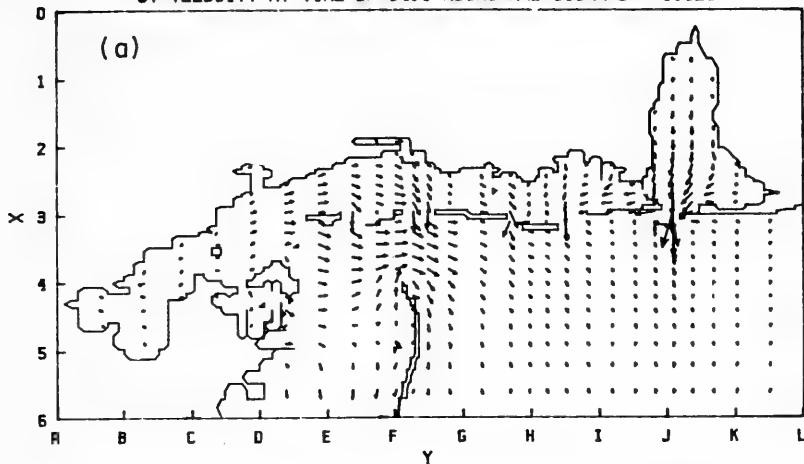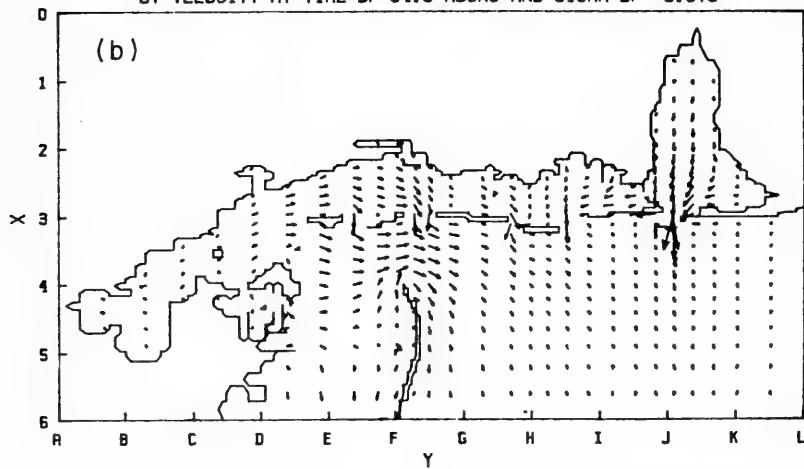
Figure 5.21. Same as Figure 5.19 except at 84 hours.
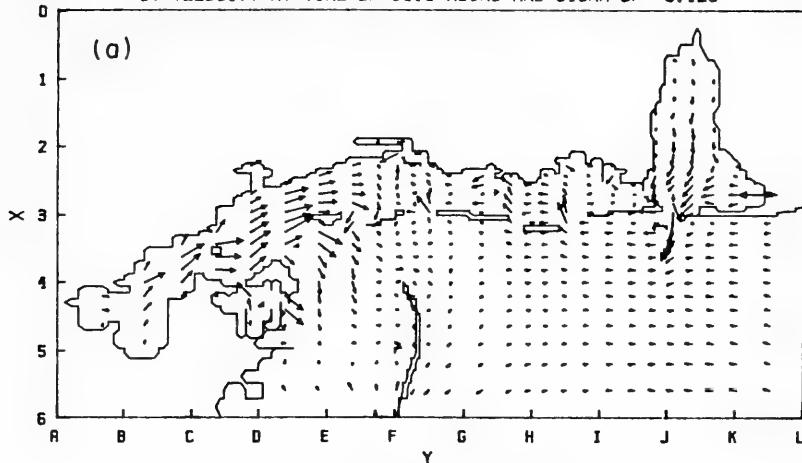
Figure 5.22. Same as Figure 5.19 except at 90 hours.

MISSISSIPPI SØUND : FILE = TI3DAX7W
UV VELØCITY AT TIME ØF 96.0 HØURS AND SIGMA ØF -0.125
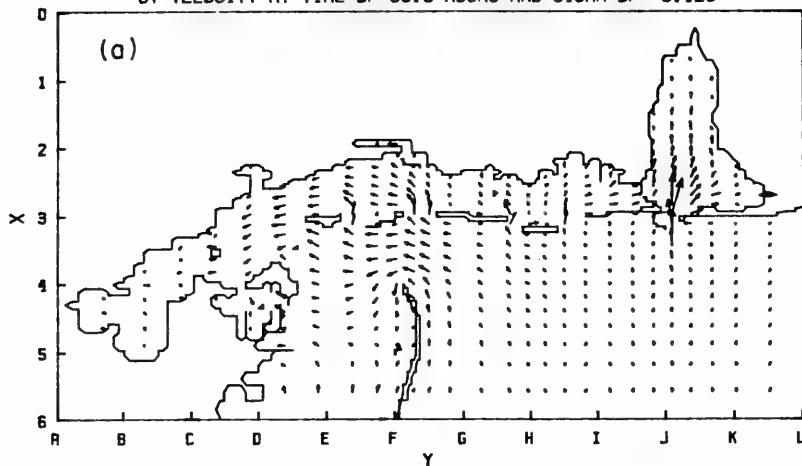
(a)

6.28E+01 (CM/SEC)
MAXIMUM VECTØR

MISSISSIPPI SØUND : FILE = TI3DAX7W
UV VELØCITY AT TIME ØF 96.0 HØURS AND SIGMA ØF -0.875

(b)

4.55E+01 (CM/SEC)
MAXIMUM VECTØR
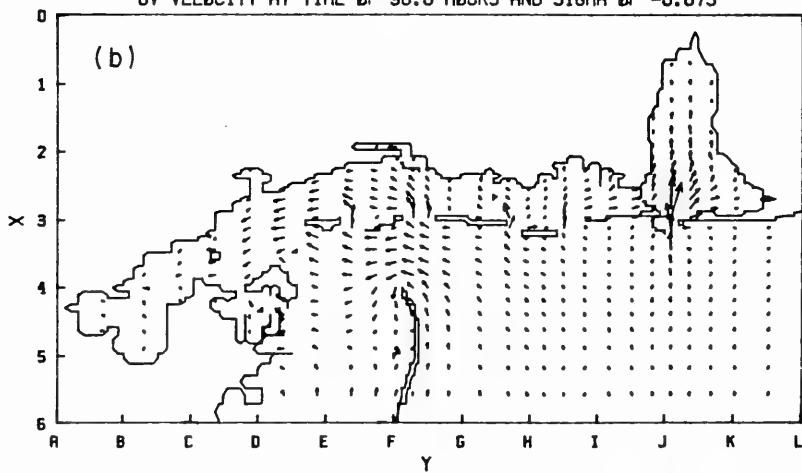
Figure 5.23. Same as Figure 5.19 except at 96 hours.

the Sound through the western tidal inlets and the Mobile Bay entrance. Relatively stronger currents are again found in the western end of the Sound. At the end of the tidal cycle, 96 hours, the velocity distributions are somewhat similar to those at the beginning of the cycle.

Detailed velocity distributions along a transect through the Mobile Bay entrance are also shown at six hour intervals through the tidal cycle in Figure 5.24.

Tide-Induced Residual Currents

Ideally, residual current can be defined as that part of the current that is left after removal of all oscillatory tidal currents. In practice, however, residual current is referred to as that part of the current that is left after removal of diurnal, semidiurnal and higher frequency tidal signals. The tide induced residual currents can be caused by a combination of the non-linear inertia effect and the influence of complex geometry and bottom topography. Of course, residual currents may also be generated by winds, density gradients and river flows.

Since the residual currents are usually a small fraction of the tidal currents, it is not easy to accurately compute them from measured current data except in such regions as the Bay of Fundy where residual currents on the order of 80 cm/sec have been recorded. However, it is relatively easy to compute the residual currents from a numerical model by time-averaging the instantaneous tidal currents over a complete tidal cycle. Based on the tidal currents described in the previous subsection, we have computed the time-averaged currents over the 24-hour period which are shown in Figure 5.25. The residual currents during this period are very weak and constitute only a few percent of the instantaneous currents. However, stronger residual currents may occur during other tidal periods. Since residual currents can affect the long-term transport of contaminants within a coastal ecosystem, further quantitative study on this subject is warranted.
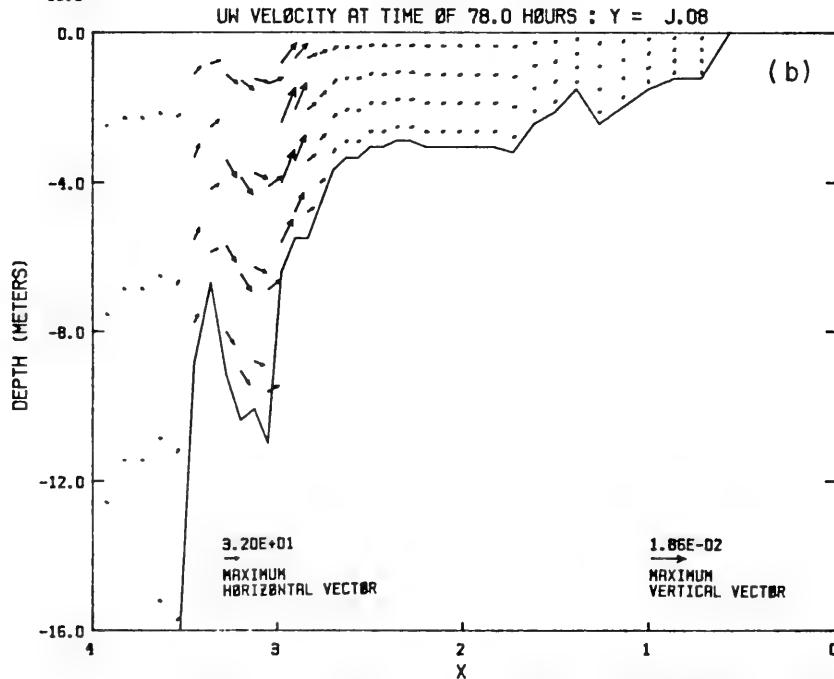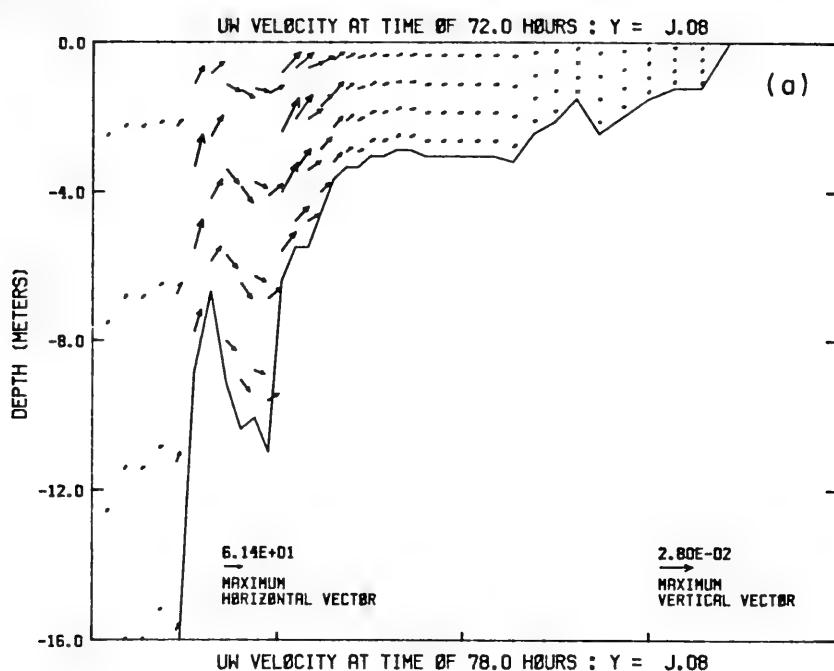
102

Figure 5.24. Velocity field within a transect across the Mobile Bay
Entrance throughout a complete tidal cycle.
(a) 72 hours;   (b) 78 hours;
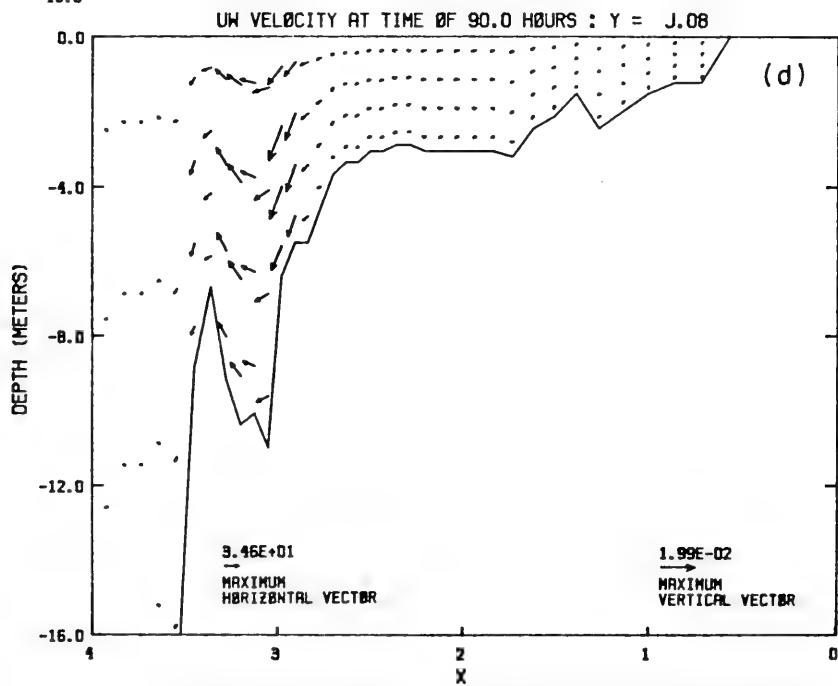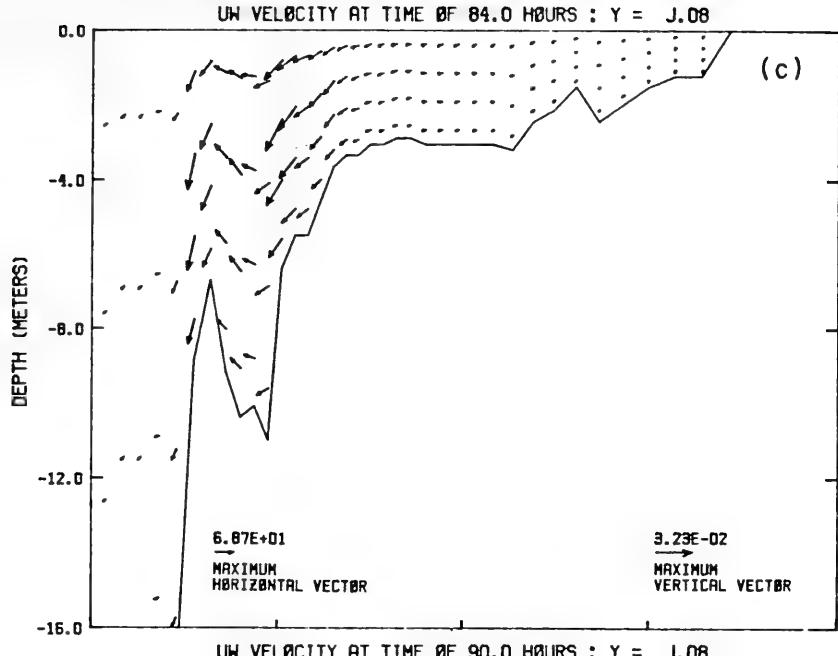
Figure 5.24. Velocity field within a transect across the Mobile Bay
Entrance throughout a complete tidal cycle.
(c) 84 hours;   (d) 90 hours;
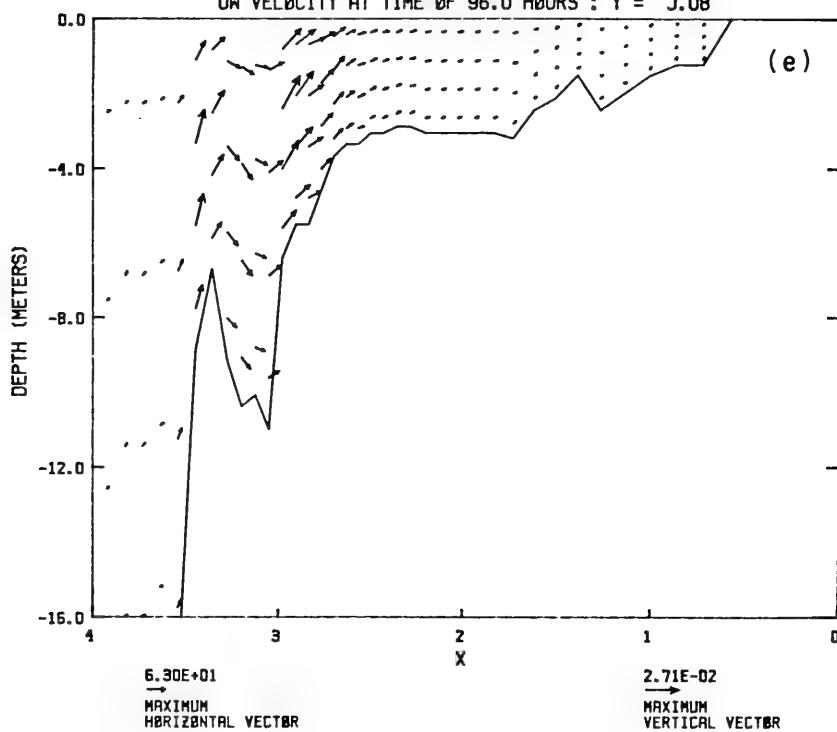
Figure 5.24. Velocity field within a transect across the Mobile Bay
Entrance throughout a complete tidal cycle.

(e) 96 hours.

MISSISSIPPI SOUND : FILE = TI3DAX7W
UV VELOCITY AT TIME OF 96.0 HOURS AND SIGMA OF -0.125
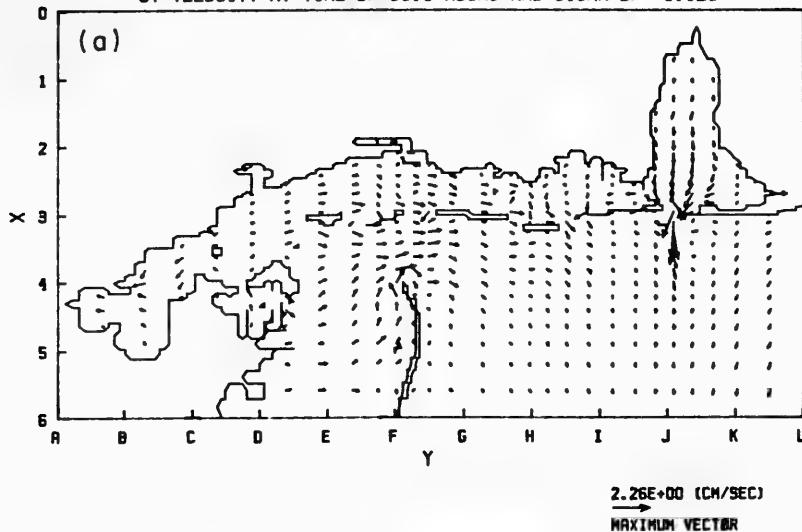
(a)

2.26E+00 (CM/SEC)
MAXIMUM VECTOR

MISSISSIPPI SOUND : FILE = TI3DAX7W
UV VELOCITY AT TIME OF 96.0 HOURS AND SIGMA OF -0.875

(b)

1.87E+00 (CM/SEC)
MAXIMUM VECTOR
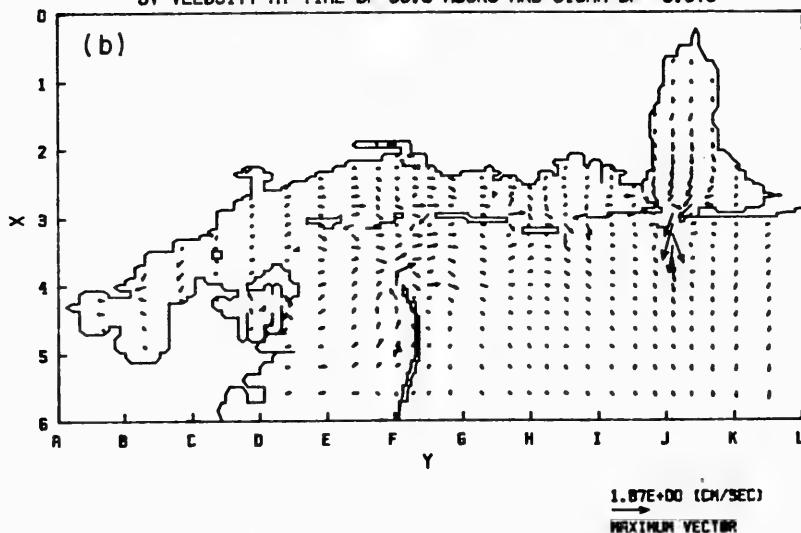
Figure 5.25. Residual currents during the complete tidal cycle
on 9/04/80.

(a) Near-surface currents;

(b) Near-bottom currents.

5.2 Wind-Driven Currents

Effect of Wind on Tidal Currents

The results presented in the above did not contain any wind-driven effect. During our study, wind data were collected at several meteorological stations surrounding the Mississippi Sound. The wind during the 5-day period between 20 Sept. and 25 Sept. 1980 was generally quite mild ($\sim$ 10 mph) from the southeast. To examine the effect of wind on the currents, we carried out a three-day simulation from 20 Sept. using a uniform wind stress of 1 dyne/cm^2 from the southeast. As shown in Figure 5.26, the southeasterly wind caused water to pile up within the Mississippi Sound at $(I,J)=(22,62)$, outside Pascagoula Harbor along the northern shore. The wind resulted in a set-up of 0.4 ft. The wind set-up at $(I,J)=(30,56)$, however, is only 0.2 ft. due to the shielding effect of the Horn Island.

The influence of wind on the current also depends on the location. Figure 5.27 shows the along-shore velocity at 2 locations over the 3-day period. At (33,28), off Cat Island, the presence of the wind did not have an appreciable effect on the tidal current. At (26,88), within the pass between the Mississippi Sound and the Mobile Bay, the wind caused significant flow from the Mobile Bay into the Sound. This resulted in a significantly larger bottom shear stress, which leads to the reduction in the amplitude of the tide-driven currents.

Currents Driven by Southeasterly Wind

Currents driven by an impulsive wind stress of 1 dyne/cm^2 from the southeast are computed by the three-dimensional hydrodynamic model. As shown in Figure 5.28, the near-surface currents after 1 day simulation time are generally less than 30 cm/sec. The near-bottom currents are 50% smaller.
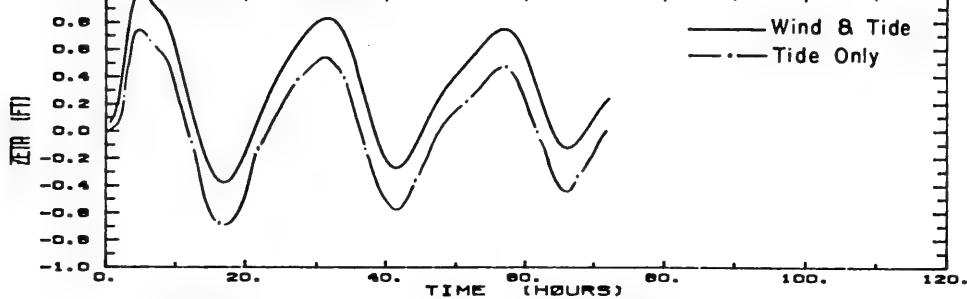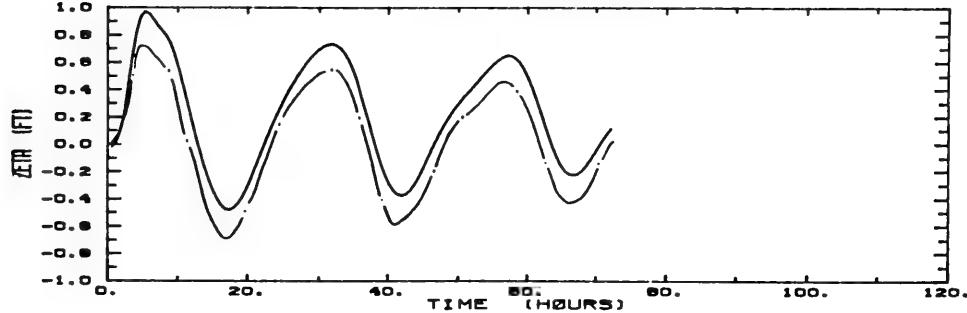
Figure 5.26. Influence of wind on surface displacements at two stations from 9/20/80 to 9/24/80.
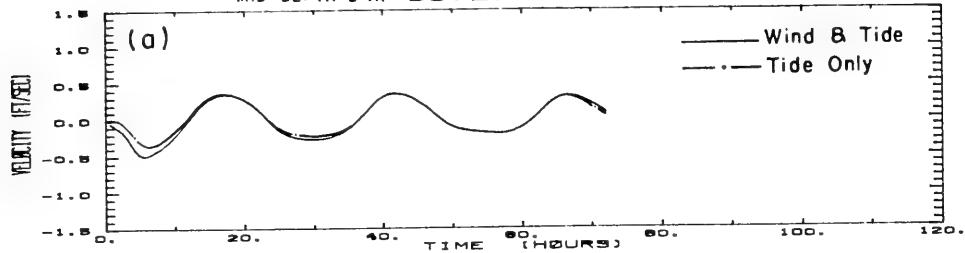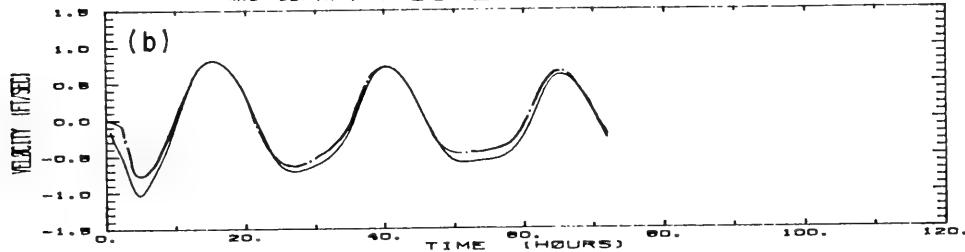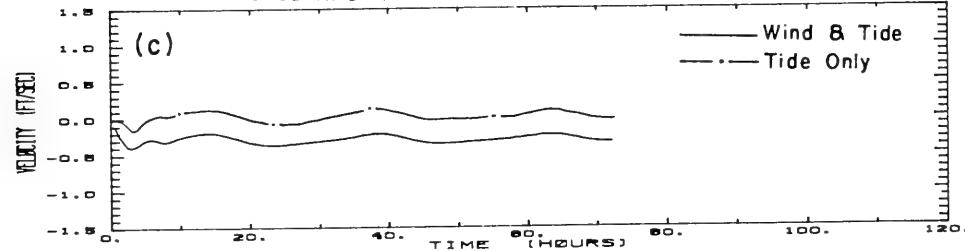
108
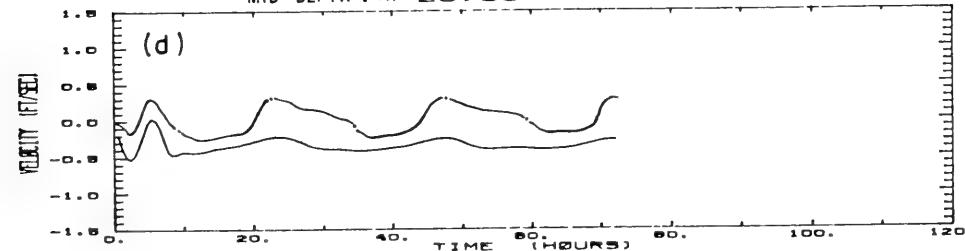
Figure 5.27.   Influence of wind on mid-depth horizontal velocities at two stations from 9/20/80 to 9/24/80.

MISSISSIPPI SØUND : FILE = TI3DAX7
UV VELØCITY AT TIME ØF 24.0 HØURS AND SIGMA ØF -0.125
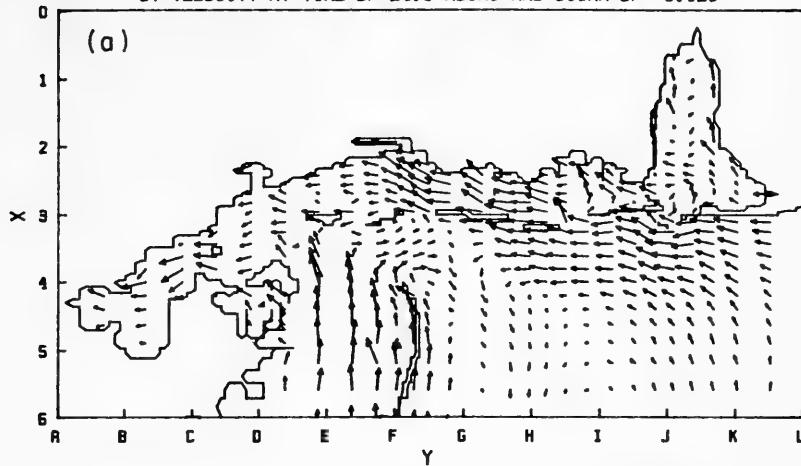
(a)

3.18E+01 (CM/SEC)
MAXIMUM VECTØR

MISSISSIPPI SØUND : FILE = TI3DAX7
UV VELØCITY AT TIME ØF 24.0 HØURS AND SIGMA ØF -0.875

(b)

1.79E+01 (CM/SEC)
MAXIMUM VECTØR
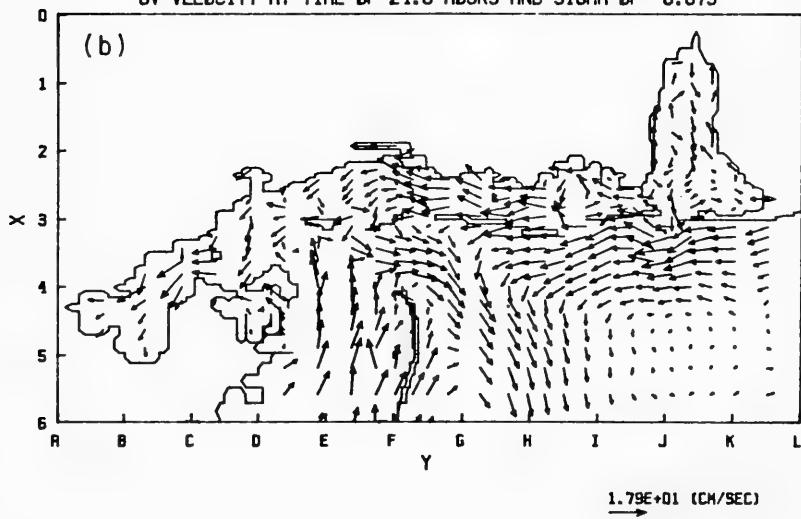
Figure 5.28. Near-surface and near-bottom horizontal velocities within
the Mississippi coastal waters due to a southeasterly
wind stress of 1 dyne/cm².

Currents Driven by a Westerly Wind

Wind-driven currents in the Mississippi Sound depend strongly on the wind direction. For example, assuming a uniform wind stress of 1 dyne/cm^2 from the west, our model results showed relatively stronger currents in the along-shore direction (Figure 5.29). Notice the near-surface and near-bottom velocities differ not only in magnitude but also in direction at some locations. This is partially associated with the pressure gradient caused by the wind set-up. As shown in Figure 5.30, wind set-up on the order of 20 cm occurs across the Mississippi Sound. The bottom stress distribution in the study area is shown in Figure 5.31. According to our laboratory flume study on the erodibility of the Mississippi Sound sediments, it is expected that the bottom shear stress generated by the strong westerly wind in winter will cause significant resuspension of sediments. The exchange of water mass between the Sound and adjacent offshore waters may result in transport of sediments into or out of the Sound.

Effect of Lateral Boundary Condition

The results shown in Figures 5.29 through 5.31 were computed with an open boundary condition assuming the surface displacement remained to be zero along the two open boundaries. While this condition is a reasonable assumption for the southern open boundary where the water is quite deep, it may be somewhat restrictive for the transverse open boundary along the east. To test the sensitivity of model results to the open boundary condition, we have performed a simulation with a zero surface slope condition along the eastern boundary. As shown in Figure 5.32, the near-surface currents and the near-bottom currents have increased from those in Figure 5.29 by more than 50%. Along the eastern boundary, currents are directed out of the computational domain. The zero surface slope condition may be valid in such a situation, but may not be valid where currents along the open boundary are directed into the computational domain.

111
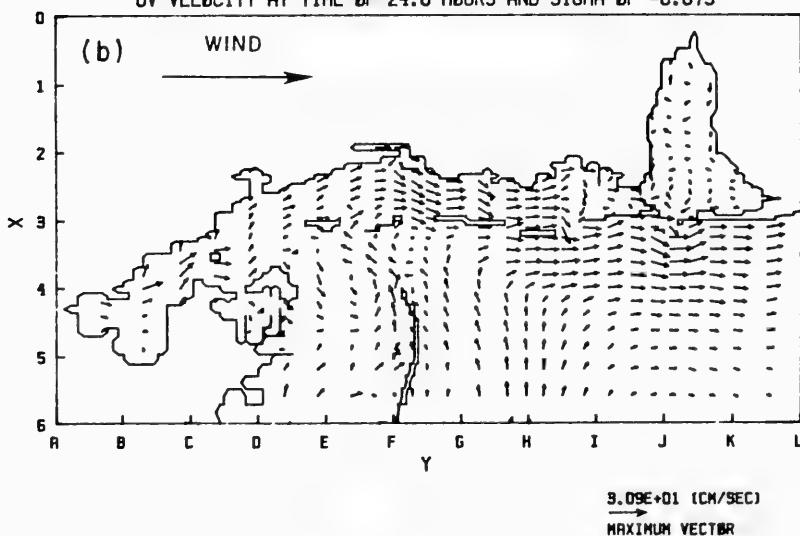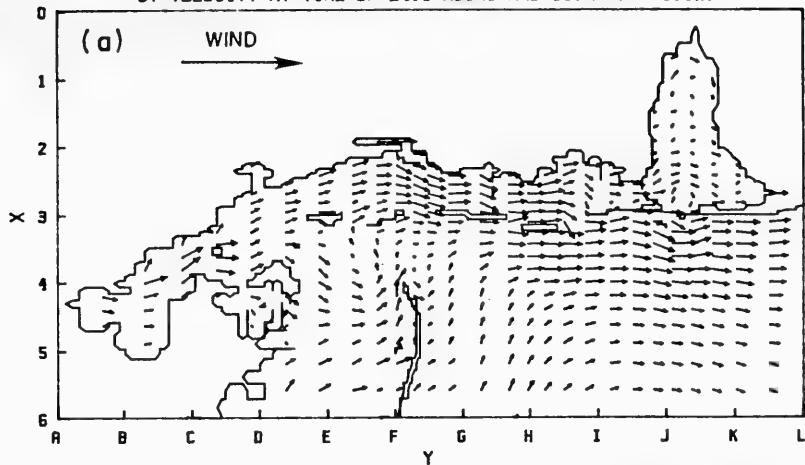
Figure 5.29. Same as Figure 5.28 except due to a westerly wind.

.
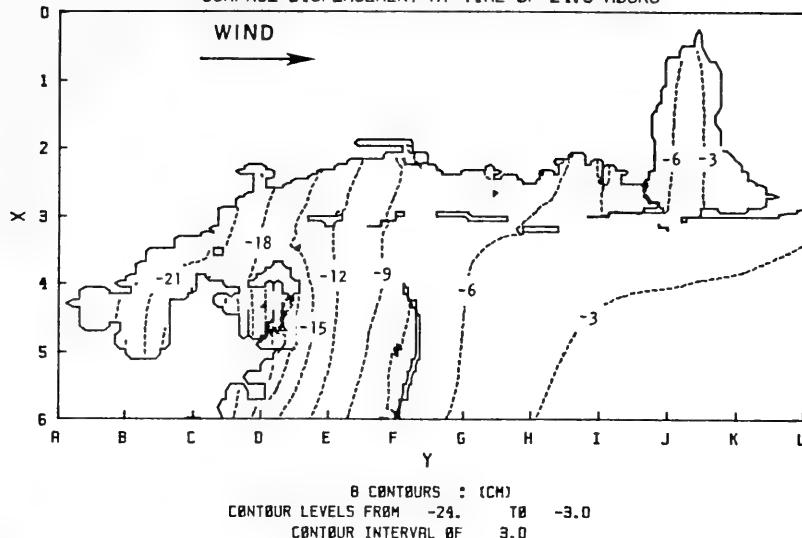
Figure 5.30. Surface displacement contours within the Mississippi coastal waters due to a westerly wind.
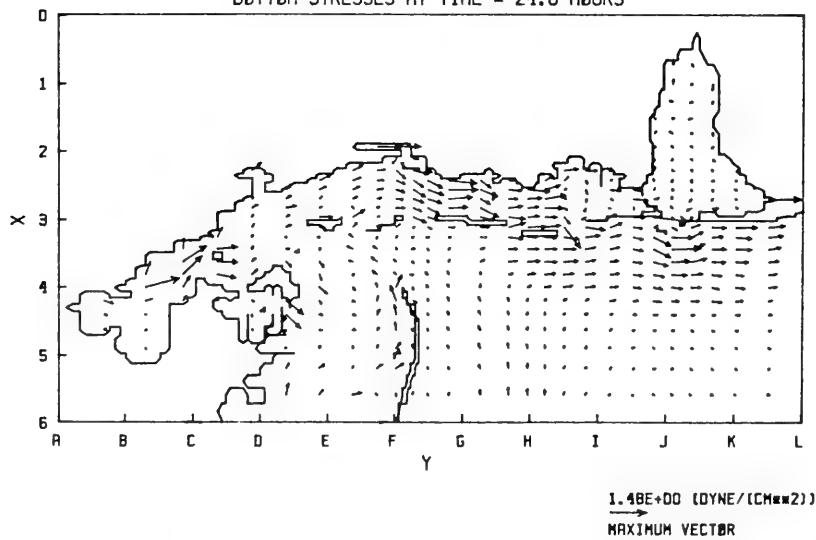
Figure 5.31. Bottom stress field within the Mississippi coastal waters due to a westerly wind.
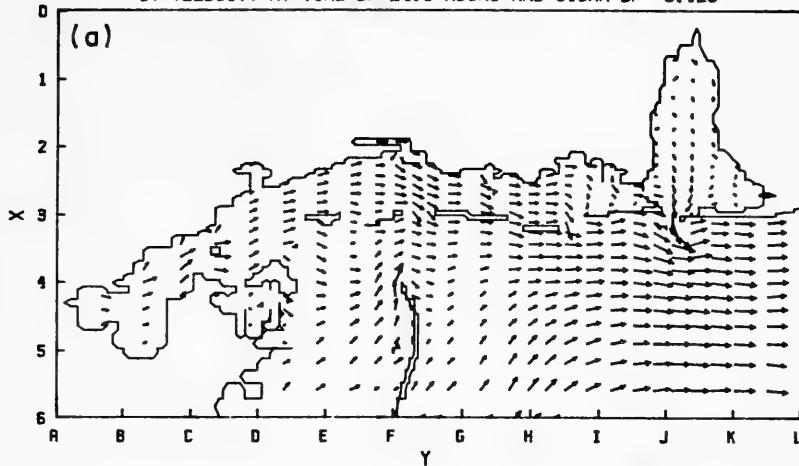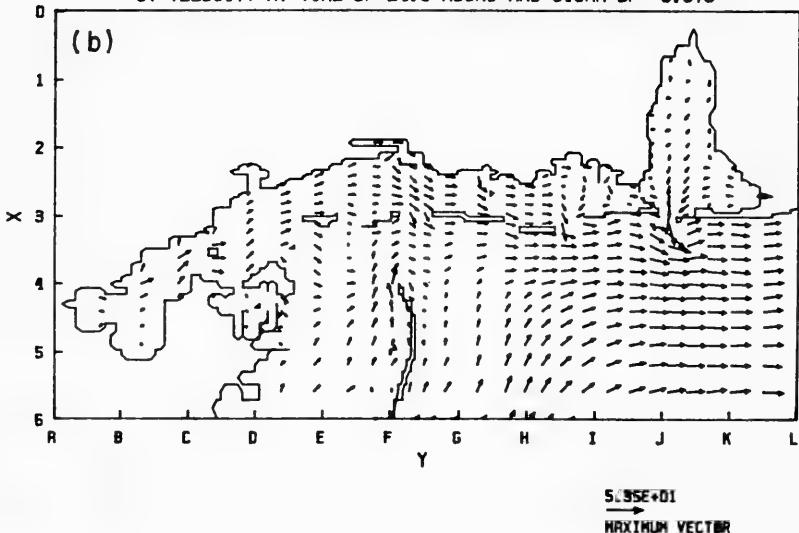
Figure 5.32.   Same as Figure 5.28 except with a different lateral
               boundary condition along the east open boundary.

114

.

Influence of Gulf Circulations

Large-scale circulations in the Gulf of Mexico, such as the Loop Currents, may affect the coastal currents in the study area. To examine this effect, the limited-area grid used here needs to be coupled with a global grid for the entire Gulf. The dynamic coupling procedure as described in detail by Sheng (1975) could be used to ensure proper transfer of information from one grid to another. The basic hydrodynamic model described in this report could be readily extended to study the entire Gulf circulation.

5.3 Density-Driven Currents

Density gradients resulting from spatial variation in temperature and/or salinity could induce currents in coastal waters. Relatively strong currents could be induced in an estuary where the light fresh river water meets with the heavy salt water from the ocean. However, transient adjustment of the density distribution is a very slow process compared to the tidal response or the wind-driven response in coastal waters. To illustrate this, we have performed a simulation in a two-dimensional estuary with a length of 15 km and a uniform depth of 10 m. River flow with a uniform velocity of 10 cm/sec at all depths enters through the left boundary. Along the open-ocean boundary, the salinity distribution varies from 20 ppt near the surface to 28 ppt near the bottom. Initially, the salinity is assumed to vary linearly in the horizontal direction from the river to the open boundary. The simulation was performed until the salinity distribution within the estuary changes little with time.

Current distribution at this steady state is shown in Figure 5.33. Strong surface currents up to 50 cm/sec are in the seaward direction while appreciable bottom currents on the order of 20 cm/sec are directed towards the river. The strong vertical shear is a direct consequence of the relatively small vertical eddy coefficient used ($1 \text{ cm}^2/\text{sec}$). The river inflow in this case is relatively strong. If the river inflow is reduced to 1 cm/sec, the steady-state currents are reduced to approximately 15 cm/sec. Bottom topography could also affect the current magnitude. Within the relatively deeper navigation channel, the density-driven currents are usually stronger than those in the shallower surrounding water. The time to reach the above
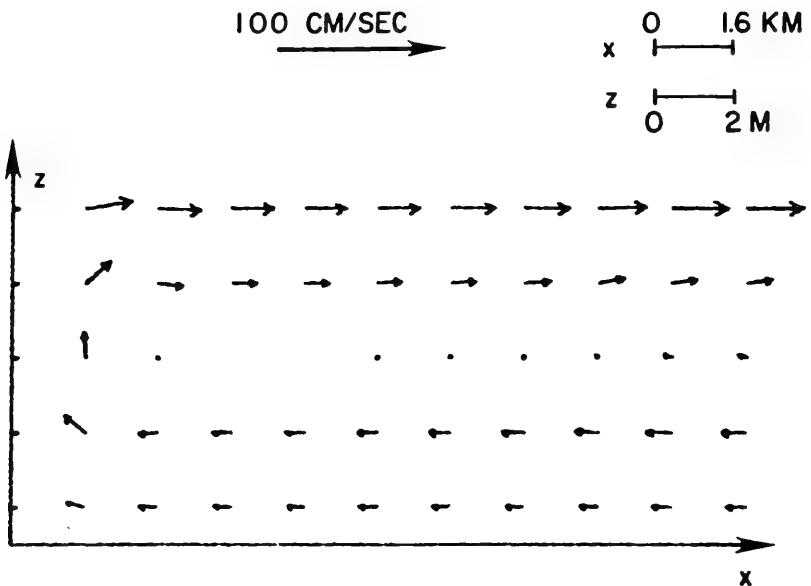
Figure 5.33. Steady-state currents driven by a fixed salinity gradient at the ocean boundary and fixed river flow at the land boundary.

steady-state is on the order of 5 days. If the dimensions of the estuary are increased, a longer adjustment time is required.

Results of the above simulation imply that in any realistic simulation of density-driven currents, the specification of the initial density distribution is extremely important. For simulations on the order of a few days, the final salinity distributions and density-driven currents are extremely sensitive to the initial values of the simulations. During the previous tidal simulations of the Mississippi Sound, salinity data was only collected within the Sound and no data was available in the offshore waters. Due to the relatively short simulation period (5 days), meaningful realistic simulation of the salinity field could not be performed without knowing the detailed offshore salinity distribution at the beginning of the simulation period. However, available salinity data indicate rather uniform salinity distribution within the Sound, in both the vertical and horizontal directions. The magnitudes of the density-driven currents are thus expected to be much smaller compared to the tide- and wind-driven currents. This is confirmed by the excellent agreement between the model's computed and measured currents, as shown in the previous sections. Density-driven currents should only be important during period of strong river inflows, particularly within the Mobile Bay.

Salinity and temperature data were collected from the transect stations of the Mississippi Sound on 9/02/80, 9/03/80, 9/08/80, and 9/04/80. The results at 1 meter depth were interpolated onto our numerical grid and are shown in Figure 5.34. It is apparent that during this period spatial gradients in temperature and salinity should have a negligible effect on the currents. Vertical gradients in temperature and salinity are also very small during the same period.

5.4 Return Currents in Bottom Waters

It was demonstrated in Section 5.3 that return currents in the bottom water could be caused by fresh water inflow into a density stratified environment.

MISSISSIPPI SØUND : DATE = 9/02/80 - 9/03/80
MEASURED SURFACE SALINITY

(a)

4 CØNTØURS : (PPT)
16.   20.   24.   26.

MISSISSIPPI SØUND : DATE = 9/08/80 - 9/09/80
MEASURED SURFACE SALINITY

(b)

5 CØNTØURS : (PPT)
16.   20.   24.   26.   28.
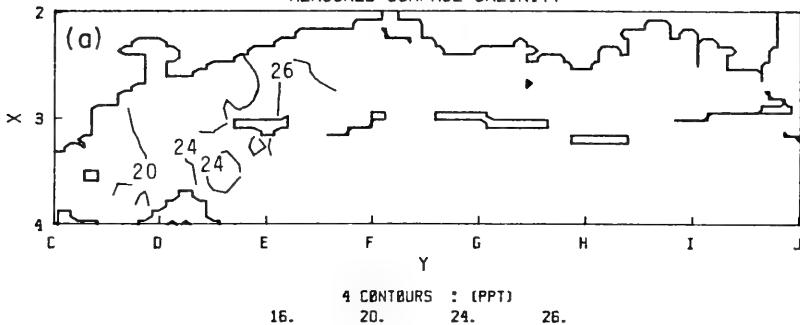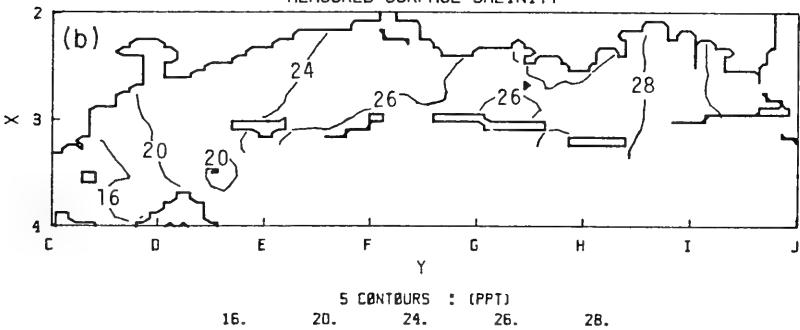
Figure 5.34.   (a)   Measured surface salinity field on 9/02/80 and
                       9/03/80.

                (b)   Measured surface salinity field on 9/08/80
                       and 9/09/80.

118

MISSISSIPPI SØUND : DATE = 9/02/80 - 9/03/80
MEASURED SURFACE TEMPERATURE

4 CØNTØURS : (DEGREE C)
30.2   30.4   30.6   30.8

MISSISSIPPI SØUND : DATE = 9/08/80 - 9/09/80
MEASURED SURFACE TEMPERATURE

4 CØNTØURS :
27.   28.   29.   30.
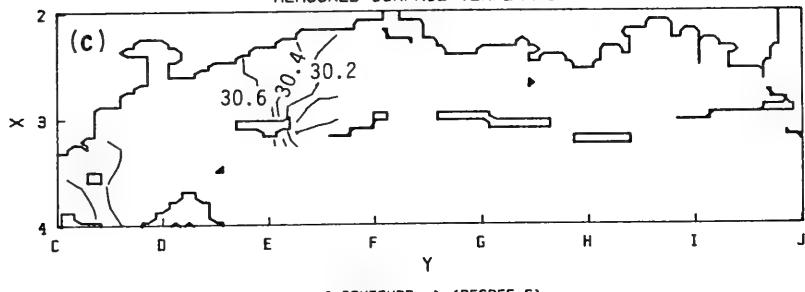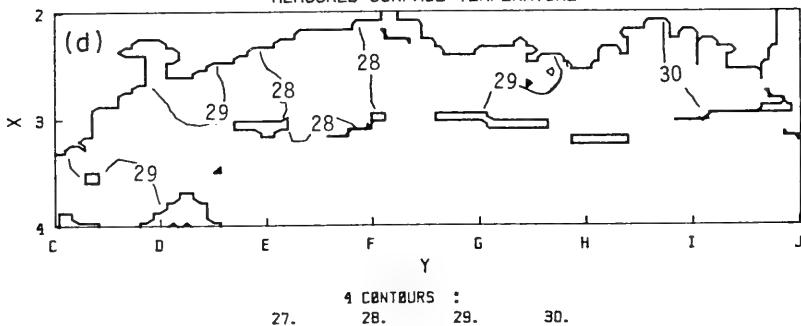
Figure 5.34.   (c)   Measured surface temperature field on 9/02/80
                       and 9/03/80.

                (d)   Measured surface temperature field on 9/08/80
                       and 9/09/80.

119

In addition, return currents in bottom waters may be caused by wind. To illustrate this, we present a simulation of Baines and Knapp's (1965) laboratory measurements on wind-driven currents in an open channel with two solid boundaries along the wind direction. Using the same $u_* D/\nu$ (~51,000) of their experiment, the model results in the middle of the channel are shown in Figure 5.35. The computed horizontal velocities shown in Figure 5.35(a) agree very well with the data and clearly exhibit the return currents caused by the wind-induced set-up. Figure 5.35(b) shows the vertical turbulent velocity w' and the vertical turbulent eddy viscosity A_v. w'/u_* agrees quite well with Baines and Knapps' data. Although the vertical profile of eddy viscosity was not measured, the simulated peak value of A_v is in agreement with their peak value estimated from their measured turbulence profile and a length scale equivalent to 20% of the water depth.

Another situation in which return currents may exist corresponds to the formation and deeping of a thermocline. Two example calculations are presented in Figures 5.36 and 5.37. Both simulations start with a uniform temperature of 6^0C everywhere in a two-dimensional basin 20 m deep and 100 km wide. In the first case, a uniform wind stress of 0.2 dyne/cm^2 is applied simultaneously with a surface heating rate of 0.01 cal/cm^2/sec. The temperature and velocity distribution in the middle of the basin at the end of 96 hours are shown in Figure 5.36(a) and 5.36(b). The temperature distribution clearly indicates the existence of a thermocline. Velocities on the order of 50 cm/sec exist in the mixed layer while return currents on the order of 15 cm/sec exist below the thermocline. The second case was computed with a wind stress of 0.5 dyne/cm^2 and a heating rate of 0.01 cal/cm^2/sec. As shown in Figure 5.37(a), a thermocline exists very near the bottom. Figure 5.37(a) shows mixed layer currents on the order of 15 cm/sec, but stronger return currents up to 25 cm/sec near the bottom.

The mixed layer calculations presented above correspond to extended periods of rather weak wind forcing and high heating rate. The presence of a stronger wind and/or tidal mixing would cause stronger turbulent mixing which may easily disrupt the sharp temperature and velocity profiles. During our study periods of the Mississippi Sound, since winds are stronger and heating rate are much lower, any pronounced vertical stratification is not expected to

.
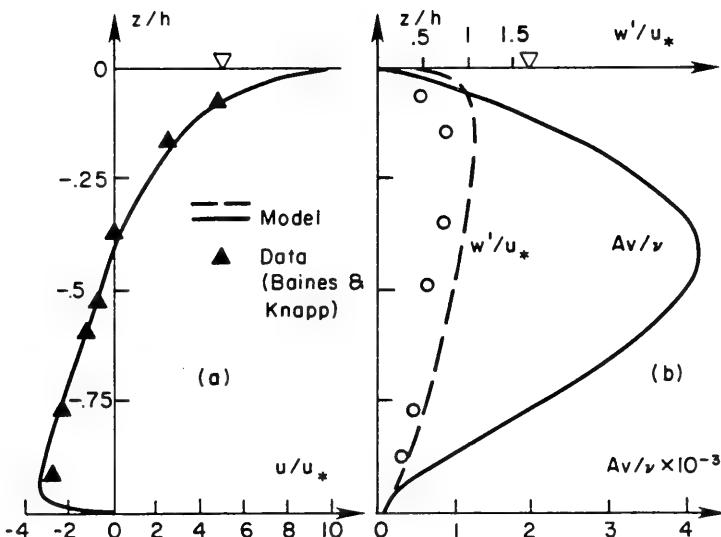
Figure 5.35   Wind driven currents in an open channel.
(a) Vertical profile of horizontal velocities.
(b) Vertical profiles of vertical turbulent velocity
and vertical eddy viscosity.
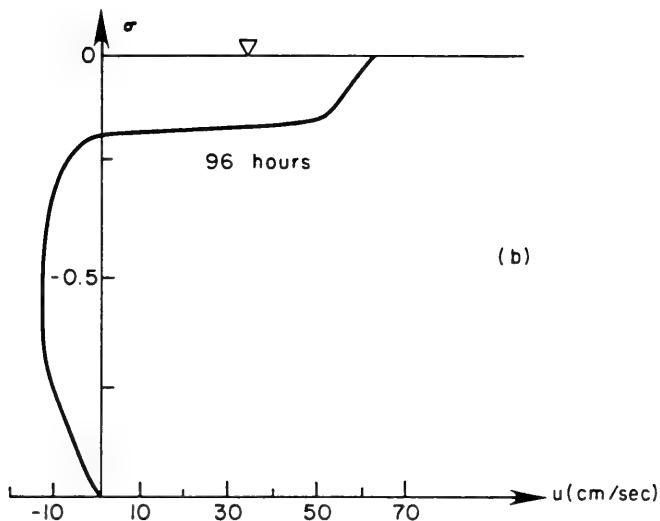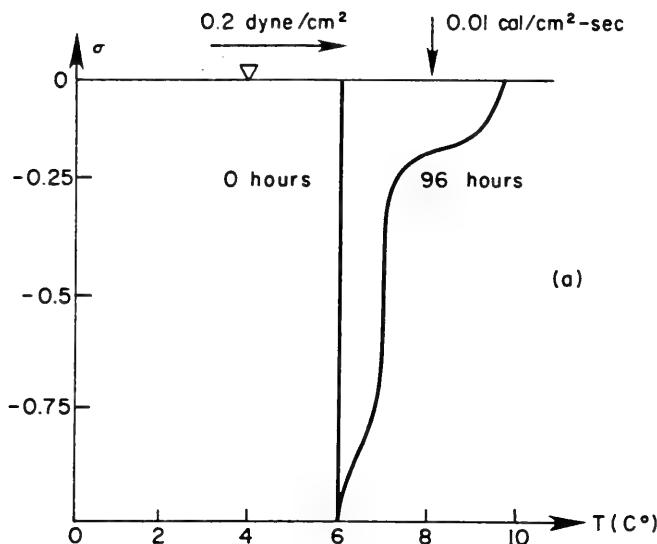
Figure 5.36   The formation and deepening of thermocline in a 20 m deep and 100 km wide basin with an applied wind stress of 0.2 dyne/cm^2 and a surface heating rate of 0.01 cal/cm^2-sec.
(a)   Temperature profile.
(b)   Velocity profile.
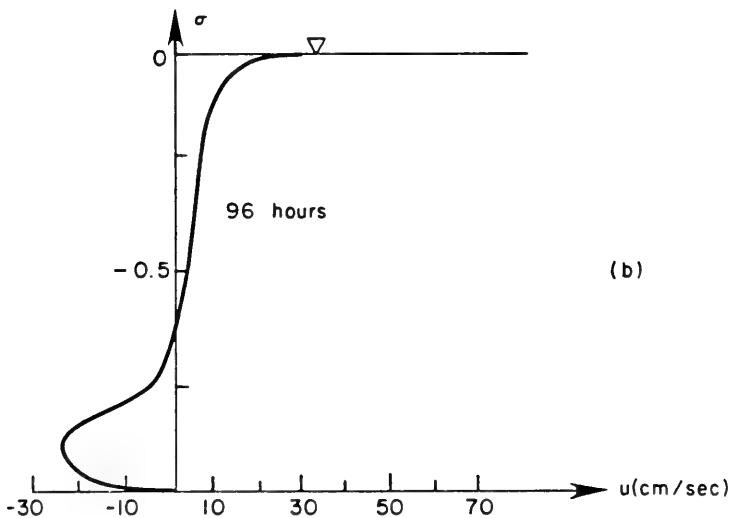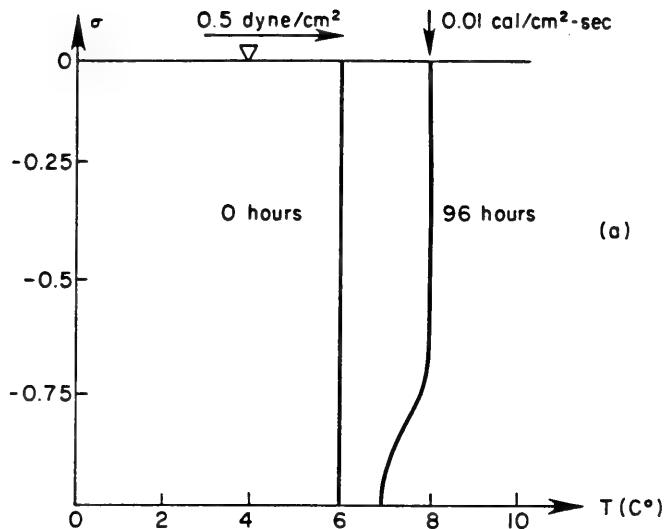
Figure 5.37. The formation and deepening of thermocline in a 20 m deep and 100 km wide basin with an applied wind stress of 0.5 dyne/cm^2 and a surface heating rate of 0.01 cal/cm^2-sec.
(a) Temperature profile.
(b) Velocity profile.

occur within the Mississippi Sound where the water is only a few meters deep. This is confirmed by the rather uniform vertical profiles of measured temperature and salinity data. However, this may not be true in the deep waters where detailed vertical profiles are not available from measurements.

6. TRANSPORT, ENTRAINMENT AND DEPOSITION OF COHESIVE SEDIMENTS

6.1 Transport Modes of Cohesive Sediments

The dispersion of cohesive sediments in a coastal environment is affected by a variety of mechanisms, as shown in Figure 6.1. After entering into the water column from rivers or bottoms, the movement of sediments is influenced by the various transport modes including convection, turbulent mixing, and gravitational settling. Exchange between the suspended sediments and the bottom sediments is governed by the entrainment and deposition modes.

The transport of cohesive sediments in the water column depends on the properties of cohesive sediments, the physico-chemical properties of the fluid, and the turbulence and the mean currents of the flow field. In general, a particle size distribution exists at any given point in the water column. Due to the dynamic nature of the flow field, this distribution is usually a function of time. In the following, the general nature of this particle size distribution will be first described. The various parameters that may affect this distribution will then be discussed.

6.2 Particle Size Distribution

In fresh water, cohesive sediments possess a relatively flat particle size distribution. This is illustrated in Figure 6.2 based on measurement of settling speed of cohesive sediments from the Mississippi Sound. Sediment particles can be approximately divided into six groups, each with a different median settling speed ranging from about 10^{-3} cm/sec to about 1 cm/sec. Assuming Stokes flow, these correspond to a relatively even distribution of particle sizes, ranging from about 4.3 μm to about 135 μm. It is apparent that, even in fresh water, due to coagulation and other causes, sediments often exist as flocs which are bigger than individual clay particles. To adequately describe the sediment dynamics, a mass conservation equation would have to be solved for each of the major groups of particles. However, relatively weak interaction exists among the various particle groups.

As the salinity of the water is increased, due to the increasing cohesion of particles, coagulation of particles becomes increasingly important. The particle size distribution in Figure 6.2 shows that, at 30 ppt salinity, about

125
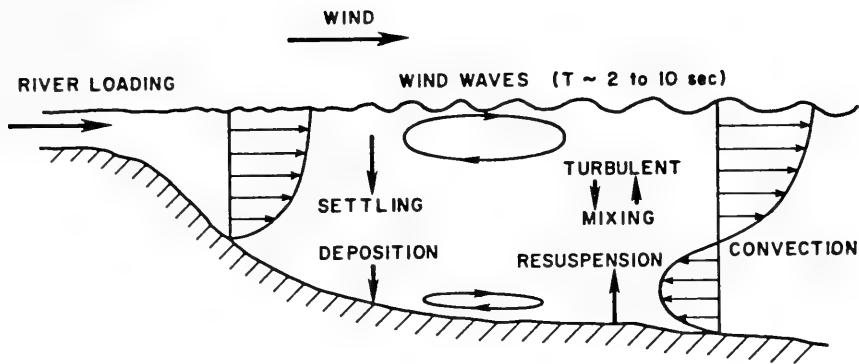
Figure 6.1.   Dominant mechanisms affecting the dispersion of sediments within a coastal environment.
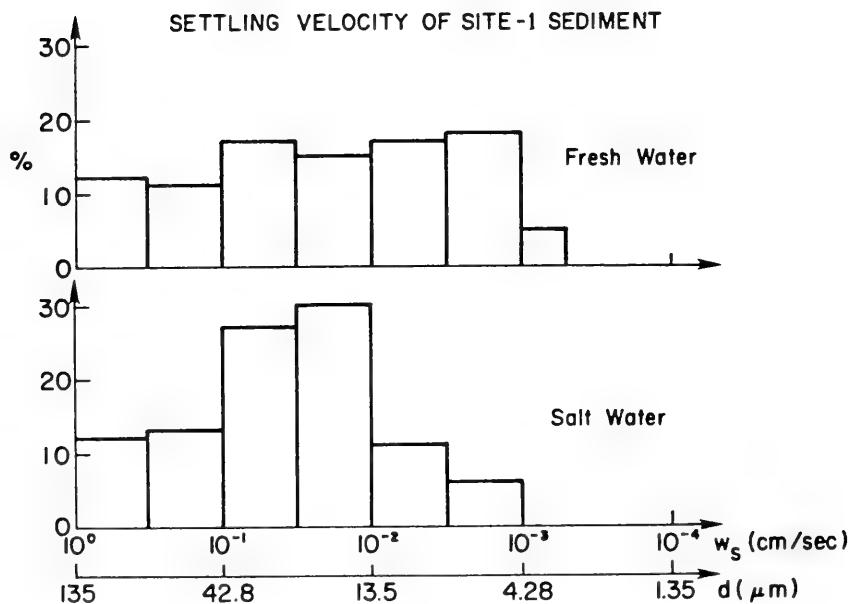
Figure 6.2.   Particle size (settling velocity) distribution of cohesive sediments in fresh and salt water.

126

60% of the sediment particles are concentrated within the size range of 13.5 μm to 42.8 μm. Thus, for cohesive sediments in a coastal environment, the dynamics of sediment particle size distribution as influenced by the coagulation process have to be addressed in a comprehensive sediment transport model. Due to the sharper particle size distribution, however, relatively fewer particle groups need to be resolved in a salt water environment. The relatively stronger coagulation leads to frequent interactions among the various particle groups. Although the coagulation process is quite complicated, and a comprehensive working model is not yet available at the present time, we will assess the present state of the art of our understanding of the important parameters affecting this process. This would be the basis for future model development.

6.3 Cohesion of Sediments

In contrast to non-cohesive sediments such as quartz sand, which generally exists as individual particles, the inter-particle forces lead to cohesion among the fine-grained cohesive sediments. Cohesive sediments are comprised primarily of colloidal clay particles and fine silt which possess colloidal properties to a lesser extent. In general, cohesive sediments from a coastal environment also include a certain amount of organic materials, bacteria, benthos and their fecal materials.

According to the difference in layer lattice crystal structures, clay minerals can be classified into three main types as kaolinite, illite, and smectite, with increasingly stronger clayey features. Within the individual crystals, positively charged cations occupy interior layers, and the negative charged hydroxyl and oxygen atoms occupy the platy surfaces. Positive charges are exposed at the crystal edges. The cations in the crystal lattice may be substituted by other ions of lower valence, thus producing a net charge deficiency which makes the surface negative charge even greater. With a small concentration of free ions in fresh water, electrostatic repulsive forces will be suppressed in favor of attractive van der Walls forces among individual clay particles. With increasing ion concentration in salt water, cohesion among particles is further enhanced and larger flocs can be formed.

In addition to the dependence on salt concentration, the cohesion among particles also depends on the surface charge density, the water temperature, the inter-particle distance, the valency of cation in water, the pH of water, and the kind of anions in water. The parameters of primary importance are: (1) total salt concentration, (2) cation exchange capacity which is an effective measure of the clayey activity, (3) sodium absorption ratio which is proportional to the ratio of exchangeable sodium to calcium plus magnesium ions found in the diffuse layer of sorbed ions near the clay surfaces, and (4) pH of the water.

Studies on the effects of various parameters on cohesion are generally carried out in low-turbulence laboratory settings. Although cohesion is the primary cause of particle coagulation in a low-turbulence environment, flow-induced collision among particles should play a more dominant role in determining the state of coagulation in generally turbulent coastal waters. Wind-induced turbulence in shallow coastal waters significantly increases the collision frequency among particles and brings about much enhanced coagulation among particles. Hence, to accurately resolve the sediment particle dynamics, turbulence must be accurately predicted. Sophisticated mathematical models (e.g., Sheng, 1982) are available for the prediction of turbulence in coastal waters. The roles of turbulence in affecting the particle collision and coagulation are described in the following.

6.4   Turbulence and the Collision/Coagulation Process

Dissipation Eddies in Coastal Waters

Turbulence in coastal waters consists of the random motion of eddy structures, ranging from the largest energy containing scales to the dissipation scales where molecular viscosity comes into play. Due to the drastic difference in the vertical and horizontal dimensions in the coastal environment, we are generally concerned with the vertical eddies. Hence, the largest scale is on the order of the largest macro-length L, such as the depth of the water column, while the smallest scale is on the order of the micro-scale λ_0 defined in terms of the turbulent energy dissipation $\epsilon = q^3/\Lambda$ as $\lambda_0 = (\eta^3/\epsilon)^{1/4}$, where q is a representative turbulent velocity and η is the molecular kinematic viscosity. Similarly, a micro-time characterizing the

time scale of fluctuations of the dissipation can be defined as $\tau_0=(\eta/\varepsilon)^{1/2}$ and a micro-acceleration within the eddy as $a_0=\lambda_0/\tau_0^2$. One can also define a micro-shear to characterize the velocity shear within the eddy as $G_0=\tau_0^{-1}$. Magnitudes of these quantities for the range of turbulence dissipation rates encountered in a shallow coastal environment are shown in Table 6.1.

<div align="center">

Table 6.1

Characteristic Quantities for Dissipation Eddies
in Coastal Waters

</div>

	ε (m^2/sec^3)	λ_0 (μm)	τ_0 (sec)	a_0/g $(---)$	G_0 (sec^{-1})
	0.001	178	0.03	0.02	33.3
Normal Condition	0.01	100	0.01	0.1	100
	0.1	56	0.003	0.6	333
	1	32	0.001	3.26	1000
Storm Condition	10	18	0.0003	20.4	3333

Since the dissipation rate is preserved through the cascade process, the fluctuation time of an eddy of scale λ is $\tau_\lambda=\tau_0(\lambda/\lambda_0)^{2/3}$ and the acceleration is $a_\lambda=a_0(\lambda/\lambda_0)^{-1/3}$. As the eddy size ($\lambda$) increases, τ_λ increases while a_λ and G_λ decrease.

Correlation Between Sediment Particles and Turbulent Eddies

The extent to which sediment particles of a given size and density are influenced by the turbulence depends on the relative magnitude of the particle relaxation time τ_r, defined as w_s/g where w_s is the settling speed, versus the fluctuation time of various turbulent eddies, τ_λ. If $\tau_r \gg \tau_0$, the particle motion is completely decoupled from the turbulence of the flow field and hence there is no influence of turbulence on the particle collision. At the other extreme, if $\tau_r \ll \tau_0$, the particles are completely correlated with all the turbulent eddies. The sediment particles experience an ensemble mean shear $\bar{G}$ comprising of contributions from all eddies. In between the two extremes,

particles will experience shear from those eddies with fluctuation times τ_λ equal to or greater than τ_r.

Let us now examine the relaxation time τ_r of sediment particles of various sizes. For simplicity, we assume Stokes flow and hence the settling speed w_s is proportional to the square of the particle radius. Assuming a particle density (ρ_s) of 2 gm/cm^3, the results are summarized in Table 6.2.

Table 6.2

Settling Speeds and Relaxation Times of Sediment Particles

Particle Radius	$w_s = \dfrac{2r^2 \, g(\rho_s - \rho_f)}{9\eta\rho_s}$	$\tau_r = w_s/g$
(µm)	(cm/sec)	(sec)
1	2.18×10^{-4}	2.22×10^{-7}
5	6.45×10^{-3}	6.55×10^{-6}
10	2.18×10^{-2}	2.22×10^{-5}
50	6.45×10^{-1}	6.55×10^{-4}
100	2.18	2.22×10^{-3}
500	54.5	6.55×10^{-2}

Based on the results in Tables 6.1 and 6.2, one can compute a critical particle radius r_c at which the relaxation time τ_r is equal to the time scale of dissipation eddy τ_0 under expected ranges of coastal turbulence (Table 6.3).

Table 6.3

Critical Particle Radii at Various Dissipation Rates

ε (m^2/sec^3)	0.001	0.01	0.1	1	10
r_c (µm)	367	212	116	67	37

The results in Table 6.3 indicate that, under normal conditions in a coastal environment, sediment particles with radii less than 100 μm will completely follow the eddy motions. Under storm conditions, however, only particles with radii less than 30 μm will completely follow the eddy motions. Considering the particle distribution shown in Figure 6.2, it is clear that a majority of the cohesive sediments from the Mississippi Sound will follow the turbulent eddy motions. At high turbulence during storm conditions, bigger particle sizes resulting from coagulation may exceed the critical radius and hence may be partially decoupled from the turbulent eddies.

Basics of Collision/Coagulation Model

Turbulence can affect the particle coagulation by increasing the collision frequency among particles in various size groups, through the turbulence induced shearing, turbulence induced acceleration, and gravitational settling. Since we are generally concerned with particles bigger than 1 μm in radius, the effect of Brownian motion on particle collision is much smaller than the turbulent contribution, and hence can be neglected. The total collision rate per unit volume between two groups of sediment particles with radius (r_1, r_2) and number density (n_1, n_2) can be expressed as:

$$N = n_1 \, n_2 \, \nu \, (r_1, r_2) \qquad (6.1)$$

where ν is the collision kernel and can be expressed as (Saffman and Turner, 1956):

$$\nu^2 = (\nu_1^2 + \nu_2^2 + \nu_3^2) \, e^2 \qquad (6.2)$$

where ν_1, ν_2, and ν_3 are the contribution from turbulent shearing, turbulent acceleration, and differential settling. These are expressed as:

$$\nu_1 = \Delta V_{12}^{(s)} \, \pi \, r_{12}^2$$

$$\nu_2 = \sqrt{1.3} \, (a_0/g) \, \Delta V_{12}^{(g)} \, \pi \, r_{12}^2$$

131

$$v_3 = \Delta V_{12}^{(g)} \pi r_{12} \tag{6.3}$$

where $\Delta V_{12}^{(s)}$ is the effective relative velocity of the sediment particles due to the shearing motion linearly proportional to the shearing rate G, $\Delta V_{12}^{(g)}$ is the absolute difference between the settling velocities of the two particle groups, and r_{12} is the collision cylinder radius equal to the sum of r_1 and r_2. Turbulent shearing dominates for smaller particles, while turbulent acceleration dominates for bigger particles. Differential settling becomes increasingly important as the difference in particle sizes increases.

The collision efficiency e is a function of the relative Reynolds number of the colliding sediment particles as well as the radius ratio of the drops. In addition, the effect of clay mineralogy and physico-chemical properties of the fluid in affecting the cohesion among particles can be included in this term.

Development of a Comprehensive Model

The first prerequisite in utilizing the above information is to have a dynamic model capable of predicting the turbulence of the flow field, in addition to the mean flow. The three-dimensional hydrodynamic model described earlier in this report can be extended to compute the turbulence of the flow field. This procedure is outlined in Sheng (1982).

Next, to include the coagulation dynamics in the sediment transport model, sediment particles should be divided into several groups, each with a mean radius and a median settling velocity. Conservation equations for the number density and the mixing ratio of each of these particle groups can be derived. In addition to the convection by currents and the gravitation settling, these equations would incorporate the transition rates among the various particle groups based on the collision rates defined by Equation (6.1).

Collisions among the very small particles generally lead to coagulation and formation of flocs. These flocs may further coagulate into even bigger flocs. As the flocs increase in size, the inter-floc cohesive forces decrease in magnitude. Hence turbulence induced collisions may lead to breaking up of

the bigger flocs. However, the bigger flocs are influenced by the weaker shearing rate associated with the larger eddies. The maximum attainable floc size depends on the type of cohesive sediments, the turbulence field, and the physico-chemical properties of fluid.

We have laid out the steps for the development of a comprehensive model describing the coagulation dynamics of cohesive sediments. However, the complete development of such a model requires further studies and is beyond the scope of the present work.

6.5 Settling Speed of Sediments

In general, the settling speeds of a group of sediment particles depend on (1) particle Reynolds number, (2) distance of particles above the bottom, (3) turbulence, (4) salinity, and (5) particle concentration. Effects of these parameters are described in the following.

For an individual particle settling in water, the terminal settling speed can be determined from a balance between the drag force and the gravitational force acting on the particle. At low particle Reynolds number, the drag force can be described by the Stokes law and the terminal settling speed is proportional to the square of particle radius as shown in Table 6.1. High Reynolds number effect needs to be included for non-Stokesian sediment particles. At very high Reynolds number, the drag coefficient asymptotes to a constant value and the terminal settling speed becomes proportional to the square root of the particle radius.

As a sediment particle settles through the water column and approaches within a few particle radii from the bottom, the drag force acting on the particle increases and the terminal settling speed is gradually reduced from its Stokesian settling speed. For smaller particles a few microns or less in radius, impaction becomes the major mechanism bringing particles to the surface. This will be discussed later in the section on deposition.

As indicated in Figure 6.2, it is not always meaningful to assign a single settling speed to a group of cohesive sediment particles collected from the natural environment. Results for sediments from Site-2 and Site-4 are shown in Figure 6.3. To obtain sediment speed distribution resembling that in

133
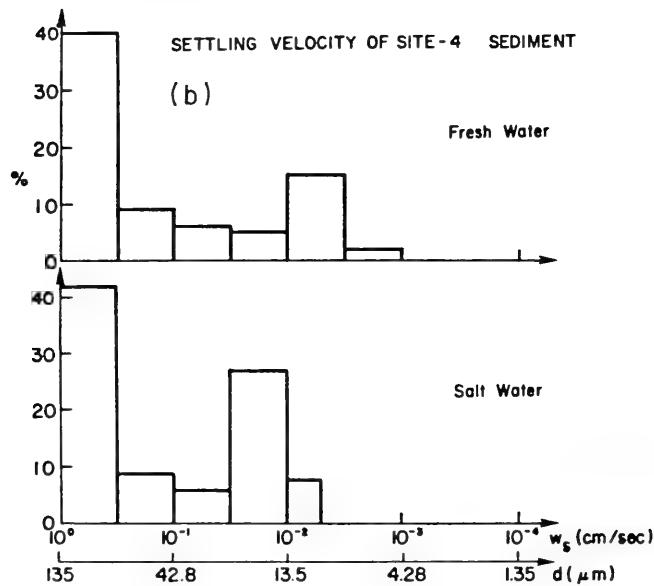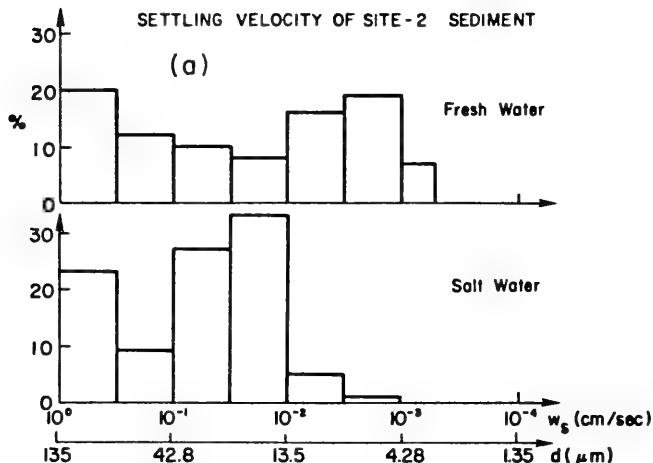
Figure 6.3.   Same as Figure 6.2 except for sediments from

(a) Site-2

(b) Site-4.   See Figure 1.3 for location of sites.

the natural environment, measurements were carried out in a settling cylinder without adding any dispersant to break up the flocs. Typical grain size analyses of the sediments, however, are carried out in a settling tube containing distilled water and 6.5 g/ℓ of sodium hexametaphosphate, a dispersant used to prevent coagulation. The settling speeds determined under such a condition are generally much smaller, reflecting the abundance of smaller micron size particles. Using the same sediments as those used in Figure 6.2, settling speeds determined in this fashion are compared with those determined earlier. As shown in Figure 6.4(a), the median settling velocity determined by the grain size analysis is on the order of 0.002 cm/sec, compared to 0.05 cm/sec in sea water (30 ppt) and 0.02 cm/sec in fresh water (0.2 ppt). Similar results obtained for Site-4 sediments are shown in Figure 6.4(b).

As indicated in the previous sections, sediment particle size distribution and hence the settling speed distribution depend on the coagulation dynamics which is influenced by the turbulence and salinity of the surrounding water. Turbulence increases the collision, while salinity increases the cohesion, among particles; thus, both tend to shift the settling speed distribution towards larger values. Most settling speed measurements, however, have been carried out in low turbulence laboratory settings. Well-designed experiments are urgently needed to quantify the influence of turbulence on the settling speeds of sediment particles.

At higher concentration of sediment particles, settling speed may be reduced due to hydrodynamic interference among the particles. This so-called "hindered settling" was studied by Batchelor (1972) in a dilute suspension of identical small rigid spheres with random positions in a Newtonian fluid. The settling speed is equal to $(1-6.55\ C)\ w_s$, where C is the concentration and w_s is the single particle settling speed in an unbounded fluid.
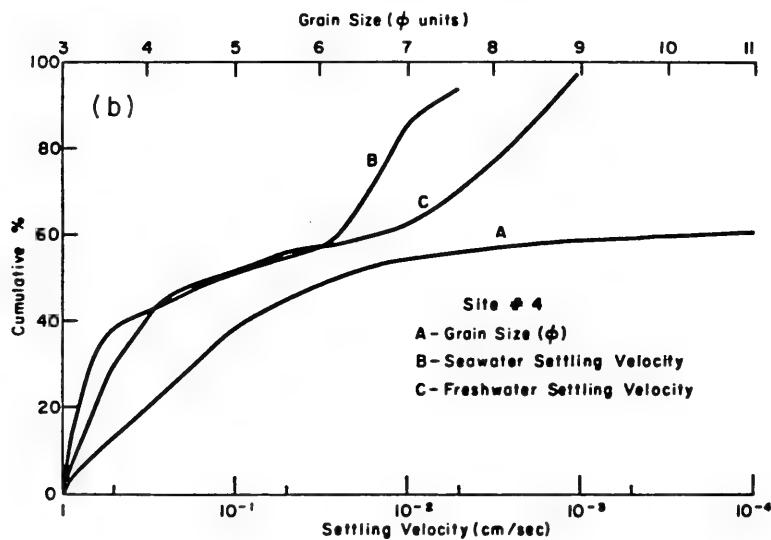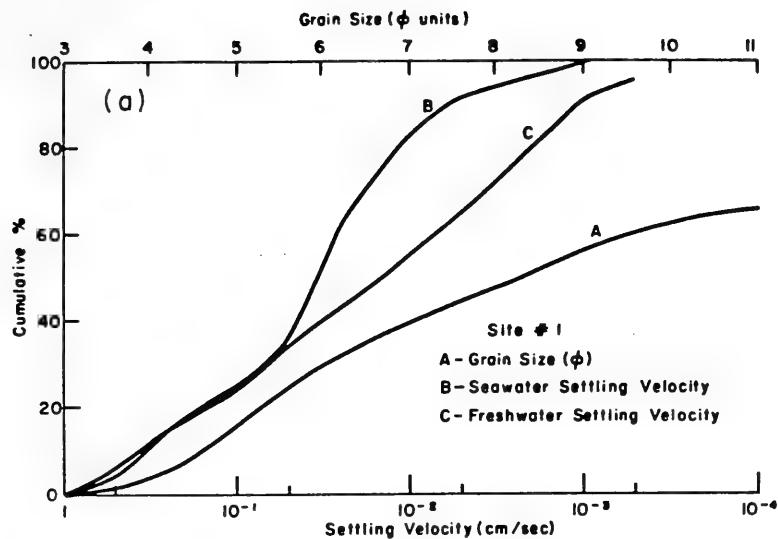
Figure 6.4.   (a) Settling velocity of Site-1 sediments determined from
                    settling cylinder measurements and grain size analysis.

               (b) Same as (a) except for Site-4 sediments.

6.6 Entrainment of Cohesive Sediments

Entrainment of cohesive sediments occurs when flow-induced shear stress at the sediment-water interface exceeds the inter-particle or inter-floc cohesive force of the surfacial sediments. Suspended sediment particles in the water column exist as flocs of various sizes depending on the hydrodynamic, chemical, and biological conditions during the entrainment process. Entrainment occurs primarily as a surface phenomenon. The hydrodynamic process within the relatively thin bottom boundary layer plays a predominant role in causing entrainment of sediments. Of course, the entrainment process also depends on properties of sediment and properties of interstitial and overlying water. Various sediment properties such as water content, organic content, and mineralogical composition have been found to appreciably affect the rate of entrainment.

To obtain quantitatively accurate estimate on entrainment of cohesive sediments, the detailed flow dynamics within the bottom boundary layer needs to be analyzed first. Next, the entrainment rates for a variety of sediments under various hydrodynamic, chemical, and biological conditions need to be determined. Although these two problems are dynamically coupled, a comprehensive quantitative analysis is extremely difficult to carry out. As a first step, they have to be treated separately. Over the shallow coastal waters, interaction of the wave-induced orbital current and the slowly-varying tide- or wind-driven current generally takes place within the bottom boundary layer. Following a discussion on the bottom boundary layer dynamics, laboratory studies on determining the entrainment rate as a function of several important parameters will be presented.

6.7 Bottom Boundary Layer Dynamics

Current-Induced Bottom Shear Stress

For fully rough turbulent flow over a flat bottom in the absence of wave-induced orbital currents, the near-bottom currents are relatively steady and follow the logarithmic variation with depth:

$$u = \frac{u_*}{k} \left[\ln \frac{z}{z_0} + \phi_s \left(\frac{z}{L} \right) \right] \tag{6.4}$$

where u_* is the friction velocity, k is the von Karman constant, zo is the roughness height, ϕ_s is a stability function and L is the Monin-Obukhov similarity length scale. Under neutral stability, $L=\infty$, $\phi_s=0$, and the velocity follows a simple logarithmic relationship. Within the bottom boundary layer, the shear stress remains relatively constant. With velocity measurements at two or more points, the shear stress and the roughness height could be determined. The above equation is the basis for deriving the drag coefficient formulation shown in Eq. (2.20). In shallow coastal waters, the depth of the constant flux region is on the order of a meter.

In shallow coastal waters, wind waves are generally present and their effect can reach the bottom. The wind waves induce orbital currents which gradually decrease with the depth. Nearly-sinusoidal motion exists in the vicinity of the bottom. The boundary layer associated with this wave-induced oscillatory motion is generally much thinner than that induced by the mean currents. Consequently, for an orbital current comparable in magnitude to the mean current, wave-induced bottom shear stress is generally much stronger than the current-induced stress.

Wave-Induced Bottom Shear Stress

Detailed flow measurements within the wave boundary layer are scarce. Comprehensive data in a coastal environment is even more scarce. Based on limited laboratory studies (e.g., Jonsson and Carlsen, 1976), empirical formulae for estimating the bottom shear stress have been developed based on ad-hoc, eddy-viscosity models. Grant and Madsen (1978) were able to obtain

reasonable estimate on mean velocities measured by Jonsson and Carlsen, but were not as successful in predicting the phase relationship. Multi-layered (Kajiura, 1968) and time-dependent (Jonsson, 1980) eddy viscosities were used to achieve reasonable agreement between computed and measuredon mean flow variables. Drag coefficients varied from 0.01 to 0.08 when amplitude-to-roughness ratio changed from 500 to 10. However, measurements of Riedel et. al (1973) indicated that the drag coefficient was 50% smaller over the entire range of amplitude-to-roughness ratio (Figure 6.5). This discrepancy was not explained by Jonsson or Reidel et.al. The shear stress value in Jonsson and Carlsen's experiments was not directly measured, but obtained indirectly from the time variation of mean velocities. In addition, none of the empirical analyses was able to accurately predict the thickness of the wave boundary layer and its variation with time, although Jonsson and Carlsen (1976) did measure the existence of a thin wave boundary layer within which a relationship similar to Equation (6.4) should hold.

The uncertainties found in the experimental and empirical analyses lead us to perform a more rigorous analysis of the wave boundary layer. The analysis was carried out with a dynamic turbulent transport model which does not require any ad-hoc adjustments of the model parameters. Detailed simulation of Jonsson and Carlsen's experiment can be found in Appendix D of this report. The model was able to accurately predict the mean flow variables throughout a complete wave cycle. Further, the phase relationship predicted by our dynamic model agrees very well with data than did any ad-hoc eddy-viscosity model. In addition, transient variation of the thickness of the wave boundary layer can be predicted. Although our model prediction on shear stress agrees well with Jonsson and Carlsen's estimate at $\theta = 180^0$, it was found that the model predicted shear stress is generally less than their indirect estimates over most of the wave cycle. We believe this is due to the error introduced in their indirect estimates of shear stresses arising from the lack of time resolution in their mean flow data. In fact, their estimate on shear stress averaged over a wave cycle contains approximately a twofold overestimation. Empirical bottom stress formula derived from fitting their data could lead to appreciable error. Although turbulent quantities were computed by our turbulent transport model, they were not measured by Jonsson and Carlsen.
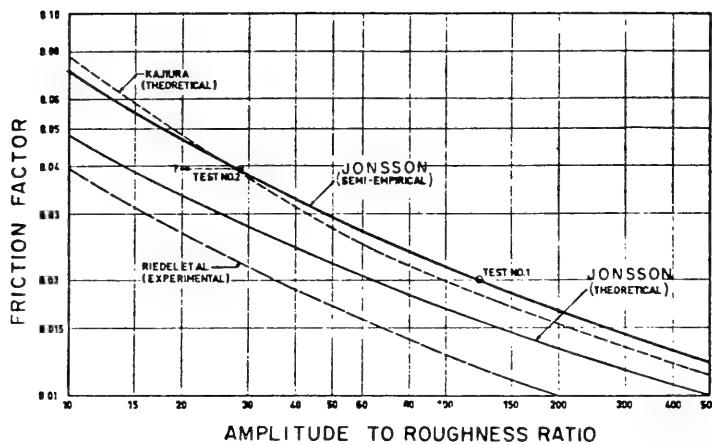
Figure 6.5.   Friction factors under a purely oscillatory turbulent
            boundary layer (from Riedel, et al., 1972) .

Wave-Current Induced Bottom Shear Stress

Slowly-varying currents and wave orbital velocities generally both contribute to the generation of bottom shear stress in shallow waters. Eddy viscosity models have been used by Grant and Madsen (1979) and Smith and McLean (1977) to investigate this process. Based on certain assumed eddy viscosity profiles and a constant thickness of wave boundary layer, their models showed that the presence of the wave enhances the bottom shear stress induced by the mean currents. While relatively inexpensive to use on a computer, the eddy viscosity model necessarily requires more effort in parameter tuning and is also not expected to be valid under all varieties of turbulent flow situations. To remove the empiricism from the model simulation, we have used a dynamic turbulent model to predict the wave-current interaction within the bottom boundary layer. In the following, we present our model simulation of some data collected during the CODE-1 (Coastal Ocean Dynamics Experiment) program.

The data were collected at a 90 m site (C3) about 1 km off the California coast. Both the USGS tripod (Geoprobe) and the WHOI tripod (Bayshore and El Camino) were deployed at the site during various time periods. For this preliminary simulation, data from the WHOI tripod (samples at 30, 50, 100, and 200 cm above bottom) are used. Due to the relatively long fetch from the north, high seas (6-8 feet) were typical, and wavelengths were sufficiently long for the wave to feel the bottom.

Velocity profiles (averaged over 6 minute intervals) at this site show typical logarithmic variation with height above the bottom. The values of u_* are typically between .22 and .66 cm/sec. Using the reference velocities at 1 m, these u_* values correspond to drag coefficients of 0.019 and 0.026, respectively. Values of the effective z_0 in the presence of the wave are 1.3 and 3 cm, an order of magnitude greater than the z_0 based on physical roughness alone.

Without parameter tuning, our model was able to simulate the increase in u_* and z_0 due to the presence of the wave. Data provided to us for one 6-minute period at 100 cm above the above, show a mean velocity (u_{100}) of 10.21 cm/sec, a wave orbital velocity (u_{wa}) of 6.09 cm/sec, a period (T) of

141

13.79 sec, and a physical roughness (z_0) of 0.2 cm. Using these data as boundary conditions to our model, the mean velocity profile in the absence of wave exhibits logarithmic variation with height (Fig. 6.6). Ursell number was much smaller than 1, thus justifying a linear wave boundary condition at 1 m. The wave orbital velocity which varies sinusoidally with time was then imposed at the boundary, and the model was allowed to run until the solutions repeated themselves from cycle to cycle, i.e., a quasi-steady state was reached. The velocity profile averaged over a complete wave cycle, as shown in Figure 6.6(a), indicates an increase in z_0 to 0.5 cm. As shown in Figures 6.6(b), turbulent kinetic energy (q^2) and Reynolds stress ($-\overline{u'w'}$) have also increased due to the presence of the wave. Fig. 6.6(c) indicates u_* $(-\overline{u'w'}/\rho)^{1/2}$ has increased from 0.6 cm/sec to 0.71 cm/sec. The estimated values of u_* and z_0 are less than those estimated by Grant and Madsen (0.9 cm/sec and 0.9 cm, respectively), which were higher than the values determined from the logarithmic profiles.

If one uses the empirical formula of Kajiura (1968) or Jonsson and Carlsen (1976), the wave-induced bottom shear stress averaged over the wave cycle is on the order of 1.3 dyne/cm^2 for the present case. Adding the current-induced stress onto it, the total bottom stress would be 1.6 dyne/cm^2, much higher than the measured value and our model estimate.

The success of the above simulation is not to be interpreted as having resolved all the problems surrounding the current and wave interaction within the boundary layer. In fact, further applications of our model to simulate the turbulent boundary layer under combined current and wave actions indicate the wave modulation may either enhance or reduce the turbulence due to the mean currents, depending on the quasi-steady turbulence level, the relative strength of wave vs. current, and the period of the waves (Sheng and Lewellen, 1982). A laboratory study by van Hoften and Karaki (1976) found that the Reynolds stress was reduced due to the presence of the wave.

CODE (Coastal Ocean Dynamics Experiment)
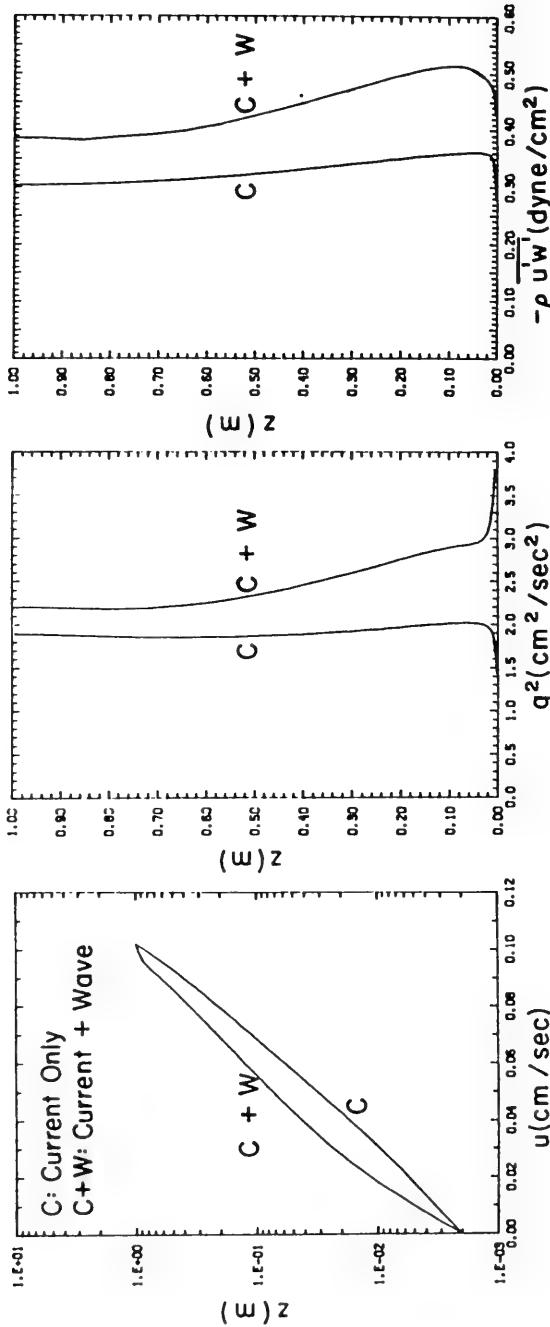
Figure 6.6. Vertical profile of:
(a) mean velocity.
(b) twice the turbulent kinetic energy, and
(c) Reynolds stress within a combined current-wave bottom
    boundary layer. $z_o = 0.2$ cm, $u_{100} = 10.21$ cm/sec,
    $U_w = 6.09$ cm/sec, and $T_w = 13.79$ sec.

143

Other Effects on Bottom Shear Stress

Bottom features and interaction between sediment particles and flow can affect the bottom shear stress. The effect of relatively small bottom features can be parameterized in terms of a roughness height z_0 that appears in the logarithmic relationship. When sizeable bottom features such as vegetation canopy or dredged material mound formed at disposal site exist, the total bottom stress includes contribution from the skin friction drag and, more importantly, the profile drag, created by the pressure difference in the flow direction on two sides of the bottom feature. Assuming the total shear stress at a certain height above the bottom feature could be measured or computed, only a fraction of this total stress contributes to the skin friction drag at the bed to cause entrainment of sediment. The partitioning between skin friction drag and profile drag depends on the detailed structure of the bottom feature and its interaction with the bottom flow. This problem has been investigated by us with a dynamic turbulence model (Appendix D).

The presence of sediment particles within the bottom boundary layer can also alter the bottom shear stress. At relatively high concentrations, the vertical distribution of sediment particles generally leads to a stable density distribution, thus lowering the drag coefficient in the quadratic stress law. In addition, the sediment particles may lead to damping of turbulence. Turbulent eddies within the bottom boundary layer have smaller length and time scales. Hence, the sediment particles generally do not follow the eddy motion, thus resulting in the damping of turbulence. Both of these effects have not been well studied but can be investigated by further extending the dynamic turbulence model presented in Appendix D.

6.8 Laboratory Studies on Sediment Entrainment

Our Study

Due to the complexity of the problem, a comprehensive theoretical model for the entrainment of cohesive sediment is not available at this time. Instead, for a given type of sediment from a given site, laboratory studies have to be performed to investigate the dependence of entrainment on various parameters. We have performed entrainment studies in an annular flume, which

144

.

is a closed and non-flow through system, as shown in Figure 6.7(a) (Sheng and Lick, 1979; Fukuda, 1979; Sheng, 1981). A contained flow system is necessary since mechanical parts such as a pump may disrupt the sediment flocs and change the particle size distribution. The flume has a rotating top plate driven by a motor. The rotation causes a shear flow in the flume which in turn yields an applied shear stress on the bottom sediments. Variation of bottom shear stress with the rotational speed of the lid is shown in Figure 6.7(b). Entrainment of cohesive sediments from fresh-water environments (Table 6.1) and Mississippi Sound (Table 6.2) have been studied. Effects of (1) bottom shear stress, (2) properties of bed, (3) salinity of overlying water, and (4) sediment type on entrainment have been investigated. The primary interest was on the rate of entrainment, rather than just the critical shear stress at which initial entrainment occurs, as a function of various parameters.

Other Studies

In addition to us, several other investigators have conducted laboratory studies on the entrainment of cohesive sediments in the past. A few examples will be given here. Partheniades (1962) and Krone (1962) studied the entrainment and deposition of San Francisco Bay mud in a recirculating flume of rectangular cross-section. Raudkivi and Hutchinson (1971) used a highly compacted kaolinite clay at sea water salinity for their entrainment study. Christensen and Das (1973) studied the entrainment of kaolinite and grundite in a circular brass tube of 2.54 cm diameter. However, they and Partheniades both primarily used a remolded bed in their respective studies. Ariathurai and Arulanadon (1978) used a rotating annular cylinder, 10.2 cm in diameter with 1.3 cm wide annular space, to study the entrainment of consolidated sediments composed of 70% silica flour. Partheniades and associates have carried out some illuminating experiments in a rotating annular flume similar to the one used by us. Until very recently, they have primarily concentrated on the depositional behavior of cohesive sediments. More recently, Mehta and Parthaneides (1979) studied the erosional behavior of kaolinite in distilled water. Several others have performed laboratory studies on entrainment and deposition of various sediments in a wide variety of facilities with varying measuring devices and techniques. These variations make the intercomparison
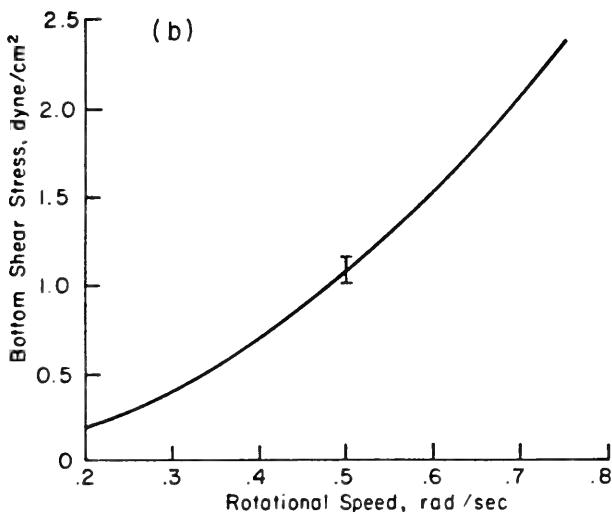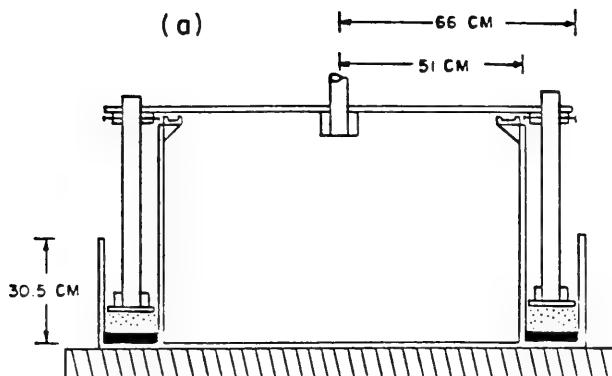
Figure 6.7. (a) Rotating laboratory flume for deposition-entrainment studies on sediments.

(b) Bottom shear stress within the flume as a function of the rotational speed of the rotating lid.

146

of different studies extremely difficult. For example, some used relatively crude instruments such as a strain gage to determine the bottom shear stress. In our studies, the bottom stress is derived from detailed flow measurements within the boundary layer.

Table 6.4

Composition of Fresh-Water Sediments
Used in Previous Entrainment Experiments

SEDIMENT TYPE	CLAY	QUARTZ	ALKALI FELDSPAR	DOLOMITE	CALCITE
Shale based	67.7%	21.8%	4.2%		
Western basin of Lake Erie	37.9%	30.4%	14.9%	12.7%	4.1%
Central basin of Lake Erie	33.7%	43.0%	17.5%	6.8%	
Pond	66.1%	27.4%	7.5%		

Despite its many advantages, rotating annulus flume usually contains secondary flow in the radial plane. The nature and strength of secondary flow depend strongly on flume configuration and flow Reynolds number. For flumes with relatively low aspect ratio, such as the one shown in Fig. 6.7(a), the secondary flow usually consists of a single circulation cell. At very high flume aspect ratio, Taylor-Goertler instability may lead to the occurrence of multiple circulation cells. A detailed quantitative study of secondary flow and its contribution to the entrainment and deposition of sediments is lacking and is much needed. Based on tangential flow measurements and boundary layer formulae, we found that the radial flow was generally less than 10% of the tangential flow in our flume with moderate rotational rates (<1 rad/sec.). A more detailed analysis can be performed by using a turbulent transport model in conjuction with skin friction and/or Reynolds stress measurement.

Table 6.5

Composition of Mississippi Sound Sediments
Used in Present Entrainment Experiments

SITE #(see Fig. 1.3)	1	2	3	4
POSITION				
LONG.	$89^{o}08.5$	$88^{o}26.1$	$88^{o}33.7$	$88^{o}46.5$
LAT.	$30^{o}16.6$	$30^{o}14.9$	$30^{o}20.4$	$30^{o}16.3$
DATE	9/25/80	9/28/80	9/25/80	9/25/80
% H_2O	60	70	75	20(?)
SAND	22	28	8	95
% SILT	31	21	29	1.6
CLAY	47	51	63	3.2
TYPE	SILTY CLAY	SANDY CLAY	CLAY	SAND
SMECTITE (MONTMORILLONITE)	79	78	68	58
% KAOLINITE	9	17	21	15
ILLITE	12	5	11	27
% TOC	1.148	1.061	2.575	2.040

Experimental Procedure

In most of our experiments, the procedure is as follows. Enough sediments are first mixed with water to make a slurry. The sieved slurry is then placed in the flume to achieve a 4 cm thick sediment bed. A constant depth of 7.6 cm of water is then filled on top of the sediments. The sediments are then completely resuspended and mixed by the rotating ring and allowed to settle and compact for a period between 1 to 10 days until it reaches the desired level of compactness. To perform the entrainment experiment, the ring rotation rate is set for a desired shear stress and

observations of the increase in suspended sediment concentration are then made. To minimize the spin-up effect, the constant shear stress is achieved by slowly increasing the rotation rate of the ring. When the applied shear stress is greater than the critical shear stress, entrainment of the sediments occurs. Suspended sediment concentration is measured at 5 min intervals until it reaches a steady-state or equilibrium value. The applied shear stress is then gradually increased to a higher value, and the increase in suspended sediment concentration is monitored as before. Ideally, this procedure could continue to higher and higher shear stresses until all the sediments are resuspended. In this study we have generally started with an applied shear stress of 1 dyne/cm^2 until a steady state is reached. The shear stress is then increased to 3 dyne/cm^2 until another equilibrium concentration is arrived. Finally, the shear stress is increased to 5 dyne/cm^2. These shear stresses are within the range of realistic shear stresses in the Mississippi Sound, as is evidenced by the results of our hydrodynamic model computations in previous sections.

In previous study by us and most other investigators, only one shear stress is applied in a single flume experiment. The present procedure of incrementing the shear stress in a single flume run results in significant saving of time and more realistic representation of the erosional events in nature. In a real estuarine or coastal environment, it is rare that the bottom shear stress would stay at the same value for an extended time period. Recently, a similar procedure was used by Parchure (1980) in studying the critical shear stress of kaolinite as a function of bed depth.

Typical Results

A typical variation of the suspended sediment concentration with time after the shear stress is applied is shown in Figure 6.8(a). Sediments from Site 1 of the Mississippi Sound were allowed to settle in the flume for one day before the shear stress was applied. At 1 dyne/cm^2, sufficient sediments are resuspended and reached an equilibrium concentration (C_{eq}) in less than two hours. As the shear stress was increased to 3 dyne/cm^2, C_{eq} increased from 530 mg/l to 14000 mg/l. C_{eq} reached 27000 mg/l at 5 dyne/cm^2. The equilibrium concentration at 1 dyne/cm^2 is smaller than that (3000 mg/l) for the shale based sediments in Table 6.2 which has a higher clay content
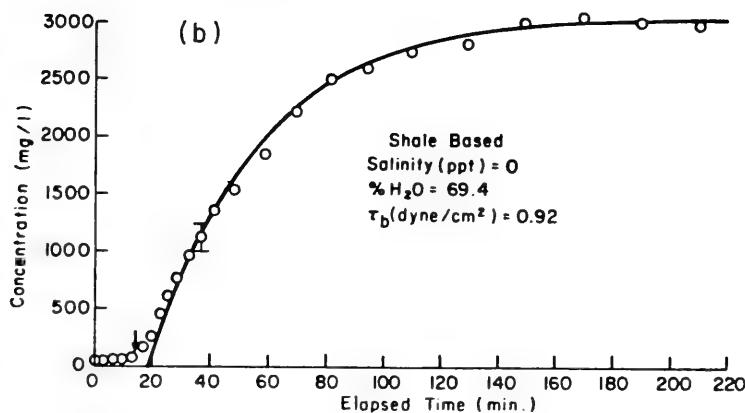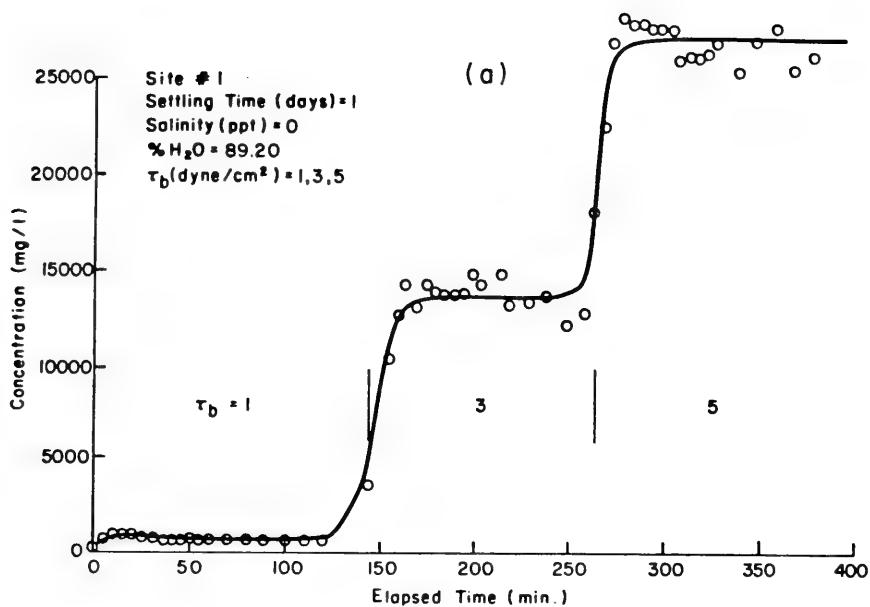
Figure 6.8. (a) Typical time history of suspended sediment concentration within the flume. Sediments from Site 1 of the Mississippi Sound and with 1 day settling

(b) Same as (a) except for shale-based sediments.

(Figure 6.8(b)).   It   should   be   pointed   out   that,   even   at   the   high
concentration of 27000 mg/l, only a small fraction of the bottom sediments are
eroded   from   the   bottom.   In fact, throughout our studies, we found that
entrainment of sediments is very much a surface phenomenon that takes place at
the   sediment   water   interface.   Consequently,   unless   exceedingly high bottom
stress takes place, bulk physical properties of even 1 cm below the initial
sediment-water interface may be largely irrelevant to most entrainment events.

Effect of Bottom Shear Stress

Similar experiments have been performed for sediments from other sites
with different settling time of sediments allowed. The effect of the bottom
shear stress on entrainment for all of our flume runs is summarized in Figures
6.9(a)   and   6.9(b)   for   fresh   water   conditions   and   salt   water   conditions,
respectively.

The critical shear stress for the Mississippi Sound sediment is on the
order of 0.8 dyne/cm^2.   As the bottom shear stress is increased from 1 to
5 dyne/cm^2, more than an order of magnitude increase in the equilibrium
concentration can be expected. Under normal range of applied shear stress,
the entrainment of cohesive sediment is generally not dependent on the bulk
properties   of   the   soil   such   as   bulk   shear   strength   or   plastic   strength.
Rather, the resistance to entrainment depends on the inter-floc strength of
sediments as modified by the physico-chemical and biological parameters within
the benthic boundary layer. At extremely high shear stress exceeding the bulk
shear strength of the sediment, the entire bed may fail and become entrained.

Effect of Bed Properties

One of the important parameters in characterizing the properties of the
surfacial sediments is the water content (or moisture content, or porosity)
which is directly related to the bulk density of the bed.   Attempts by some
previous investigators to correlate the shear strength of the bed with the
bulk density have not been satisfactory (Parchure, 1980).

In our studies, the bed is primarily prepared by allowing the sediment
slurry to settle within the flume for a time period between one to ten days.
Previous studies of Lake Erie sediments indicated that with longer settling
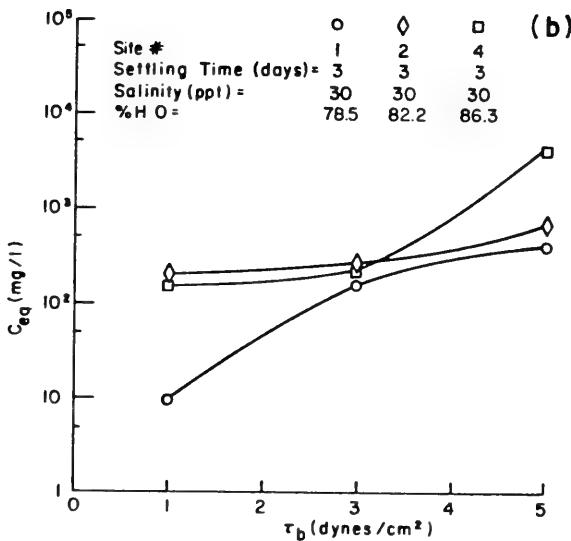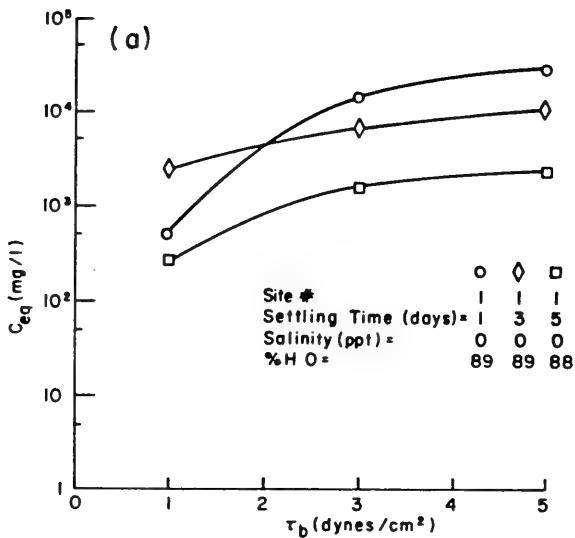
Figure 6.9.   (a)   Equilibrium concentration (C_{eq}) of suspended
                    sediments as a function of bottom shear stress (τ_b) in fresh
                    water.

              (b)   Same as (a) except in salt water.

time allowed, the water content decreases and the sediments become less erodable. In the present study of Mississippi Sound sediments, however, we have found that the water content of the sediments does not change appreciably with the settling time allowed. Despite this fact, the erodability of the sediments shows a decrease with the settling time. For the sediments from site 1, the settling time is allowed to increase from 1 day (Figure 6.8(a)) to 3 days and 5 days (Figure 6.10). The equilibrium concentration has dropped substantially with increasing settling time. The water content has only changed from 89.2% to 88.16%, a much smaller variation when compared with changes found in the Lake Erie study.

A similar trend has also been found for sediments from other sites in water of 30 ppt salinity. For example, the entrainment of Site 3 sediments for a 3-day settling and a 10-day settling are shown in Figures 6.11(a) and 6.11(b), respectively. In this case, the water content has actually increased slightly from 79% to 81%.

This trend is best summarized in Figure 6.12. It is clear that for the Mississippi Sound sediments, the erodability decreases with the settling time while the water content remains largely unchanged over a 10-day period. Hence the water content alone is not a good index of bed property. Some dynamic process which is present in both fresh and salt waters, is apparently responsible for this anomalous trend.

We have examined several possibilities to try to explain this trend:

(1) Compaction and increase of grain-grain contacts. This is not likely to occur since the entrained sediments are the very uppermost surfacial sediments and, as such, are not subject to any significant overburden pressure. Moreover, water content, even in the top 1 cm of sediments, does not change appreciably over the 10 day period.

The effect of overburden pressure on the entrainment process cannot be examined easily in a laboratory flume such as the one used for our study. The water column is only a few centimeters high in the experiment, while it is on the order of several meters or more in the field. To reproduce the overburden pressure experienced in the field

153
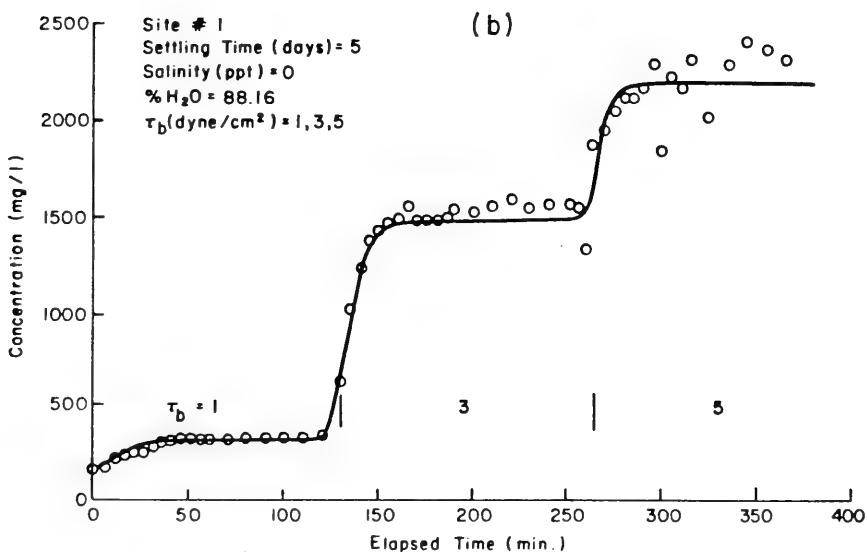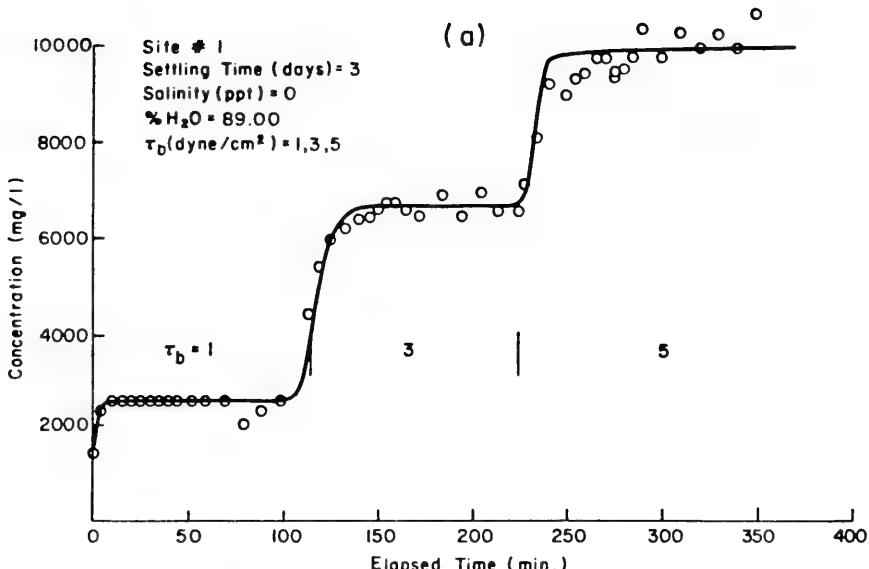
Figure 6.10. (a) Time history of suspended sediment concentration for Site 1 sediments in fresh water with 3 day settling.

(b) Same as (a), except with 5 day settling.
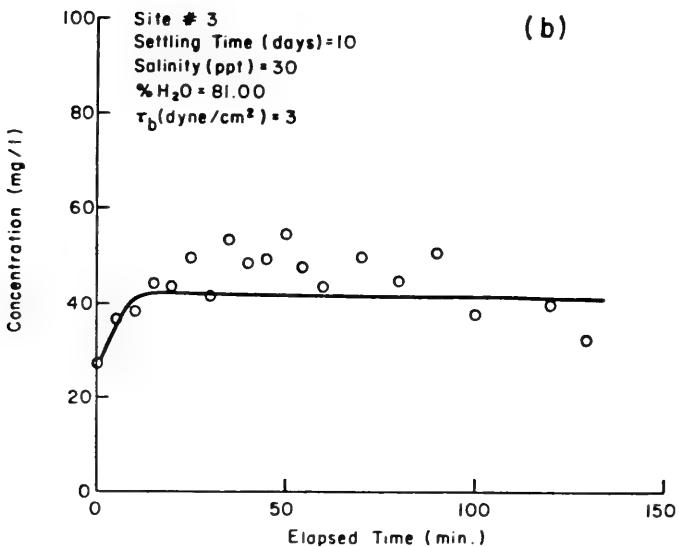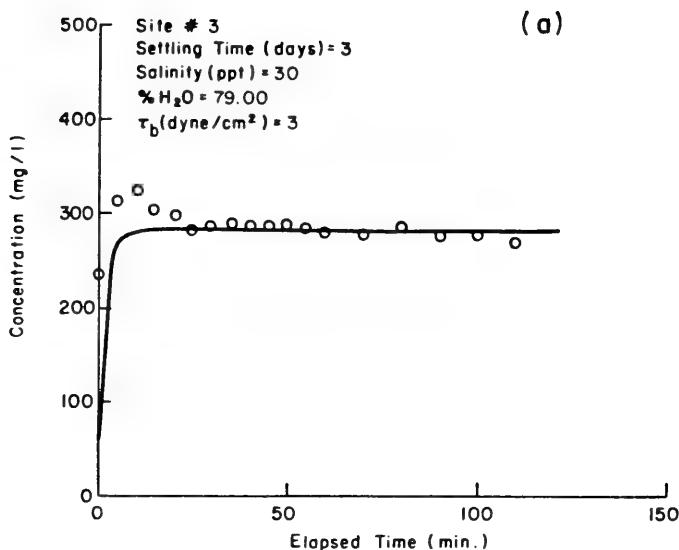
Figure 6.11. (a) Time history of suspended sediment concentration for Site 3 sediments in salt water with 3 day settling.

(b) Same as (a), except with 10 day settling.

condition, it would be necessary to generate a gravitational acceleration more than an order of magnitude of g. This would require a very different laboratory apparatus.

(2) Slow variation in clay properties (other than water content) with time. The influence of clay mineralogy properties on the entrainment of cohesive soils has been studied by several workers. Anderson (1951) claimed that Middleton's dispersion and erosion ratios are important indices in characterizing the erodability of sediments from 14 mountain watersheds in the Coastal Range of the United States. Smerdon and Beaseley (1959) concluded that plasticity index and dispersion ratio have pronounced effect on the critical shear stress of cohesive soils in open channels. Wallis and Stevan (1961) defined an erosion index in terms of cation exchange capacity. Krone (1963) related cation exchange capacity with Bingham shear strength. However, contradictory conclusions have been reported by the various workers (Kandiah, 1974). Moreover, none have examined the transient variation of the various clay properties of a given sediment type. It also seems highly unlikely that some clay properties would show the same transient behavior in two waters of vastly different salinity and ionic strength.

(3) Increase of microbial (algal, bacterial) exudates with time. The appearance and odor of the Mississippi Sound sediment samples, along with the relatively high organic content of some of the sediments, support this possibility. Actively growing bacteria and benthic algae are known to secrete micropolysaccharides that can bind fine-grained sediments (Rhoads, et al., 1978). This would decrease the erodability of the cohesive sediments. Bacteria growth increases in high organic environment and when the growth is not regulated by benthic organisms (macro-fauna). If the growth continues, the effect of bacteria and benthic algae may play a dominant role in determining the erodability of cohesive sediments. During this process, it may also render the water content of the sediments relatively unchanged with time.

In a natural environment, the bacteria growth in sediments is regulated by the presence of the benthic organisms and hence shows a seasonal variation. Grant (1981) has found a twofold change in the critical shear

.

stress for Long Island Sound sediments between winter and summer months. When the sediments are brought back to a laboratory, however, growth rate of bacteria may change because of the absence of the benthic organisms, thus resulting in a more resistable sediment structure. Before each of our flume runs, these sediments are sieved carefully to ensure that the binding effect of bacteria is reduced. However, the bacteria growth rate may increase again after the sediments are allowed to settle in the flume. Consequently, the longer the settling time is, the higher the bacteria content is and the less erodable the sediments become. In addition, the settling times of our flume runs (1 to 10 days) are comparable to the time scale of bacteria growth. The shape of the curve in Figure 6.12 also tends to support this possibility.

Being quite probable, this idea should be and can be tested by further experiments. Sterilized sediments can be added to the flume and bacterial growth monitored at the same time when entrainment of sediments is measured. In addition, a method for assaying microbial polysaccharide production could be used.

(4) Diffusion of chemical species from pure water and reaction at the surface. It could be possible for the chemical reaction to occur in waters of different salinity and ionic strength, and despite flushing of pore waters after each flume run. It needs to be tested by monitoring pore water concentration and by electromicroscope and microprobe analyses of the surface sediments.

Effect of salinity.

Typical effect of salinity on the erodability of Mississippi Sound sediments can be illustrated by comparing the entrainment results of Site 1 sediments in 0 ppt salinity water (Figure 6.8(a)) and in 30 ppt salinity water (Figure 6.13).

The critical shear stress in 30 ppt salinity water is much higher than that in the 0 ppt salinity water. In addition, the equilibrium concentration in the high salinity water is more than an order of magnitude smaller than that in the zero salinity water.

157
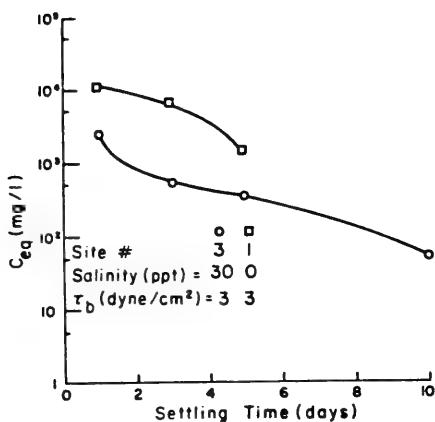
Figure 6.12.   Equilibrium concentration of suspended sediments as a
function of settling time in fresh and salt water.
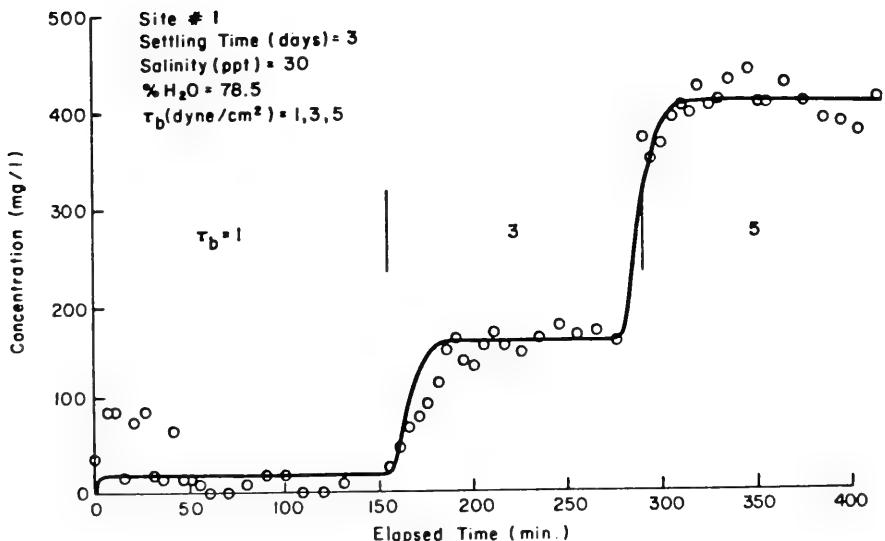
Figure 6.13.   Time history of suspended sediment concentration for
Site 1 sediments in salt water with 3 day settling.

The increased salinity of the overlying water and the pore fluid have apparently resulted in a more coagulated sediment structure, and a lower Sodium Adsorption Ratio (SAR), thus decreasing the erodability of the sediments. A higher settling speed and lower water content also contributed to the lower equilibrium concentration in high salinity water.

This trend is exactly opposite to that of the kaolinite. Yeh (1979) reported that the erodability of kaolinite decreased with the salinity of water. He also reported that kaolinite in higher salinity water formed a less densely packed bed with smaller flocs, thus resulting in higher erodability than the low salinity case. Kaolinite also has a much lower water capacity than smectite. Consequently, the variation of erodability with salinity for kaolinite is much less dramatic than for the smectite rich sediments used in our study.

Sediments from all four sites were tested for erodability in 30 ppt salinity water in our flume. Site 3 sediments were also run at an intermediate salinity value of 15 ppt. The effect of salinity on equilibrium concentration is summarized in Figure 6.14. It appears that much of the variation in erodability occurs between 0 ppt and 15 ppt salinity. A more precise functional relationship may be obtained if more flume runs are performed in this salinity range.

Effect of sediment type.

Site 2 sediments, having a higher clay content, are generally more erodable than sediments from other sites. Site 4 sediments, possessing the lowest clay content and the highest fraction of sand, appear to have a somewhat higher erodability than what it should have. This behavior is a result of the bed preparation procedure. During the settling stage, heavier sand particles settle to the bottom before the lighter clay particles or flocs. The result is that a graded bedding is produced. Much of the relatively high concentration of suspended sediments is due to the resuspension of the lighter clay particles or flocs at the surface of the bed. However, this will change somewhat if much higher shear stress is applied such that more sediments are resuspended from the bottom. This problem could be resolved by using a somewhat different procedure of bed preparation in future

159
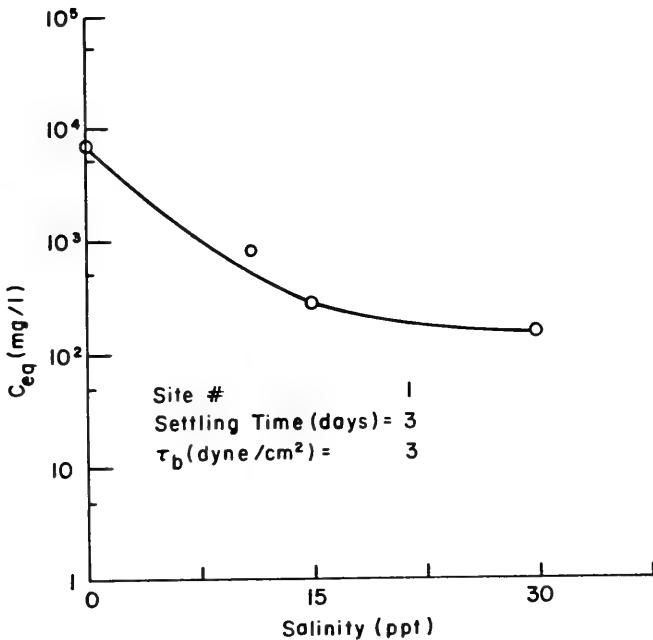
Figure 6.14.   Equilibrium concentration of suspended sediments as a function of salinity.

160

studies.

Our study confirmed that different clay minerals behave rather differently to changing environments. Alizadeh (1974) claimed that, under flocculated conditions, smectite shows higher critical shear stress than illite and kaolinite. Under dispersed conditions, however, kaolinite and illite are more resistant to entrainment than is smectite.

6.9 Deposition of Sediments

Deposition is the process by which suspended sediment particles leave the water column, temporarily or permanently, to become part of the bottom sediments. Similar process occurs in the atmosphere where atmospheric pollutants are deposited to the ground. Lewellen and Sheng (1980) performed a theoretical study on dry deposition of gaseous and particulate species in the atmosphere. Lewellen, Varma and Sheng (1972) analyzed the deposition model sensitivity. Although deposition of sediment particles is an important process affecting the ultimate fate of many pollutants, a comprehensive theoretical study has not yet been performed due to the complexity of the problem.

Deposition can be described in terms of a deposition velocity, v_d, defined as the flux of sediment particles divided by the suspended sediment concentration within the water column. Physically it is equivalent to the covariance of the turbulent fluctuations of the vertical velocity and the fluctuations of the particle concentration divided by the mean concentration. Since a concentration gradient is generally necessary to deliver a flux to the bottom, v_d is necessarily a function of the height at which the normalizing concentration is measured. Being a turbulent transport quantity, the deposition velocity depends on all of the hydrodynamic parameters affecting flow within the bottom boundary layer. It also depends on the particle coagulation process as affected by turbulence and cohesion. In addition, it depends on parameters such as detailed bottom roughness features, bottom chemistry, and benthic community which affect the bottom boundary condition.

161

Individual Resistances which Determine v_d

Deposition of sediment particles through the bottom boundary layer is influenced by the resistance of the various layers through which the particles must pass to reach the bottom. For ease of analysis, it is convenient to break up the boundary into three regions. The total resistance to deposition, defined as the inverse of the deposition velocity, is then the sum of resistances presented in each region.

$$v_d^{-1} = R_{hydrodynamic} + R_{sublayer} + R_{bottom} \tag{6.5}$$

$R_{hydrodynamic}$ represents the sum of the resistances to turbulent transport in the water column. $R_{sublayer}$ accounts for that resistance due to the thin, viscous, relatively laminar sublayer next to the bottom or the leaf surface of vegetation canopy. The third resistance is the chemical or biological resistance the particles encounter after they reach the bottom.

Hydrodynamic Resistance (R_h)

The hydrodynamic resistance to deposition can be estimated by considering the constant flux region above the bottom. This should be a reasonable approximation so long as the reference height for defining deposition velocity does not exceed approximately 100 cm.

The similarity solution which exists for the vertical gradients of velocity and particle concentration in the constant flux region can be integrated in the z direction to yield expressions for the hydrodynamic resistance which are a function of height z; bottom roughness height, z_0; stability, L^{-1}, expressed as the inverse of Monin-Obukhov length; and flow speed u at that height z. Since the resistance is inversely proportional to the flow speed, the product of the flow speed and the hydrodynamic resistance is presented. The results are shown in Figure (6.15) for three heights (1 cm, 10 cm, 100 cm) and three roughness heights (0.01 cm, 0.1 cm, 1 cm) covering the unstable range $(L^{-1} < 0)$, the neutral case $(L^{-1} = 0)$, and the stable range $(L^{-1} > 0)$.
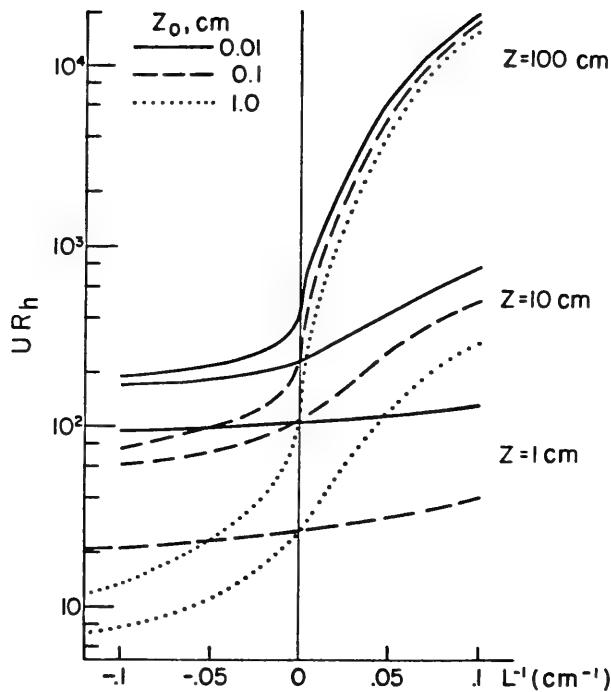
Figure 6.15. Hydrodynamic resistance to deposition as a function
of stability for three values of bottom roughness and reference
height.

Assuming a z_0 of 0.1 cm and a flow speed of 1 cm/sec at 10 cm above the bottom, Figure 6.15 shows that uR_h is about 100 at neutral stability. Thus the hydrodynamically induced deposition velocity is on the order of 0.01 cm/sec. In the presence of a stable stratification, the deposition velocity is decreased to a value of 0.0025 cm/sec when L is 10 cm. Unstable stratification, on the other hand, increases the deposition velocity to about 0.02 cm/sec when L is -10 cm. Increasing the bottom roughness, while keeping other parameters the same, the deposition velocity at 10 cm height can be increased by almost an order of magnitude.

Sublayer Resistance (R_s)

The deposition of sediment particles depends primarily on the particle diameter and particle density. The effects of particle density can be incorporated into the particle size by increasing the equivalent particle size. Particles ≤ 30 μm in radius tend to follow all of the turbulent eddies and can be diffused in the same manner as a gaseous species, except within the viscous sublayer next to a surface. Transport of particles in the sublayer is determined by three main contributions - Brownian motion, gravitational settling and inertial impaction.

For submicron size particles, Brownian diffusion dominates. Gravitational settling and inertia impaction dominate for particles with diameters of 10 μm or more. There is a transition range, for particles with diameters between 0.1 and 1 μm, wherein none of the mechanisms is very effective in bringing the particles across the sublayer. Lewellen and Sheng (1981) derived the following formula for deposition velocity within the sublayer:

$$v_d = c_f \left(\frac{D_B}{\nu}\right)^{0.7} + 0.1 \; c_f \; q \; \frac{u_*^2 \tau_r}{g} \; (1 - e^{-0.075 q^2 \tau_r / \nu}) + \tau_r g \qquad (6.6)$$

where c_f is a skin friction coefficient, D_B is the Brownian diffusion coefficient, q is the turbulence velocity, u_* is the friction velocity, and τ_r is the particle relaxation time. The three terms on the r.h.s. of (6.6) represent the effects of Brownian diffusion, inertial impaction, and gravitational settling, respectively.

The above formula has been compared with some data of particles deposited on the underside of a flat plate in the range where inertial impaction dominates (Lane and Stukel, 1978) in Figure 6.16(a). In Figure 6.16(b), this formula is compared with Sehmel's (1973) data for deposition on a smooth surface for particles in the transition regime. Both comparisons appear satisfactory. The deposition velocities shown in these figures are for particles settling in the atmosphere and hence are much bigger than those for sediment particles in water.

For cohesive sediments in marine water with a particle size distribution shown in Figure 6.2, Brownian diffusion is negligible for most of the particles. Inertial impaction and gravitational settling are the primary mechanisms for deposition through the sublayer. Gravitational settling velocity is a lower bound for the deposition velocity of these particles. In fresh water environment, however, smaller particles with diameters of 1 μm or less constitute a bigger fraction of the particle size distribution. A comprehensive formula like Equation (6.5) should yield an accurate estimate on the deposition velocity.

In the presence of a vegetation canopy, the analysis is more complicated. Simple constant flux relation (6.4) no longer holds within the vegetation canopy. The presence of the canopy introduces source and sink terms into the basic equations for momentum, heat, and species concentration. Lewellen and Sheng (1980) developed a model of turbulent flow within a canopy using a second-order closure model of turbulent transport (see Appendix D). Within the canopy, the total drag force has to be partitioned into a profile drag and a skin friction drag. Resistance to deposition within the sublayer next to the leaf surfaces can be incorporated into the canopy model to estimate the total canopy resistance to deposition. The deposition velocity within the canopy thus depends on the total leaf area per unit volume; the ratio of total wetted area to the projected frontal area; the Schmidt number of the species; the leaf surface resistance; flow speed above the canopy; and the stability above the canopy.

(a)

v_d/u_*

10^{-1}

10^{-2}

10^{-3}

10^{-4}

10^{-5}

.01   .1   1   10

$S^+ = \dfrac{\rho_p d_p^2}{18\mu} \dfrac{u_*^2}{\nu}$

○▲□●△▼ Lane & Stukel's data underneath a flat plate

$$\quad v_d = C_f\left(\frac{D_B}{\nu}\right)^{.7} + 0.1\,C_f\,q\,\frac{u_*^2\tau_r}{\nu}\,(1-e^{-.075q^2\tau_r/\nu}) + \tau_r\,g$$
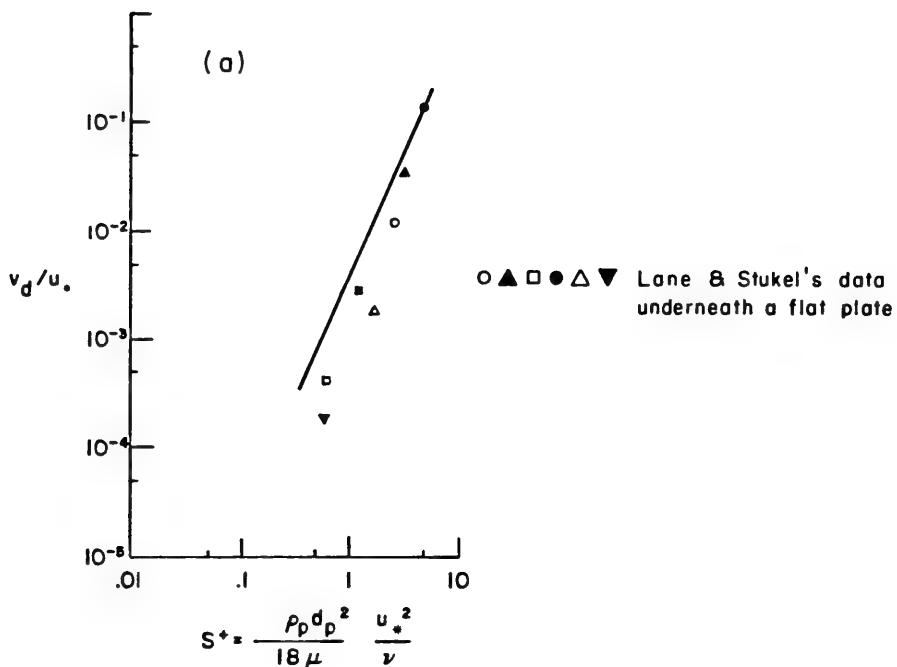
○   Sehmel's data on smooth brass surface (1973)

(b)

v_d (cm/sec)

10

1

.1

.01

.01   .1   1   10

$d\,(\mu m)$

$u_* = 0$
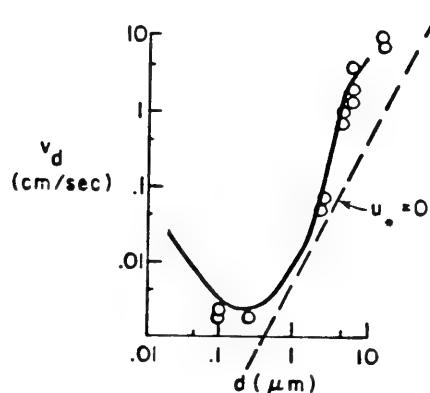
Figure 6.16.   Comparison of a deposition velocity model with data:

(a)   Lane and Stukel's data.

(b)   Sehmel's data.

166

Bottom Resistance

Physico-chemical and biological conditions at the bottom may affect the deposition of gaseous species once they reach the bottom. Blowing or suction due to the benthic organisms may affect the entrainment and deposition of particulate matter, respectively. These effects can only be included in the model empirically based on field or laboratory observations.

7. SIMULATION OF SEDIMENT DISPERSION WITHIN THE MISSISSIPPI SOUND

7.1 Mathematical Model

Equations and Boundary Conditions

The transport of sediments within the water column is described by the conservation equation for the suspended sediment concentration written in dimensional form as:

$$\frac{\partial C}{\partial t} + \frac{\partial (Cu)}{\partial x} + \frac{\partial (Cv)}{\partial y} + \frac{\partial [C(w+w_s)]}{\partial z} = \frac{\partial}{\partial x}\left(D_H \frac{\partial C}{\partial x}\right) + \frac{\partial}{\partial y}\left(D_H \frac{\partial C}{\partial y}\right)$$

$$+ \frac{\partial}{\partial z}\left(D_V \frac{\partial C}{\partial z}\right) + S \tag{7.1}$$

where C is the suspended sediment concentration, (u,v,w) are the three-dimensional fluid velocities in (x,y,z) directions computed from the hydrodynamic model, w_s is the vertical settling velocity of the sediments relative to the fluid, D_H and D_V are the turbulent eddy diffusivities in the horizontal and vertical directions, and S is a source term. The net vertical flux of sediments is specified at both the surface and the bottom:

$$- w_s C + D_V \frac{\partial C}{\partial z} = 0 \qquad\qquad @ \quad z = 0 \tag{7.2}$$

$$- w_s C + D_V \frac{\partial C}{\partial z} = v_d C - E$$

$$= v_d (C - C_{eq}) \qquad @ \quad z = -h(x,y) \tag{7.3}$$

where h(x,y) is the water depth, v_d is the deposition velocity, E is the rate of entrainment, and C_{eq} is defined as E/v_d. v_d and E are generally functions of many parameters, as described in the previous section.

Determination of Rate of Entrainment and Deposition Velocity

In our study, the values of E and v_d are determined from the laboratory flume studies. During the initial period of a laboratory experiment, only entrainment is present and little deposition takes place. Hence the rate of entrainment can be determined from the rate of increase of suspended sediment in the water column as:

$$E = \lim_{t \to 0} \frac{d}{dt} \int_{-h}^{0} C dz \qquad (7.4)$$

where -h is the water depth of the flume. As time increases, deposition also increases until eventually an equilibrium is reached between the entrainment and the deposition at the bottom of the water column, i.e.,

$$E = v_d C_{eq} \qquad (7.5)$$

Since E and C_{eq} are both known, v_d can thus be computed.

During most of our fresh water experiments, v_d was formed to be generally on the order of 0.005 cm/sec with no distinct trend of variation. v_d for salt-water experiments has been found to be on the order of 0.01 cm/sec. These values appear to be smaller than the median gravitational settling velocity as shown in Figure 6.2. Several factors could contribute to this discrepancy. First of all, the gravitational settling velocities in Figure 6.2 are measured in a settling cylinder with little turbulent mixing. The actual particle size distribution during the flume experiment could be quite different from that in the settling velocity measurement. However, no measurements on particle size or settling velocity distribution were made during the flume experiment. In addition, our analysis assumes the rate of entrainment does not vary with time during the entrainment process. In reality, however, the initial stage of entrainment usually leads to a large gradient in sediment concentration near the bottom. This causes an unstable density gradient and hence a smaller bottom shear stress and a smaller rate of entrainment. Towards the end of the experiment, when entrainment balances

·

deposition, suspended sediment concentration does not vary significantly over the water column. Hence the bottom shear stress and entrainment rate should be higher than those in the initial stage.

In a meso-scale sediment transport model, the deposition velocity v_d should depend on the location of the first grid point above the bottom. The inverse of the deposition velocity represents the sum of resistance through the various layers (constant flux layer and sublayer) between that point and the bottom. Laboratory experiments should be carried out to verify the theoretical formulation on deposition velocity as described in Section 6.9.

The rate of entrainment, E, however, exhibited distinct functional dependence on several parameters. For example, in a fresh-water study, Sheng and Lick (1979) found a bi-linear functional relationship between E and τ_b (Figure 7.1). Using this relationship for their sediment transport model, they were able to achieve reasonable agreement between model prediction and synoptic data obtained during an episodic event in Lake Erie.

The dependence of equilibrium concentration of the Mississippi Sound sediments on various parameters, as shown in the last chapter, can be transformed into relationships for the entrainment rates versus the various parameters. For example, for the site-3 sediment with a 1-day settling time, the dependence of E on τ_b is shown in Figure 7.2(a). For site-1 sediment with 3-day settling time, E versus τ_b is plotted in Figure 7.2(b). Although the critical shear stress is of similar magnitude in both cases, E is typically an order of magnitude smaller for the longer settling experiment. The effect of settling time on the entrainment rate is summarized in Figure 7.3(a). Thus, to allow accurate estimation of the entrainment rate in a coastal environment, it is extremely important to have a knowledge of the time history of the bottom sediments. Another parameter which can cause more than an order of magnitude variation in E is the salinity. This is illustrated in Figure 7.3(b).
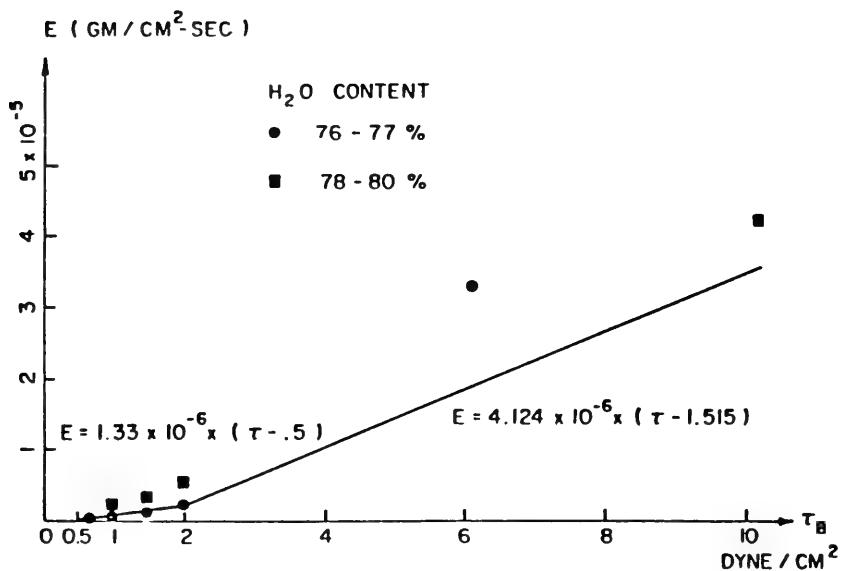
Figure 7.1.   Rate of entrainment of cohesive sediments in fresh water versus bottom shear stress.
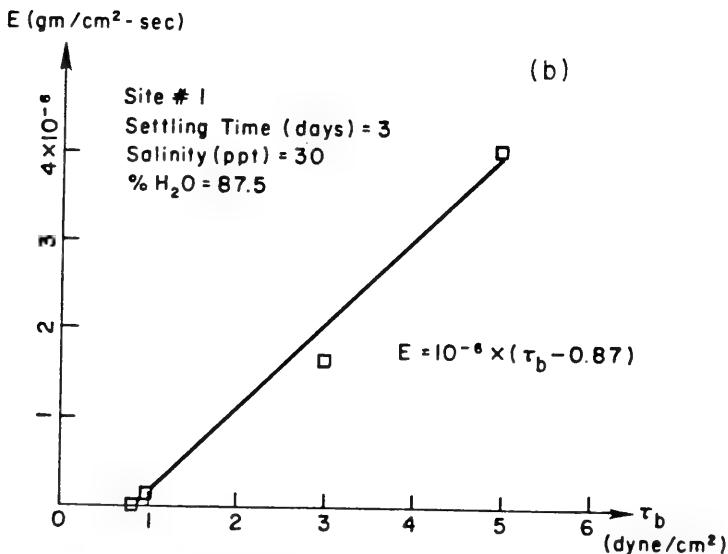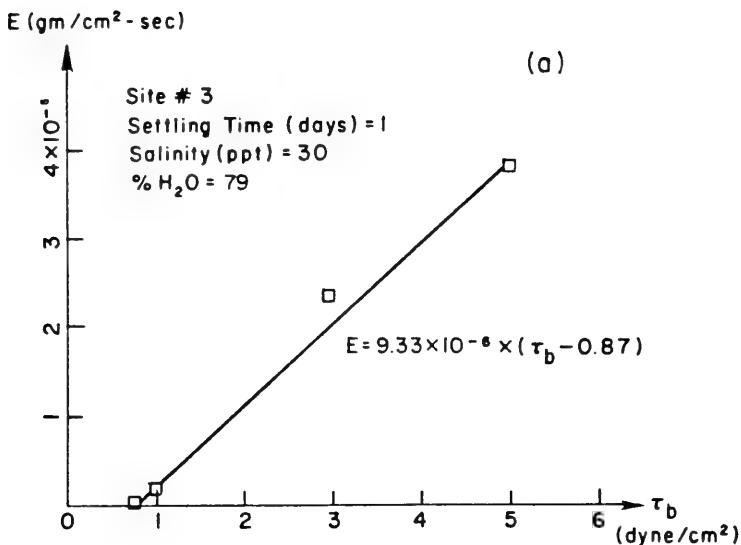
Figure 7.2.   Rate of entrainment of cohesive sediments in salt water versus bottom shear stress.

(a)   Site 3 sediments with 1 day settling.

(b)   Site 1 sediments with 3 day settling.
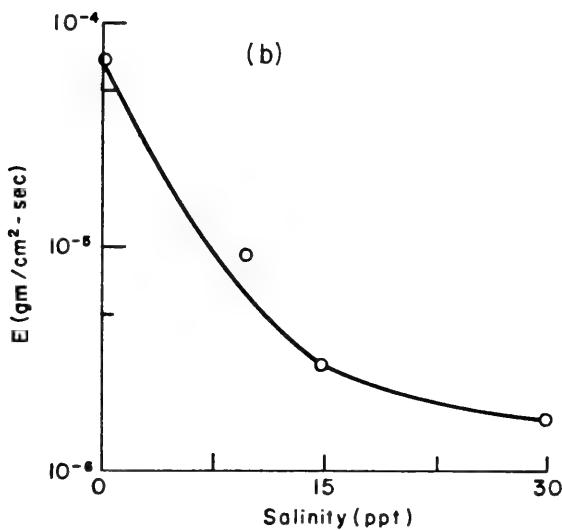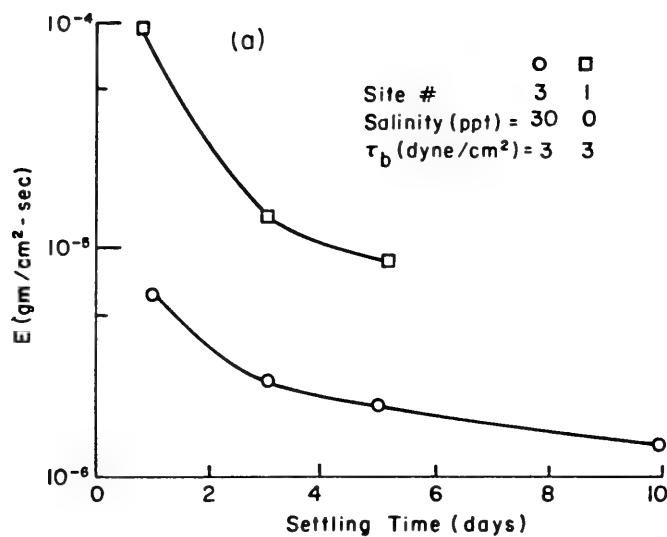
Figure 7.3. (a) Rate of entrainment as a function of settling time in fresh and salt water.

(b) Rate of entrainment as a function of salinity.

7.2 Sediment Dispersion Due to Tidal Currents

To examine the effectiveness of tidal currents in causing entrainment and transport of sediments in the Mississippi Sound, we have performed simulations based on the computed tidal currents during 4 Sept. to 5 Sept. 1980 as presented in Section 5.1.

Initially, (72 hours after 1 Sept. 1980) the suspended sediment concentration is assumed to be 500 mg/l within two 3 Km square areas, one in the middle of the Biloxi Channel and one in the middle of the Pascagoula Channel, and zero everywhere else. Sediment concentrations are then computed throughout a complete tidal cycle until the 96th hour. Four simulations are performed and described in the following.

The first simulation is concerned with the transport of a dissolved species by tidal currents. The settling velocity w_s is zero and the bottom boundary condition is that of zero net flux. The results at 24 hours later are shown in Figure 7.4. While the peak concentrations ($\sim$ 440 mg/l) are still located near their original positions, only a very small amount of the species have been transported out of the Sound. Due to vertical mixing, little difference exists between the species concentrations near the surface and near the bottom.

The second simulation is concerned with the transport of sediment particles with a settling velocity w_s of -0.05 cm/sec and a bottom boundary condition of zero flux. This idealized condition implies that there is a balance between entrainment and deposition of sediments at all locations and all times. Starting with the same initial condition as the first simulation, the results at 24 hours later are shown in Figure 7.5. Near the surface, the peak concentration has dropped to a little under 200 mg/l. Near the bottom, however, the peak concentration has increased to about 800 mg/l. Concentration distribution along the west-east transect in the Sound is shown in Figure 7.6. Appreciable variation in concentration exists in the vertical direction. A simple calculation indicates that the vertical settling time D/w_s, where D is the depth, is on the order of 1.5 hours and is comparable to the vertical diffusion time D^2/Av.

174
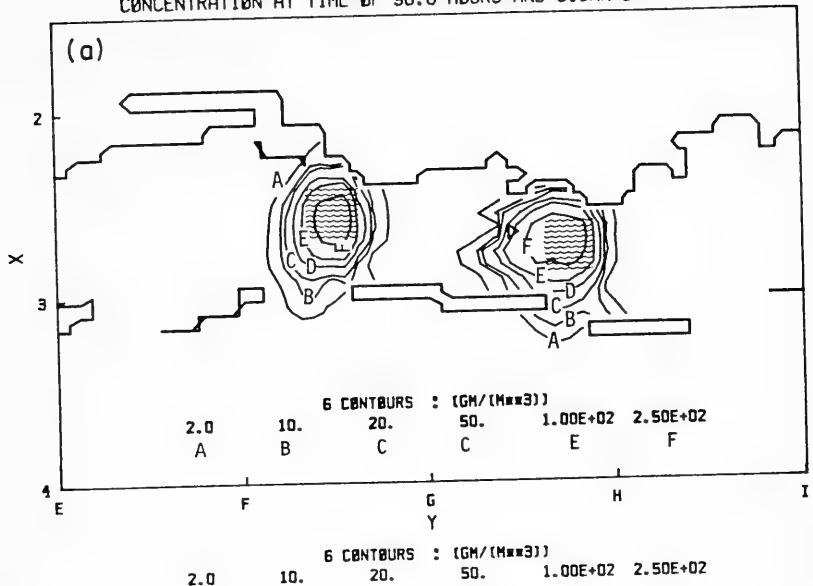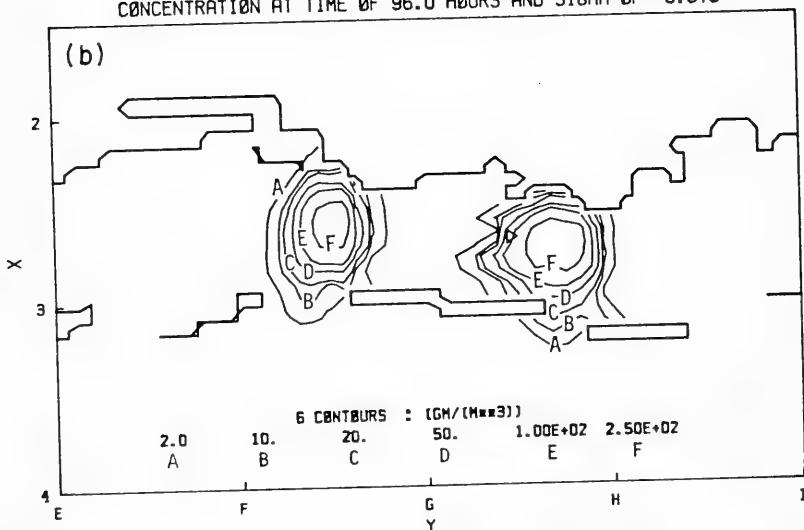
Figure 7.4. Suspended sediment concentration at the end of one complete tidal cycle on 9/04/80. No settling; Zero net flux at bottom. (a) Near-surface concentration, (b) Near-bottom concentration.

.
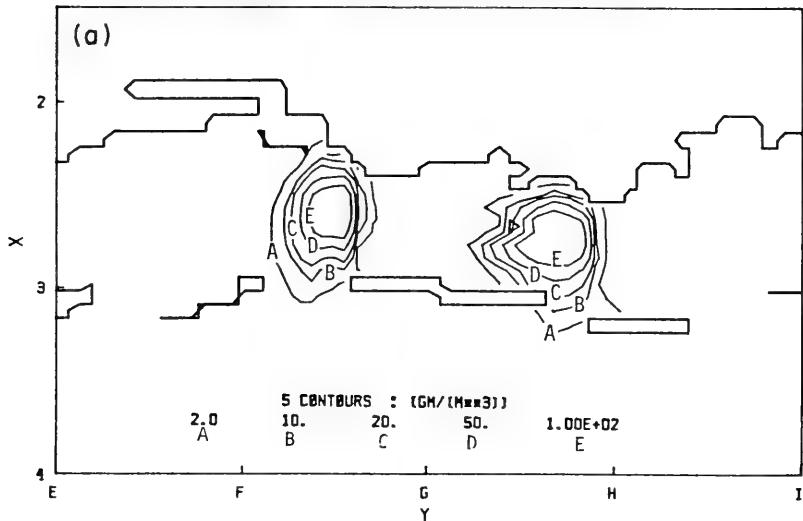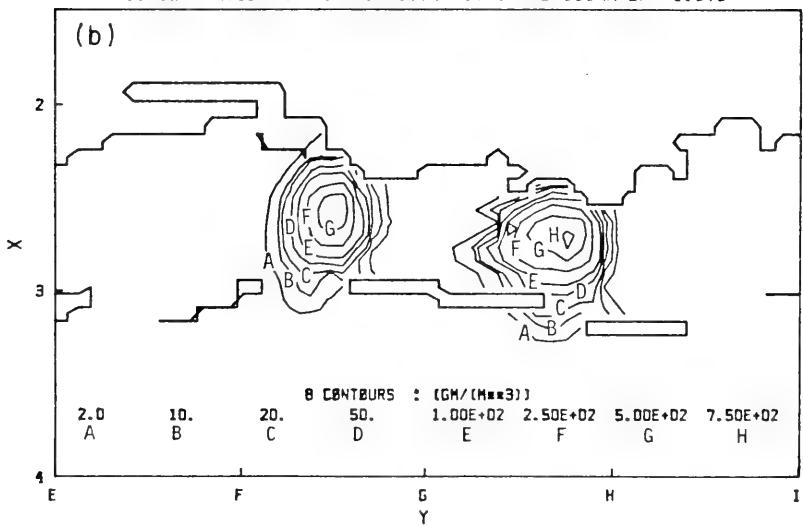
Figure 7.5.   Same as Figure 7.4 except that w_s=-0.05 cm/sec.
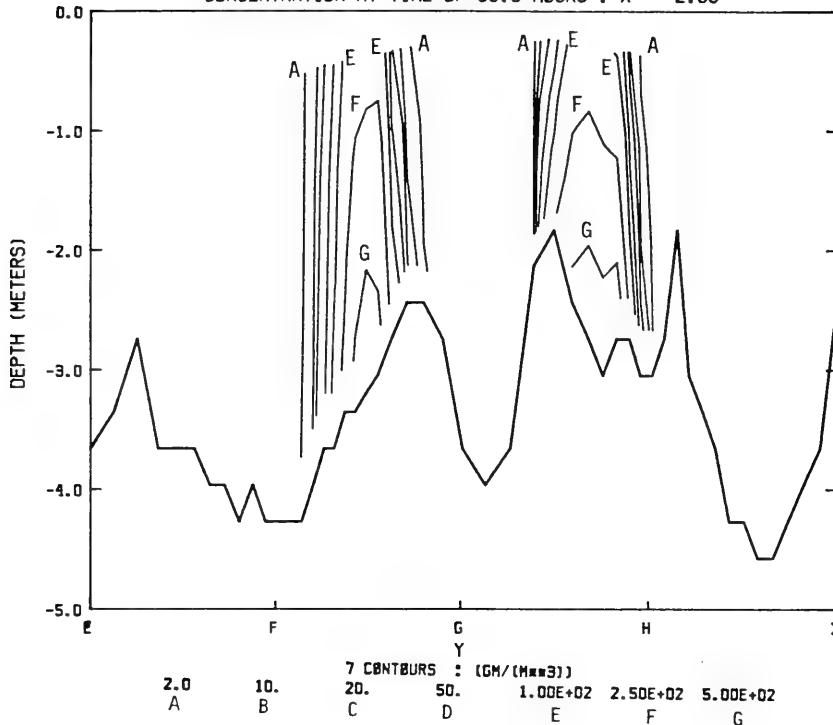
Figure 7.6.   Suspended sediment concentration within an east-west transect at the end of the tidal cycle.

In the third simulation, the sediment particles are assumed to have a settling velocity of -0.05 cm/sec and are allowed to be deposited and entrained at the bottom. However, entrainment is only allowed for the newly deposited sediments but not for the sediments which are at the bottom initially. This condition represents the limiting case when climate over the coastal environment has been rather calm over an extended time period such that the bottom sediments become highly resistable to entrainment. For the newly deposited sediments, the entrainment relationship as described in Figure 7.2 applies. A deposition velocity of 0.01 cm/sec is used. Starting with the same initial condition as the previous two simulations, most of the initial suspended sediments have settled out of the water column at 24 hours later. The peak concentration near the bottom is on the order of 10 mg/l (Figure 7.7) and is even smaller near the surface. Contours of thickness of deposited sediments at this time is shown in Figure 7.8. Maximum deposition of 0.15 cm has occurred. Little entrainment has occurred due to the relatively small bottom shear stresses generated by the tidal currents within the dumping areas. Bottom shear stresses at three locations in the Sound are shown in Figure 7.9. Although the stress at $(I,J)=(24,50)$ in the vicinity of the Biloxi Channel is on the order of 0.8 dyne/cm^2, it is not sufficient to cause entrainment of the newly deposited sediments.

For the fourth simulation, entrainment and deposition are allowed for both the newly deposited and the old sediments. The near-surface suspended sediment concentration at the end of 24 hours of simulation is shown in Figure 7.10. Maximum concentration is on the order of 1000 mg/l. The near-bottom sediment concentration is even higher. Net entrainment up to 1 cm has occurred in most of the tidal inlets (Figure 7.11) due to the high bottom shear stresses in these areas. This explains the fact why sediments found within the tidal inlets are generally composed of the coarser sand particles.

The difference between the results of this simulation and those of the previous simulation illustrates the significance of the time history of bottom sediments in affecting the entrainment process, and hence the ultimate suspended sediment concentration. After being left alone for an extended time period, sediments dumped in the low bottom stress area can form a thick mound, become extremely hard to entrain, and hence affect the local circulation

2 CONTOURS : (GM/(M**3))
2.0   10.
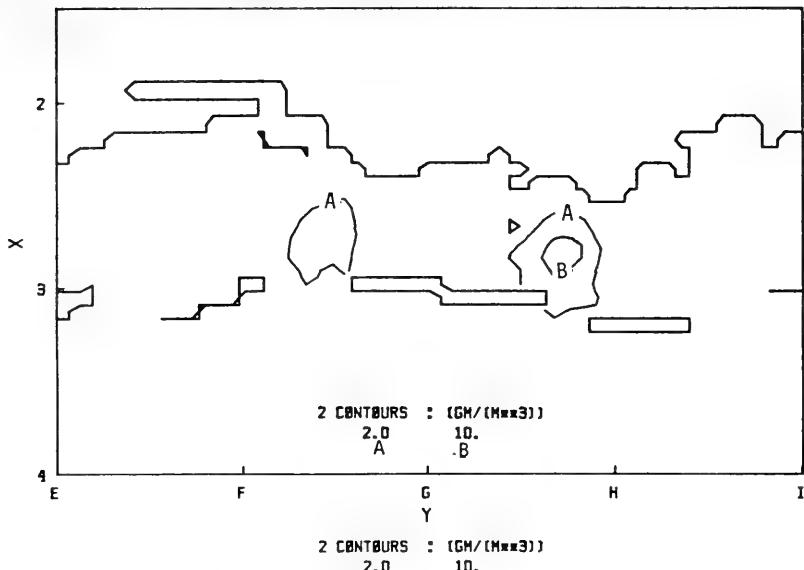
Figure 7.7.   Near-bottom suspended sediment concentration at the end
of the tidal cycle. w_s=-0.05 cm/sec;
Deposition and entrainment but no entrainment for the old
sediments.
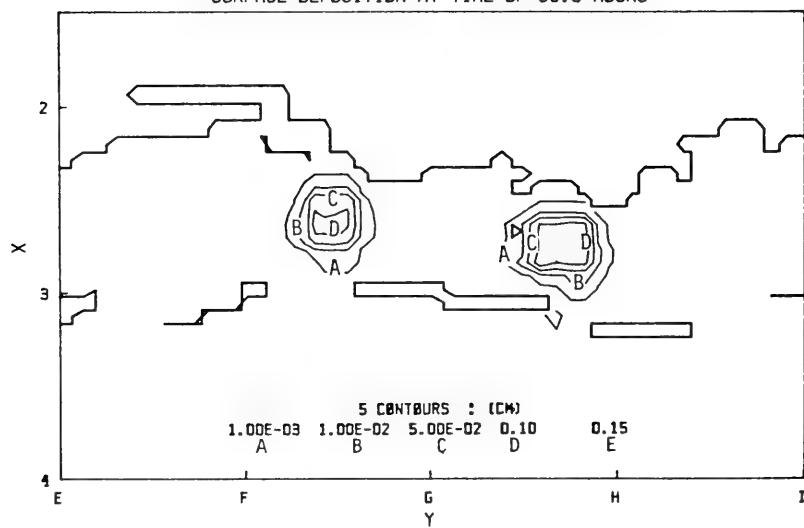
Figure 7.8.   Net thickness of deposited sediments at the end of the
tidal cycle corresponding to 7.7.
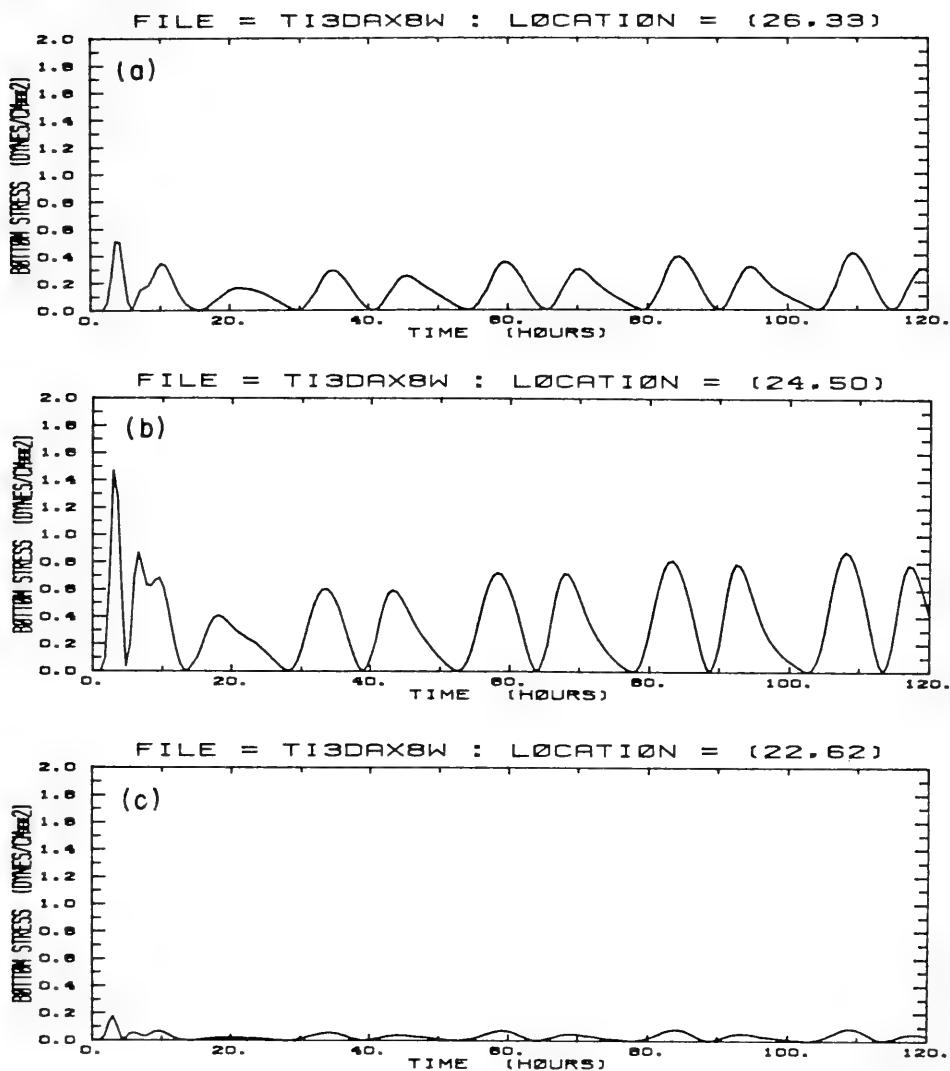
Figure 7.9. Tidally-induced bottom shear stress at three locations in the Sound.

MISSISSIPPI SØUND : FILE = SEDIAX7H
CØNCENTRATIØN AT TIME ØF 96.0 HØURS AND SIGMA ØF -0.125

9 CØNTØURS : (GM/(M**3))

| 2.0 | 10. | 20. | 50. | 1.00E+02 | 2.50E+02 | 5.00E+02 | 7.50E+02 | 1.00E+03 |
| A | B | C | D | E | F | G | H | I |
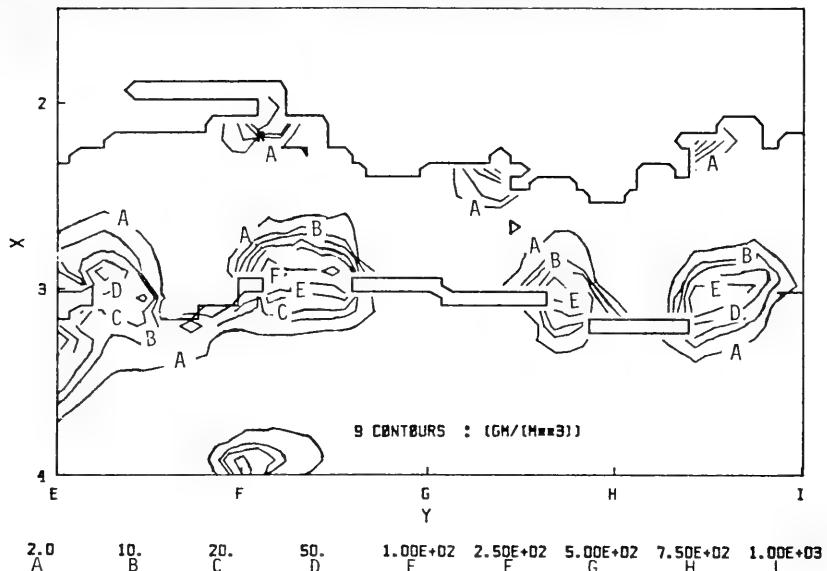
Figure 7.10.   Near-surface concentration at the end of the tidal cycle.
W_s=-0.05 cm/sec;   Deposition and entrainment for all sediments.

MISSISSIPPI SØUND : FILE = SEDIAX7H
SURFACE DEPØSITIØN AT TIME ØF 96.0 HØURS

6 CØNTØURS : (CM)

| -1.0 | -0.50 | -0.10 | -5.00E-02 | 5.00E-02 | 0.10 |
| A | B | C | D | E | F |
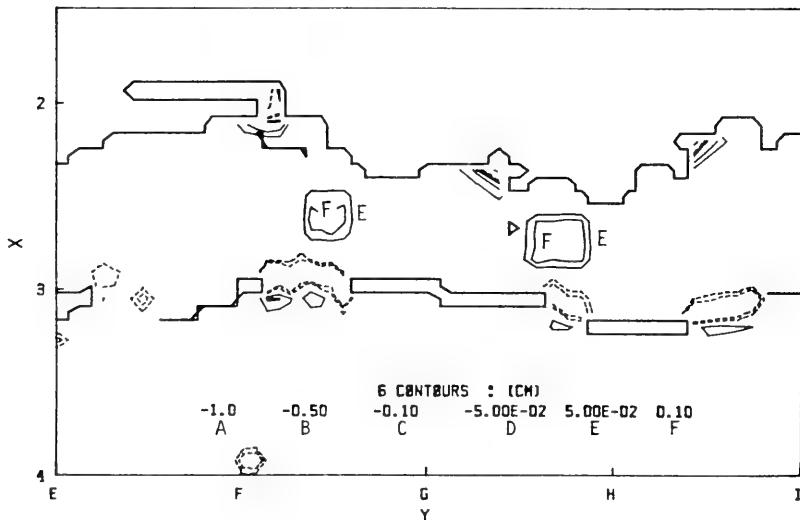
Figure 7.11.   Net thickness of deposited sediments at the end of the
tidal cycle corresponding to 7.10.

181

patterns.

7.3 Sediment Dispersion Due to Wind-Driven Currents

We now present the results of sediment transport simulations under the action of wind-driven currents due to a westerly wind as discussed in Section 5.2. All simulations start with an otherwise zero concentration field and a 500 mg/l concentration within a 3 Km square area in the Biloxi Channel. Results at the end of 24 hours are shown for three simulations: (1) a dissolved species with zero settling and zero net flux at the bottom, (2) sediments with settling (w_s=-0.05 cm/sec) and deposition (v_d=0.01 cm/sec) but entrainment for the newly deposited velocities only, and (3) sediments with the same settling and deposition velocities while entrainment allowed for both the old and new sediments.

For the first case, the concentration distribution at a constant depth of 0.5 m is shown in Figure 7.12(a). Due to the relatively strong wind-driven currents, center of the initial species concentration distribution has moved towards the East by almost 20 Km.

For the second simulation, deposition prevails and the suspended sediment concentration at 24 hours later is on the order of 20 mg/l or less (Figure 7.12(b)). Net deposition up to 0.1 cm is found in Figure 7.12(c). When entrainment is allowed for all the sediments, as shown in Figure 7.12(d), simulation, suspended sediment concentration up to 1000 mg/l is possible within the Sound. As shown in Figure 7.12(e), net entrainment up to 2 cm is found off the Pascagoula Channel and in other shallow areas. Although entrainment is found in the area immediately off the West Pascagoula River, field studies have reported the formation of a mound there. The formation of the mound has apparently taken place during time periods when relatively low wind existed in the Sound. With the increased compaction of bottom sediments, the mound had become much harder to entrain than the entrainment relationship used in the present simulation.
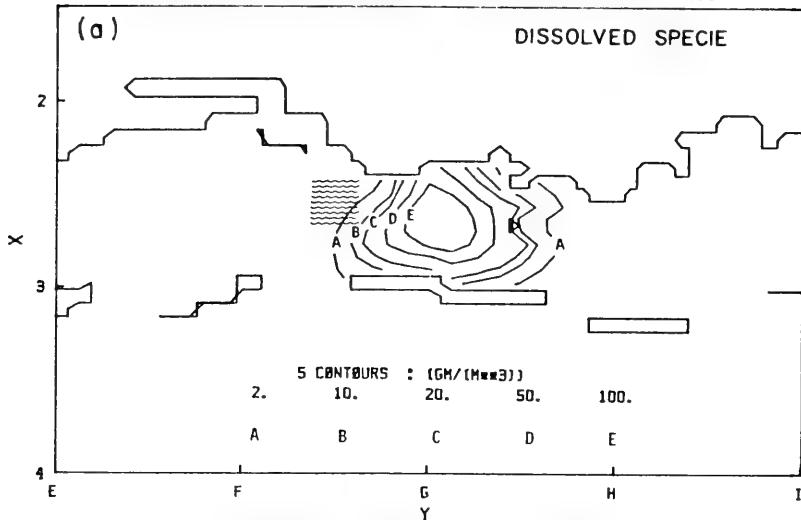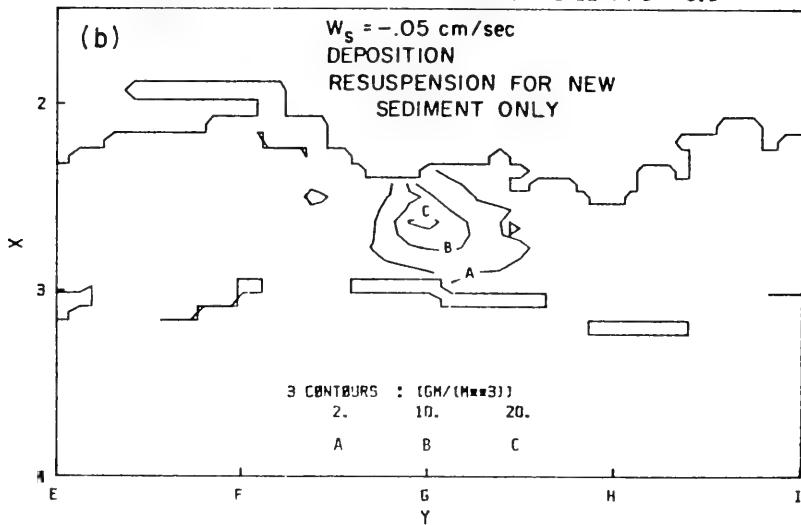
Figure 7.12. (a) Suspended sediment concentration at 0.5 m depth at the end of one day simulation. Westerly wind; No settling; Zero net flux at bottom.

(b) Same as (a) except that W_s=-0.05 cm/sec; Deposition and entrainment but no entrainment for the old sediments.

MISSISSIPPI SØUND : FILE = SEDIAX4G
SURFACE DEPØSITIØN AT TIME ØF 24.0 HØURS
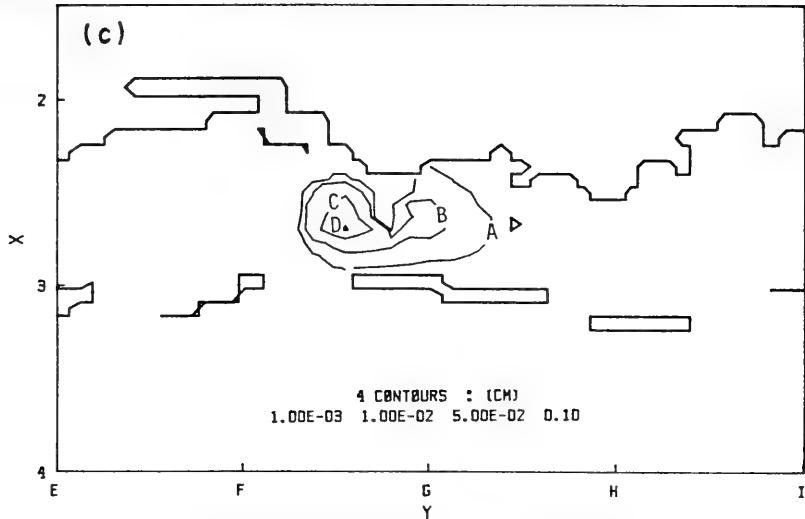
(c)

4 CØNTØURS : (CM)
1.00E-03 1.00E-02 5.00E-02 0.10

MISSISSIPPI SØUND : FILE = SEDIAX4H
CØNCENTRATIØN AT TIME ØF 24.0 HØURS AND DEPTH ØF 0.5 M

(d) W_s = −.05 cm/sec
        DEPOSITION
        RESUSPENSION

9 CØNTØURS : (GM/(M∗∗3))

2.	10.	20.	50.	100.	250.	500.	750.	1000.
A	B	C	D	E	Γ	G	H	I
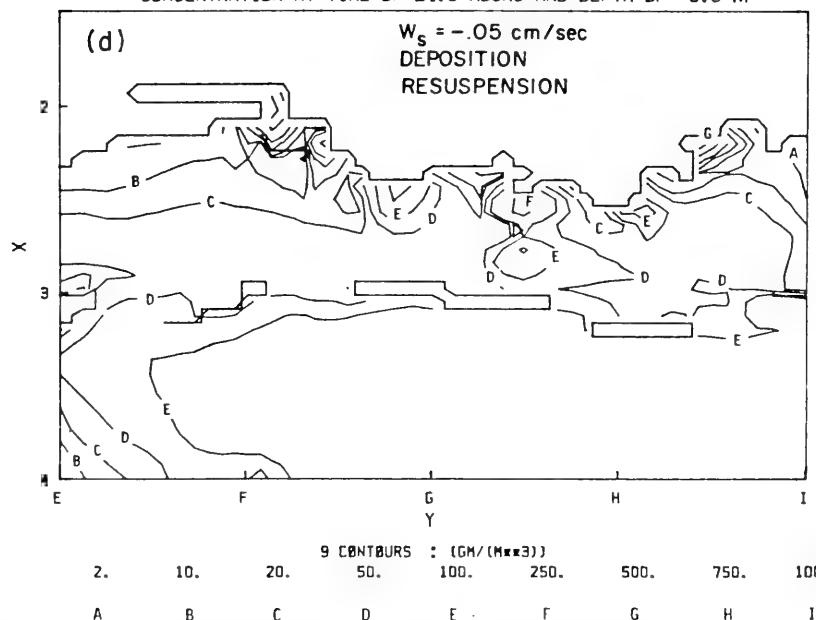
Figure 7.12. (c) Net thickness of deposited sediments at the end
                   of 1 day simulation corresponding to (b).

              (d) Same as (b) except that deposition and entrainment allowed
                   for all sediments.

184

MISSISSIPPI SØUND : FILE = SEDIAX4H
SURFACE DEPØSITIØN AT TIME ØF 24.0 HØURS

(e)

B CØNTØURS : (CM)

| -2.0 | -1.0 | -0.50 | -0.10 | -5.00E-02 | 5.00E-02 | 0.10 | 0.50 |
| A | B | C | D | E | F | G | H |
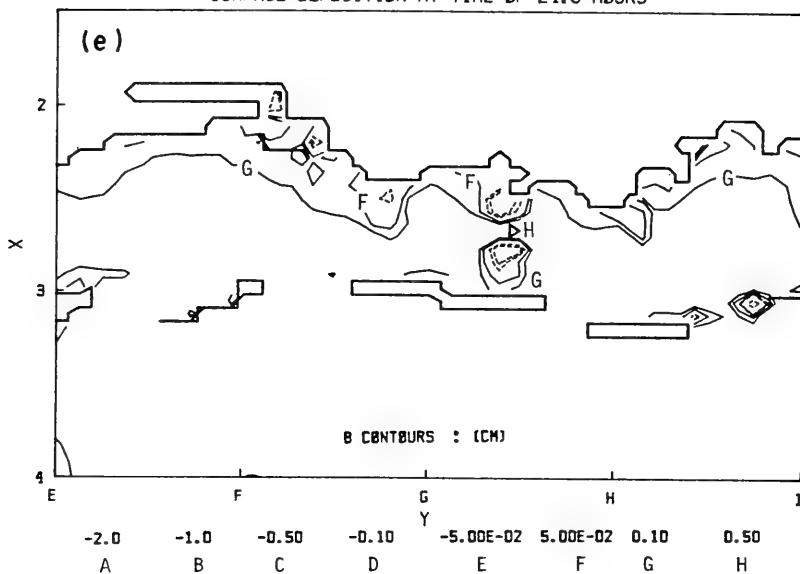
Figure 7.12. (e) Net thickness of deposited sediments at the end of 1 day simulation corresponding to (d).

7.4 Wave Effect on Sediment Dispersion

Wave Modeling

In addition to the tidal currents and wind-driven currents, bottom orbital currents induced by wind waves in the Sound can cause entrainment of the bottom sediments. The wind waves in the Sound have been studied by using a spectral wave hindcasting model (Resio and Vincent, 1977) modified for shallow water environment. Basically, wave energy in the Sound is assumed to be derived completely from within the system. While some energy may actually come into the Sound from the Gulf through the tidal inlets, this appears to be a reasonable assumption since most of the incoming waves may break outside the barrier islands before entering the Sound. Some results are presented in the following.

Figure 7.13 shows the area of wave study containing locations of the various stations. Wind data during September 1980 were recorded at four meteorological stations (MET 1, MET 2, MET 3, and MET 4) in the area. Two types of simulations were performed. The first simulation combines the hourly winds at these stations to compute an average wind for the entire Sound. The second simulation takes into account the variation of wind over the water and computes a wind velocity for each of the numeric wave stations. The second simulation generally results in somewhat higher waves and stronger bottom orbital currents than the first simulation, but contains more uncertainty with regard to the nature of over-water wind variation. For simplicity, we will only present results obtained with the uniform wind.

Wave Climate and Bottom Stresses During 9/20/80 to 9/25/80

The detailed wind velocity during 20 September through 26 September 1980 is shown in the stick diagram, Figure 7.14. Relatively mild winds are generally from the southeast except during a few hour period on September 4. Significant heights at stations 8, 10, and 17 are shown in Figure 7.15 and are generally less than 1 ft. Wave periods at all the stations, as shown in Figure 7.16, are generally on the order of 3 seconds or less.
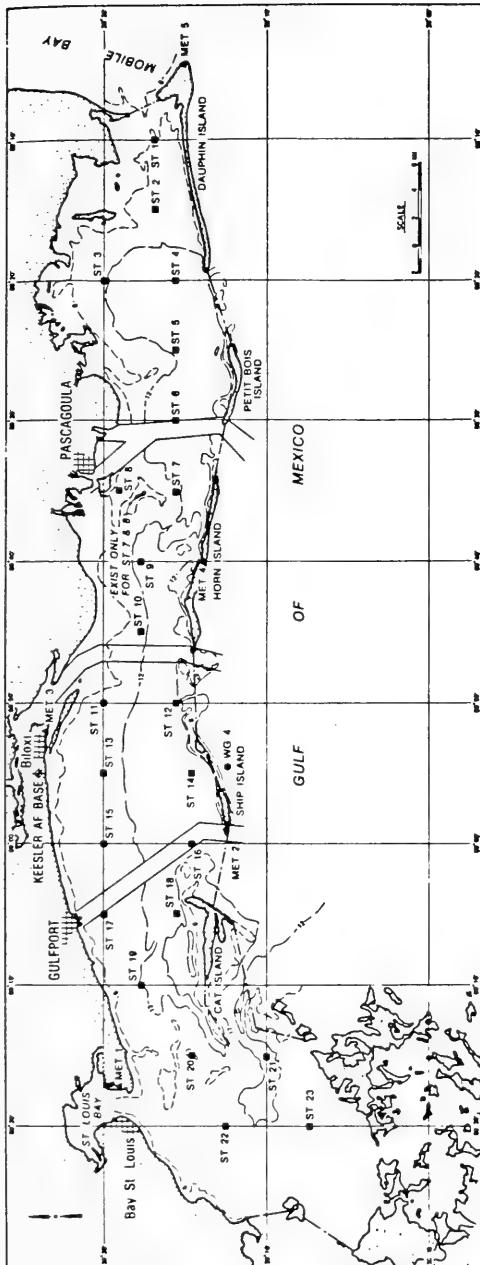
Figure 7.13. Location of stations included in studying the wave climate of the Sound.

SURFACE WINDS FOR 9/20 - 9/24

5.79E+00 (M/S)
MAXIMUM VECTOR
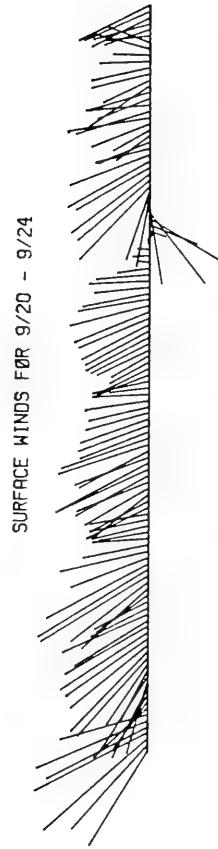
Figure 7.14. Stick diagram of wind velocities in the Sound during 9/20/80 to 9/25/80.

187
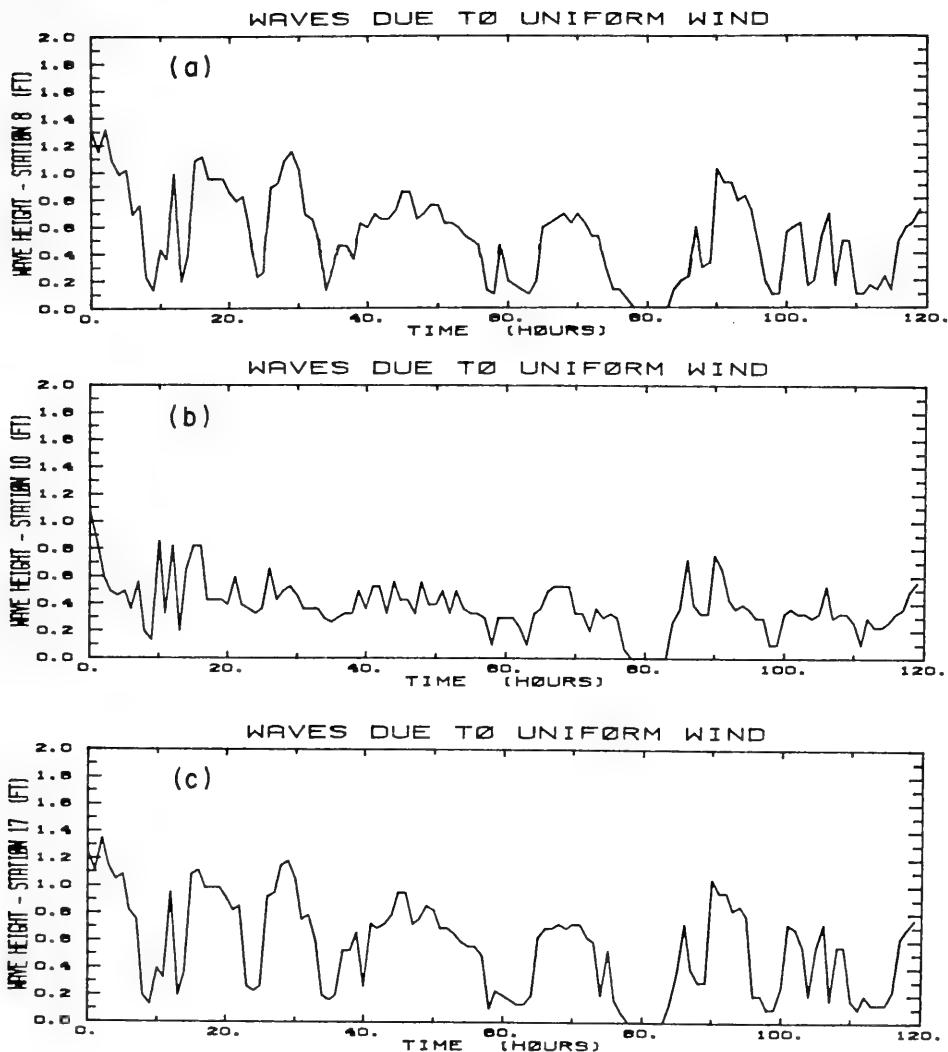
Figure 7.15. Computed wave height at three stations during 9/20/80 to 9/25/80.
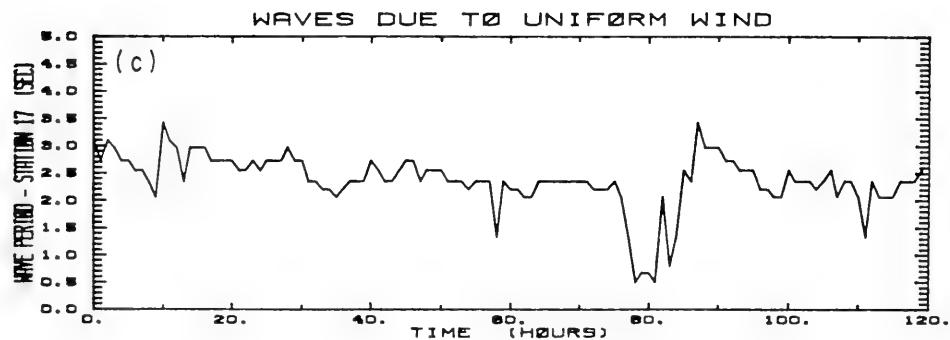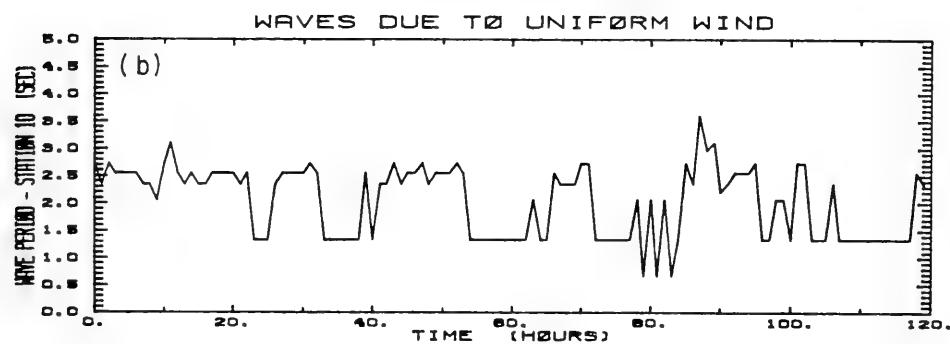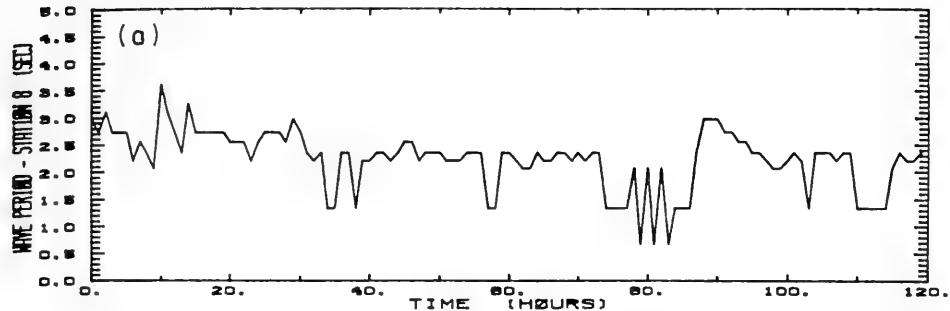
Figure 7.16.   Computed wave period at three stations during 9/20/80
to 9/25/80.

.

The bottom orbital currents due to these waves could be computed from linear wave theory and taking into account of the local water depths. Figure 7.17 shows the maximum bottom orbital currents at stations 8, 10, and 17. The currents are much stronger at stations 8 and 17 in the immediate vicinity of the north shore, while rather weak at station 10 in the middle of the Sound.

Bottom shear stresses at these stations, averaged over the wave cycles, are shown in Figure 7.18. Average bottom stresses at stations 8 and 17 are on the order of 3 dyne/cm^2, but less than 1 dyne/cm^2 at station 10. Bottom shear stresses due to the tidal currents at the same time period are shown in Figure 7.19. At the same station, the tide-induced bottom stresses are generally an order of magnitude smaller. The bottom shear stresses due to the combined effects of tidal currents and wind-driven currents are somewhat stronger and are shown in Figure 7.20. For the mid-Sound station, the tide- and wind-induced bottom stress is comparable to the wave-induced stress and both may contribute to the entrainment of sediments. For the north-shore stations, however, the wave-induced stress is still an order-of-magnitude stronger. Entrainment of sediments at these stations would primarily result from the wave effect.

Wave Climate and Bottom Stresses During 9/01/80 to 9/10/80

The wave climate and wave-induced bottom stresses during 1 September to 10 September 1980 are also computed. As shown in Figure 7.21, the wind velocity shifted from mild southeasterlies to strong northeasterlies and then to strong easterlies, before it diminished eventually. The significant wave heights at stations 8, 10 and 17 during this period are shown in Figure 7.22. High waves up to 3 feet occurred during 3 September to 5 September. The wave-induced stresses, as shown in Figure 7.23, increased substantially from the middle of 3 September. Due to the increasing fetch associated with the easterly winds, the bottom stresses become increasingly stronger from station 8 to station 10 and station 17.

Computations on wave heights and wave periods presented above were obtained by means of a spectral wave model. The results were found to be generally higher than those obtained from the SMB model (CERC, 1973), which is

190
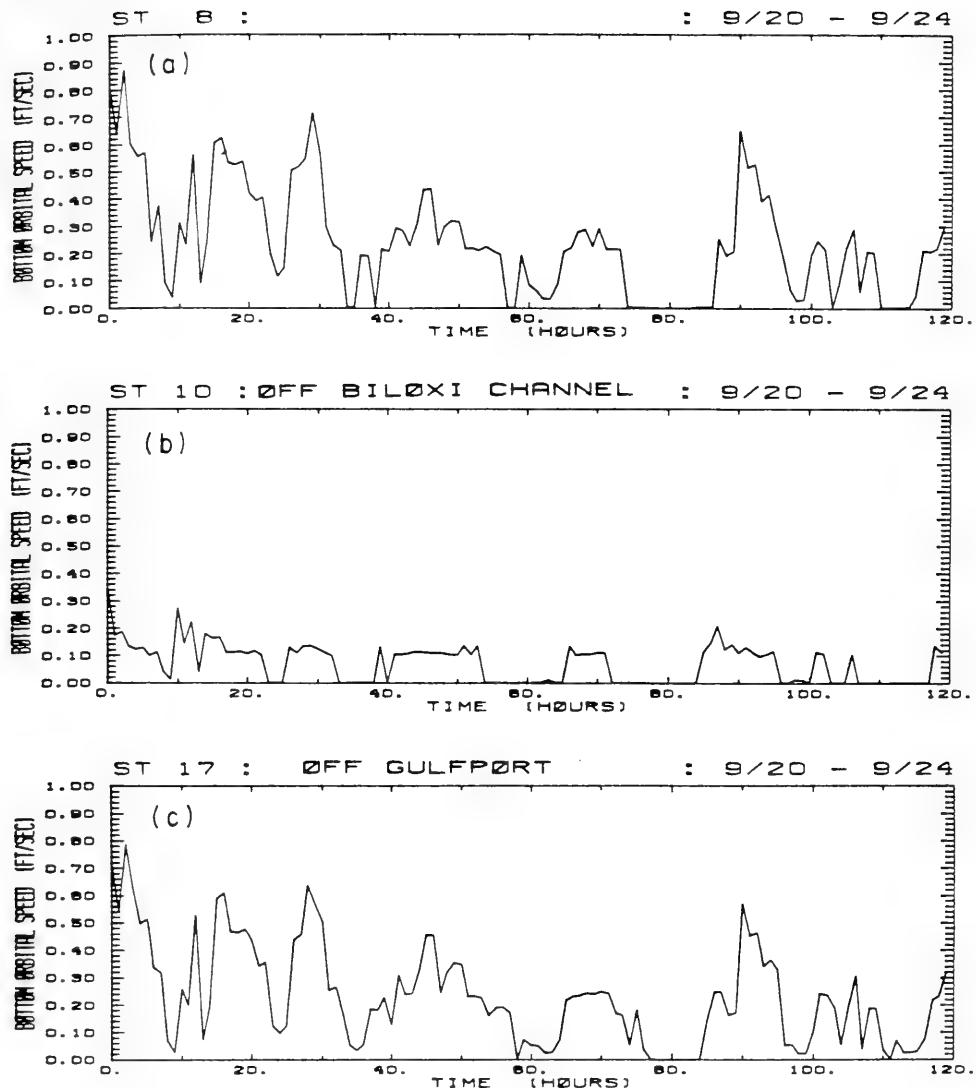
Figure 7.17. Bottom orbital speed at three stations during 9/20/80 to 9/25/80.
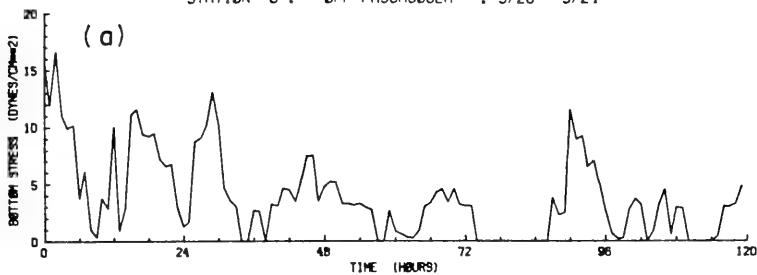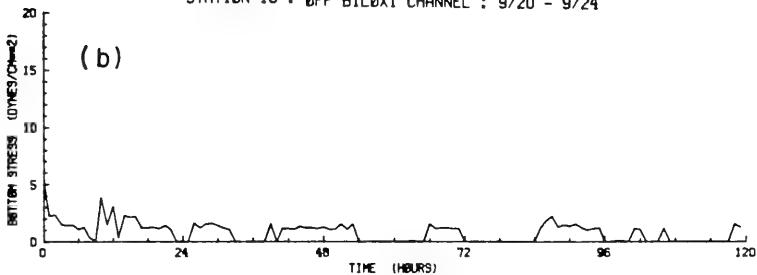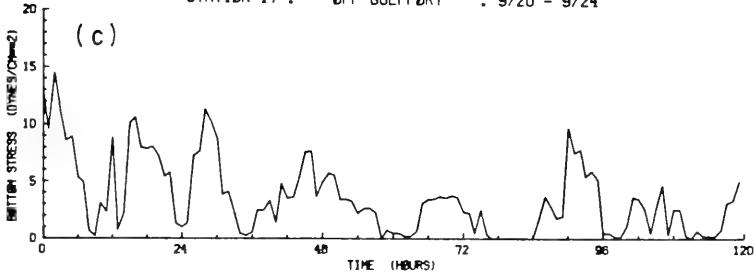
Figure 7.18. Wave-induced bottom stress at three stations during 9/20/80 to 9/25/80.

.
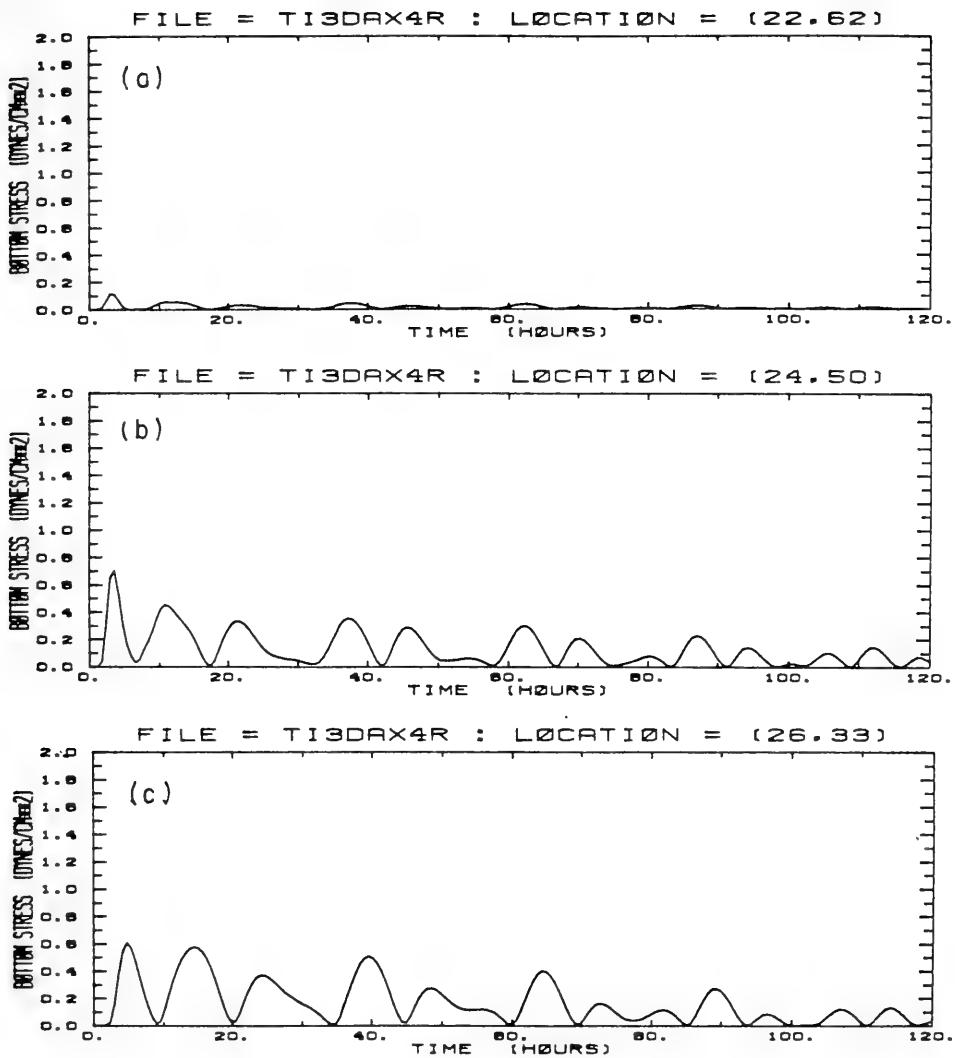
Figure 7.19. Tide-induced bottom stress at three stations during 9/20/80 to 9/25/80.

193
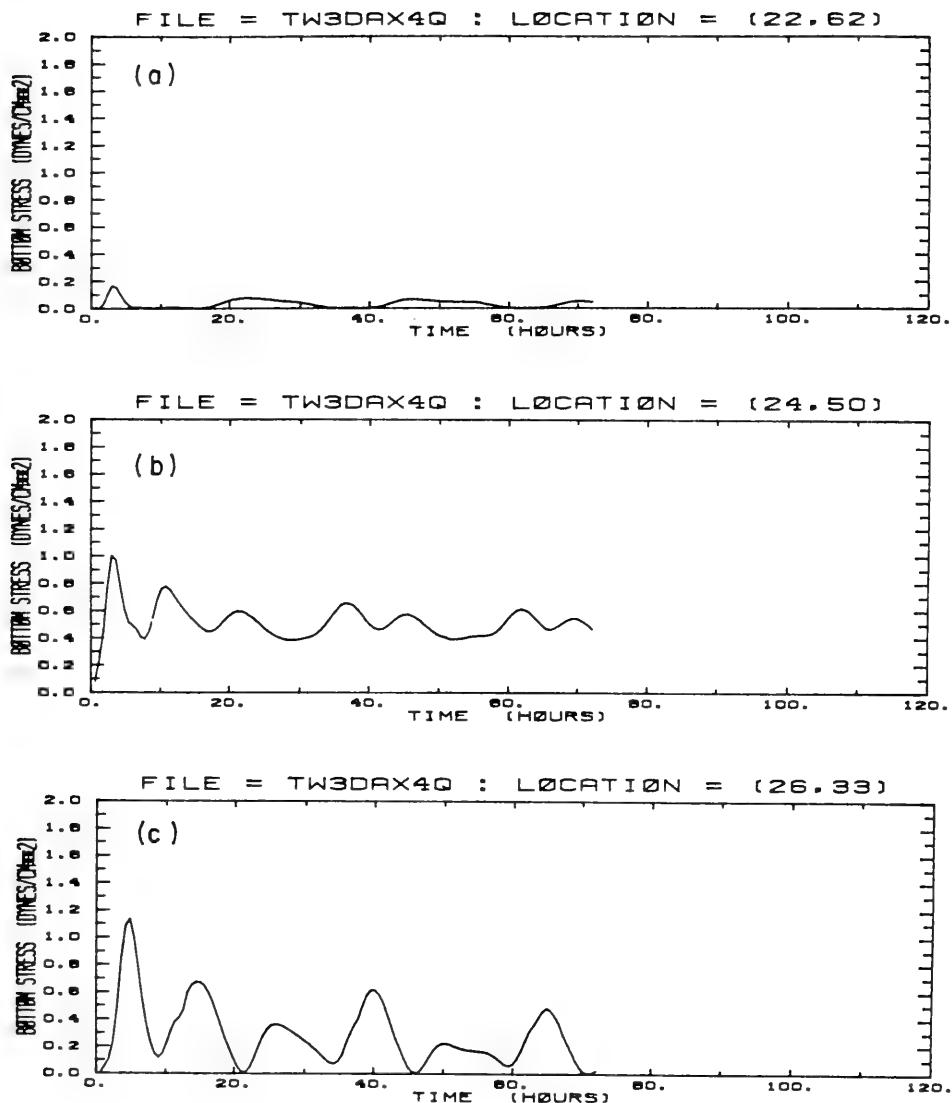
Figure 7.20. Tide- and Wind-induced bottom stress at three stations during 9/20/80 to 9/25/80.

SURFACE WINDS FØR 9/01 - 9/09
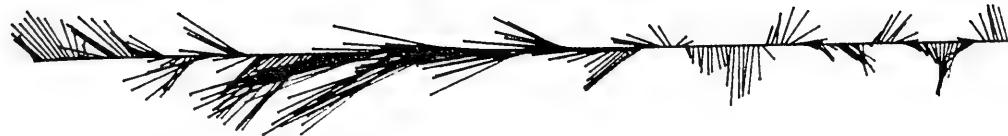
1.63E+01 [M/S]

MAXIMUM VECTØR

Figure 7.21.   Stick diagram of wind velocities in the Sound during
9/01/80 to 9/10/80.
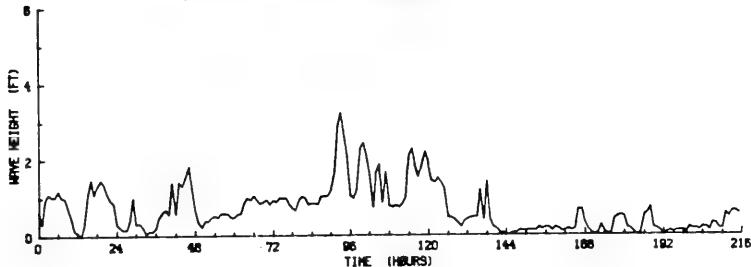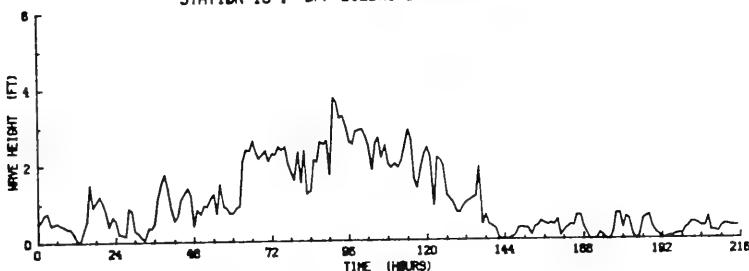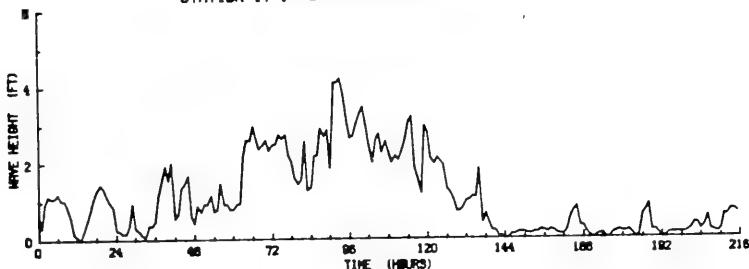
Figure 7.22. Computed wave height at three stations during 9/01/80 to 9/10/80.
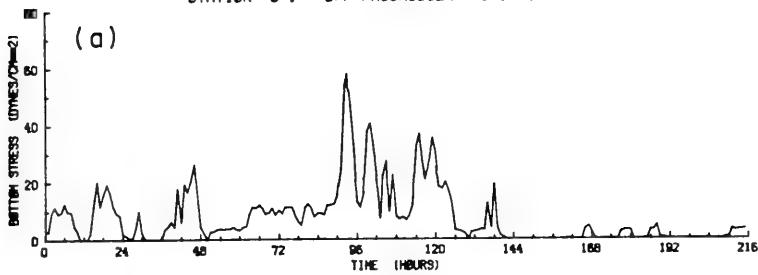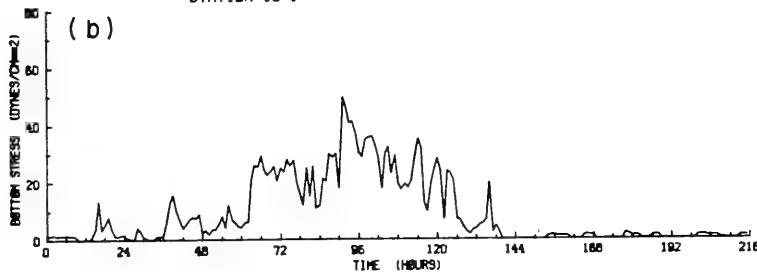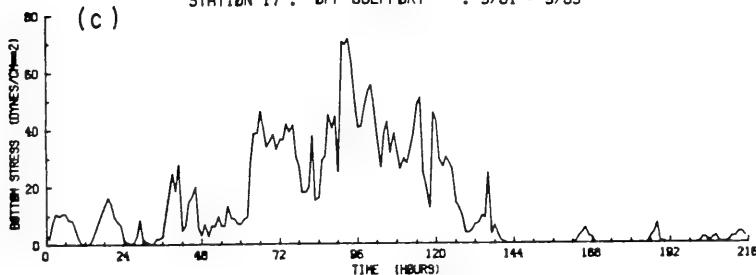
Figure 7.23. Wave-induced bottom stress at three stations during 9/01/80 to 9/10/80.

197

.

a parametric model. The wave heights were approximately 25% higher while the wave periods were 1.5 to 2 times higher. Although four wave gages were proposed to be installed in the area during our study period: two within the Sound and two offshore from the barrier islands, only two were installed and the available wave data contained too much contamination and hence did not allow a detailed comparison with the model prediction. Since any overestimation of the wave parameters could lead to overestimation of wave-induced entrainments of sediments, it is our opinion that future studies in the area should include a more careful validation of the wave model.

Sheng (1980) compared various wave hindcasting models with data from the shallow coastal waters in Lake Erie. It was found that several models, which were originally designed for the deep-water environment, did very poorly in shallow waters. One such model was actually used in a study on wave-induced sediment transport in the Long Island Sound (Bokuniewicz et al., 1977).

7.5 Deposition, Entrainment, and Transport of Sediments during 9/02/80 to 9/08/80

Ship Survey Data

Ship surveys were conducted on 9/2/80 and 9/3/80. It was originally planned to take water samples from all the transect stations as shown in Figure 7.24. The 9/2/80 survey covered all the western stations between the Grand Island and the Ship Island. Due to high wave conditions on 9/3/80, the planned survey for the eastern Sound was halted. The water samples collected at half Secchi depth below the surface and 2 feet above the bottom were analyzed by Isphording (1980) for suspended sediment concentrations. His analysis for all stations indicated concentrations near the surface were generally higher than those near the bottom more than twofold. At station T-4, the surface concentration was found to be 596 mg/l while the bottom concentration was only 13.8 mg/l. Although this is possible to occur locally at some points, it is unlikely that such a remarkably high surface concentration could have prevailed over such a large area under the given climactic conditions. A concurrent measurement on the water turbidity was conducted from the survey ship with a nephelometer. The nephelometer data at all stations indicated generally higher turbidity near the bottom. It is thus
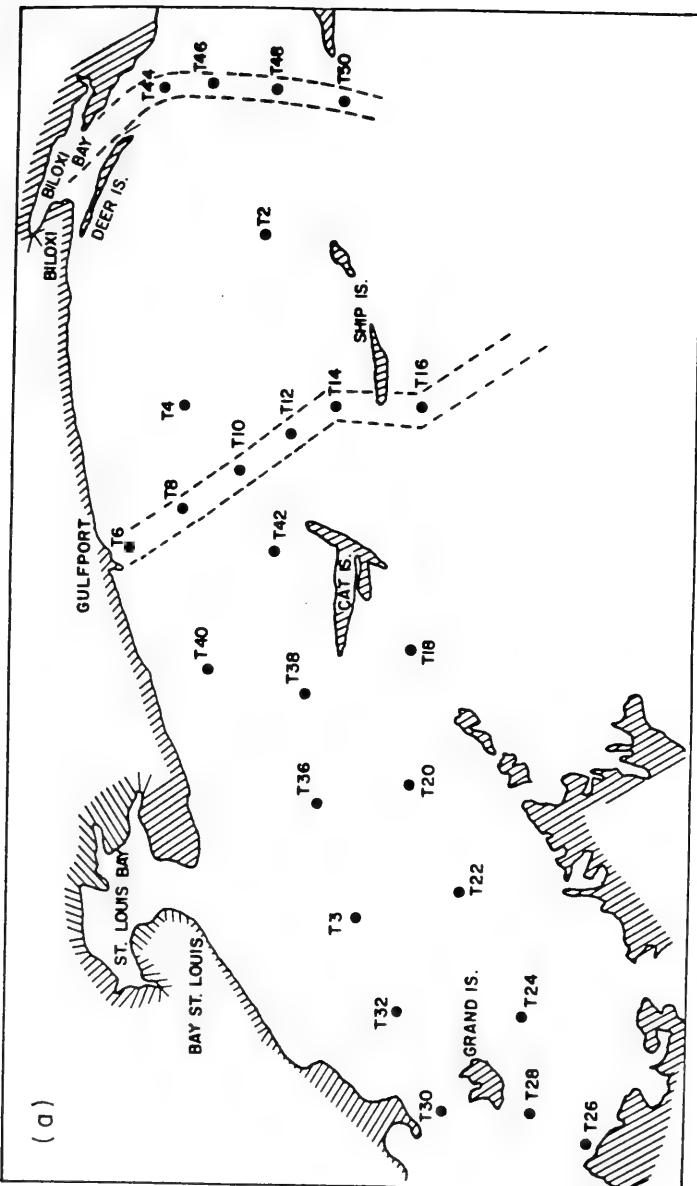
Figure 7.24. (a) Locations of transect sections in the western portion of Mississippi Sound.

.

.
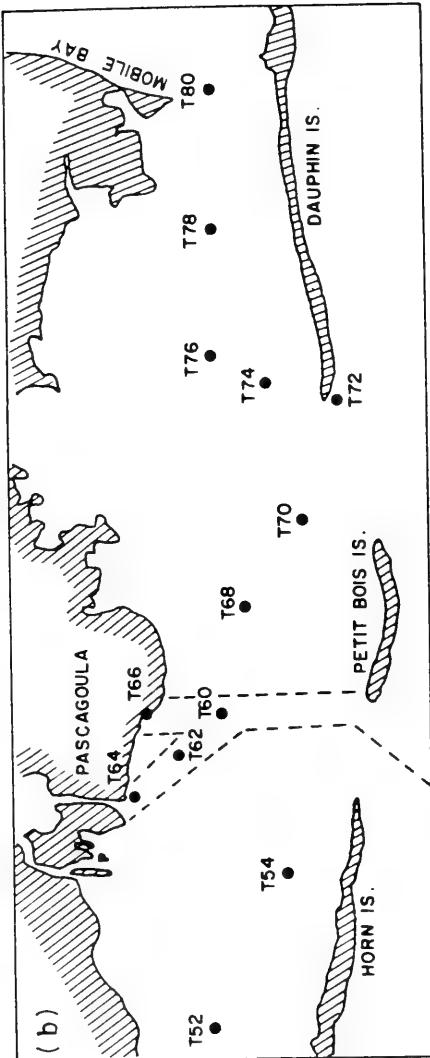
Figure 7.24. (b) Locations of transect sections in the eastern portion of Mississippi Sound.

judged that the water sampler analysis was probably conducted with the surface samples and the bottom samples reversed. The resulting surface and bottom concentrations on 9/2/80 are then interpolated onto our numerical grid and are shown in Figure 7.25. Surface concentrations are on the order of 20 mg/l while bottom concentrations are on the order of 70 mg/l.

Several days later, on 9/8/80, another survey was carried out in the western sound. On 9/9/80, the survey proceeded from the Ship Island to the Pascagoula Channel. On 9/10/80, the remaining stations in the eastern Sound were surveyed. The resulting concentration measurements are interpolated onto our grid and are shown in Figure 7.26. It is apparent that both the surface and the bottom concentrations have decreased slightly from those obtained on 9/2/80.

Model Simulation

Using the model computed bottom stresses and the deposition and entrainment relationship derived from laboratory experiments, we have computed the time variation of the suspended sediment concentration within the bottom 1 m at several stations.

Initially, the suspended sediment concentration was assumed to be zero. Relatively calm weather conditions prior to the steady period indicates the bottom sediments are fairly compacted during the initial period. Entrainment relationship corresponding to a 5-day settling time is used in the calculation. The results at stations 8, 10, and 17 are shown in Figure 7.27.

From the results, it is apparent that the high wave-induced bottom stresses have led to entrainment during 9/3/80 to 9/7/80. From then on, however, wind speeds decreased substantially and wind directions changed from the strong easterlies to the weak northerlies which had very short fetches and little wave energies. Deposition thus prevailed over most of the Sound to yield the low concentration distribution on 9/8/80 and 9/9/80. The near-bottom concentration at stations 8 and 17 are on the order of 100 mg/l on 2 September, and on the order of 40 mg/l on 8 September. All of the model simulated results agree quite well with the available ship survey data at the end of the simulation period (indicated by the circles in Figure 7.27). It is
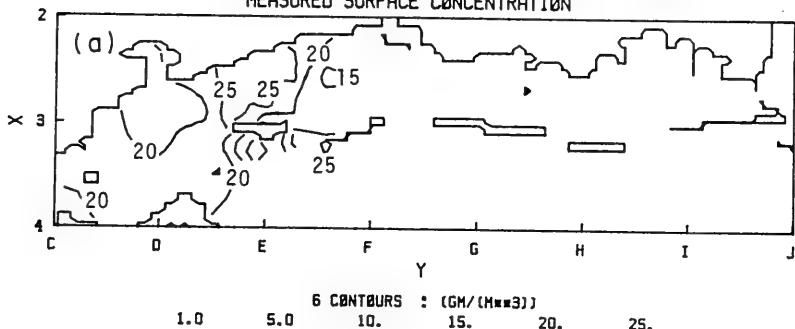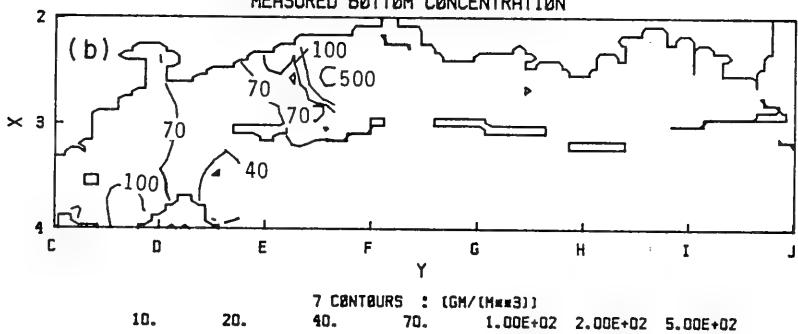
Figure 7.25. (a) Measured near-surface suspended sediment concentration in the Sound during 9/02/80 to 9/03/80.
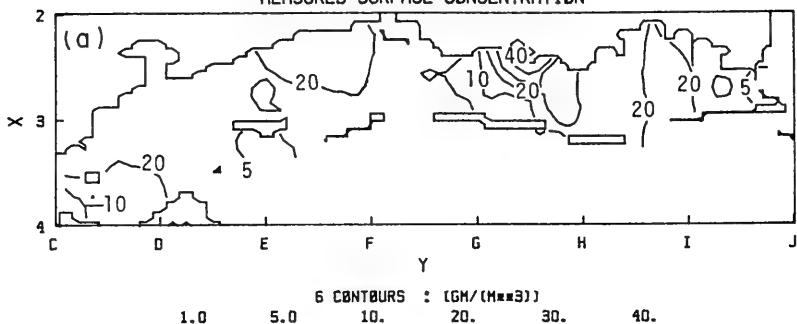
(b) Same as (a) except for near-bottom concentration.
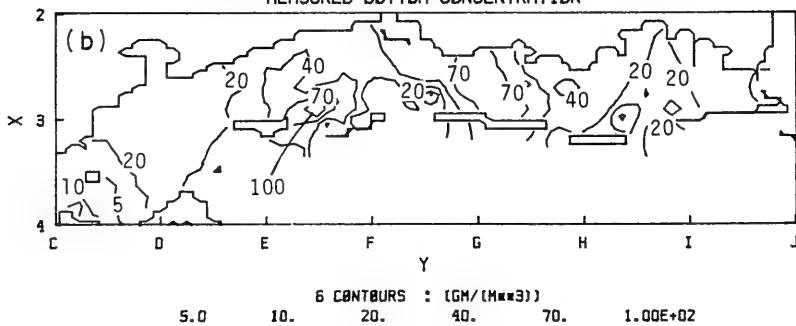
Figure 7.26. (a) Measured near-surface suspended sediment concentration in the Sound during 9/08/80 to 9/09/80.

(b) Same as (b) except for near-bottom concentration.
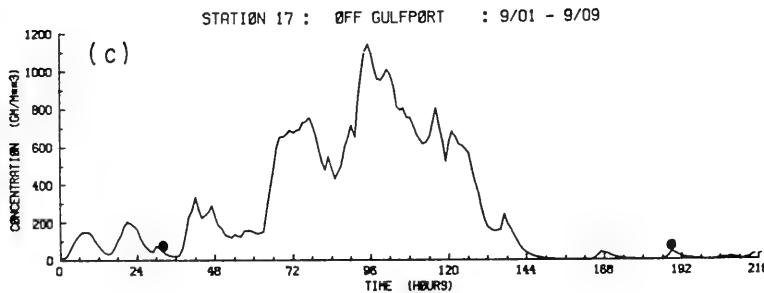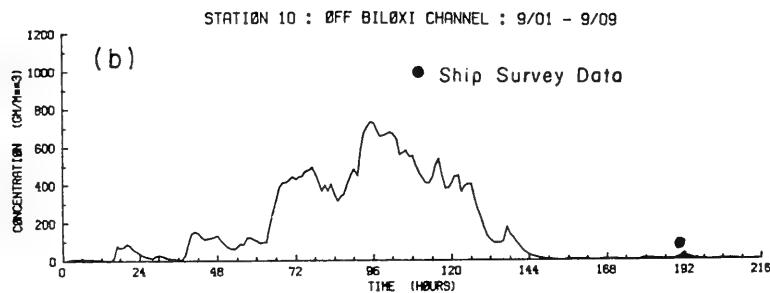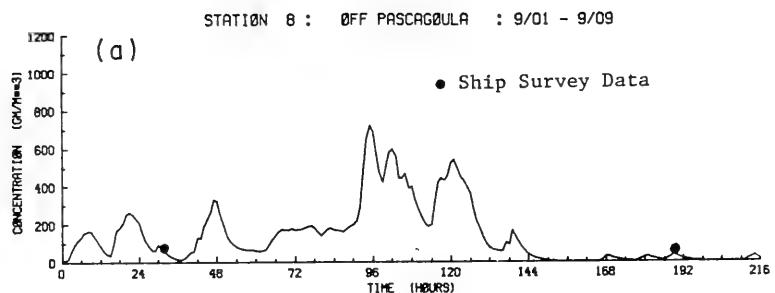
Figure 7.27. Simulated near-bottom suspended sediment concentration at three stations during 9/01/80 to 9/10/80.

204

interesting to see that, in between the ship surveys, bottom concentration over 1000 mg/l had been reached at station 17. Detailed verification of the model simulation would require continuous measurements of concentration or turbidity at properly selected stations. This could be accomplished with a field study which incorporates in-situ measurements, ship surveys and remote sensing. During the period with strong easterlies, due to the stronger wave action, concentration is generally higher in the western Sound. The easterlies also caused significant transport of suspended sediments towards the west.

7.6 Deposition, Entrainment, and Transport of Sediment during 9/20/80 to 9/25/80

Ship Survey Data

Sediment concentration distributions interpolated from the ship survey data on 9/20/80 and 9/21/80 are shown in Figure 7.28. Low concentration between 10 mg/l and 20 mg/l exists near the surface, while higher concentration up to 200 mg/l exists near the bottom. This is consistent with our computations on the bottom shear stresses as presented in Section 7.4. The relatively strong bottom stresses on 9/20 and 9/21 apparently resulted in the entrainment of sediments and the higher near-bottom concentration.

A subsequent ship survey conducted on 9/24/80 and 9/25/80 showed rather low suspended sediment concentration (~ 20 mg/l) throughout the water column (Figure 7.29).

Model Simulation

.Our bottom stress computations indicated that relatively high bottom shear stresses existed during 9/20/80 and the first several hours on 9/21/80. This resulted in the relatively high bottom sediment concentrations at all stations. During 9/23/80 and 9/24/80, significant wave-induced bottom stresses only existed for approximately 10 hours. Thus the higher bottom concentrations observed on 9/20/80 had decreased appreciably on 9/24/80 due to deposition.
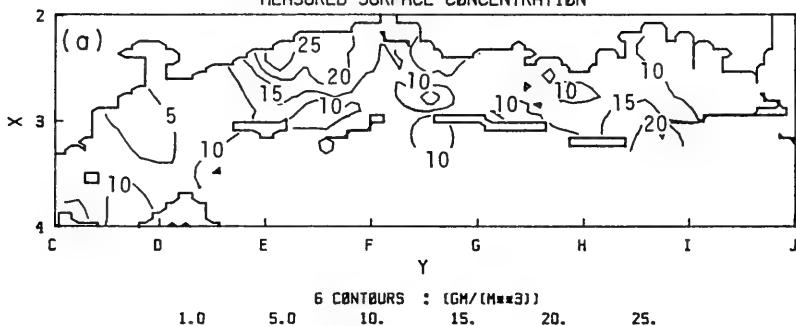
.
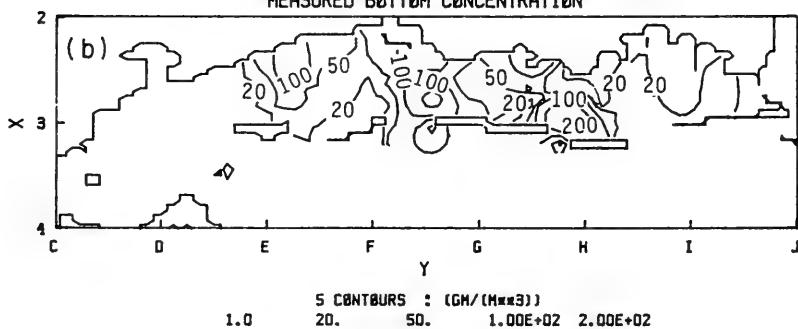
Figure 7.28. (a) Measured near-surface suspended sediment concentration in the Sound during 9/20/80 to 9/21/80.
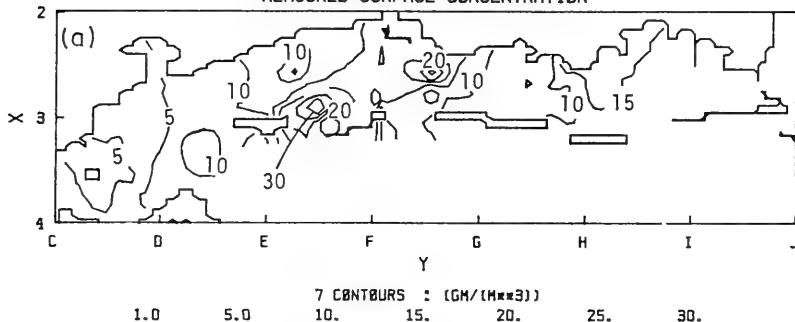
(b) Same as (a) except for near-bottom concentration.
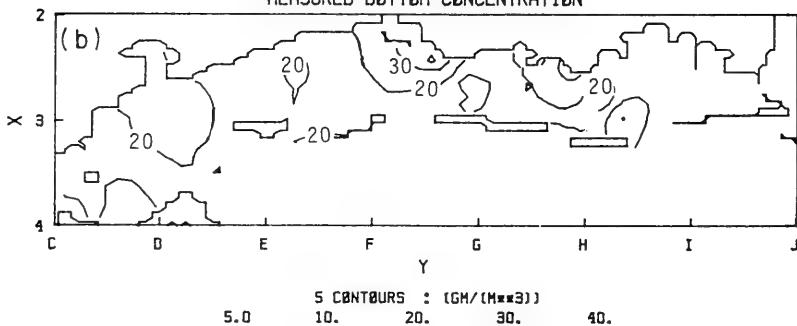
Figure 7.29. (a) Measured near-surface suspended sediment concentration in the Sound during 9/24/80 to 9/25/80.

(b) Same as (a) except for near-bottom concentration.
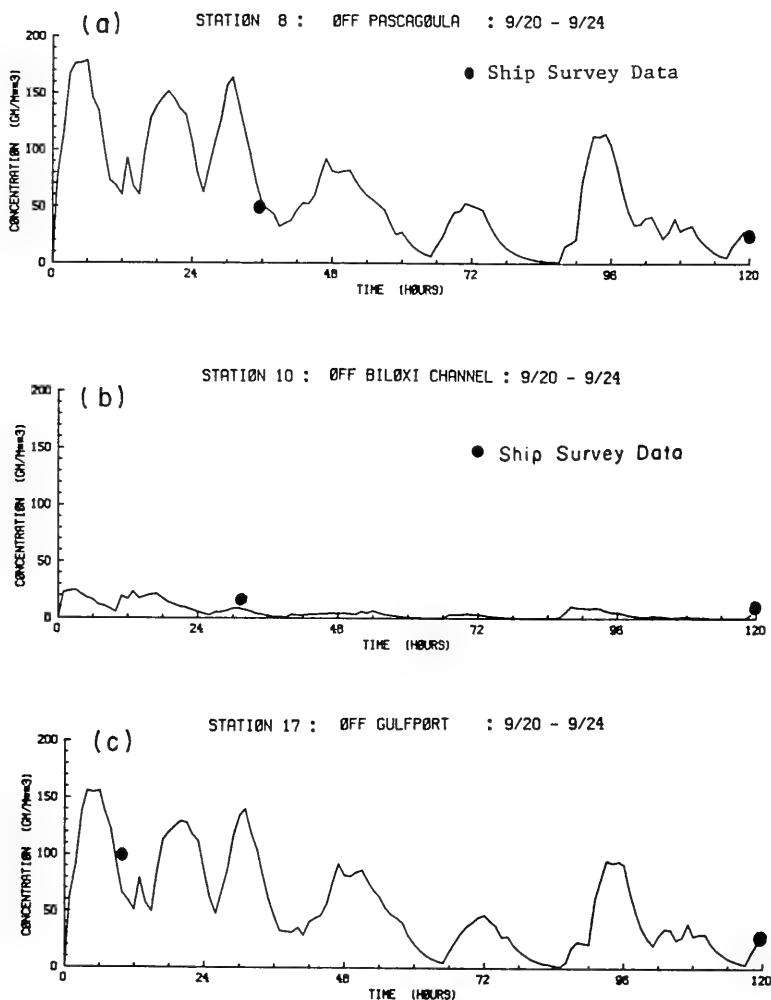
Figure 7.30. Simulated near-bottom suspended sediment concentration at three locations during 9/20/80 to 9/25/80.

Again, the model simulated sediment concentrations at all stations agree well with the ship survey data. Due to the relatively mild wind from the southeast, concentration levels during this period are generally smaller than those during 9/01/80 to 9/10/80. Transport of sediments is also weaker due to the smaller wind-driven currents in this period.

7.7 Summary

We have performed model simulations on the relative importance of tidal currents, wind-driven currents, and wave in causing sediment movement within a coastal environment. With the limited amount of data, we were able to perform realistic simulations of sediment movement within the Mississippi Sound and achieved reasonable agreement with data. During the study periods, significant deposition, entrainment, and transport of sediments were found within the Mississippi Sound. Future studies should concentrate on simulation of sediment movement during the sporadic high-energy events which have primary influences on the total sediment budget within the Sound. Remote sensing data on suspended sediment concentration can provide synoptic information over a large coastal area, hence could be used to provide better data for model initiation and verification.

.

8. CONCLUSIONS AND RECOMMENDATIONS

The framework of a comprehensive model for coastal currents and sediment dispersion is formulated. Results of the present study and future studies needed are summarized in the following for various components of the overall model.

An efficient three-dimensional and comprehensive numerical model of coastal currents has been developed and is operational. It may be used to provide detailed computations of the currents within several tidal cycles or time scales of a storm event. With some modification, it could be combined with a vertically-integrated model for long-term computations on the order of weeks, months, or longer.

Applications to the Mississippi Sound and adjacent offshore waters showed that large spatial and temporal variation of currents and bottom shear stresses exist within the area. Model simulations during 9/20/80 to 9/25/80 and 6/12/80 to 6/16/80 agree very well with measured data on surface displacements and currents.

To better understand the effect of open Gulf circulation on the currents in the study area, the present three-dimensional model may be modified to compute the entire Gulf circulation on a relatively coarse grid. The results will then provide boundary conditions for the finer-grid, limited-area model used in the present study. Further studies on density-driven currents should also be planned with comprehensive measurement programs.

The role of turbulence in affecting the deposition, entrainment and transport of cohesive sediments has been large oversimplified in the past. We have provided a thorough review and quantitative analysis on these aspects. For example, for cohesive sediments in a coastal environment, our analysis indicates that sediment particle dynamics is important and can be modeled by considering a number of particle groups and the coagulation process. Theoretical study on deposition of cohesive sediment is lacking and is needed.

Detailed dynamics within a turbulent boundary layer, under pure wave or wave-current interaction, has been studied by means of a turbulent transport model. Model predictions compare well with data and are more accurate than

simpler parametric models. Our study also indicated that the presence of the wave may either enhance or reduce the bottom shear stress due to the mean currents. Further study using this model is needed, as well as well-designed field or laboratory measurements, to elucidate the complex dynamics within the bottom boundary layer.

Entrainment and deposition of the Mississippi Sound sediments was studied by means of a rotating annular flume. It was found that bottom shear stress, salinity, sediment type, and time history of bottom sediments have great influence on the entrainment rate of sediments. The water content (or bulk density) alone was found to be insufficient to characterize the erodability (or stability) of the Mississippi Sound sediments. Bacteria, macrofauna, and organic matter may be important in affecting the erodability of the sediments. Any model of sediment dispersion should include the time-history of the bottom sediment as a parameter.

More flume studies should be performed to better understand the effect of various parameters on the erodability of sediments. The result will lead to a better understanding of the bed stability in the area, thus a better planning of dredging and disposal activities. Dredging or disposal at an unstable site should be avoided. On the other hand, depending on the parameters, disposal of sediments at a new site may have a stabilizing or de-stabilizing effect.

Dispersions of sediment due to tidal currents, wind-driven currents, and waves have been studied. Waves are found to be generally more effective in causing entrainment of sediments. Model simulation of two events in September 1980 showed reasonable agreement with data.

Measurements of flow and concentration data usually consist of a finite set of data in a random field. To achieve meaningful model comparison with data, a long time series of data is required at any given point to obtain the proper mean value and variance. In addition, models capable of resolving the variances as well as the mean variables should be used.

211

REFERENCES

Alizadeh, A., 1974; "Amount and Type of Clay and Pore Fluid Influences on the Critical Shear Stress and Swelling of Cohesive Soils," Ph.D. Dissertation, U.C. Davis.

Anderson, H.W., 1951; "Physical Characteristics of Solids Related to Erosion," J. Hydr. Div. ASCE, 104, No. HY2, pp. 279-283.

Arakawa, A., 1966; "Computational Design for Long-Term Numerical Integration of the Equations of Fluid Motion: Two-Dimensional Incompressible Flow. Part 1," J. Comp. Phys., 1, pp. 119-143.

Arakawa, A., 1970; "Numerical Simulation of Large-Scale Atmospheric Motions," Dept. Meteor., UCLA.

Ariathurai, R., R.C. MacArthur and R.B. Krone, 1977; "Mathematical Model of Estuarial Sediment Transport," Technical Report D-77-12, Waterways Experiment Station, Vicksburg, MS.

Ariathurai, R. and K. Arulanadan, 1978; "Erosion of Cohesive Soils," J. Hydro. Div. ASCE, 104, No. HY2, pp. 279-283.

Asselin, R., 1972; "Frequency Filters for Time Integrations," Mon. Wea. Rev., 100, pp. 487-490.

Baer, L., L.C. Adams, and S.I. Adelfang, 1968; "Experiments in Oceanic Forecasting for the Advective Region by Numerical Modeling, Part 2, gulf of Mexico," J. Geophys. Res., 73, pp. 5091-5104.

Baines, W.D. and D.J. Knapp, 1965; "Wind Driven Water Currents," J. Hyd. Div. ASCE, 91, No. HY2, pp. 205-221.

Batchelor, G.K., 1972; "Sedimentation in a Dilute Dispersion of Spheres," J. Fluid Mech., 52, 2, pp. 245-268.

Bennett, J.R., 1977; "A Three-Dimensional Model of Lake Ontario's Summer Circulation, I. Comparison with Observations," J. Phys. Oceano., 7, pp. 591-601.

Blumberg, A.F., 1975; "A Numerical Investigation into the Dynamics of Estuarine Circulation," Chesapeake Bay Institute Report No. 91, Baltimore, MD.

Blumberg, A.F. and G.L. Mellor, 1981; "A Numerical Calculation of the Circulation in the Gulf of Mexico," Dynalysis Report No. 66, 159 pp.

Bokuniewicz, H.J., J. Gebert, R.B. Gorden, P. Kaminsky, C.C. Pilbeam, M. Reed, and C. Tuttle, 1977; "Field study of the effects of storms on the stability and fate of dredged material in subaqueous disposal areas," Tech Rep. D-77-22, Waterways Experiment Station, Vicksburg, MS.

Boone, P.A., 1973; "Depositional Systems of the Alabama, Mississippi, and Western Florida Coastal Zone," _Gulf Coast Assoc. Geol. Soc. Trans._, 23, pp. 226-277.

Boris, J.P. and D.L. Book, 1976; "Flux-Corrected Transport III: Minimum Error FCT Algorithm," _J. Comp. Phys._, 20, 397.

Bowden, K.F. and P. Hamilton, 1975; "Some Experiments with a Numerical Model of Circulation and Mixing in a Tidal Estuary," _Est. Coastal Mar. Sci._, 3, 281.

Brown, W.S. and R.P. Trask, 1980; "A Study of Tidal Energy Dissipation and Bottom Stress in an Estuary," _J. Phys. Oceano._, 10, pp. 1742-1754.

Bryan, K., 1969; "A Numerical Method for the Study of the Circulation of the World Ocean," _J. Comput. Phys._, 4, pp. 347-376.

Businger, J.A., J.C. Wyngaard, Y. Izumi, and E.F. Bradley, 1971; "Flux-Profile Relationships in the Atmospheric Surface Layer," _J. Atmos. Sci._, 28, pp. 181-189.

Butler, H.L., 1980; "Evolution of a Numerical Model for Simulating Long-Period Wave Behavior in Ocean-Estuarine Systems," in _Estuarine and Wetland Processes_, (P. Hamilton, Ed.), Springer-Verlag, Berlin, Heidelberg, pp. 368-378.

Butler, H.L. and Y.P. Sheng, 1982; "ADI Procedures for Solving the Shallow-Water Equations in Transformed Coordinates," _Proc. 1982 Army Num. Anal. and Comp. Conf._, Army Research Office, pp. 365-380.

Chen, H.S., 1981; "A Finite-Element Model of Storm Surge and Circulation for Chesapeake Bay and its Atlantic Nearshore," _Oceans 81 Conference Record_, pp. 815-819.

Christensen, R.W., and B.M. Das, 1973; Hydraulic Erosion of Remolded Cohesive Soils, in "Soil Erosion: Causes and Mechanics, Prevention and Control," _Special Report 135_, Highway Research Board, Washington, D.C., pp. 52-74.

Christmas, J.Y. (ed.), 1973; "Cooperative Gulf of Mexico Estuarine Inventory and Study, Mississippi," Gulf Coast Research Laboratory, Ocean Springs, Mississippi, 434 pp.

Cox, R.A., F. Culkin and J.P. Riley, 1967; "The Electrical Conductivity/Chlorinity Relationship in Natural Sea Water," _Deep-Sea Research_, 14, pp. 203-220.

Csanady, G.T., 1963; "Turbulent Diffusion in Lake Huron," _J. Fluid Mech._, 17, pp. 360-384.

Deardorff, J.W., 1968; "Dependence of Air-Sea Transfer Coefficients on Bulk Stability," _J. Geophys. Res._, 73, pp. 2549-2557.

Donaldson, C. duP., 1973; "Atmospheric Turbulence and the Dispersal of Atmospheric Pollutants," in AMS Workshop on Micrometeorology, (D.A. Haugen, ed.), Science Press, Boston, pp. 313-390.

Edinger, J.G. and J.C. Geyer, 1967; "Heat Exchange in the Environment," Edison Electric Institute, N.Y., Pub. No. 65-902.

Eleuterius, C.K., 1973; "The Marshes of Mississippi," Gulf Coast Research Laboratory Report.

Eleuterius, C.K., 1977; "Location of the Mississippi Sound oyster reefs as related to salinity of bottom water during 1973-1975," Gulf Coast Research Lab. Report.

Erikson, C.C., 1978; "Measurements and Models of Fine Structure, Internal Gravity Waves and Wave Breaking in the Deep Ocean," J. Geophys. Res., 83, pp. 2989-3009.

Forristal, G.Z., R.C. Hamilton, and V.J. Cardone, 1977; "Continental Shelf Currents in Tropical Storm Delia: Observations and Theory," J. Phys. Oceano., 7, pp. 532-546.

Fukuda, M., 1979; "Entrainment of Cohesive Sediments in Fresh Water," Ph.D. Dissertation, Case Western Reserve University.

Garrett, C., 1975; "Tides in Gulfs," Deep Sea Res., 22, 1, pp. 23-25.

Gaul, R.D., 1967; "Circulation over the Continental Margin of the Northeastern Gulf of Mexico," Ph.D. dissertation, Texas A & M University, 172 pp.

Grant, W., 1981; Personal Communication.

Grant, W.D. and O.S. Madsen, 1978; "Bottom Friction Under Waves in the Presence of a Weak Current," NOAA Tech Report, ERL-MESA., 150 pp.

Grant, W.D. and O.S. Madsen, 1979; "Combined Wave and Current Interaction with a Rough Bottom," J. Geophys. Res., 84, pp. 1797-1808.

Garrett, C. and W.H. Munk, 1972; "Space-Time Scales of Internal Waves," Geophy. Fluid Dyn., 3, 225 pp.

Garrett, C. and W.H. Munk, 1975; "Space-Time Scales of Internal Waves, A Progress Report," J. Geophys. Res., 80, 291 pp.

Hansen, K.W., 1974; "Calculation of Normal Modes for the American Mediterranean Seas," Tech. Report No. 26, University of Chicago.

Haq, A., W. Lick, and Y.P. Sheng, 1974; "The Time-Dependent Flow in Large Lakes with Applications to Lake Erie," Technical Report, Dept. Earth Sciences and Dept. Mechanical and Aerospace Engineering, Case Western Reserve University.

Harleman, D.R.F., 1975; Real-Time Models for Salinity and Water-Quality Analysis in Estuaries, in "Estuaries, Geophysics, and the Environment," National Academy of Science, pp. 84-92.

Hicks, B.B., 1972; "Some Evaluation of Drag and Bulk Transfer Coefficients Over Water Bodies of Different Sizes," Boundary Layer Meteor., 8, pp. 515-524.

Hirsh, R.S., 1975; "Higher Order Accurate Difference Solutions of Fluid Mechanics Problems by a Compact Differencing Technique," J. Comp. Phys., 19, pp. 90-109.

Hirsh, J.E. and G.G. Williamson, 1979; "Analysis and Simulation of Flow Downstream of a Variable Twist Segmented Wing," A.R.A.P. Report No. 398.

Huang, J.C.K. and P.W. Sloss, 1981; "Simulation and Verification of Lake Ontario's Mean State," J. Phys. Oceano., 11, 11, pp. 1548-1566.

Hurlbert, H.E. and J.D. Thompson, 1980; "A Numerical Study of Loop Current Intrusions and Eddy Shedding," J. Phys. Ocean., 10, pp. 1611-1651.

Ippen, A.T. and D.R.F. Harleman, 1961; "Analytical Studies of Salinity Intrusion in Estuaries and Canals," Phase 1: One-Dimensional Analysis, Technical Bulletin No. 5, Committee on Tidal Hydraulics, U.S. Army Corps of Engineers.

Isphording, W.C., 1980; "Raw Data of Mississippi Sound Bottom Sediments," Report of Investigation.

Jespersen, D.E., 1974; "Arakawa's Method is a Finite Element Method," J. Comp. Phys., 16, pp. 383-390.

Jonsson, I.G., 1980; "A New Approach to Oscillatory Rough Turbulent Boundary Layers," Ocean Engng., I, pp. 109-152.

Jonsson, I.G. and N.A. Carlsen, 1976; "Experimental and Theoretical Investigations in an Oscillatory Rough Turbulent Boundary Layer," J. Hydr. Res., 14, pp. 45-60.

Kajiura, K., 1968; "A Model of the Bottom Boundary Layer in Water Waves," Bull Earthq. Res. Inst., 46, pp. 75-123.

Kandiah, A., 1974; "Fundamental Aspects of Surface Erosion of Cohesive Soils," Ph.D. Dissertation, University of California.

Kent, R.E. and D.W. Pritchard, 1959; "A Test of Mixing Length Theories in a Coastal Plain Estuary," J. Mar. Res., 18, pp. 62-72.

Koh, R.C.Y. and Y.C. Chang, 1973; "Mathematical Model for Barged Ocean Disposal of Wastes," Rep. PA-66012-73-029, U.S.E.P.A.

Kreiss, H.O., 1975; "A Comparison of Numerical Methods Used in Atmospheric and Oceanographic Applications," in Numerical Models of Ocean Circulation, Nat. Acad. Sci. U.S., pp. 255-279.

215

Krone, R.B., 1962; "Flume Studies of the Transport of Sediment in Estuarial Shoaling Processes," Contract Report, U.S. Army Engineers, San Francisco District.

Krone, R.B., 1963; "A Study of Rheologic Properties of Estuarial Sediments," Report Hydr. Eng. Lab, University of California, Berkeley.

Lamb, H., 1932; Hydrodynamics, 6th ed., Dover, New York.

Lane, D.D. and J.J. Stukel, 1978; "Aerosol Deposition on a Flat Plate," J. Aerosol Sc., 9, pp. 191-197.

Leendertse, J.J., 1970; "A Water Quality Simulation Model for Well-Mixed Estuaries and Coastal Seas," 1, Principles of Computation, RM-6230-rc, Rand Corporation, Santa Monica, CA.

Leendertse, J.J. and S.K. Liu, 1975; "A Three-Dimensional Model for Estuaries and Coastal Seas," Vol. II, Aspects of Computation, Rand Report R-1764-OWRT.

Lewellen, W.S., 1977; "Use of Invariant Modeling," in Handbook of Turbulence, Vol. 1 (W. Frost, ed.), Plenum Publishing Corp., pp. 237-280.

Lewellen, W.S. and Y.P. Sheng, 1980; "Modeling of Dry Deposition of SO_2 and Sulfate Aerosols," Report EPRI EA-1452, Electric Power Research Institute, Palo Alto, CA.

Lewellen, W.S. and Y.P. Sheng, 1981; "Modeling Tornado Dynamics," U.S. Nuclear Regulatory Commission Report NUREG/CR-1585, 227 pp.

Lewellen, W.S., A.K. Varma and Y.P. Sheng, 1972; "Dry Deposition Model Sensitivity," Proc. S.C.A.D.E.R. Conf., Santa Monica, CA.

Mason, P.J. and R.I. Sykes, 1978; "A Simple Cartesian Model of Boundary Layer Flow over Topography," J. Comp. Physics, 28, pp. 198-210.

Mehta, A.J. and E. Partheniades, 1979; "Kaolinite Resuspension Properties," J. Hydr. Div. ASCE, 105, No. HY4, pp. 411-416.

Munk, W.H. and E.P. Anderson, 1948; "Notes on the Theory of the Thermocline," J. Mar. Res., 1, pp. 276-295.

Murthy, C.R., 1976; "Horizontal Diffusion Characteristics in Lake Ontario," J. Phys. Oceano., 6, pp. 76-84.

Nihoul, J.C.J. and F.C. Ronday, 1982; "Three-Dimensional Marine Models for Impact Studies," Proc. 18th International Conf. on Coastal Engineering, Capetown, So. Africa.

Outlaw, D.G., 1981; "Preliminary results from Harmonic Analysis of Mississippi Sound Tide Data," Memorandum for Record, Waterways Experiment Station, Vicksburg, Mississippi.

Pagenkopf, J.R., D. Dykstra and M.W. Lorenzen, 1977; "Water Quality Modeling," Report for NSRPB, TC66.

Pao, R.F., 1967; Fluid Dynamics, 497 pp.

Parchure, T.M., 1980; "Effect of Bed Shear Stress on the Erosional Characteristics of Kaolinite," Technical Report, University of Florida.

Partheniades, E., 1962; "A Study of Erosion and Deposition of Cohesive Soils in Salt Water," Ph.D. Dissertation, University of California, Berkeley.

Platzman, G.W., 1972; "Two-Dimensional Free Oscillations in Natural Basins," J. Phys. Oceanog., 2, 2, pp. 117-130.

Raudkivi, A.J. and D.L. Hutchinson, 1971; "Erosion of Cohesive Soils," Proceedings of the 14th Australasian Conference on Hydraulics and Fluid Mechanics, Monash University, Melbourne, Australia, pp. 360-366.

Reid, R.O. and R.E. Whitaker, 1981; "Numerical Model for Astronomical Tides in the Gulf of Mexico, Vol. I: Theory and Application," Dept. Oceanog., Texas A & M University, College Station, TX.

Resio, D.T. and C.L. Vincent, 1977; "A Numerical Hindcast Model for Wave Spectra on Water Bodies with Irregular Shoreline Geometry," Technical Report H-77-9, Waterways Experiment Station, Visksburg, MS.

Rhoads, D.C., J.Y. Yingest, and W.J. Ullman, 1978; "Sea Floor Stability in Central Long Island Sound, Part 1: Temporal Changes and Erodability of Fine-Grained Sediments," in Estuarine Interactions, (M.L. Wiley, Ed.), Academic Press, pp. 221-244.

Riedel, H.P., J.W. Kamphuis, and A. Brebner, 1973; "Measurement of Bed Shear Stresses under Waves," Proc. 13th Conf. Coastal Engrg., I, 31, pp. 587-603, ASCE, New York.

Roache, P.J. 1972; Computational Fluid Dynamics, Hermosa Publishers, Albuquerque.

Saffman, P.G. and J.S. Turner, 1956; "On the Collision of Drops in Turbulent Clouds," J. Fluid Mech., 1, pp. 16-30.

Schmalz, R.A., 1983; "Numerical Model Investigation of Mississippi Sound and Adjacent Areas," WES Technical Report in Preparation, U.S. Army Eng. Waterways Exp. Stn., Vicksburg, MS.

Sehmel, G.A., 1973; "Particle Eddy Diffusivities and Deposition Velocities for Isothermal Flow and Smooth Surfaces," J. Aerosol Sci., 4, pp. 125-138.

Sheng, Y.P., 1975; "Wind-Driven Currents and Dispersion of Contaminants in the Near-Shore Regions of Large Lakes," Contract Report H-75-1, Waterways Experiment Station, Vicksburg, MS.

217

Sheng, Y.P., 1980; "Modeling Sediment Transport in a Shallow Lake," in Estuarine and Wetland Processes, (P. Hamilton, ed.), Springer-Verlag, Berlin, Heidelberg, pp. 299-337.

Sheng, Y.P., 1981a; "Second-Quarter Progress Report on Modeling the Hydrodynamics and Dispersion of Sediments in the Mississippi Sound," A.R.A.P. Tech Memo No. 81-03.

Sheng, Y.P., 1981b; "Modeling the Hydrodynamics and Dispersion of Sediments in the Mississippi Sound," A.R.A.P. Report No. 455.

Sheng, Y.P., 1982; "Hydraulic Applications of a Second-Order Closure Model of Turbulent Transport," in Applying Research to Hydraulic Practice, (P. Smith, Ed.), ASCE, pp. 106-119.

Sheng, Y.P. and W.S. Lewellen, 1982; "Current and Wave Interaction within the Benthic Boundary Layer," EOS, 63, 3, pp. 72-73.

Sheng, Y.P. and W. Lick, 1972; "Wind-Driven Currents in a Partially Ice-Covered Lake," Proc. 16th Conf. Great Lakes Res., pp. 1001-1008.

Sheng, Y.P. and W. Lick, 1979; "The Transport and Resuspension of Sediments in a Shallow Lake," J. Geophys. Res., 84, pp. 1809-1826.

Sheng, Y.P. and W. Lick, 1980; "A Two-Mode Free-Surface Numerical Model for the Three-Dimensional Time-Dependent Currents in Large Lakes," U.S. Environmental Protection Agency Report EPA-600/3-80-047.

Sheng, Y.P., W. Lick, R. Gedney, and F. Molls, 1978; "Numerical Computation of the Three-Dimensional Circulation in Lake Erie; A Comparison of a Free-Surface and a Rigid-Lid Model," J. Phys. Oceano., 8, pp. 713-727.

Sheng, Y.P., H. Segur, and W.S. Lewellen, 1978; "Application of a Spatial Smoothing Scheme to Control Short-Wave Numerical Oscillation," A.R.A.P. Tech Memo 78-8.

Shureman, P., 1941; "Manual of Harmonic Analysis and Prediction of Tides," U.S. Department of Commerce, Coast and Geodetic Survey, Special Pub. No. 98.

Simons, T.J., 1974; "Verification of Numerical Models of Lake Ontario, Part I: Circulation in Spring and Early Summer," J. Phys. Oceano., 4, pp. 507-523.

Smerdon, E.T. and R.P. Beaseley, 1959; "Relation of Compaction and Other Soil Properties to Erosion Resistance of Soils," Trans. ASAE 8.

Smith, J.D. and S.R. McLean, 1977; "Spatially Averaged Flow over a Wavy Surface," J. Geophys. Res., 82, pp. 1735-1746.

Sternberg, R.W., 1972; "Predicting Initial Motion and Bedload Transport of Sediment Particles in the Shallow Marine Environment," in Shelf-Sediment Transport, (D.P. Swift, ed.), Dowden, Hutchinson, Ross, Stroudsburg, PA.

Swain, A. and J. Houston, 1982; "A Numerical Model to Predict Morphometric Changes of a Beach due to Longshore and Onshore-Offshore Sediment Transport," in Abstracts 18th International Conf. Coastal Eng., Capetown, So. Africa.

Tee, K.T., 1976; "Tide-Induced Residual Current, a Two-dimensional Non-Linear Numerical Tidal Model," J. Mar. Res., 34, pp. 603-628.

Thiele, F., 1978; "Accurate Numerical Solutions of Boundary Layer Flows by the Finite-Difference Method of Hermitian Type," J. Comp. Phys., 28, pp. 138-159.

T.V.A., 1972; "Heat and Mass Transfer Between a Water Surface and the Atmosphere," T.V.A. Report No. 0-6803.

Upshaw, G.F., W.B. Creath, and F.L. Brooks, 1966; "Sediments and Macrofauna off the Coasts of Mississippi and Adjacent States," Mississippi Geol. Survey Bull., 106, 127 pp.

U.S. Army Engineers, Mobile District, 1979; "Dredged Material Disposal Study (Stage 1), Reconnaissance Report."

van de Kreeke, J. and S.S. Chiu, 1980; Tide-Induced Residual Flow in "Mathematical Modeling of Estuarine Physics," (J. Sunderman, ed.), Springer-Verlag, Berlin, Heidelberg, New York.

van Hoften, J.D.A. and S. Karaki, 1976; "Interaction of Waves and a Turbulent Current," Proc. 15th International Conf. Coastal Eng.

Wallis, J.R., and L.J. Stevan, 1961; "Erodability of some Wildland California Soils Related to Their Metallic Cation Exchange Capacity," J. Geophys. Res., 66, p. 4

Welander, P., 1957; "Wind Action on a Shallow Sea, Some Generalizations of Ekman's Theory," Tellus, 9, pp. 47-52.

West, R.T., and R.O. Reid, 1972; "A Baroclinic Prognostic Numerical Circulation Model," Contributions to the Physical Oceanography of the Gulf of Mexico, Vol. II, (L.R.A. Capurro and J.L. Reid, Eds.), Gulf Publishing Company, pp. 177-209.

Wilson, B.W., 1960; "Note on Surface Wind Stress Over Water on Low and High Speeds," J. Geophys. Res., 65, pp. 3377-3382.

Yeh, H.Y., 1979; "Resuspension of Flow Deposited Cohesive Sediment Beds," Tech Report, University of Florida.

Zalesak, S.T., 1979; "Fully Multi-Dimensional Flux-Corrected Transport Algorithms for Fluids," J. Comp. Phys., 31, pp. 375.

.

APPENDIX A

VERTICAL STRETCHING OF THE COORDINATES

APPENDIX A

Vertical Stretching of the Coordinates

The vertical stretching of the coordinates for the three-dimensional, free-surface model is obtained by letting

$$x' = x; \quad y' = y; \quad \sigma = \frac{z - \zeta(x,y,t)}{h(x,y) + \zeta(x,y,t)} = \frac{z - \zeta}{H} \qquad (A-1)$$

By chain rule, first-order derivatives in the original coordinates (x,y,z) are related to those in the transformed coordinates (x',y',σ) as:

$$\frac{\partial}{\partial x} = \frac{\partial}{\partial x'} - \frac{1}{H} \frac{\partial \zeta}{\partial x} \frac{\partial}{\partial \sigma} - \frac{\sigma}{H} \frac{\partial H}{\partial x} \frac{\partial}{\partial \sigma} \qquad (A-2)$$

$$\frac{\partial}{\partial y} = \frac{\partial}{\partial y'} - \frac{1}{H} \frac{\partial \zeta}{\partial y} \frac{\partial}{\partial \sigma} - \frac{\sigma}{H} \frac{\partial H}{\partial y} \frac{\partial}{\partial \sigma} \qquad (A-3)$$

$$\frac{\partial}{\partial z} = \frac{1}{H} \frac{\partial}{\partial \sigma} \qquad (A-4)$$

The vertical velocity w in the (x,y,z) coordinates is related to that in the transformed coordinates $(\omega \equiv d\sigma/dt)$ as:

$$w = \frac{dz}{dt} = \frac{d}{dt} (\sigma H + \zeta)$$

$$= H\omega + \sigma \left(u \frac{\partial h}{\partial x} + v \frac{\partial h}{\partial y} \right) + (1+\sigma) \frac{d\zeta}{dt} \qquad (A-5)$$

Utilizing (A-2) through (A-5), the continuity equation and the advective terms of the x-momentum equation in the original coordinates can be transformed as:

$$\frac{\partial u}{\partial x} + \frac{\partial v}{\partial y} + \frac{\partial w}{\partial z} = 0 \rightarrow \frac{\partial Hu}{\partial x'} + \frac{\partial Hv}{\partial y'} + H \frac{\partial \omega}{\partial \sigma} + \frac{\partial \zeta}{\partial t} = 0 \qquad (A-6)$$

$$\frac{\partial u}{\partial t} + \frac{\partial uu}{\partial x} + \frac{\partial uv}{\partial y} + \frac{\partial uw}{\partial z}$$

$$+ \frac{1}{H} \left[\frac{\partial Hu}{\partial t} + \frac{\partial (Hu^2)}{\partial x'} + \frac{\partial (Huv)}{\partial y'} + H \frac{\partial u\omega}{\partial \sigma} + (1+\sigma) \frac{\partial u}{\partial \sigma} \frac{\partial \zeta}{\partial t} \right] \qquad (A-7)$$

The diffusion terms in the momentum equations involve the second-order derivatives which are:

$$\frac{\partial}{\partial x} \quad \frac{\partial}{\partial x} \quad = \frac{1}{H} \left[\frac{\partial}{\partial x'} \left(H \frac{\partial}{\partial x'} \right) - \frac{\partial}{\partial \sigma} \left(\sigma \frac{\partial H}{\partial x} \frac{\partial}{\partial x'} \right) - \sigma \frac{\partial}{\partial x'} \left(\frac{\partial H}{\partial x} \frac{\partial}{\partial \sigma} \right) \right.$$

$$+ \frac{1}{H} \left(\frac{\partial H}{\partial x} \right)^2 \frac{\partial}{\partial \sigma} \left(\sigma^2 \frac{\partial}{\partial \sigma} \right) - \frac{\partial}{\partial x'} \left(\frac{\partial \zeta}{\partial x} \frac{\partial}{\partial \sigma} \right) - \frac{\partial \zeta}{\partial x} \frac{\partial^2}{\partial \sigma \partial x'}$$

$$+ \left. \left(\frac{\partial \zeta}{\partial x} \right)^2 \left(\frac{1}{H} \frac{\partial^2}{\partial \sigma^2} \right) + \frac{z}{H} \frac{\partial \zeta}{\partial x} \frac{\partial H}{\partial x} \frac{\partial}{\partial \sigma} \left(\sigma \frac{\partial}{\partial \sigma} \right) \right] \qquad (A-8)$$

$$= \frac{1}{H} \frac{\partial}{\partial x'} \left(H \frac{\partial}{\partial x'} \right) + \text{Higher Order Terms}$$

An alternative way to derive the transformed equations is to perform tensor transformation on the dependent as well as the independent variables.

APPENDIX B

LATERAL STRETCHING OF THE COORDINATES

APPENDIX B

Lateral Stretching of the Coordinates

In the lateral stretching of the coordinates, the x grid and the y grid are treated independently. Grid in each direction is divided into several regions, each with a certain number of non-uniformly spaced grid points. These points are then mapped into a uniformly spaced computational grid with equal number of points via Eq. (2.22). The coefficients in the equations are determined by matching the functional as well as their derivatives at the boundaries between regions. Derivatives in the original coordinates (x,y) are related to those in the stretched coordinates (α, Υ) as:

$$\frac{\partial}{\partial x} = \frac{\partial \alpha}{\partial x} \frac{\partial}{\partial \alpha} \equiv \frac{1}{\mu_x} \frac{\partial}{\partial \alpha} \qquad (B-1)$$

$$\frac{\partial^2}{\partial x^2} = \frac{1}{\mu_x} \frac{\partial}{\partial \alpha} \left(\frac{1}{\mu_x} \frac{\partial}{\partial \alpha} \right) \qquad (B-2)$$

$$\frac{\partial}{\partial y} = \frac{\partial \Upsilon}{\partial y} \frac{\partial}{\partial \Upsilon} \equiv \frac{1}{\mu_y} \frac{\partial}{\partial \Upsilon} \qquad (B-3)$$

$$\frac{\partial^2}{\partial y^2} = \frac{1}{\partial y} \frac{\partial}{\partial \Upsilon} \left(\frac{1}{\mu_y} \frac{\partial}{\partial \Upsilon} \right) \qquad (B-4)$$

where μ_x and μ_y are stretching coefficients which vary from region to region. Details of determination of the lateral stretching coefficients can be found in Schmalz (1983).

APPENDIX C

EQUATION OF STATE

.

Equation of State

The equation of state used in the present study is (Cox et al., 1967):

$$\Delta\overline{\rho} = \sigma_t = 10^3 \, (\rho-1) = \sum_{ij} a_{ij} \, T^i \, C_s^j$$

$$[Kg/m^3] \qquad\qquad\qquad [^\circ C] \quad [ppt] \qquad\qquad (C-1)$$

where the coefficients A_{ij} are

$$a_{00} = 8 \times 10^{-2} \; ; \; a_{01} \; ; \; a_{02} = 1.3 \times 10^{-4} \; ; \; a_{03} = -6.1 \times 10^{-8} \; ;$$

$$a_{10} = 5.9 \times 10^{-2} \; ; \; a_{11} = 3.3 \times 10^{-3} \; ; \; a_{12} = 2.9 \times 10^{-6} \; ;$$

$$a_{20} = -8 \times 10^{-3} \; ; \; a_{21} = 3.9 \times 10^{-5} \; ;$$

$$a_{30} = 4.77 \times 10^{-5} \qquad\qquad\qquad\qquad\qquad (C-2)$$

APPENDIX D

HYDRAULIC APPLICATIONS OF A SECOND-ORDER CLOSURE MODEL
OF TURBULENT TRANSPORT

Hydraulic Applications of a Second-Order Closure
Model of Turbulent Transport

By

Y. Peter Sheng[1]

INTRODUCTION

Eddy-viscosity models have been widely used for the hydraulic analyses of turbulent transport phenomena in oceans, lakes, and estuaries. If sufficient data is available to establish the validity of the required parameters in the subject models, then the predictions of the models in that particular application give reasonably acceptable results. However, when sufficient data are not available and the parameters for a specific application must be extrapolated from much different situations, the resulting predictions are highly speculative.

For example, sediment transport in coastal waters usually occurs in highly oscillatory flow with appreciable density stratification. The flow may also cause bed forms which in turn affect the flow. In such a situation, large errors could result from the use of standard eddy-viscosity models since these models do not contain the accurate physics describing: (1) the time lag between the mean flow gradients and the turbulent transport; (2) the time-dependent damping of the turbulent transport due to stable density gradients and the counter-gradient turbulent transport due to unstable density gradients; and (3) the partitioning between skin friction drag and profile drag in the vicinity of an arbitrary roughness element.

This paper highlights a turbulent transport model developed to make accurate predictions in turbulent flows where data is unavailable or hard to obtain, using as its strength modeling constants evaluated in situations far-removed from the flow of application. The basic turbulent transport model, originally developed by Donaldson and his associates at A.R.A.P. (1,11,12), involves the retention of the second-order turbulent correlation equations that affect the mean flow variables. The added physics contained in the second-order closure model permit one to directly calculate the phenomena mentioned in the previous paragraph, without resorting to some ad-hoc eddy viscosity fixes.

In the following, I will first give a brief description of the turbulent transport model. I will then discuss three example hydraulic applications of this model to (1) an oscillatory turbulent boundary layer, (2) the transport of momentum, heat, and species within a vegetation canopy, and (3) coastal currents driven by tide, wind, or

---

[1]Consultant, Aeronautical Research Associates of Princeton, Inc., P.O. Box 2229, Princeton, N.J. 08540.

density gradient. Emphasis is placed on the first application and detailed comparison with data. In the second example, a canopy model with some preliminary application is presented. In the third example, adaptation of a condensed version of the turbulent transport model to a mesoscale hydrodynamic model of coastal, estuarine, and lake currents will be outlined.

A TURBULENT TRANSPORT MODEL

The model equations of motion for an incompressible fluid in the presence of both a gravitational and a Coriolis body force, with the mean variables denoted by capitals and the turbulent fluctuations by lower-case, may be written in general tensor notation as follows:

$$\frac{\partial U_i}{\partial t} + U_j \frac{\partial U_i}{\partial x_j} = - \frac{\partial \overline{u_i u_j}}{\partial x_j} - \frac{1}{\rho} \frac{\partial P}{\partial x_i} + g_i \frac{(\Theta-\Theta_o)}{\Theta_o} - 2\varepsilon_{ijk}\Omega_j U_k + \frac{\partial}{\partial x_j}\left(\nu \frac{\partial U_i}{\partial x_j}\right) \quad (1)$$

$$\frac{\partial U_i}{\partial x_i} = 0 \quad (2)$$

$$\frac{\partial \Theta}{\partial t} + U_j \frac{\partial \Theta}{\partial x_j} = - \frac{\partial \overline{u_j \theta}}{\partial x_j} + \frac{\partial}{\partial x_i}\left(\kappa \frac{\partial \Theta}{\partial x_i}\right) \quad (3)$$

$$\frac{\partial \overline{u_i u_j}}{\partial t} + U_k \frac{\partial \overline{u_i u_j}}{\partial x_k} = -\overline{u_i u_k}\frac{\partial U_j}{\partial x_k} -\overline{u_j u_k}\frac{\partial U_i}{\partial x_k} + g_i \frac{\overline{u_j \theta}}{\Theta_o} + g_j \frac{\overline{u_i \theta}}{\Theta_o} - 2\varepsilon_{ik\ell}\Omega_k \overline{u_\ell u_j}$$

$$- 2\varepsilon_{j\ell k} \Omega_\ell \overline{u_k u_i} + 0.3 \frac{\partial}{\partial x_k}\left(q\Lambda \frac{\partial \overline{u_i u_j}}{\partial x_k}\right) - \frac{q}{\Lambda}\left(\overline{u_i u_j} - \delta_{ij}\frac{q^2}{3}\right) - \delta_{ij}\frac{q^3}{12\Lambda} \quad (4)$$

$$\frac{\partial \overline{u_i \theta}}{\partial t} + U_j \frac{\partial \overline{u_i \theta}}{\partial x_j} = - \overline{u_i u_j}\frac{\partial \Theta}{\partial x_j} - \overline{u_j \theta}\frac{\partial U_i}{\partial x_j} + g_i \frac{\overline{\theta^2}}{\Theta_o} - 2\varepsilon_{ijk}\Omega_j \overline{u_k \theta}$$

$$+ 0.3 \frac{\partial}{\partial x_j}\left(q\Lambda \frac{\partial \overline{u_i \theta}}{\partial x_j}\right) - \frac{0.75q}{\Lambda}\overline{u_i \theta} \quad (5)$$

$$\frac{\partial \overline{\theta^2}}{\partial t} + U_j \frac{\partial \overline{\theta^2}}{\partial x_j} = - 2 \overline{u_j \theta}\frac{\partial \Theta}{\partial x_j} + 0.3 \frac{\partial}{\partial x_j}\left(q\Lambda \frac{\partial \overline{\theta^2}}{\partial x_j}\right) - \frac{0.45q\overline{\theta^2}}{\Lambda} \quad (6)$$

$$\frac{\partial \Lambda}{\partial t} + U_j \frac{\partial \Lambda}{\partial x_j} = 0.35 \frac{\Lambda}{q^2}\overline{u_i u_j}\frac{\partial U_i}{\partial x_j} + 0.6bq + 0.3 \frac{\partial}{\partial x_i}\left(q\Lambda \frac{\partial \Lambda}{\partial x_i}\right)$$

$$- \frac{0.375}{q} \left(\frac{\partial q\Lambda}{\partial x_i} \right)^2 + \frac{0.8\Lambda}{q^2} g_i \frac{\overline{u_i \theta}}{\Theta_o} \tag{7}$$

Boussinesque approximation is assumed to be valid such that tne only effect of the density stratification is in the gravitational body force term in the momentum equation (1). Equation (3), a diffusion equation for the temperature perturbation, can be written in terms of the density perturbation. For simplicity, diffusion equation for tne salinity perturbation or other species concentration is not included here. The overbars in the equation denote ensemble-averaged values.

Many of the right hand side terms in the second-order correlation equations, including the stratification and the rotation terms, are determined precisely and hence did not require any modeling. The last three terms in Equation (4) and the last two terms in Equations (5) and (6) are modeled terms representing the effects of third-order correlation, pressure correlation, and viscous dissipation. Four model coefficients appear in these equations. All the right-hand side terms in Equation (7) had to be modeled. Model constants are determined from analyzing a wide class of flow situations and remain invariant for any new applications. Boundary conditions required for the above equations will be described later in the specific examples.

AN OSCILLATORY TURBULENT BOUNDARY LAYER

Oscillatory turbulent shear flow is encountered in a variety of practical flow situations such as blood flow in arteries, flow past helicopter blades, and oceanic bottom boundary layer under a wave. The important role of wave boundary layer in affecting the suspended sediment concentration in shallow water environments has been quantitatively demonstrated by Sheng (15).

Detailed measurements in oscillatory turbulent boundary layers are scarce. Jonsson and Carlsen (7) measured the detailed flow within an oscillating water tunnel with a fixed bottom, while Keiller and Sleath (9) measured the flow near an oscillating wall. Horikawa and Watanabe (3) measured the bottom boundary layer under a progressive wave in a wave tank. By far, the experiments of Jonsson and Carlsen (I will abbreviate with JC) are still the most comprehensive ones. They considered the more realistic case of a fully turbulent flow over a rough bottom. Jonsson (6) found that flow over a rough bottom becomes fully turbulent when the Reynolds number based on the bottom orbital velocity and the free stream amplitude reaches 10^4.

In JC's experiment (Figure 1), an 8.39 sec wave with a maximum mean free stream velocity of 2 to 2.22 m/sec and a nearly sinusoidal time variation was imposed on a water depth of 23 cm. Using a micropropeller, they measured the detailed vertical profiles of ensemble-averaged horizontal velocity within tne water tunnel at 15° intervals through several wave cycles.

Due to the lack of quantitative understanding of the turbulent transport processes, all existing theoretical analyses of oscillating turbulent boundary layer are based on some ad-hoc eddy viscosity

models. Multi-layered (8) and time-dependent (6) eddy viscosities had to be used to achieve reasonable prediction of certain parameters. Grant and Madsen (2) predicted the velocity profiles of JC's experiment with reasonable accuracy, but failed to predict the phase relationship accurately.
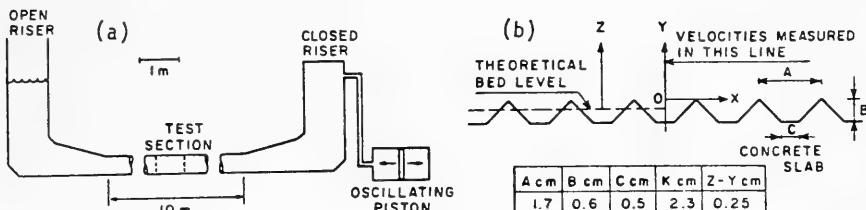
Fig. 1.   Jonsson and Carlsen's oscillatory flow facility: (a) the water tunnel, (b) the bottom roughness elements.

Using the one-dimensional version of the turbulent transport model described above, we performed a simulation of the oscillatory turbulent boundary layer measured by JC. The computational domain extends vertically from $Z=Z_0=0.077$ cm at the bottom to $Z=17$ cm at the top.   For simplicity, we assume the mean longitudinal velocity at the top to be sinusoidal with an amplitude of 2m/sec. Turbulent correlations at the top are assumed to be negligible. A time-periodic horizontal pressure gradient which balances the time variation of wave orbital velocity at the top boundary, was imposed at all vertical levels. At the lower boundary, all turbulent correlations are assumed to have a zero gradient, except that the gradient of $\overline{uw}$ balances the horizontal pressure gradient. Mean velocities are taken as zero at the bottom. To avoid the necessity of having to resolve the extremely small turbulence time scales in the immediate vicinity of the bottom, Λ is assumed to vary linearly with height below a certain height, and is determined from the dynamic equation (7) from there on. The nonlinear inertia terms are neglected, a valid assumption so long as the wave orbital velocity is much smaller than the phase speed of the wave.   The model was run for several cycles until the results reached a quasi steady state, i.e., when results do not change from cycle to cycle.

The mean velocity profiles computed by our model at $\phi=0^\circ$, 45°, 90°, 135°, and 180° are shown in Figure 2. Excellent agreement between our results and JC's data was achieved. At peak amplitude, our model prediction shows a slightly higher overshoot at the mid-level. It is interesting to note that the velocity profiles at 45° and 135° are quite different. Adverse pressure gradient is imposed on the flow at 45°, while favorable pressure gradient is imposed on the flow at 135°. Since the measured free stream velocity is not exactly sinusoidal, the measured velocity profiles have been normalized for comparison with model results.

238

The turbulent shear stress $-\overline{uw}$ computed by our model is also compared with JC's data. As shown in Figure 3, the agreement is very good at $\phi=180°$. However, the agreement is not as good at other ϕ's. Johnson and Carlsen did not measure the shear stresses directly, but instead computed them indirectly from the momentum equation. Due to the relatively coarse time resolution ($\Delta\phi=15°$), errors could be introduced in determining the time derivative of the mean velocities. The computed bottom shear stress does indicate a phase lead of approximately $25°$ over the free-stream velocity, which was also measured by JC. Although our model also computes all the other second-order turbulent correlations, no comparison with data could be made since they were not measured.
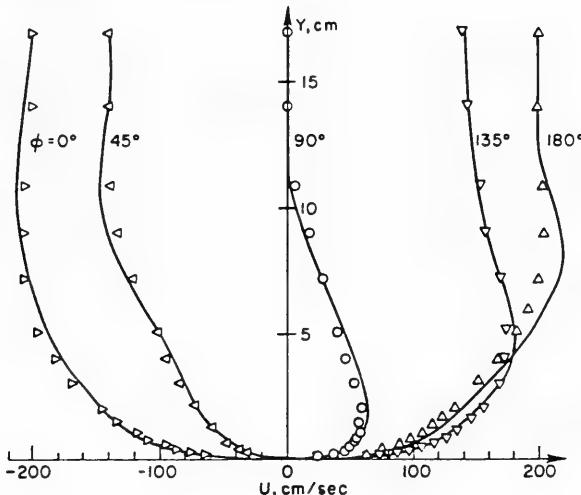
Fig. 2. Velocities vs. height measured from top of roughness element (—— model result, ▷ ◁ ○ ▽ △ JC's data).

The phase lags of horizontal velocities at various levels computed with our model compare very well with JC's data (Figure 4). The horizontal velocity near the bottom shows a phase lead of about $25°$. Grant and Madsen's eddy viscosity model predicted a much worse phase relationship. As shown in Figure 4, their computed phase lead is actually off by more than 25% near the bottom.

In slowly-varying turbulent boundary layers, there exists a thin layer near the bottom within which the turbulence is at equilibrium with the mean flow gradients and the mean flow variables vary logarithmically with height. This so-called logarithmic layer was also detected in JC's experiment on an oscillatory turbulent boundary layer. However, none of the previously mentioned theoretical analyses were able to predict the thickness of this layer and its variation with time. Figure 5 shows the variation of the log-layer thickness within

239
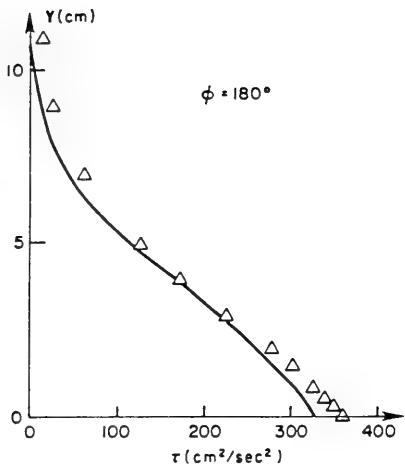
Fig. 3. Turbulent shear stresses vs.
height (—— model result,
△ JC's result).
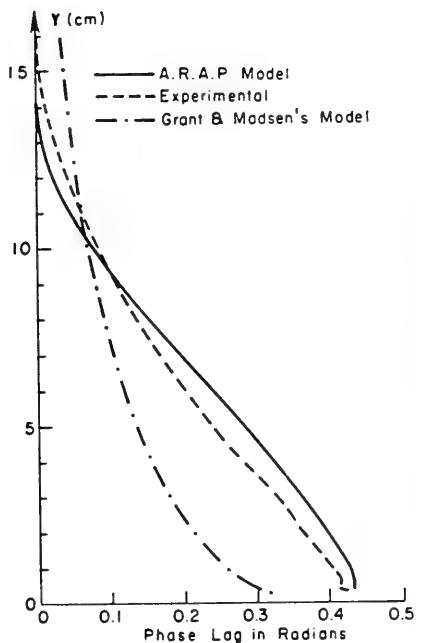
Fig. 4. Vertical profile of phase
lag between mean velocities
and free stream velocity.
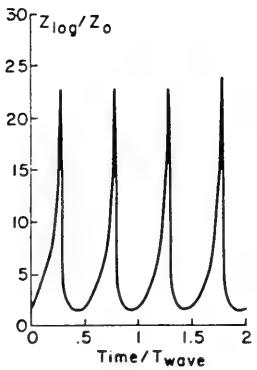
Fig. 5. Computed log-layer thickness
as a function of time over
two wave cycles.

two wave cycles as computed by our model. The log-layer attains its
peak thickness of approximately 25 Z_o shortly after the free-stream
velocity reaches the peak amplitude, and almost completely diminishes
shortly before the free-stream velocity reaches zero. This is
consistent with the velocity profiles shown in Figure 2. For this
analysis, the log-layer thickness is defined as the layer within which
the turbulent kinetic energy is 95% or more of its wall value. If one
defines a log-layer thickness based on the profile of $\overline{uw}$, then the
thickness is slightly increased.

Our model also computes the dynamic length scale of turbulence, Λ, which is a representation of the mean turbulent eddy size. The ratio between this length scale and the total velocity variance, q, represents the time scale associated with the eddy motion. In sediment-laden flows, the relaxation time of sediment particles (W_s/g, where W_s=settling speed) relative to the time scale of turbulent eddies determines whether the particles follow the turbulent eddy motions or not. For a given particle size, there exists a height below which the sediment particles do not follow the turbulent eddy motions and hence the interaction between the particles and the turbulent eddies has to be considered. In such case, the use of a dynamic turbulence model, as opposed to an eddy-viscosity model, is highly desirable and recommended. Tooby et al.(9) performed an interesting laboratory study on the "vortex trapping mechanism" in affecting the suspended sediment concentration in an oscillatory turbulent boundary layer. To include such a mechanism in a predictive model for sediment concentration, it is essential to consider the interaction between sediment particles and turbulent eddies by means of a turbulent transport model such as ours.

TRANSPORT OF MOMENTUM, HEAT, AND MASS WITHIN A VEGETATION CANOPY

A canopy of vegetation represents a complex lower boundary for hydraulic and atmospheric flows (Figure 6). For flow well above this canopy, it is usually adequate to characterize the boundary in terms of only an aerodynamic roughness, Z_o. But when one is interested in the flow within the canopy or immediately above it, a more detailed representation is required.

Flow in vegetated waterways has been modeled empirically (e.g., 4, 10). Although such empirical models may be useful for qualitative flow analysis, a more complete model is required for quantitative estimation of the transfer of momentum, heat, and species within the vegetated environment. Second-order closure models for canopy flow have recently been developed by Wilson and Shaw (20), and Lewellen and Sneng (13). The principal difference between these two models is that the latter consider heat and species transport as well as momentum transport. Lewellen and Sheng also used a more general representation of the drag per unit volume of the vegetation. The model can predict the variation in surface layer heat and species transport as a function of surface Reynolds number, Prandtl number, Schmidt number, and plant area density distribution. Although the basic canopy model was originally designed to aid in the prediction of the dry deposition of gaseous SO_2 and particulate sulfate in the atmosphere, it is quite general and hence provides a basic framework for extension to hydraulic applications.

The canopy introduces source and sink terms into the basic conservation equations. The total drag force due to the canopy is composed of a skin friction drag and a profile drag. The skin friction drag forces of the canopy can be estimated by multiplying the shear stress across the laminar sublayer near the leaf surfaces by the total leaf surface area per unit volume. In addition to the skin friction drag, however, a more important pressure drag is generally imposed by the pressure difference between the upwind and downwind surfaces of a leaf or other object in the flow. We take the total drag term due to

the canopy as

$$D_i = \left[c_f A_w + c_p A_f (1+U_j^2/q^2)^{1/2} \right] q U_i; \text{ with } c_f = c_1 \left(\frac{\nu}{q\Lambda} \right)^{1/4} \tag{8}$$

where c_f is the skin friction drag coefficient and c_p is the profile drag coefficient. The frontal area per unit volume, A_f, and the wetted area per unit volume, A_w, appear in Equation (8). These two areas differ at least by a factor of two and in moderate flow conditions when the leaf aligns itself with the flow they can differ by an order of magnitude.

The sink terms in the energy and species equations may be obtained similarly by considering the transfer of heat and species across the sublayer as

$$\dot{Q} = c_f \left(\frac{\kappa}{\nu} \right)^{0.7} A_w q (\Theta - \Theta_s) \tag{9}$$

$$\dot{C} = c_f \left(\frac{D}{\nu} \right)^{0.7} \left[1 + c_f \left(\frac{D}{\nu} \right)^{0.7} q R_s \right] A_w q C \equiv c_c A_w q C \tag{10}$$

In summary, a term $-D_i$ is added to the mean momentum equation (1), a term $-\dot{Q}$ is added to the mean energy equation (4), and the mean species equation can be written as

$$\frac{\partial C}{\partial t} + U_j \frac{\partial C}{\partial x_j} = -c_c A_w q C - \frac{\partial(\overline{u_i c} - \mathcal{A}_s C)}{\partial x_i} + \frac{\partial}{\partial x_i} \left(D \frac{\partial C}{\partial x_i} \right) \tag{11}$$

Both a source and a sink term need to be added to the Reynolds stress equations:

$$\frac{\partial \overline{u_i u_j}}{\partial t} = 2c_p(U_k^2 + q^2)^{1/2} A_f \overline{u_i u_j} \delta_{ij} - 2c_f A_w q \overline{u_i u_j} \text{ (no sum i,j)} + \ldots \tag{12}$$

The first term represents the creation of wake turbulence due to the profile drag, while the second term recognizes that the skin friction can also dissipate the turbulent fluctuation of velocity. The profile drag can also break up the eddies to increase the dissipation, but this is accounted for in the model by introducing an additional constraint for Λ which is inversely proportional to the plant area density, i.e., $\Lambda \leq \alpha/(c_p A)$. Additional sink terms are added to the temperature and species correlation equations for $\overline{u_i \theta}$, $\overline{u_i c}$, $\overline{\theta^2}$, $\overline{c^2}$, and $\overline{c\theta}$.

The computational domain extends from z=0 at the bottom to z=2h, twice the canopy height. At the top boundary, the mean variables are

242

specified while the turbulent correlations have zero gradient. At the lower boundary, the mean velocities are zero while the temperature is specified. Gradients of all turbulent correlations are zero, except $\overline{w\theta}$ and $\overline{wc}$ which are given from sublayer relationships similar to Equations (9) and (10).

Detailed measurements of mean flow variables and turbulent correlations within vegetated hydraulic environments are unavailable at the present time. Therefore, for model verification, we used the detailed flow measurements within a corn canopy obtained by Shaw et al. (14).

The vertical profile of plant area density of the canopy is shown in Figure 7. We used the measured distribution of Ah shown in Figure 6 as $A_f h$; $\alpha=0.1$ and $C_D=0.16$. $C_1 A_w/A_f$ was given a value of 1 such that the skin friction drag is about one-third of the profile drag within the canopy, a relation measured experimentally by Thom (18). Based on these parameters, our model predictions agree closely with the measured mean longitudinal velocity Reynolds stress, and standard deviation of longitudinal and vertical velocities (Figure 8). Most of the momentum is absorbed within the upper part of the canopy and little is transported to the ground.
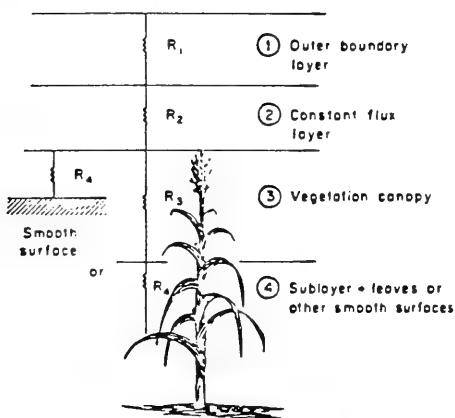
Fig. 6. Four regions of planetary or oceanic boundary layer in the presence of vegetation canopies. R_1, R_2, R_3, and R_4 indicate resistance to species deposition.
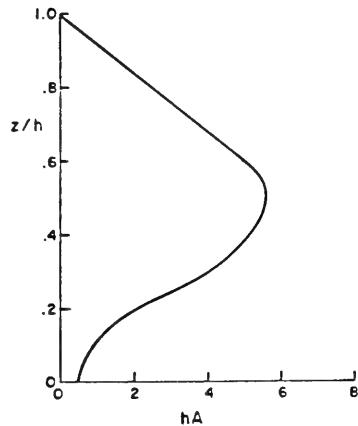
Fig. 7. Profile of plant area density of a corn canopy.

The same basic model was applied to simulate the heat transfer within the corn canopy measured by Shaw et al. in October 1971. The crop changed from 290 cm tall at the beginning of the experiment on
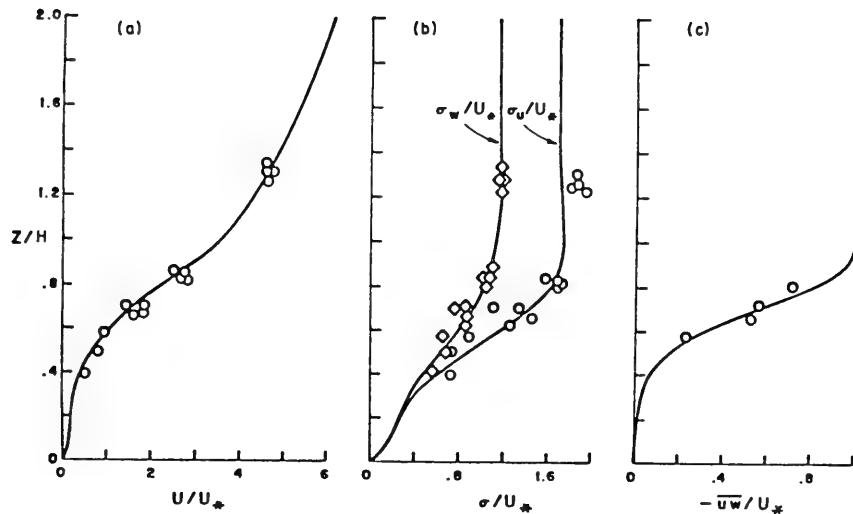
Fig. 8.   Comparison of A.R.A.P. model predictions with data above
a corn canopy.
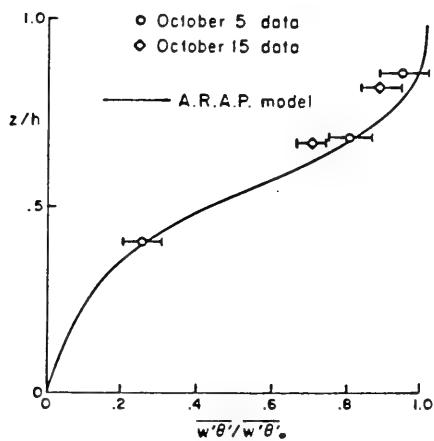
Fig. 9.   Heat transfer within a corn canopy.

October 5 to a noticeably less dense stand of 260 cm height on October
15.   As shown in Figure 9, there is good agreement between the computed
and observed heat transfer rate within the canopy on both dates.

244

Sheng and Butler (15) developed an efficient three-dimensional, time-dependent numerical model of coastal, estuarine, and lake currents. Special computational features included in the model are: (1) a time-splitting technique which separates the computation of the slowly-varying internal mode (3-D variables) from the computation of the fast-varying external mode (water level and vertically-integrated velocities), (2) an efficient ADI algorithm for the computation of the external mode, (3) a vertically-stretched coordinate that allows the same order of accuracy in the vertical direction at all horizontal locations, and (4) an algebraically-stretched horizontal grid that allows concentration of grid lines in regions of special interest. These features make the model suitable for long-term simulation of the dynamic response of coastal, estuarine, and lake waters to winds, tides, and meteorological forcing.

It remains a challenge for hydraulic engineers and oceanographers to properly resolve the turbulent transport phenomena in such meso-scale circulation models. In Sheng and Butler (15), turbulence parameterization is based on the assumption that the production of turbulence equals the dissipation of turbulence. Quadratic stress laws are assumed at the air-sea interface and the bottom. To improve the predictability of the three-dimensional hydrodynamic model, the turbulent transport model described early in this paper could be utilized. The basic model, as represented by Equations (1) through (7) and appropriate boundary conditions, could be applied to the general three-dimensional time-dependent flow. In such a case, however, the numerical computation of all the dynamic equations represents a formidable task. To keep the problem manageable, I believe a condensed version of the turbulent transport model should be used. Assuming a high Reynolds number local equilibrium, the Reynolds stress and heat flux equations form a set of algebraic relationships between the turbulent correlations and the mean flow derivatives. The turbulent dynamics is carried by the dynamic equation for $q^2 = \overline{u_i u_i}$:

$$\frac{\partial q^2}{\partial t} + U_j \frac{\partial q^2}{\partial X_j} = -2\overline{u_i u_j} \frac{\partial U_i}{\partial x_j} - 2g_i \frac{\overline{u_i \theta}}{\Theta_o} + \frac{\partial}{\partial x_i}\left(q_\Lambda \frac{\partial q^2}{\partial x_i}\right) \qquad (13)$$

and Equation (7) for the turbulent macroscale Λ. An extra term needs to be added to each of the $\overline{u_i u_i}$ equations to allow Equation (13) to be added without making the system overdetermined. This approximation allows for much better representation of the turbulent boundary layers in the ocean than do the standard eddy-viscosity models, and should be valid so long as the time scale of turbulence, Λ/q, is less than the time scale of the mean flow.

CONCLUSIONS AND RECOMMENDATIONS

A turbulent transport model suitable for hydraulic applications has been presented. The model gives accurate prediction of the oscillatory turbulent boundary layer measured by Jonsson and Carlsen without having to change any of the model constants. The basic model is being utilized to study the current-wave interaction within the benthic boundary layer (16). A canopy model suitable for atmospneric as well as hydraulic applications is presented, although the effects of additional parameters such as leaf stiffness need to be addressed. By combining the canopy model with a mesoscale ocean circulation model, one can accurately estimate the coastal currents in salt marsnes. The basic canopy model may also be carried over for studying the flow and sediment transport in the vicinity of bed forms. Adaption of a condensend version of the complete turbulent transport model into a three-dimensional, time-dependent numerical model of coastal currents is also discussed. The proposed task should lead to significant improvements in the predictability of coastal circulation models.

ACKNOWLEDGEMENTS

APPENDIX I. - REFERENCES

1. Donaldson, C. duP., "Atmospheric Turbulence and the Dispersal of Atmospheric Pollutants," in *Proceedings of Workshop on Meteorology,* American Meteorological Society, ed. by D. A. Haugen, Science Press,]973, pp. 313-390.

2. Grant, W. D. and Madsen, O. S., "Bottom Friction Under Waves in the Presence of a Weak Current," *NOAA Tech. Rep. ERL-MESA,* 1978, 150 pp.

3. Horikawa, K. and Watanabe. A., "Laboratory Study on Oscillatory Boundary Layer Flow," *Proc. 11th Conf. Coastal Engng.,* Vol. 1, 1969, pp. 467-486.

4. Jackson, G. A., "Effects of a Kelp Bed on Coastal Currents," *EOS, Trans. Amer. Geophys. Union,* Vol. 63, No. 3, 1982, p. 84.

5. Jonsson, I. G., "Measurements in the Turbulent Wave Boundary Layer," *Proc. 10th Congr. Int. Ass. Hydr. Res.,* Vol. 1, 1963, pp. 85-92.

6. Jonsson, I. G., "A New Approach to Oscillatory Rough Turbulent Boundary Layers," *Ocean Engng.,* Vol. 7, 1980, pp. 109-152.

7. Jonsson, I. G. and Carlsen, N. A., "Experimental and Theoretical Investigations in an Oscillatory Rough Turbulent Boundary Layer," *J. Hydr. Res.,* Vol. 14, 1976, pp. 45-60.

8. Kajiura, K., "A Model of the Bottom Boundary Layer in Water Waves," *Bull. Earthq. Res. Inst.*, Vol. 46, 1968, pp. 75-123.

9. Keiller, D. C. and Sleath, J. F. A., "Velocity Measurements Close to a Rough Plate Oscillating in Its Own Plane," *J. Fluid Mech.*, Vol. 73, 1976, pp. 673-691.

10. Kouwen, N., Unny, T. E., and Hill, H. M., "Flow Retardance in Vegetated Channels," *J. of the Irrig. and Drain. Div.*, ASCE, Vol. 95, 1969, pp. 6633-6580.

11. Lewellen, W. S., "Use of Invariant Modeling," in *Handbook of Turbulence*, Vol. 1, ed. by W. Frost, T. H. Moulden, Plenum, 1977, pp. 237-280.

12. Lewellen, W. S., "Modeling the Lowest 1 Km of the Atmosphere," *AGARDograph*, No. 267, 1981, 88 pp.

13. Lewellen, W. S. and Sheng, Y. P., "Modeling of Dry Deposition of SO_2 and Sulfate Aerosols," *EPRI Report No. EA-1452*, Electric Power Research Institute, Palo Alto, CA, 1980.

14. Shaw, R. H., Silversides, R. H., and Thurtell, G. W., "Some Observations of Turbulence and Turbulent Transport Within and Above Plant Canopies," *Boundary Layer Meteorology*, Vol. 5, 1974, pp. 429-449.

15. Sheng, Y. P., "Modeling Sediment Transport in a Shallow Lake," in *Estuarine and Wetland Processes*, ed. by P. Hamilton, Springer-Verlag, 1980, pp. 299-337.

16. Sheng, Y. P. and Butler, H. L., "A Three-Dimensional Numerical Model of Coastal, Estuarine, and Lake Currents," *Proceedings 1982 Army Numerical Analysis and Computers Conference*, Army Research Office.

17. Sheng, Y. P. and Lewellen, W. S., "Current and Wave Interaction Within the Benthic Boundary Layer," *EOS, Trans. Amer. Geophys. Uni* , Vol. 63, No. 3, 1982, pp. 73-74.

18. Thom, A. S., "Momentum, Mass and Heat Exchange of Plant Communities," *Vegetation and the Atmosphere*, Vol. 2, 1975, pp. 57-109.

19. Tooby, P. F., Wick, G. F., and Issacs, J. D., "The Motion of a Small Sphere in a Rotating Velocity Field: A Possible Mechanism for Suspending Particles in Turbulence," *J. Geophys. Res.*, Vol. 82, No. 15, 1977, pp. 2096-2100.

20. Wilson, N. R., and Shaw, R. H., "A Higher Order Closure Model for Canopy Flow," *J. Appl. Meteorol.*, Vol. 16, 1977, pp. 1197-1205.

A	Plant area density
A_f	Frontal plant area density
A_w	Wetted plant area density
C	Mean species concentration
c	Species fluctuation
c_c	Species diffusion coefficient
c_f	Skin friction drag coefficient
c_p	Profile drag coefficient
c_1	Empirical constant
D	Species diffusivity
g	Gravitational acceleration
h	Height of vegetation canopy
k	Nikuradse roughness parameter
P	Mean pressure
q	Root-mean velocity fluctuation
R_1, R_2, R_3, R_4	Resistance to deposition in the four regions shown in Figure 6
T_w	Wave period
t	Time
U_i, U_j, U_k	Mean velocity components
u_i, u_j, u_k	Fluctuating velocity components
U	Mean longitudinal velocity
W	Mean vertical velocity
W_s	Settling speed of particles
x, y	Horizontal coordinates
z	Vertical coordinate
Z_o	Aerodynamic roughness
α	Model constant
$δ_{ij}$	Kronecker delta
$ε_{ijk}$	Alternating tensor
Λ	Turbulent macroscale
H	Mean temperature
Θ	Temperature fluctuation
K	Thermal diffusivity
$δ_u$	Standard deviation of U
$δ_w$	Standard deviation of W
ν	Kinematic viscosity
ρ	Density
φ	Phase angle
Ω	Earth's rotation

HYDRAULIC APPLICATIONS OF A SECOND-ORDER CLOSURE
MODEL OF TURBULENT TRANSPORT

ABSTRACT: A turbulent transport model suitable for hydraulic
applications is presented. The basic model retains the dynamic
equations of second-order turbulent correlations that affect the
mean flow, and hence allows much more accurate predictions than the
standard eddy-viscosity models do. Three example applications of
this model are given: (1) an oscillatory turbulent boundary layer,
(2) the transport of momentum, heat, and species within a vegetation
canopy, and (3) coastal currents driven by wind, tide, or density
gradient. Results of the first example are discussed in detail.

APPENDIX E

ADVECTIVE SCHEMES

APPENDIX E

Advective Schemes

The finite-difference simulation of dispersion of contaminants (heat, salt, sediments, etc.) over large coastal regions is often carried out with a limited number of grid points. In this case, the choice of the convective scheme becomes very crucial. In general, it is desirable to have a convective scheme which can maintain accuracy, positivity, and conservation in the results.

In this appendix, four convective schemes with differing amounts of numerical diffusion and dispersion are compared. These schemes are: (1) the upwind difference scheme (Roache, 1972), (2) the combined upwind and central difference scheme (Sheng, 1975), (3) the central difference scheme with smoothing (Sheng, Segur, and Lewellen, 1978), and (4) the flux-corrected transport scheme (Boris and Book, 1976; Zalesak, 1979). The details of these schemes are briefly described in the following.

We will consider the conservation equation of a passive contaminant in two spatial dimensions (x and z):

$$\frac{\partial C}{\partial t} + \frac{\partial uC}{\partial x} + \frac{\partial wC}{\partial z} = 0 \qquad (E-1)$$

where the flow field (u,w) is computed from some hydrodynamic model. Various numerical schemes have been developed to approximate the convection terms in the above equation. Numerical schemes introduce errors in the form of artificial numerical diffusion and/or numerical dispersion which often manifests itself in the form of short-wave oscillations (with wavelength typically twice the spatial grid spacing). In the present section, four convective schemes are described with respect to Eq. (E-1) and the numerical grid shown in Figure E.1. The finite difference form of Eq. (E-1) can be written in the following general form:

$$C^{n+1}_{i,k} = C^n_{i,k} - \frac{\Delta t}{\Delta x \Delta z} (f_R - f_L + g_T - g_B) \qquad (E-2)$$
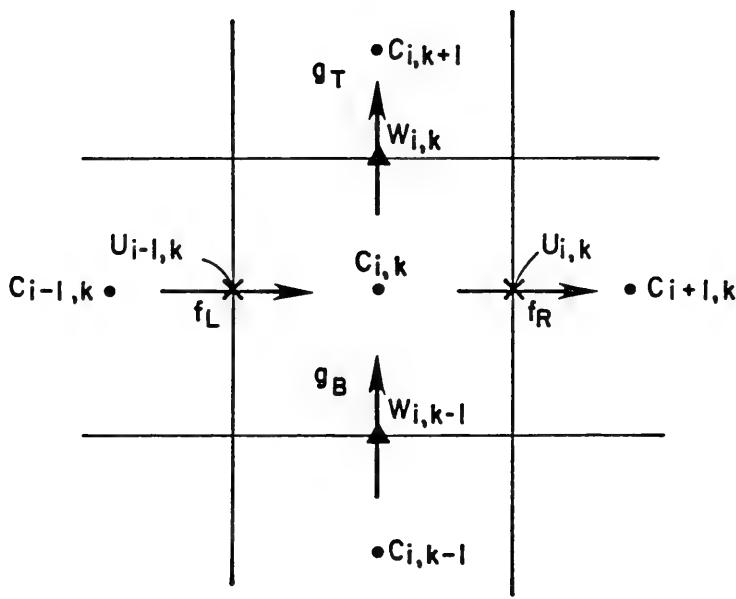
Figure E.1 – Grid structure for solving the two-dimensional transport
equation.

`

where f_R and f_L are the mass flux across the right and left boundary of the grid cell surrounding $C_{i,k}$, while g_T and g_B are mass flux across the top and bottom boundary.

Upwind Difference Scheme

In the upwind scheme, the fluxes are defined according to the direction of the flow along each boundary, e.g.,

$$f_R = \quad u_{i,k} \cdot C_{i+1,k} \qquad \text{if } u_{i,k} < 0$$

$$u_{i,k} \cdot C_{i,k} \qquad \text{if } u_{i,k} > 0 \qquad \text{(E-3)}$$

Combined Upwind and Central Difference Scheme

Sheng (1975) combined the upwind and central difference schemes in the following fashion:

$$f_R = \begin{cases} u_{i,k} \cdot C_{i,k} & \text{if } u_{i,k} > 0 \text{ and } C_{i,k} < C_{i+1,k} \\[2mm] u_{i,k} \cdot (C_{i,k} + C_{i+1,k})/2 & \text{if } u_{i,k} > 0 \text{ and } C_{i,k} > C_{i+1,k} \\[2mm] u_{i,k} \cdot C_{i+1,k} & \text{if } u_{i,k} < 0 \text{ and } C_{i,k} > C_{i+1,k} \\[2mm] u_{i,k} \cdot (C_{i,k} + C_{i+1,k})/2 & \text{if } u_{i,k} < 0 \text{ and } C_{i,k} < C_{i+1,k} \end{cases} \qquad \text{(E-4)}$$

This will reduce the strong numerical diffusion introduced by the upwind scheme except when it is needed to avoid the possibility of generating negative concentrations.

Central Difference Scheme with Spatial Smoothing

The central difference scheme contains less numerical diffusion than the upwind scheme but often produces numerical noise in the form of grid-to-grid oscillation, particularly when the grid points are too sparse to adequately resolve a given change in a variable. In the absence of strong physical damping, growth of these short-wave oscillations seriously deteriorates the numerical solution and may even lead to instability. We have designed a spatial smoothing scheme (Sheng, Segur, and Lewellen, 1978) to damp these short-wave oscillations out of the numerical solution while maintaining reasonable accuracy in the background solution.

Given a solution profile at an instant of time, the smoothing scheme first chests for the slopes and curvatures at each point. For example, a typical profile of a one-dimensional variable V containing short-wave oscillations is shown in Figure E.2. The profile at a typical point C is considered to contain a peak (no smoothing applied otherwise) if:

$$\Delta_R + \Delta_L > \mu \Delta_T \tag{E-5}$$

where

$$\Delta_R = \left| V_{j+1} - V_j \right| / \Delta x$$

$$\Delta_L = \left| V_j - V_{j-1} \right| / \Delta x$$

$$\Delta_T = \left| V_{j+1} - V_{j-1} \right| / 2\Delta x$$

and μ is a constant not smaller than 2. If Eq. (E-5) is satisfied, the curvature at C is then compared with those at two neighboring points to see if the peak is associated with short-wave or long-wave oscillations. It is considered to be a short-wave oscillation if:

$$\Delta^2 \times \Delta_R^2 < 0 \tag{E-6}$$

or
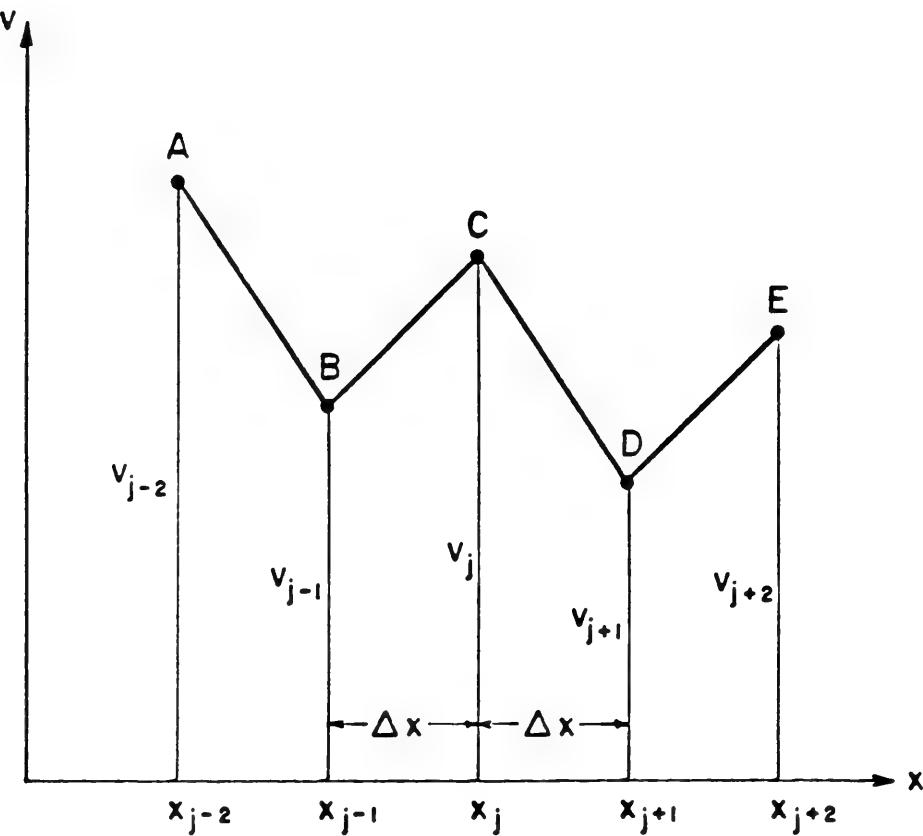
Figure E.2 - A typical profile containing short-wave oscillations.

$$\Delta^2 \times \Delta_L^2 < 0 \qquad \text{(E-7)}$$

where

$$\Delta^2 = (V_{j+1} + V_{j-1} - 2V_j)/(\Delta x)^2$$

$$\Delta_R^2 = (V_{j+2} + V_j - 2V_{j+1})/(\Delta x)^2$$

$$\Delta_L^2 = (V_j + V_{j-2} - 2V_{j-1})/(\Delta x)^2$$

If Eq. (E-5) and either Eq. (E-6) or (E-7) is true, smoothing is applied in the following manner:

$$\hat{V}_j = V_j + \beta(V_{j+1} + V_{j-1} - 2V_j) \qquad \text{(E-8)}$$

where $\hat{V}_j$ is the smoothed result at C, and β is a positive constant.

First, the central difference scheme in the following form is applied to solve Eq. (E-1):

$$f_R = u_R \cdot (C_{i+1,k} + C_{i,k})/2 \qquad \text{(E-9)}$$

At the end of a computational step, the solution profiles along the horizontal direction are first checked and smoothing is applied when necessary. Profiles along the vertical direction are then checked and smoothed in a similar manner. The smoothing scheme performed remarkably in many of the problems we tested (Sheng, Segur, and Lewellen, 1978; Lewellen and Sheng, 1981). Extensive tests indicated that $\beta = 1/4$ and $\mu = 4$ gave the best results.

Flux-Corrected-Transport (FCT) Scheme

This scheme was developed originally by Boris and Book (1973), subsequently improved several times (Boris and Book, 1976), and most recently implemented by Zalesak (1979). This method is a two step method involving a low order calculation and a correction to a higher order. The correction is controlled to maintain stability and sharp change of the physical variables. The upwind scheme is used to compute the first order result:

$$C_{i,k}^{td} = C_{i,k}^{n} - \frac{\Delta t}{\Delta x \Delta z} (f_R^{(1)} - f_L^{(1)} + g_T^{(1)} - g_B^{(1)}) \qquad \text{(E-10)}$$

where $C_{i,k}^{td}$ is the first order (transported and diffused) concentration, $f_R^{(1)}$ is computed according to Eq. (E-3).

A higher order scheme, e.g., the central difference scheme, can be applied to compute higher order fluxes $f_R^{(2)}$, $f_L^{(2)}$, $g_T^{(2)}$, and $g_B^{(2)}$ according to Eq. (E-9). Antidiffusive fluxes are then defined as:

$$A_R = f_R^{(2)} - f_R^{(1)}$$
$$A_L = f_L^{(2)} - f_L^{(1)} \qquad \text{(E-11)}$$
$$A_T = g_T^{(2)} - g_T^{(1)}$$
$$A_B = g_B^{(2)} - g_B^{(1)}$$

It is these antidiffusive fluxes that are limited in the FCT scheme (Zalesak, 1979) such that:

$$A_R^C = A_R \cdot D_{i+1/2,k} \qquad 0 < D_{i+1/2,k} < 1$$
$$A_L^C = A_L \cdot D_{i-1/2,k} \qquad 0 < D_{i-1/2,k} < 1 \qquad \text{(E-12)}$$
$$A_T^C = A_T \cdot D_{i,k+1/2} \qquad 0 < D_{i,k+1/2} < 1$$
$$A_B^C = A_B \cdot D_{i,k-1/2} \qquad 0 < D_{i,k-1/2} < 1$$

Thus:

$$C_{i,k}^{n+1} = C_{i,k}^{td} - \frac{\Delta t}{\Delta x \Delta z} (A_R^C - A_L^C + A_T^C - A_B^C) \qquad \text{(E-13)}$$

The detailed of choosing the coefficients D's can be found in Zalesak (1979).

.

Comparison of Four Schemes

The problem considered here is the transport of a passive dye by wind-driven currents in a two-dimensional basin (Figure E.3). Initially, dye of 1000 mg/ℓ concentration is injected into the four numerical grids on the upper left corner while the background concentration is zero everywhere. The concentration contours at the end of one-day simulation are shown in Figures E.4 through E.7. Due to the strong numerical diffusion of the upwind scheme, the peak in Figure E.4 has dropped to 454 and the front of the 100 mg/ℓ contour has almost reached the right boundary. The results of the combined upwind and central difference scheme in Figure E.5 are appreciably improved over the upwind results. The central difference scheme with smoothing maintains the peak closest to its original value of 1000 mg/ℓ, as shown in Figure E.6. The smoothing scheme generally works quite well in the interior region (Sheng, Segur, and Lewellen, 1978), but is not able to remove a few negative concentration values adjacent to the boundary. The flux-corrected transport scheme, as shown in Figure E.7, is able to maintain a peak close to that in Figure E.6, and in the mean time does not produce negative concentration values.

In conclusion, it appears that both the central difference scheme with smoothing and the flux-corrected transport scheme are superior to the upwind scheme. In the absence of negative concentration values, the two schemes are quite comparable. If the problem of interest contains sharp gradients near the boundaries, or contains very little background diffusion, the flux-corrected transport scheme should be used. Otherwise, either scheme may be applied. The ability of the smoothing scheme in controlling short-wave oscillations has also been demonstrated in realistic meteorological problems (Lewellen and Sheng, 1981).
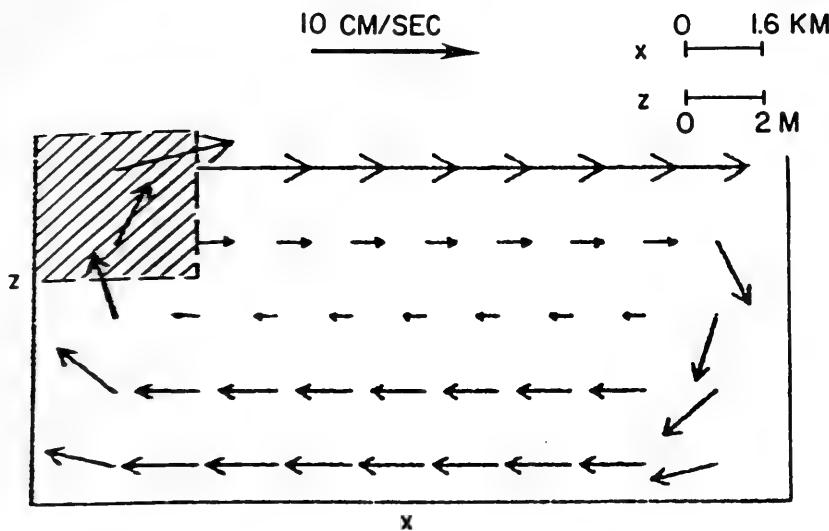
Figure E.3 - Steady-state, wind-driven currents caused by a 5 m/sec wind in a two-dimensional enclosed basin. Dye of 1000 mg/l is being released at the upper left corner.
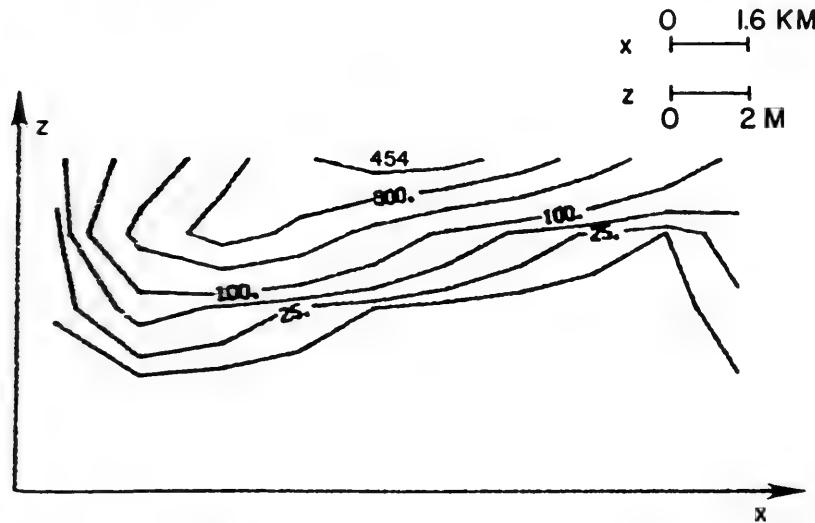
Figure E.4 - Dye concentration after 1 day of release and driven by the currents in E.3. Computed with upwind scheme.

261
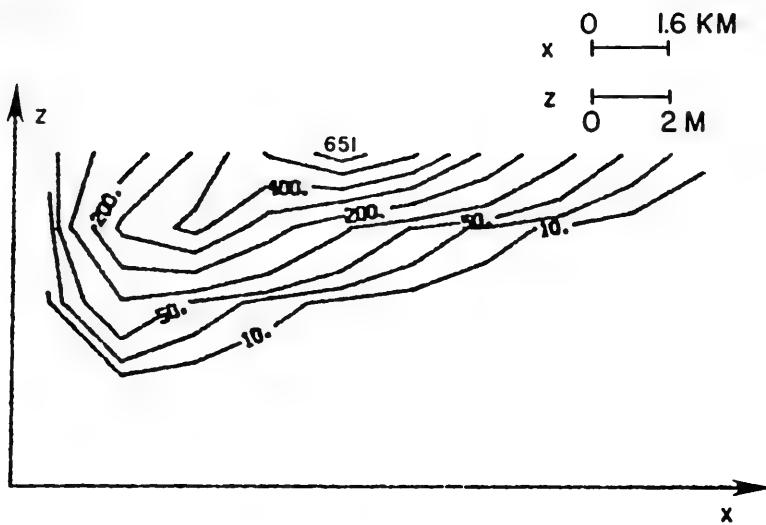
Figure E.5 - Same as E.4 except computed with the combined upward and and central difference scheme.
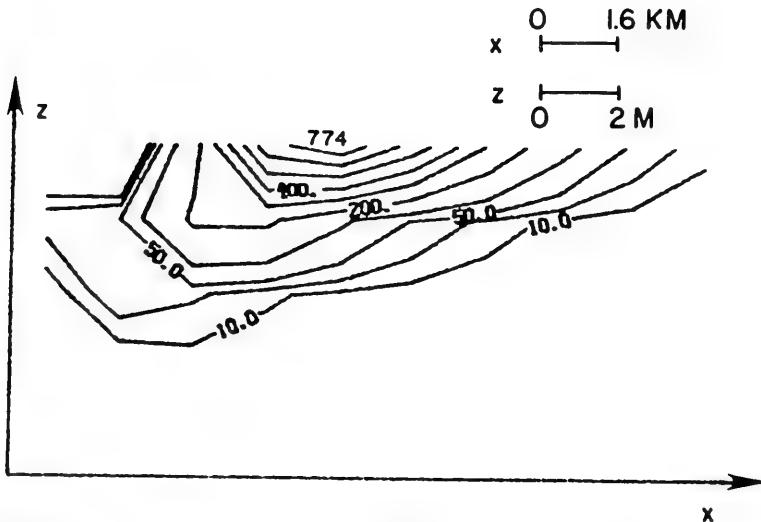
Figure E.6 - Same as E.4 except computed with central difference scheme with smoothing.
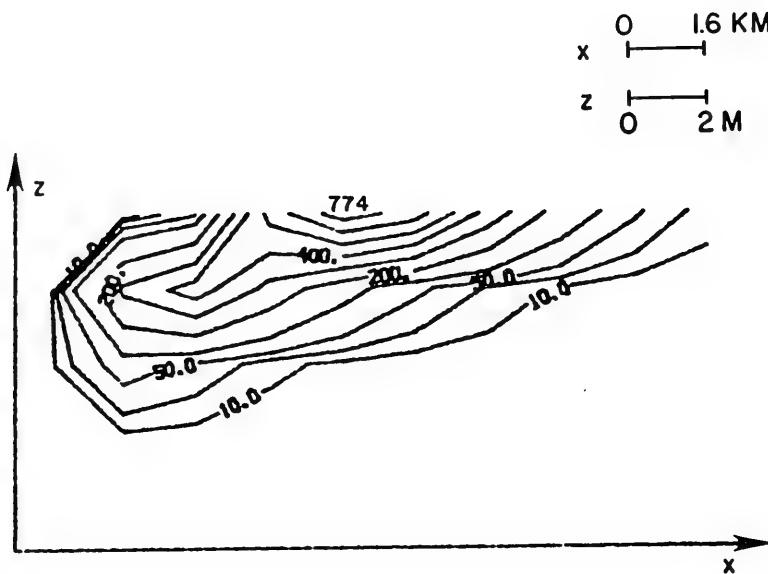
Figure E.7 - Same as E.4 except computed with FCT scheme.

.

.

APPENDIX F

MODELING COASTAL CURRENTS & SEDIMENT TRANSPORT

MODELING COASTAL CURRENTS AND SEDIMENT TRANSPORT

by

Y. Peter Sheng[1]
and
H. Lee Butler[2]

ABSTRACT

An efficient three-dimensional model of coastal currents and
sediment transport has been developed. Simulations of tide- and
wind-driven currents and sediment transport in the Mississippi Sound
are presented. Results of a laboratory study on settling,
resuspension, and deposition of sediment are briefly described. Wave
effect on sediment resuspension is also addressed.

INTRODUCTION

Sediment transport in shallow coastal waters is an important
coastal engineering problem. Many coastal waters, e.g. the Mississippi
Sound, are receiving greater environmental concern due to increasing
utilization of their resources, including dredging of shipping channels
and disposal of dredged materials. To develop a regional plan of
dredged material disposal alternatives, one should not only be
concerned with the short-term fate of dredged material at specific
sites, but more importantly the subsequent resuspension, transport, and
deposition of sediment due to combined current and wave actions,
particularly during the sporadic high-energy events.

The various physical processes that can affect the distribution of
sediment in a coastal environment are shown in Figure 1. Definitive
quantitative understanding of the various processes is crucial to the
success of any large-scale model. Recent improvements in numerical
estimation of currents and waves and the increased availability of
field data and satellite imageries has made it feasible to carry out
meaningful large-scale simulation studies of sediment transport events
(e.g. Sheng and Lick, 1979; Sheng, 1980). In this paper, we highlight
a systematic study of the sediment transport in the shallow coastal
waters of the Mississippi Sound and adjacent continental shelf waters
in the Gulf of Mexico.

---

[1]Aeronautical Research Associates of Princeton, Inc., P.O. Box 2229,
Princeton, NJ 08540 U.S.A.
[2]Wave Dynamics Division, Hydraulics Laboratory, U.S. Army Engineer
Waterways Experiment Station, P.O. Box 631, Vicksburg, MS 39180
U.S.A.

In the following, a three-dimensional hydrodynamic model will be presented first, followed by a realistic simulation of tide- and wind-driven currents in the Mississippi Sound and adjacent shelf waters. Transport, resuspension, and deposition of cohesive sediments are then discussed, followed by a discussion on the bottom boundary layer and wave effect.
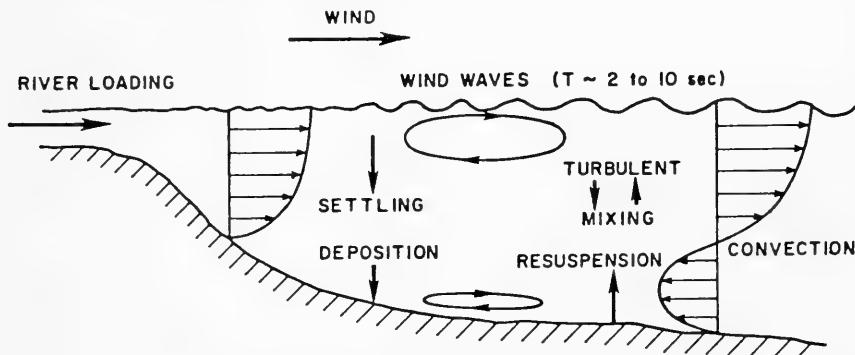
Figure 1.   Schematics of Dominant Mechanisms Affecting Sediment Distribution in Shallow Coastal Waters.

A THREE-DIMENSIONAL NUMERICAL MODEL OF COASTAL CURRENTS

In order to study the dynamic response of coastal waters to tides, winds, and meteorological forcing, a three-dimensional, free-surface, time-dependent model is often desired. In addition, stratification and complex topography have to be properly resolved. For relatively long-term application, computational efficiency of the model is extremely important. Traditional three-dimensional, free-surface models (e.g., Leendertse and Liu, 1975) require an exceedingly small time step (associated with the propagation of gravity wave over the distance of a horizontal grid spacing), and hence require extraneous computational costs.

Special features of the present model include (1) a "mode-splitting" procedure which allows efficient computation of the vertical flow structures (internal mode), (2) an efficient ADI scheme for the computation of the vertically-integrated variables (external mode) (3) an implicit scheme for the vertical diffusion terms, (4) a vertically and horizontally stretched coordinate system, and (5) a turbulence parameterization which requires relatively little tuning.

Governing Equations and Boundary Conditions

The basic equations describing the large-scale motion in a large body of water consist of a continuity equation, momentum equations, conservation equations of heat and salinity, and an equation of state. For simplicity here, the last three equations have been combined into an equation for the density. Inherent assumptions are: (1) pressure

Sheng

distribution is hydrostatic in the vertical direction, (2) Boussinesq approximation is valid, and (3) non-constant eddy viscosities and diffusivities are used to describe the turbulence. The resulting equations are as follows:

$$\frac{\partial u}{\partial x} + \frac{\partial v}{\partial y} + \frac{\partial w}{\partial z} = 0 \tag{1}$$

$$\frac{\partial u}{\partial t} = -\left(\frac{\partial u^2}{\partial x} + \frac{\partial uv}{\partial y} + \frac{\partial uw}{\partial z}\right) + fv - \frac{1}{\rho_0}\frac{\partial p}{\partial x} + \frac{\partial}{\partial z}\left(A_v \frac{\partial u}{\partial z}\right) + \nabla_H \cdot (A_H \nabla_H u) \tag{2}$$

$$\frac{\partial v}{\partial t} = -\left(\frac{\partial uv}{\partial x} + \frac{\partial v^2}{\partial y} + \frac{\partial vw}{\partial z}\right) - fu - \frac{1}{\rho_0}\frac{\partial p}{\partial y} + \frac{\partial}{\partial z}\left(A_v \frac{\partial v}{\partial z}\right) + \nabla_H \cdot (A_H \nabla_H v) \tag{3}$$

$$\frac{\partial p}{\partial z} = -\rho g \tag{4}$$

$$\frac{\partial \rho}{\partial t} = -\frac{\partial u\rho}{\partial x} + \frac{\partial v\rho}{\partial y} + \frac{\partial w\rho}{\partial z} + \frac{\partial}{\partial z}\left(K_v \frac{\partial \rho}{\partial z}\right) + \nabla_H \cdot (K_H \nabla_H \rho) \tag{5}$$

where x and y are the horizontal coordinates; z is the vertical coordinate pointing vertically upward to form a right-handed coordinate system with x and y; u, v, and w are the three-dimensional velocities in the x, y, and z directions; t is time; f is the Coriolis parameter; g is the gravitational acceleration; p is the pressure; ρ is the density; A_H, and K_H are the horizontal eddy coefficients; A_V and K_V are the vertical eddy coefficients; and

$$\nabla_H \cdot (A_H \nabla_H E) = \frac{\partial}{\partial x}\left(A_H \frac{\partial E}{\partial x}\right) + \frac{\partial}{\partial y}\left(A_H \frac{\partial E}{\partial y}\right) \tag{6}$$

At the free surface, the appropriate boundary conditions are: (a) the wind stress is specified,

$$\rho_0 A_v \left(\frac{\partial u}{\partial z}, \frac{\partial v}{\partial z}\right) = (\tau_{sx}, \tau_{sy}) = \rho_a C_{da} (u_w^2 + v_w^2)^{1/2} (u_w, v_w) \tag{7}$$

where τ_{sx} and τ_{sy} are the wind stresses in the x and y directions respectively, ρ_a is the air density, C_{da} is the drag coefficient and (u_w, v_w) are the wind velocities at a certain height above the surface; (b) the kinematic condition is satisfied,

$$w = \frac{\partial \zeta}{\partial t} + u \frac{\partial \zeta}{\partial x} + v \frac{\partial \zeta}{\partial y} \tag{8}$$

where ζ is the elevation of the free surface; (c) the dynamic condition is satisfied, i.e., $p=p_a$, where p_a is the atmospheric pressure; and (d) the density flux, i.e., the heat flux and the salt flux, is specified.

At the bottom, the boundary conditions are: (a) a quadratic stress law is valid:

Sheng

$$\rho_0 A_v \left(\frac{\partial u}{\partial z}, \frac{\partial v}{\partial z}\right) = (\tau_{bx}, \tau_{by}) = \rho C_d (u_1^2 + v_1^2)^{1/2} (u_1, v_1) \tag{9}$$

where τ_{bx} and τ_{by} are the bottom shear stresses, C_d is the skin-friction coefficient, and (u_1, v_1) are the velocities at the first grid point above the bottom, and (b) heat flux (or temperature) and the salt flux are specified.

Grid Structure

Anticipating appreciable variation of bottom topography in the horizontal direction, the x,y,z coordinate system is vertically-stretched to a x,y,σ coordinate system, such that an equal number of grid points exist in the shallow coastal and the deep offshore areas (Figure 2a). The transformation takes the form:

$$\sigma = \frac{z - \zeta(x,y)}{h(x,y) + \zeta(x,y)} = \frac{z - \zeta}{H} \tag{10}$$

where h (x,y) is the local water depth and $\zeta(x,y)$ is the free-surface
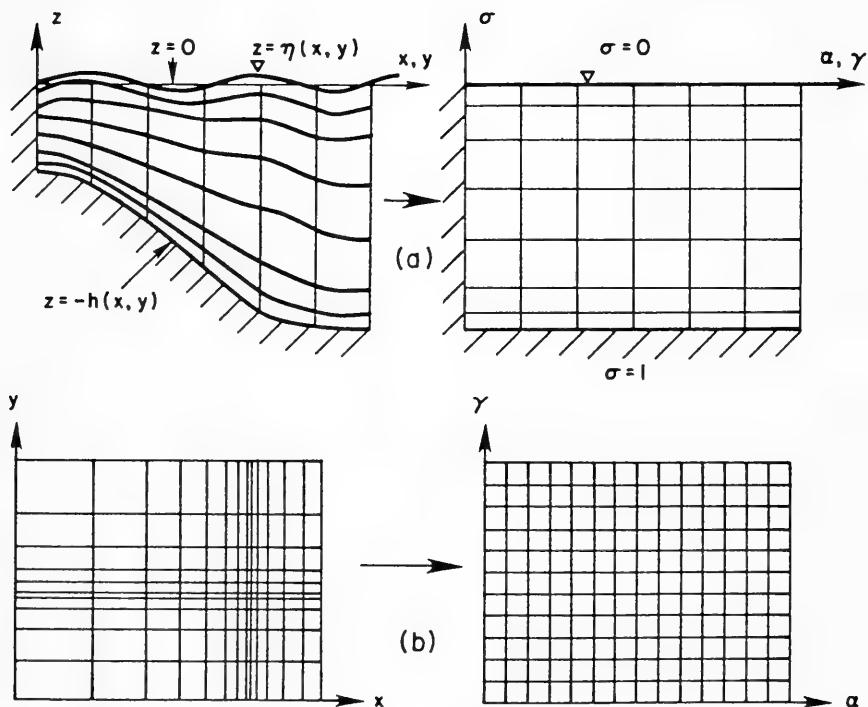
Figure 2(a). Vertical Stretching of the Coordinates,
(b). Horizontal Stretching of the Coordinates.

270   Sheng

elevation. Such a transformation leads to (1) the same order of numerical accuracy in the vertical direction at all horizontal locations, and (2) a smooth representation of the bottom topography. Although additional terms are introduced by this transformation, the advantages warrant its application. Models using regular rectangular grid in the vertical direction cannot accurately resolve the shallow coastal area unless a large number of grid points is used in the deeper offshore area. In addition, if the bottom is approximated by a series of rectangular steps, estimate on bottom stress may be distorted and hence is not suitable for studying sediment transport problems.

To better resolve the complex shoreline geometries and bottom features, a non-uniform grid is often required in the x and y directions (Butler and Sheng, 1982). To allow ease in numerical analysis and as shown in Figure 2b, this non-uniform grid (x,y,z) is further mapped into a uniform grid (α,γ,σ):

$$x = a_x + b_x \alpha^{c_x} \quad ; \qquad y = a_y + b_y \gamma^{c_y} \tag{11}$$

The transformed three-dimensional equations of motion in α,γ,σ grid system are rather complex. Detailed equations and boundary conditions in non-dimensional form can be found elsewhere (Sheng, 1981). Staggered numerical grid is used in both the horizontal and vertical directions.

External Mode

In the present study, numerical computation of the vertical flow structures (internal mode), which are governed by slower dynamics, are separated from the computation of the vertically-integrated variables (external mode). This so-called "mode splitting" technique resulted in significant improvement of the numerical efficiency of a three-dimensional hydrodynamic model for Lake Erie (Sheng et al., 1978). It allows for computation of the three-dimensional flow structures with minimal additional cost over computation of the two-dimensional flow with a vertically-integrated model.

The external mode is described by the water level (ζ) and the vertically-integrated mass fluxes $(U,V) \equiv \int_{-1}^{0} (u,v) \, H d\sigma$. Performing vertical integration of the transformed three-dimensional equations of motion, and rewriting (α,γ) as (x,y) for simplicity, we obtain:

$$\frac{\partial \zeta}{\partial t} + \frac{1}{\mu_x} \frac{\partial U}{\partial x} + \frac{1}{\mu_y} \frac{\partial V}{\partial y} = 0 \tag{12}$$

$$\frac{\partial U}{\partial t} = -\left[\frac{1}{\mu_x} \frac{\partial}{\partial x} \left(\frac{U^2}{H} \right) + \frac{1}{\mu_y} \frac{\partial}{\partial y} \left(\frac{UV}{H} \right) + H(u\omega)_{\sigma=0} \right] - fV - \frac{gH}{\mu_x} \frac{\partial \zeta}{\partial x} + \frac{1}{\rho_0} (\tau_{sx} - \tau_{bx})$$

$$- \frac{1}{\rho_0 \mu_x} \int_{-1}^{0} \left[gH \int_{\sigma}^{0} \frac{\partial \rho}{\partial x} \, d\sigma + g \frac{\partial H}{\partial x} \left(\int_{\sigma}^{0} \rho d\sigma + \sigma \rho \right) \right] H d\sigma + (H.D.)_x \tag{13}$$

$$\frac{\partial V}{\partial t} = -\left[\frac{1}{\mu_x}\frac{\partial}{\partial x}\left(\frac{UV}{H}\right) + \frac{1}{\mu_y}\frac{\partial}{\partial y}\left(\frac{V^2}{H}\right) + H(v\omega)_{\sigma=0}\right] + fU - \frac{gH}{\mu_y}\frac{\partial\zeta}{\partial y} + \frac{1}{\rho_0}(\tau_{sy}-\tau_{by})$$

$$- \frac{1}{\rho_0\mu_y}\int_{-1}^{0}\left[gH\int_{\sigma}^{0}\frac{\partial\rho}{\partial y}\,d\sigma + g\frac{\partial H}{\partial y}\left(\int_{\sigma}^{0}\rho d\sigma+\sigma\rho\right)\right]Hd\sigma + (H.D.)_y \tag{14}$$

where $\mu_x \equiv dx/d\alpha$ and $\mu_y \equiv dy/d\gamma$ are the stretching coefficients, $\omega \equiv d\sigma/dt$ is the vertical velocity in the stretched coordinate, and $(H.D.)_x$ and $(H.D.)_y$ are the horizontal diffusion terms. Notice that the bottom stresses (τ_{bx}, τ_{by}) are determined from the latest three-dimensional velocity profiles available from the internal mode computation, and hence are more accurate than the traditional vertically-integrated models which assume the bottom stress is proportional to the local vertically-integrated velocity or its square.

Treating implicitly all the terms in the continuity equation, while only the time derivatives and the surface slopes in the momentum equations, one can obtain the following finite-difference equations:

$$(I+\phi\lambda_x+\phi\lambda_y)W^{n+1} = [I+(I-\phi)\lambda_x+(I-\phi)\lambda_y]W^n + \Delta tD^n \tag{15}$$

where

$$\lambda_x = \frac{A\Delta t}{\mu_x\Delta x}\delta_x; \quad \lambda_y = \frac{B\Delta t}{\mu_y\Delta y}\delta_y;$$

$$A = \begin{pmatrix} 0 & 1 & 0 \\ gH & 0 & 0 \\ 0 & 0 & 0 \end{pmatrix}; \quad B = \begin{pmatrix} 0 & 0 & 1 \\ 0 & 0 & 0 \\ gH & 0 & 0 \end{pmatrix}; \quad D = \begin{pmatrix} 0 \\ D_x \\ D_y \end{pmatrix}; \quad W = \begin{pmatrix} \zeta \\ u \\ v \end{pmatrix} \tag{16}$$

where (Δx, Δy) are the spatial grids, Δt is time step, D_x and D_y are terms in Eqs. (13) and (14) excluding the time derivatives and the surface slopes, superscripts n+1 and n indicate present and previous time step of integration, δ_x and δ_y are central difference spatial operators, and ϕ is a weighting factor, $0<\phi<1$. If $\phi=0$, Eq. (15) reduces to a two-step explicit scheme. If $\phi>0$ the resulting schemes are implicit, with $\phi=1/2$ corresponding to the Crank-Nicholson scheme and $\phi=1$ corresponding to the fully implicit scheme. Eq. (15) can be factorized such that solution can be obtained by consecutive tridiagonal matrix inversions in the x-direction and y-direction. Further, we employ a method that solves only two variables during each sweep. This method allows very large time step to be used and has been found to be more stable than the traditional ADI method. Courant number based on the maximum propagation speed of surface gravity wave, $(gH_{max})\cdot\Delta t/\Delta x$, may now be as large as 100, compared to the limit of 1 for the explicit method. The maximum step is now governed by the CFL condition based on vertically-averaged advection speed in the system.

In the full three-dimensional model, the external mode computation

is carried out in conjunction with the internal mode computation. Depending on the problem of interest, the internal mode may be computed every so often with a time step equal to or greater than the external time step.

Internal Mode

The internal mode of the flow is described by the vertical flow structures and the density. Defining perturbation velocities as $u' \equiv u-U/H$ and $v' \equiv v-V/H$, the equations for the internal mode are obtained by subtracting the vertically-averaged momentum equations from the three-dimensional equations:

$$\frac{1}{H} \frac{\partial Hu'}{\partial t} = B_x - \frac{D_x}{H} + \frac{1}{H^2} \frac{\partial}{\partial \sigma} \left[A_v \frac{\partial}{\partial \sigma} \left(\frac{Hu'+U}{H} \right) \right] \tag{17}$$

$$\frac{1}{H} \frac{\partial Hv'}{\partial t} = B_y - \frac{D_y}{H} + \frac{1}{H^2} \frac{\partial}{\partial \sigma} \left[A_v \frac{\partial}{\partial \sigma} \left(\frac{Hv'+V}{H} \right) \right] \tag{18}$$

where B_x and B_y represent all terms in the transformed three-dimensional momentum equations except the surface slopes and the vertical diffusion terms, and D_x and D_y are defined in Eq. (16). Notice that the above equations retain the three-dimensionality and hence are different from the model of Nihoul and Ronday (1983) which is actually a superposition of a two-dimensional model and a vertical one-dimensional model.

The above equations do not contain the surface slope terms and hence a large time step may be used in the numerical computation. In the present model, a two-time-level or three-time-level scheme with a vertically implicit scheme is generally used. The bottom friction terms are also treated implicitly to ensure unconditional numerical stability in shallow waters. Care must be taken to ensure that the vertically-integrated perturbation velocities at each horizontal location (i,j) always equal to zero.

Once the equations for (u',v') are solved, and (u,v) obtained, vertical velocity ω and density ρ may be computed. As mentioned before, the internal mode may be computed as often as the external mode or as desired and as dictated by the problems of interest. The numerical time step for the internal mode is limited by the CFL condition based on the advection speed. In the present study, the drag coefficient C_d in the quadratic bottom stress law Eq. (9) is generally specified as a function of the bottom roughness (z_0), the distance above the bottom (z_1), at which (u_1,v_1) is computed, and the stability function of the bottom flow (ϕ_s):

$$C_d = k^2 \left(\ell n \frac{z_1}{z_0} + \phi_s \right)^{-2} \tag{19}$$

where k is the von Karman constant. It can be shown that the stability may increase (unstable case) or decrease (stable case) the drag

coefficient by as much as 40% (Sheng, 1980).

Turbulence Parameterization

A semi-empirical theory of vertical mixing is used in this study. The effect of stratification, as measured by the Richardson number, Ri, on the intensity of vertical turbulent mixing is parameterized by a number of empirical stability functions:

$$A_v = A_{vo} \, \phi_1 \, (Ri); \quad K_v = K_{vo} \, \phi_2 \, (Ri); \quad Ri = \frac{-g}{\rho} \frac{\partial \rho}{\partial z} \left[\left(\frac{\partial u}{\partial z} \right)^2 + \left(\frac{\partial v}{\partial z} \right)^2 \right]^{-1} \tag{20}$$

where A_{vo} and K_{vo}, are the eddy coefficients in the absence of any density stratification and ϕ_1 and ϕ_2 are stability functions. Traditionally, these stability functions have been determined empirically by comparing model output with measured data. As shown in Figure 3a, great discrepancy exists among the various empirical forms of the stability functions. In addition, the critical Richardson numbers, at which turbulence is completely damped by buoyancy, given by these formulas are much too high (10) compared to the measured value of 0.25 (Erikson, 1978). To unify this discrepancy, stability functions may be determined from a second-order closure model of turbulence. Assuming a balance between turbulence production and dissipation, i.e., the so-called "super-equilibrium" condition (Donaldson, 1973), we can obtain a simpler set of algebraic relationships between the turbulent correlations and mean flow gradients. As shown in Figure 3b, such a stability function leads to a
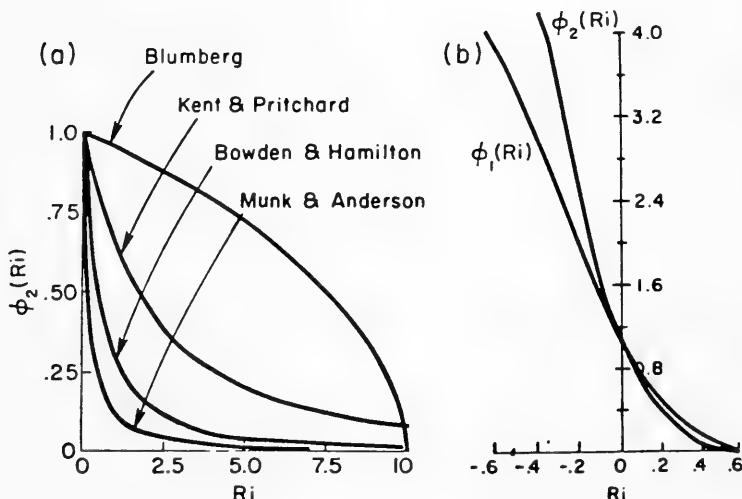

Figure 3.   Stability Function vs. Richardson Number:
            (a). Empirical Formulations,
            (b). "Superequilibrium" Formulation Derived from Reynolds Stress Model.

.

critical Richardson number much closer to 0.25. In addition, such a formulation allows the definition of finite eddy coefficients in the unstable range (Ri < 0). In order to utilize these relationships, a turbulence length scale which varies with depth and Richardson number has to be prescribed empirically.

SIMULATION OF TIDE- AND WIND DRIVEN CURRENTS

The three-dimensional numerical model of coastal currents has been applied to simulate the tide- and wind-driven currents in the Mississippi Sound and adjacent continental shelf waters of the Gulf of Mexico. As shown in Figure 4, the horizontal grid is composed of 116 grid points in the y-direction and 60 grid points in the x-direction. The smallest grid spacing in the computational domain is on the order of 1 km. The water depth varies from only a few meters within the Mississippi Sound and the Mobile Bay to over 1000 m along the southern boundary.
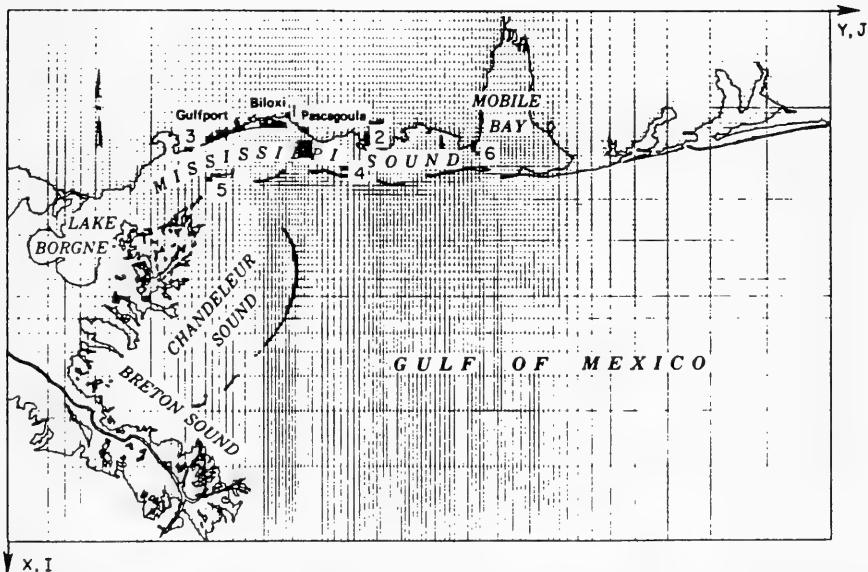
Figure 4.   Computational Grid for Mississippi Sound Simulation.

Tides in the Gulf of Mexico

Gulf tides differ from tides in most other places in the world due to the dominance of the diurnal components K1, O1 and P1 collectively over the semi-diurnal components M2 and S2, except along the west Florida coast. Reid and Whitaker (1981) developed a numerical tide model for the Gulf based on the vertically-integrated, linearized tidal equations to portray the barotropic response of the Gulf to tidal forcing. Forcing at ports was also included with an impedance type condition. Detailed data from 20 tidal gages located in open coastal

waters of the Gulf were used for the fine tuning of their model. Their study confirmed that diurnal tide in the Gulf is primarily a co-oscillating tide driven by adjoining Atlantic Ocean and Caribbean Sea.

The water level response for a given tidal constituent is usually expressed in terms of the surface displacement ζ (Schureman, 1941):

$$\zeta = F(t) \, A(\lambda,\phi) \, \cos \left[\, \omega_0 t + \chi - G \, (\lambda,\phi) \right] \tag{21}$$

where λ is the longitude, ϕ is the latitude, A is the mean amplitude over 18.6 years and G the Greenwich phase or epoch at given position (λ,ϕ), ω_0 is tidal frequency, χ is the astronomical argument, while F is the nodal factor, a slowly varying function of time. Tides at particular stations are characterized by A and G for individual constituents. In our study, A's and G's for 5 constituents (O1, K1, P1, S2 and M2) along the open boundaries of our grid are supplied from Reid and Whitaker's model. Surface displacements at the open boundary stations are determined from a linear combination of those due to the five tidal constituents.

Tidal Currents off the Mississippi Coast

As a first example, tides during 20 Sept. to 25 Sept. 1980 are computed with our three-dimensional model. The surface displacements at four stations (see Figure 4 for locations) within the Mississippi sound are compared with measured data in Figure 5. Notice that the measured data have been filtered such that variations due to short-period oscillations on the order of a few hours or less are not included. Initially, the diurnal tides are predominant. Towards the end of the five-day period, the diurnal tides become somewhat less predominant while the semi-diurnal tides became gradually more apparent. Good agreement is found at all stations.

In this simulation, a relatively large time step of 12 minutes was used for both the external and the internal modes. Seven grid points are used in the vertical direction. A relatively smooth bottom with a roughness length, z_0, of 0.1 cm was assumed. A parabolic length scale, Λ, was assumed in the vertical direction.

The tide-driven horizontal currents at mid-depth are shown in Figure 6 for two stations in the Mississippi Sound. Currents on the order of 30 cm/sec exist at both stations. Again, reasonable agreement is found between data and model results.

The horizontal velocity field at 1 m depth, after 3 days of simulation, is shown in Figure 7. Relatively large currents exist at the various tidal inlets and in the area between the Ship Island and the Chandelier Island. Except in these areas, at this instant of time, bottom shear stress generated by the tidal currents are generally less than 0.8 dyne/cm^2. Hence little sediment resuspension is expected. However, during strong spring tides, such as those during the period of 12 June to 16 June, 1980, relatively stronger currents and bottom shear stresses in excess of 0.8 dyne/cm^2 could prevail within the tidal

Sheng

SURFACE ELEVATIØN AT 18.44 – STATION 1

SURFACE ELEVATIØN AT 22.62 – STATION 2

SURFACE ELEVATIØN AT 24.25 STATION 3

SURFACE ELEVATIØN AT 30.56 STATION 4
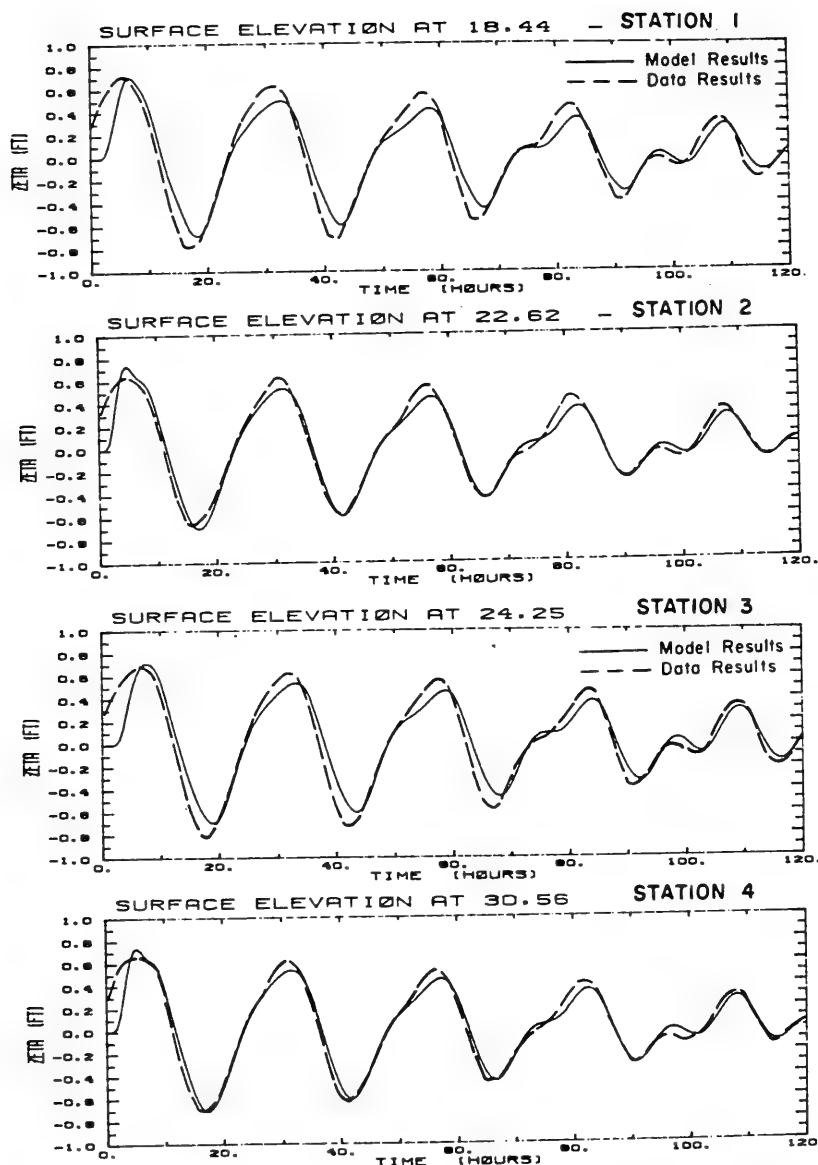
20 SEPT., 1980   25 SEPT., 1980

Figure 5.   Surface Elevation at Four Locations (see Fig. 4)
              from 20 Sept. to 25 Sept., 1980.

277   Sheng
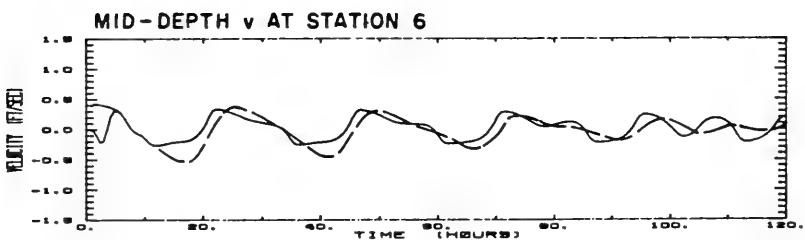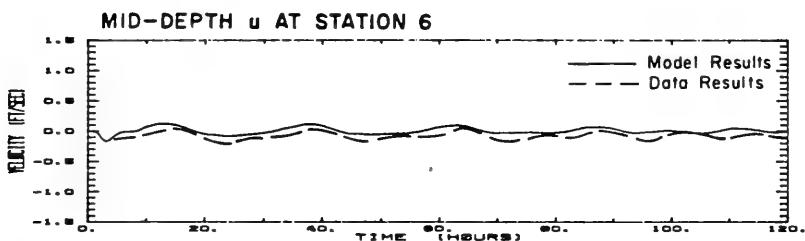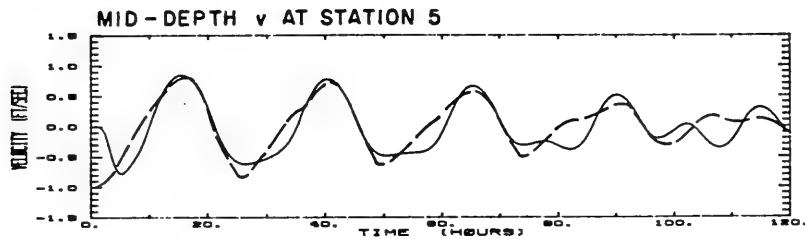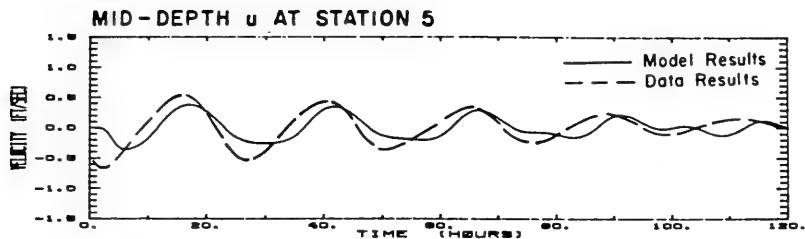
Figure 6.   Mid-Depth Horizontal Velocities at Stations 5 and 6
              from 20 Sept. to 25 Sept., 1980. Tide Forcing Only.

inlets and other shallow areas. Resuspension of cohesive sediment in
these areas might occur and leave behind the coarser non-cohesive
sediment.
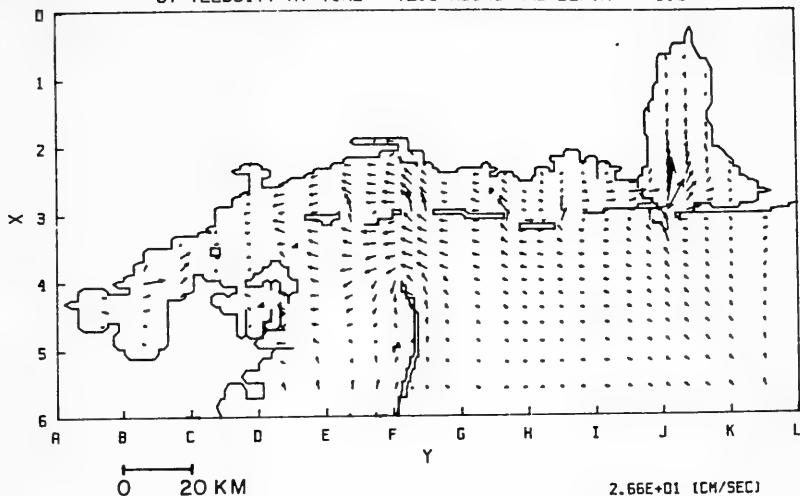
Figure 7.   Tide–Driven Horizontal Velocities at 1 m Depth in the
             Vicinity   of   the   Mississippi   Sound   at   0   hr,
             23 Sept., 1980.

Wind-Driven Currents off the Mississippi Coast

The results presented in the above did not contain any wind-driven
effect.   During   our   study,   wind   data   were   collected   at   several
meteorological stations surrounding the Mississippi Sound.   The wind
during the 5-day period was generally quite mild ($\lesssim$ 5 m/sec) from the
Southeast. To examine the effect of wind on the currents, we carried
out a three-day simulation from 20 Sept., using a uniform wind stress
of 1 dyne/cm^2 from the Southeast. The southeasterly wind caused water
to pile up within the Mississippi Sound, with a set-up on the order of
12 cm along the Northern shore, and only 6 cm behind the barrier
islands.

The influence of wind on the current also depends on the location.
Figure 8 shows the along-shore velocity at 2 locations over the 3-day
period. At Station 5, off Cat Island, the presence of the wind did not
have appreciable effect on the tidal current. At Station 6, within the
pass between the Mississippi Sound and the Mobile Bay, the wind caused
significant flow from the Mobil Bay into the Sound. This resulted in a
significantly larger bottom shear stress which leads to the reduction
in the amplitude of the tidal currents.

Wind-driven currents in the Mississippi Sound depend strongly on
the wind direction. For example, assuming a uniform wind stress of
1 dyne/cm^2 from the West, our model results showed relatively stronger
currents   in   the   along-shore   direction   (Figure 9).   Notice   the
near-surface and near-bottom velocities differ not only in magnitude
but also in direction at some locations. This is partially associated

279   Sheng
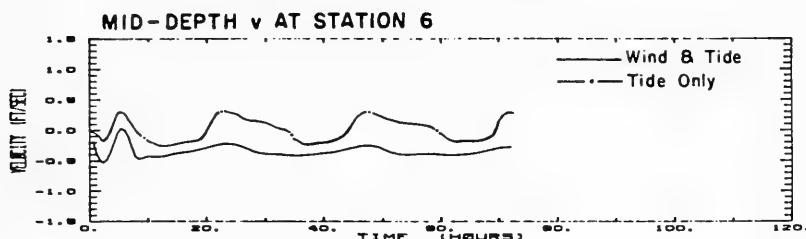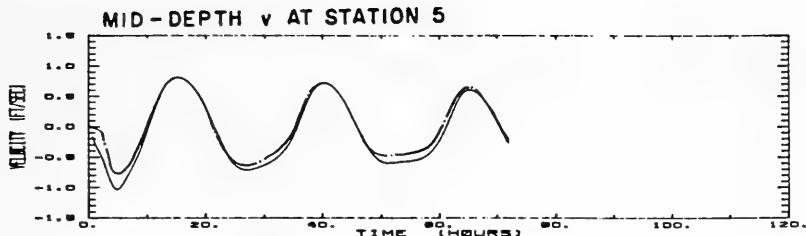
Figure 8. Mid-Depth Along-Shore Velocity at Stations 5 and 6 from 20 Sept. to 23 Sept., 1980. Tide and Wind Forcings.

with the pressure gradient caused by the wind set-up, which is on the order of 20 cm across the Mississippi Sound. According to a laboratory flume study on the erodibility of the Mississippi Sound sediments (Sheng, 1981), it is expected that the bottom shear stress generated by the strong Westerly wind in winter may cause significant resuspension of sediments.

TRANSPORT, RESUSPENSION, AND DEPOSITION OF COHESIVE SEDIMENTS

Transport Modes

The transport of cohesive sediment in the water column can be described by a conservation equation, similar to the heat or salinity equation, for the suspended sediment concentration. An equation similar to Eq. (5) can be written for the sediment concentration C. However, the vertical velocity in the sediment concentration equation should be composed of the sum of the fluid velocity (w) and a settling speed of the particles (w_s). In fresh water, the settling speed of cohesive sediment from a coastal environment shows a relatively flat spectral distribution. As the salinity increases, the sediment particles form aggregates and the spectral distribution becomes much sharper (Fig. 10). In this study, for simplicity, we assume the cohesive sediment in the Mississippi Sound can be described by one single settling speed. The settling speed of bottom sediment samples from the Sound was measured in laboratory, without adding dispersant to the samples, and a median settling speed determined.

The behavior of sediment in the water column depends on the

Sheng

UV VELOCITY AT TIME OF 24.0 HOURS AND SIGMA OF -0.125

(a) WIND

3.95E+01 (CM/SEC)

UV VELOCITY AT TIME OF 24.0 HOURS AND SIGMA OF -0.875

(b) WIND

3.09E+01 (CM/SEC)
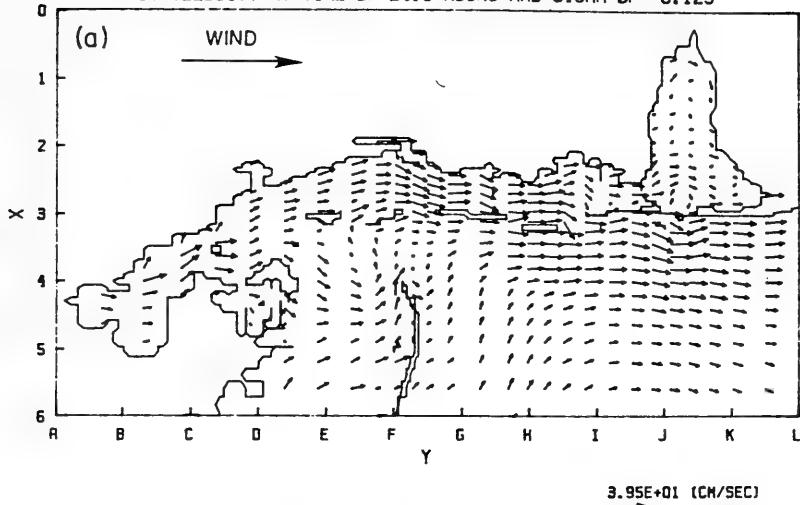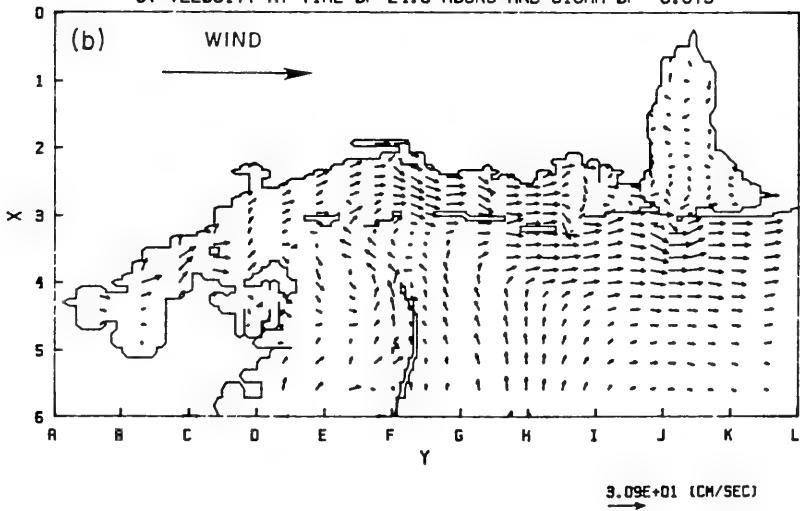
Figure 9.   Horizontal Velocities in the Vicinity of the Mississippi
             Sound at 24 hrs after the Application of a Westerly Wind
             with τ_y = 1.0 dyne/cm^2.
        (a). Near-Surface Currents, and
   (b). Near-bottom Currents.

Sheng
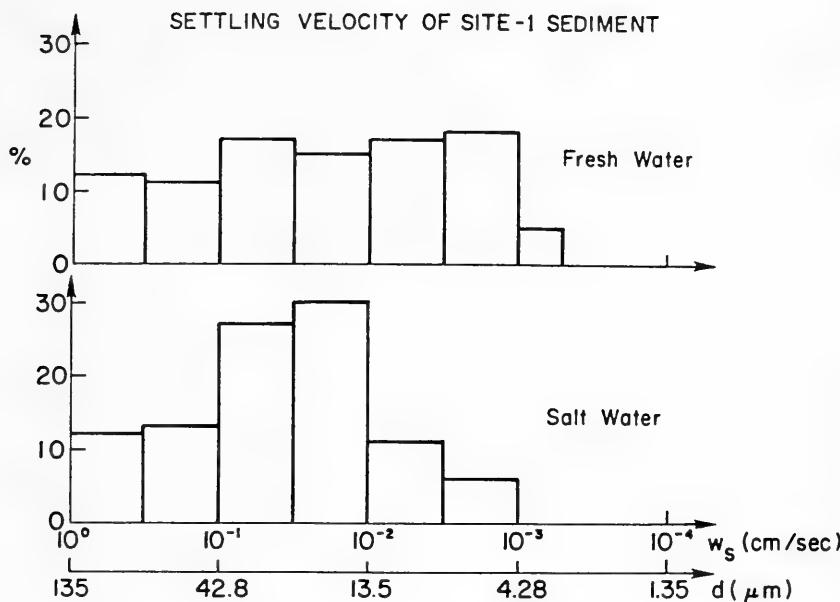
Figure 10.   Settling speed of Mississippi Sound Sediments in Fresh
and Salt Water.

cohesion and collision of sediment particles. Clay mineralogy and
other chemical parameters determine the cohesion of sediment particles.
However, in coastal waters where flow is generally turbulent, collision
between particles play a more dominant role than cohesion in
determining the state of flocculation. The frequency of collision
between various groups of particles depends on the turbulent shearing
rate on the dissipation scale and differential settling. Although our
hydrodynamic model is capable of computing the small-scale turbulent
shearing rate, there is insufficient data at this time to allow for
precise determination of model coefficients for the flocculation model.

Resuspension and Deposition Modes

    Resuspension and deposition of sediment at the sediment-water
interface play important roles in the distribution of suspended
sediment concentration. In general, resuspension and deposition depend
on (1) the hydrodynamic forces generated at the bed within the
turbulent bottom boundary layer; (2) bed properties such as sediment
composition, water content, bed preparation (settling) time, and
organic matter, bacteria, and benthos; and (3) fluid properties
including salinity, temperature, and pH of pore water and overlying
water.

    Effects of dominant parameters (shear stress, water content, bed
preparation time, and salinity) on resuspension and deposition were

282   Sheng

investigated in a laboratory flume (Sheng 1981; Sheng et al. 1982).
To prepare the bed, sediments are introduced into the flume,
resuspended, and allowed to settle for a period of 1 to 10 days. A
given bottom shear stress is then applied and the time history of
sediment concentration recorded until an equilibrium concentration is
reached, at which the resuspension balances the deposition. As shown
in Figure 11, resuspension as indicated by the equilibrium
concentration depends strongly on the applied shear stress. More than
an order of magnitude increase in equilibrium concentration can be
expected when the shear stress is increased by a factor of 5. Salinity
affects the aggregation of particles and hence the erodability of the
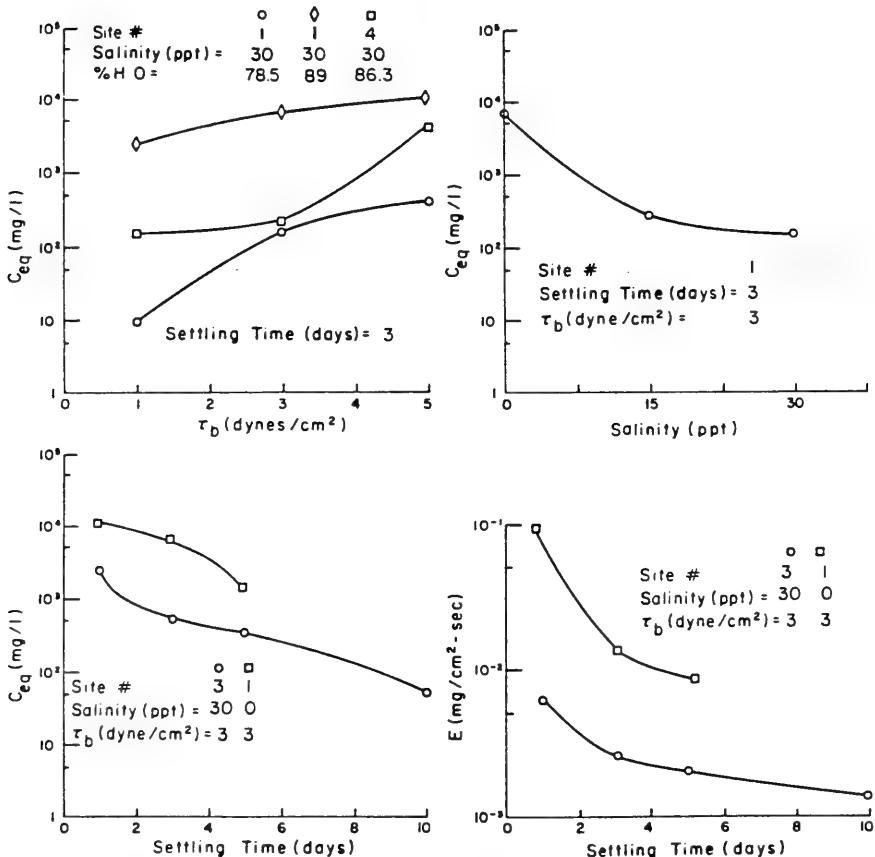

Figure 11(a). Equilibrium Suspended Sediment Concentration in
                Laboratory Flume as a Function of Applied Shear Stress,
         (b). Effect of Salinity,
         (c). Effect of Time History of the Bed, and
         (d). Resuspension Rate as a Function of Time History of the
                Bed.

Sheng

bottom sediments. The sediment becomes harder to erode at higher salinity, with most variation occurring between 0 and 15 ^{o}/oo. The sediment also becomes harder to erode as more time is allowed for the preparation of the bed. From the laboratory flume data, proper bottom boundary conditions for the sediment transport model can be derived in terms of the rate of resuspension (E) and deposition ($V_d C$) (Sheng, 1981). The bottom boundary condition for the sediment concentration (C) equation can be written as:

$$\text{Net Upward Flux} = w_s C - K_v \frac{\partial C}{\partial z} = E - V_d C \qquad (22)$$

where the deposition velocity $V_d > 0$ while the settling velocity $W_s < 0$.

Sediment Movement in the Mississippi Sound Due to a Westerly Wind

As an example to illustrate the important role of resuspension and deposition, we performed a 1-day simulation of sediment movement due to a Westerly wind.

Initially, the background concentration is assumed to be zero everywhere except within a square area (shown in Figure 5) where the concentration is 500 mg/l (newly introduced sediment). The sediment concentration is then computed with three different bottom boundary conditions: (1) zero net flux and zero settling speed, (2) with deposition and resuspension, but no resuspension of old sediment (vs. the newly introduced sediment) is allowed, and (3) deposition and resuspension allowed at all locations. For (2) and (3), a settling
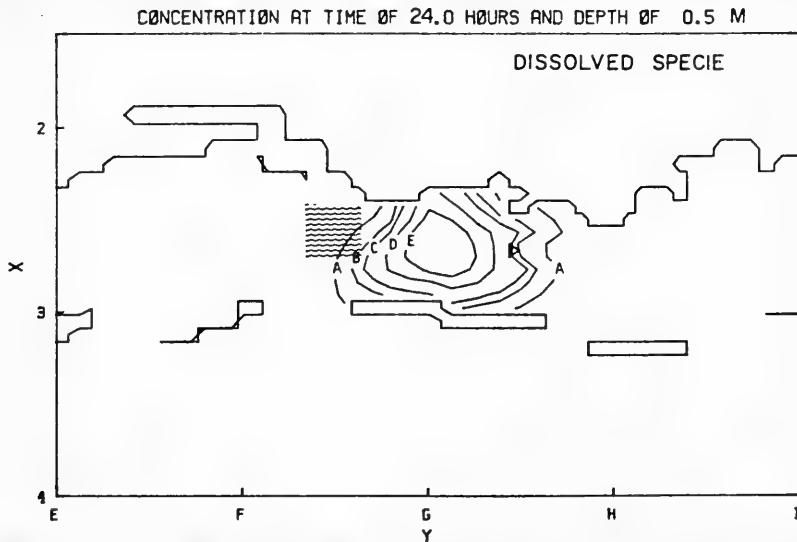

Figure 12.   Suspended Sediment Concentration at 0.5 m Depth at the End of 1-day Simulation. Westerly Wind; No Settling; Zero Net Flux at Bottom.

Sheng

CØNCENTRATIØN AT TIME ØF 24.0 HØURS AND DEPTH ØF 0.5 M

$W_S = -.05$ cm/sec
DEPOSITION
RESUSPENSION FOR NEW
SEDIMENT ONLY
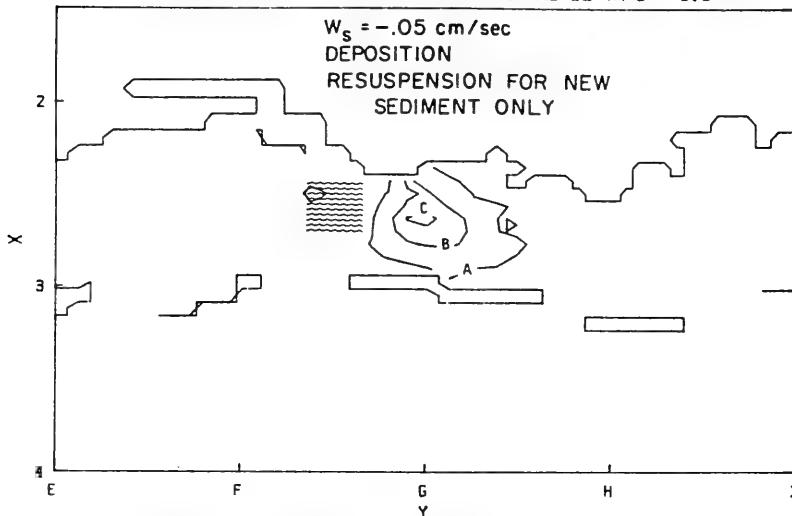
Figure 13. Same as Figure 12 except that $w_s = -0.05$ cm/sec; Deposition but no Resuspension for Old Sediment.

CØNCENTRATIØN AT TIME ØF 24.0 HØURS AND DEPTH ØF 0.5 M

$W_S = -.05$ cm/sec
DEPOSITION
RESUSPENSION

|← 20 km →|

9 CØNTØURS : [GM/(M**3)]
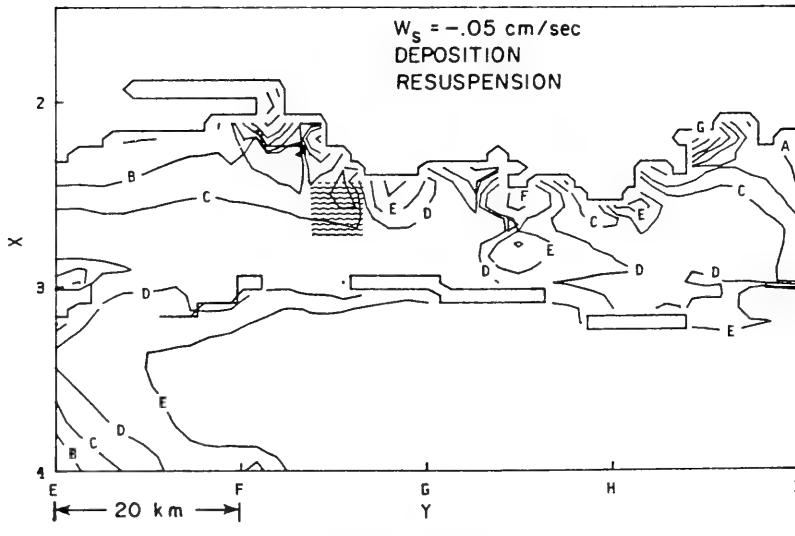
| 2.	10.	20.	50.	100.	250.	500.	750.	1000.
A	B	C	D	E	F	G	H	I

Figure 14. Same as Figure 12 except that $w_s = -0.05$ cm/sec; Deposition and Resuspension.

285   Sheng

speed of 0.05 cm/sec was used. The results at 0.5 m depth at the end of one-day simulation are shown in Figures 12, 13 and 14. It is clear that resuspension of sediment plays a dominant role in redistributing sediment. The difference in results for (2) and (3) reflects the importance of quantifying the time history of bottom sediments, which strongly affects the erodability as shown in Fig. 11.

BOTTOM BOUNDARY LAYER AND WAVE EFFECT ON SEDIMENT RESUSPENSION

The wave climate during the September period of 1980 was studied by means of a spectral wave hindcasting model modified for shallow water. The blockage effect of the barrier islands allows us to assume that most of the wave energy in the Mississippi Sound was derived from the wind fetch within the Sound. From 20 to 25 Sept., wind was generally from the Southeast at about 5 m/sec. Results of the wave model indicate wave height generally under 30 cm and wave period under 3 sec. At a station off Gulfport (Station 17), the wave-induced bottom stress was the highest among all stations and on the order of 5 dyne/cm^2 during the first day (Fig. 15a). However, wave-induced stress over most of the sound was generally not very strong, as can be seen in Fig. 15b, the bottom stress at a station off the Biloxi channel (Station 10) was generally less than 1.3 dyne/cm^2. These findings are consistent with the sediment concentration data collected during this time period, which showed a slight initial increase in concentration followed by primarily depositional events. We also found that linear wave theory and empirical bottom stress formula tend to overestimate the wave-induced bottom stress within an oscillatory boundary layer.
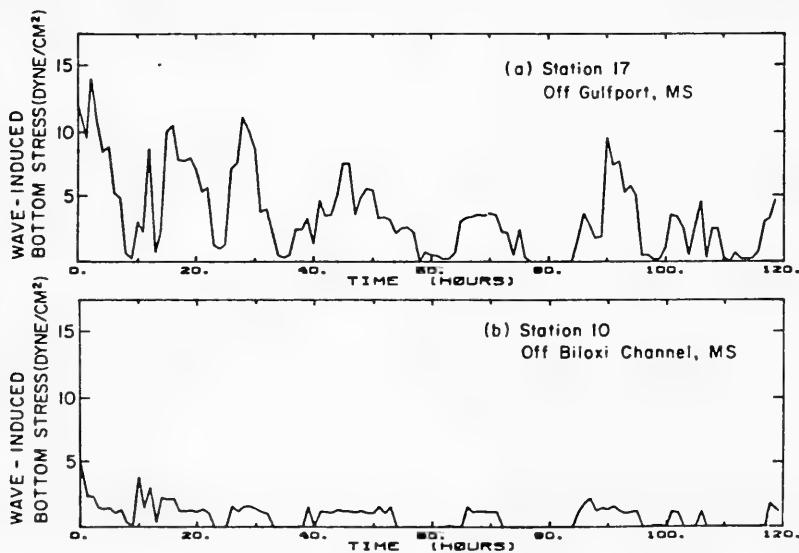

Figure 15.   Wave-Induced Bottom Stress at two Locations in the Mississippi Sound from 20 to 25 Sept., 1980.
         (a). Station 17 off Gulfport, MS.
         (b). Station 10 off Biloxi Channel.

Sheng

Detailed turbulent dynamics of the bottom bounday layer under a pure wave (Sheng, 1982) and current-wave interaction (Sheng and Lewellen, 1982) have also been studied using a Reynolds stress model. Contrary to the general belief, the presence of the wave was found to not always enhance the current-induced stress.

CONCLUSIONS AND RECOMMENDATIONS

An efficient three-dimensional numerical model of coastal currents has been developed and is operational. The model is suitable for detailed short-term simulations as well as longer-term simulations. Currents in Mississippi Sound and adjacent offshore waters have been computed with the three-dimensional model. Results obtained during a five-day period in September 1980 agree very well with the measured data. Large spatial and temporal variation of bottom shear stresses exist within the area. Rate of resuspension of the Mississippi Sound sediments (primarily Smectite) has been determined experimentally and was found to increase with increasing shear stress, decreasing salinity, and shorter time-history of the bottom sediment. Studies are needed to elucidate the effect of turbulence on flocculation the current-wave interaction within the bottom boundary layer, and the inclusion of sediment time-history as a parameter in the mathematical model.

ACKNOWLEDGEMENT

References

Blumberg, A.F., 1975: "A Numerical Investigation into the Dynamics of Estuarine Circulation," Chesapeake Bay Institute Report No. 91, Baltimore, MD.

Bowden, K.F. and P. Hamilton, 1975: "Some Experiments with a Numerical Model of Circulation and Mixing in a Tidal Estuary," Estuarine Coastal Marine Sci., 3, 281.

Butler, H.L. and Y.P. Sheng, 1982: "ADI Procedures for Solving the Shallow-Water Equations in Transformed Coordinates," Proc. 1982 Army Num. Anal. and Comp. Conf., Army Research Office, pp. 365-380.

Donaldson, C.duP., 1973: "Atmospheric Turbulence and the Dispersal of Atmospheric Pollutants," in AMS Workshop on Micrometeorology (D.A. Haugen, ed.), Science Press, Boston, pp. 313-390.

Erikson, C.C., 1978: "Measurements and Models of Fine Structure, Internal Gravity Waves and Wave Breaking in the Deep Ocean," J. Geophys. Res., 83, pp. 2989-3009.

.

Kent, R.E., and D.W. Pritchard. 1959: "A Test of Mixing Length Theories in a Coastal Plain Estuary," J. Mar. Res., 18, pp. 62-72.

Leendertse, J.J., and S.K. Liu, 1975: "A Three-Dimensional Model for Estuaries and Coastal Seas, II: Aspects of Computation," Rand Report R-1764-OWRT.

Munk, W.H. and E.P. Anderson, 1948: "Notes on the Theory of the Thermocline," J. Mar. Res., 1, pp. 276-295.

Nihoul, J.C.J. and F.C. Ronday, 1983: "Three-Dimensional Marine Models for Impact Studies," Proc. 18th Int'l Conf. Coastal Eng., This Volume.

Reid, R.O. and R.E. Whitaker, 1976: "Wind-Driven Flow of Water Influenced By a Canopy," J. Waterways, Harbors and Coastal Eng. Div., Proc. ASCE, pp. 63-77.

Schureman, P. 1941: "Manual of Harmonic Analysis and Prediction of Tides," U.S. Department of Commerce Special Pub. No. 98, 317 pp.

Sheng, Y.P., 1980: "Modeling Sediment Transport in a Shallow Lake," in Estuaries and Wetland Processes (P. Hamilton, ed.), Springer-Verlag, Berlin, Heidelberg, pp. 299-337.

Sheng, Y.P., 1981: "Modeling the Hydrodynamics and Dispersion of Sediments in the Mississippi Sound," A.R.A.P. Report No. 455, 107 pp.

Sheng, Y.P., 1982: "Hydraulic Applications of a Second-Order Closure Model of Turbulent Transport," in Applying Research to Hydraulic Practice, (P. Smith, Ed.), ASCE, pp. 106-119.

Sheng, Y.P. and W.S. Lewellen, 1982: "Current and Wave Interaction within the Benthic Boundary Layer," EOS, 63, 3, pp. 72-73.

Sheng, Y.P. and W. Lick, 1979: "The Transport and Resuspension of Sediments in a Shallow Lake," J. Geophys. Res., 84, C4, 1809-1826.

Sheng, Y.P., W. Lick, R. Gedney, and F. Molls, 1978: "Numerical Computation of the Three-Dimensional Circulation in Lake Erie; A Comparison of a Free-Surface and a Rigid-Lid Model," J. Phys. Oceano., 8, pp. 713-727.

Sheng, Y.P., P.L. McCall, and J.B. Fisher, 1982: "Entrainment of Cohesive Sediments of the Gulf of Mexico," EOS, 63, 18, p. 358.